12-2010

Gamma Ray Bursts as Probes of Dust in the Evolving Universe

Adria Updike
Clemson University, aupdike@clemson.edu

Recommended Citation

Updike, Adria, "Gamma Ray Bursts as Probes of Dust in the Evolving Universe" (2010). *All Dissertations*. 656.
https://tigerprints.clemson.edu/all_dissertations/656

GAMMA RAY BURSTS AS PROBES OF DUST IN THE EVOLVING UNIVERSE

A Dissertation
Presented to
the Graduate School of
Clemson University

In Partial Fulfillment
of the Requirements for the Degree
Doctor of Philosophy
Physics and Astronomy

---

by
Adria C. Updike
December 2010

Accepted by:
Dr. Dieter H. Hartmann, Committee Chair
Dr. Sean D. Brittain
Dr. Mark D. Leising
Dr. Jeremy R. King

Abstract

Dust is ubiquitous in the universe. Understanding where it comes from and where we observe it can have major implications to all astronomical observations. In this study, we investigate how gamma ray bursts (GRBs) can be used as probes of dust in the evolving universe. Making the simplification that silicate dust comes from core collapse supernovae and that graphite dust is produced in the winds of low- to intermediate-mass stars, we present numerical simulations of the resulting dust evolution in GRB hosts and show how the SEDs evolve. Dust extinction laws are re-derived from scattering theory of small particles and the dependence of the extinction laws on varying dust properties are explored. Finally, we compare the predictions of our simulations of dust evolution and our modeled extinction laws to 82 GRB SEDs spanning the last 13 years. We measure the column densities of graphite and silicate along the line of sight to these GRBs as well as the overall visual extinction A_V in the co-moving frame and the dust-to-gas ratios. We find no clear evolutionary trend with respect to the A_V values or the graphite-to-silicate ratio as a function of redshift. However, we do detect more silicate than graphite in nearly every burst, implying high production rates of silicate in core-collapse supernovae, and we discover a graphite component previously undetected in 14 GRBs in our sample. These results are examined in the context of our evolutionary models, and we discuss the implications for star formation in the early universe.

Acknowledgments

I would like to acknowledge my committee, Dieter Hartmann, Jeremy King, and Sean Brittain, for their comments and suggestions.

This dissertation greatly benefited from discussions with D. Alexander Kann, Thomas Krühler, Marco Nardini, Patricia Shady, Richard Ardent, Eli Dwek, Eric Bubar, and Bethany Johns.

Thanks also go to my parents, Claudia and Ron Updike, and to my sister Tessa for their support.

Table of Contents

List of Tables

List of Figures

Chapter 1

Introduction

1.1 Gamma Ray Bursts

Gamma ray bursts (GRBs) were first discovered in 1967 by the Vela satellites (Klebesadel et al., 1973) put in orbit to monitor violations of the Nuclear Test Ban Treaty. The first indication the bursts were extragalactic in origin came in 1992 with the publication of the BATSE (Burst and Transient Source Explorer instrument on the Compton Gamma Ray Telescope) source catalog (Meegan et al., 1992) showing a isotropic distribution of bursts on the sky (see Figure 1.1). The cosmological nature of bursts was finally established in 1997 with the measurement of the redshift of GRB 970228 (van Paradijs et al., 1997) firmly establishing GRBs as extragalactic in origin and their potential as probes of the evolving universe.

1.1.1 The Fireball Model

The standard model for GRB emission is that of a relativistic fireball, first proposed by Cavallo & Rees (1978). Internal shock collisions give rise to the observed gamma ray emission, while external shocks colliding with the external medium produce the afterglow observed in the x-ray, UV, optical, NIR, and often radio regimes. In this analysis, we will be concentrating on the spectral energy distributions (SEDs) of GRBs in the UV-optical-NIR regime. For this, it is important to understand the mechanisms that give rise to the observed SEDs.

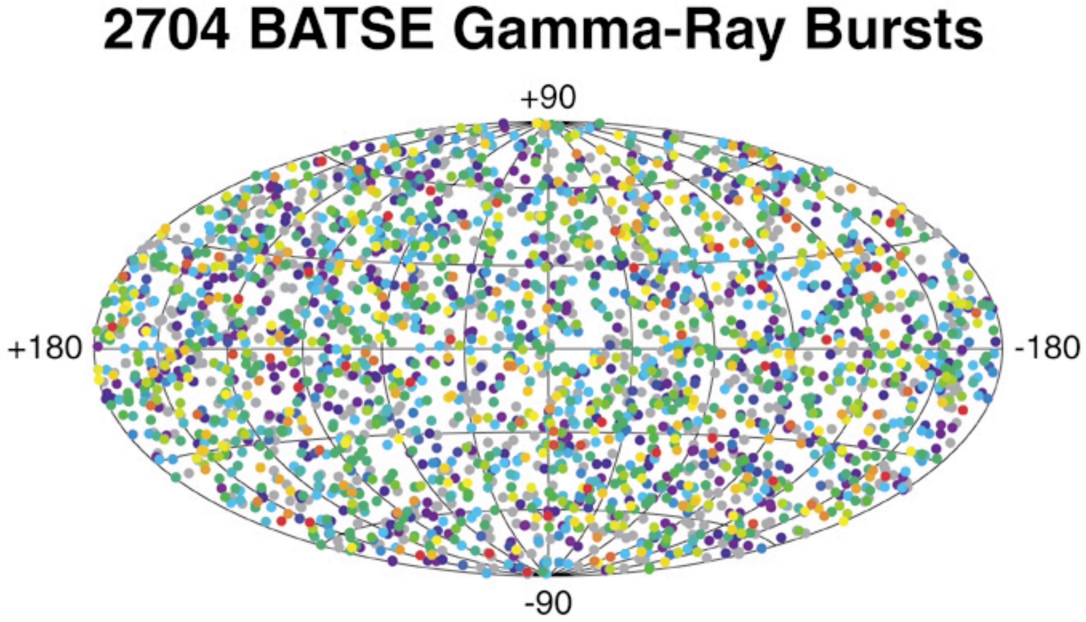

Figure 1.1: The spacial distribution of GRBs observed by BATSE, from Meegan et al. (1992).

Sari et al. (1998) proposed a population of electrons with energies γ_e and a power law distribution $N(\gamma_e) \sim \gamma_e^{-p}$ emitting synchrotron radiation to explain the observed gamma ray emission from early GRB observations. The Lorentz factor of the electrons $\gamma_e > \gamma_m$, where γ_m is the minimum Lorentz factor calculated as $\gamma_m = \varepsilon_e(p-2)/(p-1)(m_p/m_e)\Gamma$ and ε_e is a fraction of the shock energy deposited on the electrons. The typical energy of the electrons is $E_{min} = \gamma_m m_e c^2$. The spectral index p was originally thought to have to be greater than 2, but many cases have now been found in which $p < 2$ with the constraint that the electron energy is finite (e.g., Panaitescu & Kumar, 2001; Panaitescu, 2005).

Electrons with energies above some critical energy γ_c will cool to γ_c on a cooling timescale t (in the frame of the observer), where $\gamma_c = (6\ \pi m_e c)/(\sigma_T \Gamma B^2 t)$. B is the magnetic field and σ_T is the Thomson scattering cross section. As the electrons cool, the frequencies and energies emitted vary, resulting in a segmented SED (Sari et al., 1998, see Figure 1.2). The lowest frequency segment consists of the tails of the electron emission spectra and the overall flux F_ν is proportional to $\nu^{1/3}$. The intermediate frequency SED dependence will vary according to whether the electrons follow a slow or fast cooling mode, and the highest energy electrons cool quickly, emitting most of their energy at the synchrotron frequency with a flux dependence $F_\nu \propto \nu^{-p/2}$.

In the fast cooling case, $\gamma_m > \gamma_c$ and the electrons must cool to γ_c. When $\gamma_c > \gamma_m$, only electrons with $\gamma_e > \gamma_c$ will cool within a time t; these electrons do not make up the bulk of the electron distribution, so this is the slow cooling case. Fast cooling is thought to occur during the initial GRB energy release ($t < t_0$), followed by slow cooling ($t > t_0$). All of the GRB SEDS in our sample were observed during the slow cooling phase.

Following the work of Sari et al. (1998), we can determine the flux F_ν observed during the slow cooling phase.

$$F_\nu = \begin{cases} (\nu/\nu_m)^{1/3} F_{\nu,max} & \text{for } \nu_m > \nu \\ (\nu/\nu_m)^{-(p-1)/2} F_{\nu,max} & \text{for } \nu_c > \nu > \nu_m \\ (\nu_c/\nu_m)^{-(p-1)/2} (\nu/\nu_c)^{-p/2} F_{\nu,max} & \text{for } \nu > \nu_c \end{cases} \tag{1.1}$$

The cooling frequency ν_c depends on the initial bulk Lorentz factor of the material as well as the magnetic field strength B. At the time the SED of a GRB is observed, the cooling break will lie somewhere between the far-infrared wavelengths and the x-ray regime. As we can see in Figure 1.2, the difference in the spectral index β on either side of the cooling regime differs by a factor of 1/2; after the break, the slope becomes steeper.

Many people have tried to fit the UV/optical/NIR SEDs with a single power law, which assumes no cooling break between the regimes; Schady et al. (2007) in particular had luck with this for a set of seven early *Swift*-observed GRBs, several of which are included in this analysis, finding no significant difference between a single power-law fit and a broken power-law with index difference 1/2 to take the cooling break into account. However, other bursts (e.g., Updike et al., 2008) found a significantly better fit to the complete SED with a cooling break included.

For this analysis, we will not include the x-ray portion of the SED. Nearly half of our sample was taken before the *Swift* era, so there is no one set of x-ray data to be used, and we do not have accompanying light curve data with which to constrain the cooling break or multiple epoch SEDs. We will further assume that the cooling break does not occur within our frequency range, and only fit a single value for the spectral index β. This is a potential source of error in our fitting routines. The SEDs in our sample were constructed to correspond to a time of one hour after the GRB trigger (gamma ray emission first observed), and we can see from Figure 1.2 that the location cooling break frequency ν_c is proportional to $t^{-1/2}$ in the observer frame; at early times, the cooling frequency

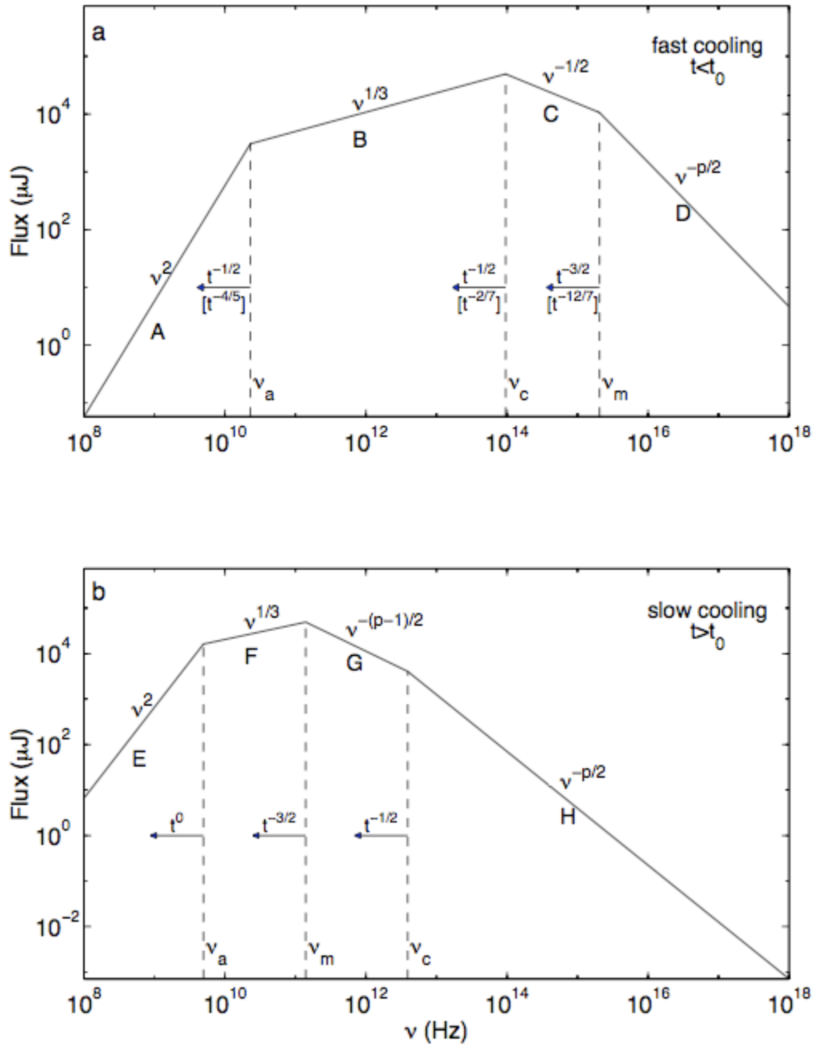

Figure 1.2: Synchrotron emission spectrum for a GRB from Sari et al. (1998). Several frequencies characteristic of synchrotron emission are shown, including the synchrotron self-absorption frequency (ν_a), the average electron frequency (ν_m) and the cooling frequency (ν_c). As the electrons cool, emitting photons, the cooling frequency moves through the spectrum towards lower frequencies. All of the GRBs in our sample were observed during the slow cooling regime, and we make the standard assumption that the cooling frequency lies between the x-ray and optical/UV regime.

is large, and then decreases. Thus, we will assume for this analysis that the cooling frequency is greater than that of our bluest data point and that the flux $F_\nu \propto \nu^{-(p-1)/2}$, or $\beta = (p-1)/2$.

Note that the spectrum of the GRB is a simple power law under the above assumption in the region we are interested in (UV, optical, and NIR). The simple nature of the spectrum can be reproduced photometrically without the need for spectroscopy; due to the rapid fading nature of bursts, spectroscopy is not always possible or available. For our analysis, we make the standard assumption that the only deviation from a power law spectrum are the result of either dust extinction of Lyman-α absorption. This makes GRBs potentially very useful probes of the early universe. Quasars have also been used as probes of dust (e.g., Maiolino et al., 2004; Kulkarni et al., 2007) but due to the complicated spectra of a quasar, spectroscopic data is necessary to extract useful information about dust composition.

1.1.2 *Swift* and Hydrogen Column Densities

The *Swift* satellite, launched in 2004, has detected hundreds of GRBs. It includes BAT, the burst alert telescope, XRT, the x-ray telescope, and UVOT, the ultraviolet and optical telescope. The XRT on *Swift* measures hydrogen column densities along GRB sightlines by employing oxygen as a tracer of hydrogen and measuring soft x-ray absorption by oxygen (both neutral and ionized). Assuming solar abundances (Anders & Grevesse, 1989), the hydrogen column density is extracted using the XSPEC package (Arnaud, 1996).

The hydrogen column densities extracted by *Swift* do not agree well with those extracted from DLA systems probed by optical and UV spectroscopy. Soft x-ray absorption usually leads to column densities an order of magnitude higher than those observed through optical spectroscopy, leading authors to conclude that the x-rays are probing highly ionized gas invisible in the UV (Watson et al., 2007). For this analysis, we will utilize *Swift* XRT measurements of neutral hydrogen column densities N_H for our dust-to-gas measurements, keeping in mind that our estimates will be a lower limit on the dust-to-gas ratio, which could be as much as an order of magnitude higher. However, the large set of *Swift* XRT data makes this a more useful measure of N_H than extracting it from the few individual papers that were able to measure it in a DLA system.

Next, we investigate the origin and evolution of extinction-causing dust in galaxies.

1.2 Cosmic Chemical Evolution

1.2.1 Big Bang Nucleosynthesis

As first proposed by Alpher et al. (1948), the big bang can explain the origin of the light elements (hydrogen, helium, lithium, and beryllium). Between 3 and 20 minutes after the big bang, density and temperature in the early universe supported the necessary conditions for nucleosynthesis, resulting in the production of helium, lithium, and beryllium, as well as deuterium. After about 379,000 years, hydrogen formed during the epoch of recombination (Spergel et al., 2007), and the universe was made up of about 75% hydrogen, 25% helium, and 0.01% deuterium, and trace amounts lithium and beryllium (percentages given by mass).

1.2.2 Stellar Nucleosynthesis

Elements heavier than those created in big bang nucleosynthesis were later created in massive stars and the resulting supernova explosions. The earliest stars (referred to as Population III stars) were likely extremely massive with no metallicity (exclusively hydrogen and helium). Hydrogen burning via the pp cycle created helium in these massive stars. As the hydrogen in the core became depleted, the core contracted due to the loss of radiation pressure from fusion, creating the conditions in massive stars for the next phase of nucleosynthesis; helium burning begins around 2×10^8 K, resulting in the creation of carbon through the triple-alpha process (which can also result in the production of oxygen as carbon fuses with helium). After the helium burning stage, the stellar core contracts once again, and as it reaches 6×10^8 K, carbon burning produces magnesium, neon, sodium, oxygen through the triple-alpha process. Further contraction leads to neon burning at temperatures of 1.2×10^9 K, leading to oxygen and magnesium. Oxygen burning begins at 1.5×10^9 K after an inert core of oxygen and magnesium have formed in the star, producing sulfur, phosphorus, and silicon, and magnesium and helium form silicon as well. After the oxygen burning process is complete, the remaining sulfur and silicon can begin burning at temperatures in the range of $2.7 - 3.5 \times 10^9$ K to create argon, calcium, titanium, chromium, iron, and nickel through the alpha process, at which point no further elements can be formed through an exothermic process. The radioactive beta-plus decay of ^{56}Ni leads to ^{56}Co followed by an additional beta-plus decay leaves us with ^{56}Fe. At this point, the stellar core contracts even further, creating a black hole at the center and blowing off the outer layers of the star in a type II supernova explosion (core-collapse supernova). Heavier elements can now be formed through neutron-caputure (*r*-process) from the resulting release of neutrons (Clayton, 1983; Carroll & Ostlie, 1996).

The second generation of stars (Population II stars) use existing carbon and oxygen from Population I supernova to create helium and nitrogen through the CNO cycle, while those with masses less than 1.2 $M_\odot$ are not massive enough for the CNO cycle and use the pp cycle instead.

Population II and later Population I stars will be much less massive on average than the original Population III stars, and thus will not undergo all of the previously-discussed fusion reactions. While hydrogen burning is the definition of a star, only stars with masses greater than about 0.5 $M_\odot$ can fuse helium, stars with about 3 $M_\odot$ will be capable of creating the necessary conditions in the core for helium burning to carbon, and those with masses greater than 8 $M_\odot$ can burn carbon as well.

1.2.3 Stellar Evolution

Many of the heavy elements created by massive stars will be locked up in the resulting stellar remnants. Stars with solar masses in the range 0.07 - 10 $M_\odot$ will end their lives as white dwarf stars. Stars with masses less than 0.5 $M_\odot$ are thought to end up as a helium white dwarf mainly composed of helium nuclei (Laughlin et al., 1997).

Between 0.5 and 8 $M_\odot$, carbon and oxygen form in the star leading to a carbon-oxygen core with helium- and hydrogen-burning shells. As this star moves from hydrogen to helium burning, it evolves off the Main Sequence and onto the Asymptotic Giant Branch (AGB, see Figure 1.3). As a final step in its evolution, the outer layers of the star are blown off to create a planetary nebula, leaving a carbon-oxygen white dwarf star (Carroll & Ostlie, 1996).

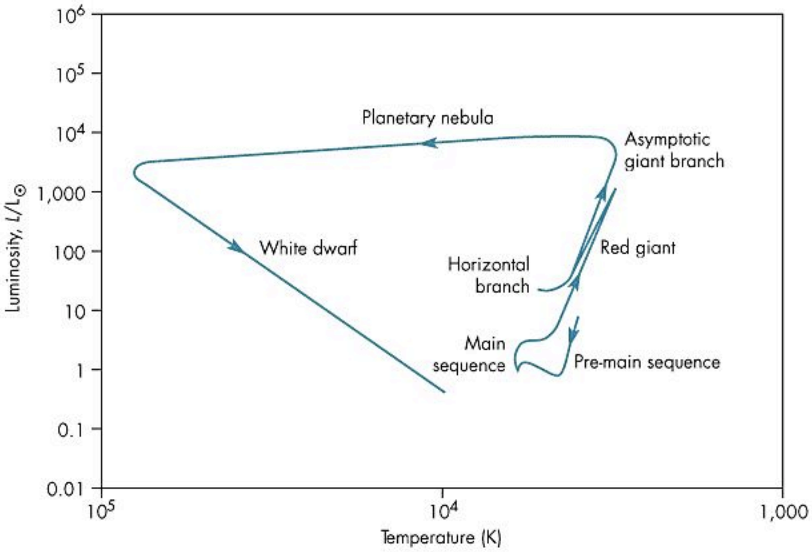

Figure 1.3: AGB star evolution on the Hertzsprung-Russel diagram from Albert Zijlstra's website, http://iapetus.jb.man.ac.uk/Teaching/IntroAstro/StellarEvolution.html.

For stars greater than 8 $M_\odot$, carbon and heavier element burning will commence as discussed above. Below 10 $M_\odot$, the star may result in a white dwarf composed of oxygen, neon, and magnesium (having insufficient mass to fuse neon, Nomoto, 1984). Stars above 10 $M_\odot$ will explode as type II supernovae, leaving behind a neutron star (if the initial stellar mass was between 10 and 20 $M_\odot$) or black hole (if the initial solar mass exceeded 10 $M_\odot$) in the process.

1.2.4 Chemical Evolution

The processes discussed above outline the production of light and heavy elements in our universe. As time progresses, we expect to see an increase in the metallicity of stars now forming as opposed to those that formed in the early universe when overall metallicity was low. As we can see in Figure 1.4 from Savaglio (2010), quasar Damped Lyman-alpha (DLA) systems show an overall trend towards lower metallicity at higher redshifts, as expected from cosmic chemical evolution models. However, GRB DLA systems do not show the same trend. Though fewer in number than QSO DLA systems, we do not see clear evolution in GRB DLA systems towards lower metallicity at higher redshifts as expected. This suggests GRB hosts might not be good indicators of chemical evolution; while QSO systems probe intervening systems, GRBs probe their own host galaxy and any inhomogeneities within that galaxy. Star forming regions in which GRB progenitor stars form maybe be artificially enhancing the metallicity in that specific region, which is then reflected in the DLA.

In this work, we will look for evidence of chemical evolution in the dust composition of gamma ray burst (GRB) host galaxies as a function of redshift. In the upcoming sections, we discuss the role that dust plays in the universe, how and where it is formed, its effect on light, and how we can observe it. We will then introduce GRBs as probes of dust.

1.3 Dust in the Universe

Dust refers to particles from a few molecules to about a millimeter in size, and makes up about 1% of the interstellar medium in our own galaxy. Dust is ubiquitous in the universe, reprocessing up to 50% of the light we receive. Thus it is vital that we understand the effects of dust on light in order to fully understand the implications of our observations.

The first documented observations of light absorption were by Wilhelm Struve in the mid-nineteenth century; he completed counts of stars in multiple directions and showed that the number

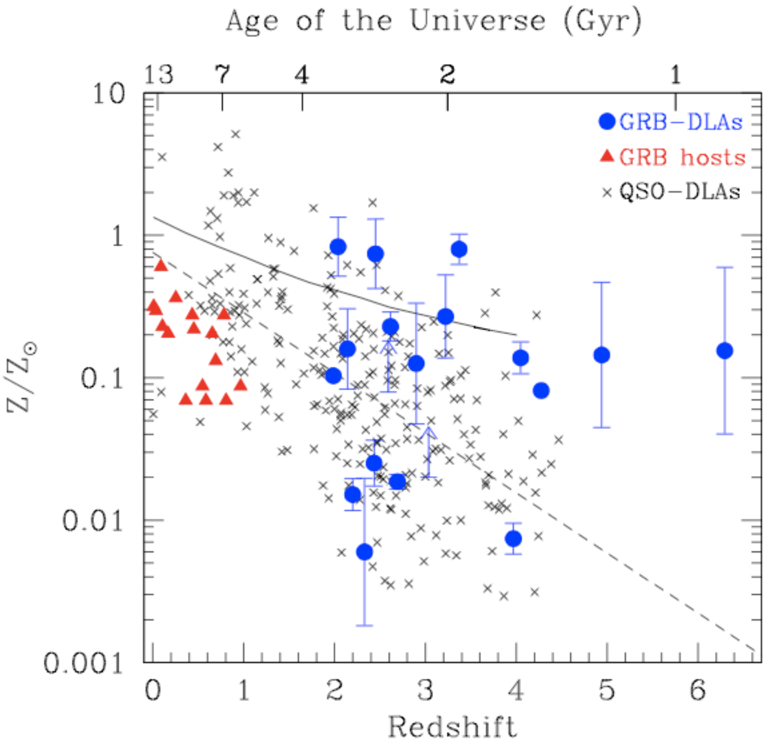

Figure 1.4: Quasar and gamma ray burst host galaxies and damped Lyman-alpha systems as a function of redshift (Savaglio, 2010). While quasars show an overall trend towards lower metallicity at higher redshifts, GRB host galaxies do not.

of stars appeared to decrease with distance from the Sun, leading him to hypothesize that the light from more distant stars was somehow being blocked from reaching us (Struve, 1847; Whittet, 2003). This work was expanded on by Barnard, who suggested that the darker regions in the sky may contain matter that scattered and absorbed starlight (e.g., Barnard, 1913). This was confirmed years later by Trumpler, who was deriving the distances to open clusters using photometric and spectroscopic observations, and noted that his distances had a systematic error due to absorbers along the line of sight, increasing with distance (Trumpler, 1930). Trumpler to showed that the amount of extinction as a function of distance was roughly inversely proportional to the wavelength in the optical regime, suggesting the absorption was caused by small particles close to the size of the wavelength of light hitting them. A detailed coverage of scattering and absorption by particles can be found in Section 2. The preceding observations led to wide-scale studies of dust in our galaxy and others in an attempt to understand the role that dust plays in the universe.

1.3.1 Source Extinction by Dust

The brightness of a star in a particular band λ located within the MW is expressed by Eq. 1.2,

$$m_\lambda = M_\lambda + 5\ \log_{10} d - 5 + A_\lambda \tag{1.2}$$

where m_λ is the apparent magnitude of the star, M_λ is the absolute magnitude of the star, d is the distance to the star (in pc) and A_λ is the number of magnitudes by which the star is extincted. The number of magnitudes of extinction obviously will depend on the distance to the star - namely, the optical depth. We know that the intensity of light from a source depends upon the optical depth to the source,

$$I_\lambda = I_{\lambda,0}\, e^{\tau_\lambda} = d. \tag{1.3}$$

With an optical depth τ_λ of zero, the intensity of the light is not diminished. The difference in magnitude between two sources can be expressed as

$$m_1 - m_2 = -2.5 \log_{10}\left(\frac{F_1}{F_2}\right). \tag{1.4}$$

Combining Eq. 1.4 and Eq. 1.3, where m_1 is the emitted light from the star m_λ and m_2 is the light received from the star $m_{\lambda,0}$ and A_λ is the difference $m_\lambda - m_{\lambda,0}$,

$$m_\lambda - m_{\lambda,0} = -2.5 \log_{10}\ e^{-\tau_\lambda} = 2.5\tau_\lambda \log_{10} e = 1.086\tau_\lambda = A_\lambda \tag{1.5}$$

The optical depth of a medium is simply the integral of the number density of particulate scatters multiplied by the cross-sectional area of the scattering particles.

$$\tau_\lambda = \int_{a_-}^{a_+} n_d\, \sigma_\lambda da = N_d\, \sigma_\lambda \tag{1.6}$$

The quantity N_d is the dust grain column density. A longer version of this derivation can be found in Rybicki & Lightman (1986) and Carroll & Ostlie (1996).

1.3.2 Theories of Dust Formation

1.3.2.1 Dust Formation in Supernovae

Supernovae as a possible source of interstellar dust (Hoyle & Wickramasinghe, 1970; Clayton, 1975) had been suggested many years before it was conclusively observed. Light echoes from SN1979c (Dwek, 1983) hinted at dust, but it was not until SN1987A that it was directly observed (Moseley et al., 1989). However, determining the exact amount of dust that formed was observationally challenging as it depended quite strongly on assumptions about mixing in the SN itself. Ercolano et al. (2007) reported the detection of carbon and silicate dust in SN1987A using *Spitzer*, followed by similar detections in other supernovae (i.e., Sugerman et al., 2006). How much dust is really being produced in these supernovae?

Early attempts to answer the question (Todini & Ferrara, 2001) initially appeared useful (Maiolino et al., 2004; Perley et al., 2010) but ultimately relied on poor assumptions; this particular model relied on classic nucleation theory, but the timescales over which dust forms through nucleation are much longer than the time scales on which the medium in a supernova remnant changes significantly. A more recently proposed kinetic approach (Cherchneff & Dwek, 2009, 2010) uses the formation of small molecular clusters to build large molecules and grains. The results of these recent analyses will be used in this analysis.

1.3.2.2 Nucleation in Stellar Atmospheres

Nucleation refers to the formation of grains in stellar atmospheres by the cooling and condensation of gases into monomers (an atom or molecule) and the subsequent build up of monomers into clusters through random encounters. Classically, a gas will condense when its partial pressure exceeds the vapor pressure, which happens most efficiently at temperatures well below the condensation temperature of the material. As these condensed particles collide with others of the same species, they build up into grains or drops. Through this process, grains are built up which are chemically identical to the original gas content.

However, nucleation theory is limited in scope. In the atmospheres of stars, nucleation time scales may be too large to occur due to lower pressures. Nucleation theory does not describe the buildup of multi-element grains.

Dust can form in the outer atmospheres of massive stars where the atmospheric temperature has dropped below the condensation temperature of the dust grains. These intermediate mass stars have evolved off the main sequence into the giant branch, and include giants, supergiants, and asymptotic giant branch (AGB) stars. Bode (1988) estimated the site for dust formation in stellar atmospheres between 10 and $10^4 - 10^5$ stellar radii (R_S) assuming a grain condensation temperature of 1000 K. As the number density of particles decreases linearly with distance from the star, grain formation is most likely to take place in the high density ($n \sim 10^{19}$ particles m^{-3}) regions close to the central star. The high density of elements in the stellar wind outflow make this an ideal environment for the formation of dust grains on rapid time scales. Stellar winds from intermediate mass stars move outwards at velocities on the order of 10 km/s. However, many of these stars will end their lives as planetary nebulae, with higher rates of gas outflow (20 - 50 km/s) which may result in the re-processing of many materials formed as outlined below.

The types of grains that can form in stellar atmospheres depends largely on the relative abundances of several elements, particularly nitrogen, carbon, and oxygen, in the star itself. Nitrogen forms the stable gaseous form N_2 readily at high temperatures and can maintain that form at lower temperatures; carbon and oxygen form the stable gas CO which can also exist at lower temperatures. Therefore, nitrogen from the winds of massive stars will be locked up in N_2 and unavailable to form grains. The relative ratio of carbon to oxygen determines which, if either, will be available to grain formation as the early formation of CO gas will lock up the less abundant element. Massive stars may go through many periods of mass loss, and the ratio of carbon and oxygen expelled in these incidents may not be the same.

The most abundant molecules in gaseous form which can contribute to solids are Fe, Mg, SiO, and H_2O. These are still in gaseous form around T $\sim$ 1500 K, where the first rare metals (tungsten, corundum, perovskite) begin to condense. As these metals are not abundant, they contribute little to the dust content of the ISM. Around 1200 to 800 K, the more abundant solids begin to form; magnesium silicates and metallic iron, leading to the chemical production of magnesium silicate oxides (enstatite, forsterite). The temperature falls to 700 K and below as we continue to move away from the massive star, the rest of the metallic elements condense, and iron oxidizes (forming FeO). Water-ice begins to form around 200K and below.

A carbon-rich environment (number of carbon atoms exceeds the number of oxygen atoms by at least 10%) leads to favorable conditions for the formation of PAHs (polycyclic aromatic hydrocarbons). A good deal of hydrogen must also exist for this to occur.

Red giant stars, the late evolutionary stage of stars in the mass range of 0.5 – 10 $M_\odot$, can be enriched by carbon through a convective 'dredging up' process, bringing carbon to the surface of the star and hence enriching the stellar atmosphere and resulting dust products with carbon (in particular, ^{12}C from helium burning). When either carbon or oxygen is represented in higher amounts than the other, the one with lower abundance will be locked up in CO form and the resulting higher abundance element will be responsible for either the formation of silicate or graphite grains in the stellar atmosphere.

Low mass (M, K spectral type) stars typically undergo a mass loss on the order of 10^{-7} $M_\odot$ per year in their red giant phase. The contribution to the overall dust content of the galaxy may appear negligible until one recalls that the majority of stars are cool, low mass stars. As the spectral type decays (photospheric temperature drops) we find higher rates of mass loss for stars. It has been suggested (Wannier et al. 1990) that dust plays a role as a catalyst for mass loss in low-mass stars.

In the atmospheres of low-mass stars, the radiation pressure from the radiation hitting the particles far exceeds the gravitational attraction of the particle to the star (by $\sim$ 2000 times for carbon grains; $\sim$ 40 for silicates – it depends on the size of the particle as well as its absorbing and scattering properties). The aforementioned properties also determine the size to which the grain will grow before being ejected from the atmosphere of the star. As the grains are pushed away from the star through radiation pressure, the gas in the atmosphere induces frictional drag forces on the particles, which in turn imparts momentum to the gas, driving additional mass loss.

It is estimated that low mass stars can contribute up to 40% of the dust formed in the galaxy today (Gehrz 1989, etc.). However, it can take more than 10 Gyr for these stars to evolve to the point where they are ejecting dust, making them more recent contributors to the dust mass of the galaxy.

1.3.3 Observational Evidence of Dust Composition

Studies of interstellar depletions (Savage & Sembach, 1996) as compared to Solar System abundances (i.e., Anders & Grevesse, 1989) tell us that a good deal of elements are locked up in the solid phase (i.e., dust) and are thus not observed in the gas phase through spectroscopy (assuming systems near us have similar metallicities). These depletions increase in molecular clouds, which can be accounted for by higher densities of material hitting dust grains with greater frequency and

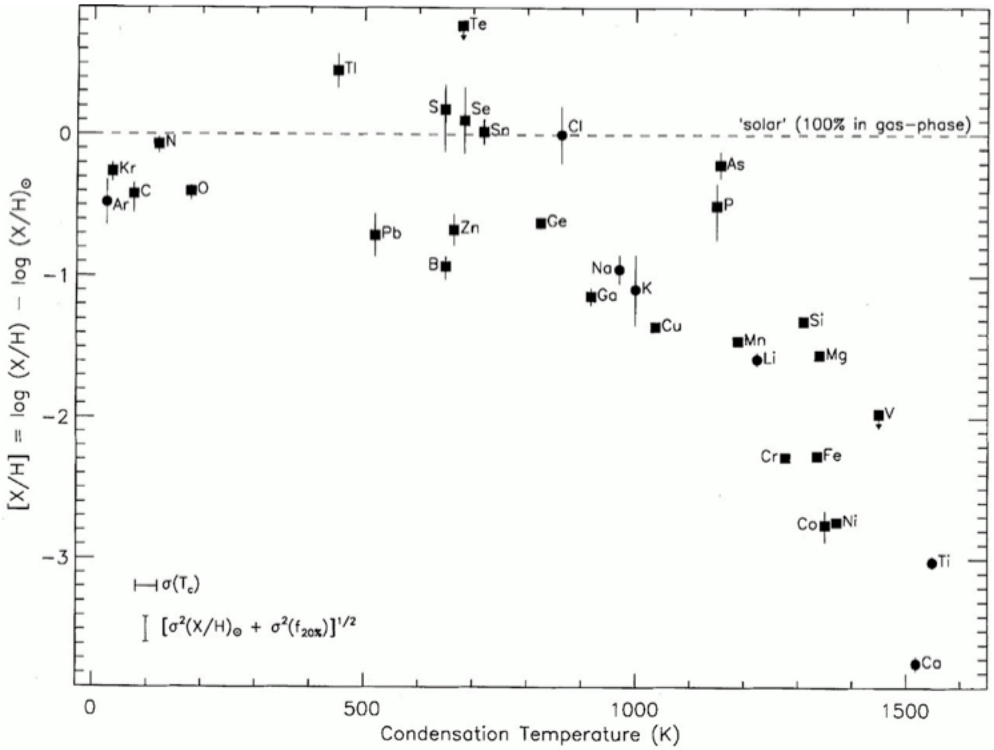

Figure 1.5: Graph of interstellar depletions from Savage & Sembach (1996). Elements with high condensation temperatures are found to be the most depleted.

depleting onto the grains.

Fig. 1.5 shows the elemental depletions for diffuse clouds from Savage & Sembach (1996) as a function of condensation temperature. Condensation temperature is defined as the temperature at which 50% of the material has condensed into solid form. Elements which can condense at high temperatures are more depleted along this line of sight towards ζ Oph. In stellar atmospheres, elements with higher condensation temperatures will condense first, resulting in greater depletion.

1.4 Organization

In this paper, we start by calculating the extinction properties of graphite and silicate particles and the construction of extinction curves in Section 2. We then apply these models to GRB SED data and discuss fitting routines in Section 3. In Section 4, we model dust in evolving galaxies and attempt to predict evolutionary trends in our data. In Section 5 we discuss the results of our dust extinction fits in the context of our galaxy evolution models.

Table 1.1: Solar System Abundances

Element	Atomic Number	ppm
H	1	10^6
C	6	360
N	7	93
O	8	676
Na	11	2
Mg	12	39
Al	13	3
Si	14	35
P	15	0.4
S	16	19
Ca	20	2
Cr	24	0.5
Fe	26	32
Ni	28	2

Chapter 2

Dust Extinction Law Calculations

2.1 Introduction

Dust extinction produces modifications to the spectral energy distribution (SED) of a gamma ray burst (GRB) along the line of sight through the host galaxy. A GRB SED is a simple power law caused by synchrotron emission from electrons. The presence of dust in the host galaxy causes wavelength-dependent extinction and can be modeled by a combination of silicate and graphite particles.

This model can prove valuable for probing the star formation history of the universe. If we assume all silicate dust comes from core-collapse supernovae (Todini & Ferrara, 2001; Cherchneff & Dwek, 2010) and all graphite dust comes from low- to intermediate-mass evolved stars (asymptotic giant branch, or AGB stars, Karakas, 2010), we can use this model to constrain the period at which AGB stars first began to contribute dust to galaxies. GRBs are a potential probe of this changing dust composition in time.

We begin by introducing the method for calculating dust extinction as a function of wavelength, particle size, temperature, and composition (Section 2.2). We then discuss the particular cases of silicate (Section 2.3.1) and graphite (Section 2.3.2).

2.2 Calculating Extinction

We will assume a mixture of graphite and silicate particles for our dust composition. The particles will be approximated as spheres. The optical depth (directly proportional to the extinction A_λ) can be found using Equation 2.1 (Tielens, 2005).

$$\tau_\lambda = \int_{a_-}^{a_+} n(a)\, C_{ext}\, da \tag{2.1}$$

In the preceding equation, a is the particle radius (in units of cm), *n(a)* is the particle size distribution, and C_{ext} is equal to $\sigma_d\ Q_{ext}$, where σ_d is the geometric cross section πa^2 and Q_{ext} is the extinction efficiency coefficient which can be a function of the wavelength, particle size, temperature, and composition of the dust particle. We employ the particle size distribution proposed by Mathis et al. (1977) (MRN distribution) of $n(a) = \Sigma_d\, C(a/a_0)^{-3.5}$, where Σ_d is the column density of dust and C is a normalization constant. $n(a)$ has units of cm^{-3}.

We want to determine C such that

$$\int_{a_{min}}^{a_{max}} C \left(\frac{a}{a_0}\right)^{-\beta} da = 1. \tag{2.2}$$

Using the preceding equation, we find that $C = 500\ \mu\text{m}^{-1}$ for the MRN distrubtion: $a_{min} = a_0 = 0.005\ \mu$m, $a_{max} = 0.25\ \mu$m, and $\beta = 3.5$.

Equation 2.1 now becomes

$$\tau_\lambda = \int_{a_-}^{a_+} \pi\, a^2\, C\, \Sigma_d \left(\frac{a}{a_0}\right)^{-3.5} Q_{ext}\, da. \tag{2.3}$$

The quantity we will be calculating in this section is Q_{ext}. In order to precede with the calculation, first we need to understand the optical properties of the materials in question; namely, astronomical silicate and graphite. The conducting and dielectric properties of these materials will determine the scattering and absorption characteristics of our dust grain distribution.

2.3 Grain Composition

The main characteristics of the materials we are interested in are the optical properties; the ability of the material to scatter and absorb radiation. These are determined by the dielectric

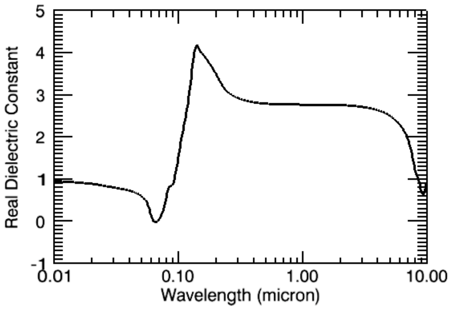

Figure 2.1: Real dielectric indices for astronomical silicate, adapted from Draine (1985) .

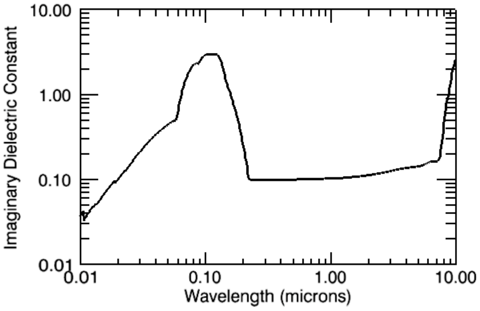

Figure 2.2: Imaginary dielectric indices for astronomical silicate, adapted from Draine (1985).

constants, which are in turn related to the real and complex indices of refraction of the material. The real dielectric constant is responsible for determining the scattering properties of a material; the imaginary dielectric constant determines the absorption properties. The dielectric constant is written $\epsilon = \epsilon_1 + i\epsilon_2$, where ϵ_1 is the real dielectric constant and ϵ_2 is the imaginary dielectric constant. The index of refraction is donated $m = n + ik$, where n is the real index of refraction and k is the complex index of refraction. These are related to the dielectric constants via the relations $\epsilon = m^2$, $\epsilon_1 = n^2 - k^2$, and $\epsilon_2 = 2nk$. In the following subsections, we explore the optical properties of astronomical silicate and graphite.

2.3.1 Astronomical Silicate

We employ the astronomical silicate model presented in Draine & Lee (1984) and Draine (1985) for the real and complex optical constants. Astronomical silicate is mainly composed of olivine (Mg_2SiO_4) and perovskite ($MgSiO_3$) and is produced in type II supernovae shells and AGB stellar outflows. The model has been modified according to the results of Kim & Martin (1995) who found that an absorption feature near 6.5 μm^{-1} originally included in this model is not observed.

Note that the dielectric curves for silicate are based on in part astronomical observations, not fully on laboratory measurements; experimentalists have have trouble replicating the states of these compounds found in space in the lab.

Silicate is a dielectric in the wavelength regime we are interested in (namely UV, optical, and NIR); the imaginary dielectric constant is minimized over this range as we can see in Figure 2.2.

The indices are plotted in Fig. 2.1 and Fig. 2.2 for the real and imaginary components. We can use this data and the IDL function *interpolate* to find the optical constants for silicate in the wavelength range 0.1 μm to 10 μm (1,000Å to 100,000Å).

2.3.2 Graphite

Graphite is produced in AGB stars. The main form we consider here is graphite, which has an ordered, crystalline structure; less ordered forms like polycyclic aromatic hydrocarbons (PAHs) and amorphous carbon are smaller than the minimum dust particle size considered in this analysis and more ordered forms, such as diamond, are rare enough to not significantly effect the overall extinction curve.

Determining the index of refraction for graphite is more complicated; due to its conducting properties, the dielectric constants have both a temperature and particle size dependance. We will divide the dielectric constants into the components perpendicular $\epsilon_{\perp}$ and parallel $\epsilon_{\parallel}$ to the c axis, which is normal to the basal plane. Each of these ϵ values can be further defined as $\epsilon = 1 + \delta\epsilon^{b} + \delta\epsilon^{f}$ for the bound and free electron components. The value $\delta\epsilon^{b}$ is compiled from various sources (Philipp, 1977; Tosatti & Bassani, 1970) which measured the imaginary dielectric constant (the real dielectric constant is then calculated via the Kramers-Kronig relation); the value $\delta\epsilon^{f}$ is calculated using Equation 2.4

$$\delta\epsilon^{f} = \frac{(-\omega_p\ \tau)^2}{(\omega\tau)^2 + i\omega\tau} \tag{2.4}$$

where the plasma frequency ω_p is given by Equation 2.5

$$\omega_p(10^{14}s^{-1}) = 4.33(1 - 6.24\times10^{-3}T + 3.66\times10^{-5}\,T^2)^{1/2} \tag{2.5}$$

for the field perpendicular to c and $\omega_p = 1.53$ for the parallel field, and

$$\tau_{bulk} = \frac{4.2\times10^{-11}}{1 + 0.322\,T + 0.00130\,T^2} \tag{2.6}$$

is the effective collision rate for the perpendicular field and $\tau_{bulk} = 1.4 \times 10^{-14}$ for the parallel field. In addition, τ_{bulk} is further modified by the particle size,

$$\tau^{-1} = \tau_{bulk}^{-1} + \frac{v_{eff}}{\beta a} \tag{2.7}$$

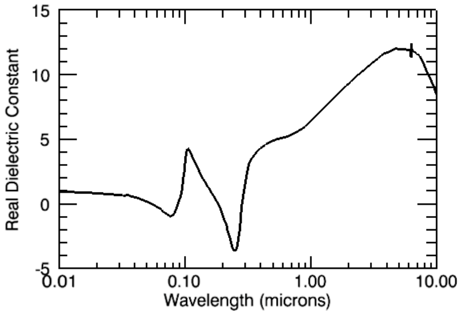

Figure 2.3: Real dielectric indices for the perpendicular component of graphite, adapted from Draine (1985) .

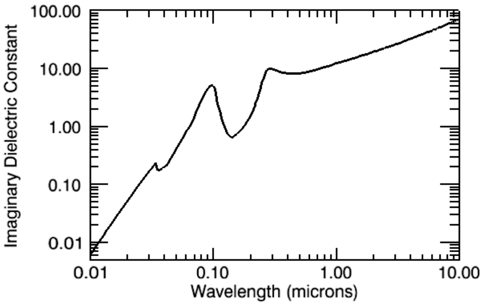

Figure 2.4: Imaginary dielectric indices for the perpendicular component of graphite, adapted from Draine (1985) .

where β is a constant of order unity and v_{eff} is the effective carrier velocity in the basal plane, given by

$$v_{eff} = v_F(1 + T/T_F)^{1/2} \tag{2.8}$$

for a given Fermi velocity of $v_F = (2kT_F/m_{*,e})$ for an electron hole mass $m_{*,e} = 0.039\ m_e$ and Fermi temperature $T_F = 255$ K (Soule et al., 1964; Williamson et al., 1965). The above set of equations were taken from Draine & Lee (1984).

The resulting dielectric curves for the real (Fig. 2.3 and Fig. 2.5) and imaginary (Fig. 2.4 and Fig. 2.6) components are shown. These are for the bound component only; we find that the free electron component does not significantly contribute to the dielectric constant over the temperature ranges relevant to this study (but see Section 2.6).. However, it has been included in this calculation for completeness.

2.4 Extinction Theory

We consider three extinction theories relevant to the wavelength and particles sizes in this paper. We begin by defining $x = 2\pi$a$/\lambda$ and m as the complex index of refraction of the material. In the case $|m|x < 1000$, Mie theory is used (wavelength of light hitting the particle is within a few orders of magnitude of the particle radius). When $|m|x >$ and $|m$-1$|x < 0.001$ we use Rayleigh-Gans theory, and when $|m|x >$ and $|m$-1$|x > 0.001$ (particles size is large compared to wavelength of light) we use geometric optics to calculate extinction (Laor & Draine, 1993).

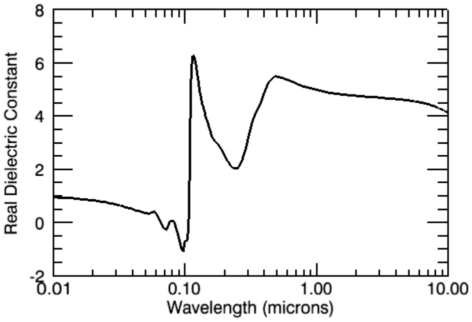

Figure 2.5: Real dielectric indices for the parallel component of graphite, adapted from Draine (1985) .

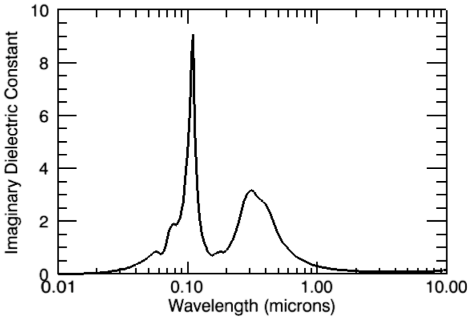

Figure 2.6: Imaginary dielectric indices for the parallel component of graphite, adapted from Draine (1985) .

2.4.1 Mie Theory

Mie theory for the scattering of light off small particles is worked out in detail in van de Hulst (1957) and here follows from the work of Wickramasinghe (1973). We begin with the definition of Q_{ext} as derived from Mie theory.

$$Q_{Mie} = \frac{2}{x^2} \sum_{n=1}^{\infty} (2n+1)\ \mathrm{Re}(a_n + b_n) \tag{2.9}$$

Here, n is the summation index $n = 1, 2, 3$, etc. The equations for a_n and b_n are given below in terms of Bessel function recursive relationships.

$$a_n = \frac{\left(\frac{A_n(y)}{m} + \frac{n}{x}\right) \mathrm{Re}\{\zeta_n(x)\} - \mathrm{Re}\{\zeta_{n-1}(x)\}}{\left(\frac{A_n(y)}{m} + \frac{n}{x}\right) \zeta_n(x) - \zeta_{n-1}(x)} \tag{2.10}$$

$$b_n = \frac{\left(m\ A_n(y) + \frac{n}{x}\right) \mathrm{Re}\{\zeta_n(x)\} - \mathrm{Re}\{\zeta_{n-1}(x)\}}{\left(m\ A_n(y) + \frac{n}{x}\right) \zeta_n(x) - \zeta_{n-1}(x)} \tag{2.11}$$

The relevant recursive relations are as follows assuming $y = mx$, where $m = n + ik$, n here being the real index of refraction (not the summation index) and k being the complex index of refraction. n and k are known as the optical constants, and they are related to the dielectric constants ϵ_1 and ϵ_2 through the relations $\epsilon_1 = n^2 + k^2$ and $\epsilon_2 = 2nk$.

$$\zeta_n(x) = \frac{2n-1}{x} \zeta_{n-1}(x) - \zeta_{n-2}(x) \tag{2.12}$$

$$\zeta_0(x) = \sin(x) + i\cos(x) \tag{2.13}$$

$$\zeta_1(x) = \cos(x) - i\sin(x) \tag{2.14}$$

$$A_n(y) = \frac{-n}{y} + \left(\frac{n}{y} - A_{n-1}(y)\right)^{-1} \tag{2.15}$$

$$A_0(y) = \frac{\cos(y)}{\sin(y)} \tag{2.16}$$

These relations allow for an iterative solution to a_n and b_n. We find that $n = 20$ will bring each solution to within 0.1% or better of the convergence value.

2.4.2 Rayleigh-Gans Theory

Rayleigh-Gans theory for light scattering off very small particles can be found worked out in Bohren & Huffman (1983) and here follows from Laor & Draine (1993). We begin by approximating the absorption efficiency factor Q_{abs}.

$$Q_{abs} \approx \frac{8}{3}\,\mathrm{Im}(m)\,x \tag{2.17}$$

The scattering efficiency coefficient is then approximated as

$$Q_{sca} \approx \frac{32|m-1|^2x^4}{27+16x^2} \tag{2.18}$$

so the extinction efficiency coefficient for Rayleigh-Gans theory is then

$$Q_{RG} = \frac{32|m-1|^2x^4}{27+16x^2} + \frac{8}{3}\,\mathrm{Im}(m)\,x. \tag{2.19}$$

2.4.3 Geometric Optics

Following the derivation of Laor & Draine (1993) we define the geometric optics extinction efficiency coefficient as a function of the Rayleigh-Gans extinction efficiency coefficient.

$$Q_{GO} = \frac{Q_{RG}}{\sqrt{1 + 0.25\, Q_{RG}^2}} \tag{2.20}$$

For the rest of the paper, Q_{ext} will refer to whichever of the above extinction laws applies in the given regime.

2.4.4 Extinction Curves

At this point, we have calculated $\zeta = \tau_\lambda / \Sigma_d$, the optical depth divided by the dust column density. This quantity as a function of wavelength can now be calculated for graphite and silicate; the extinction curves are shown in Figure 2.7.

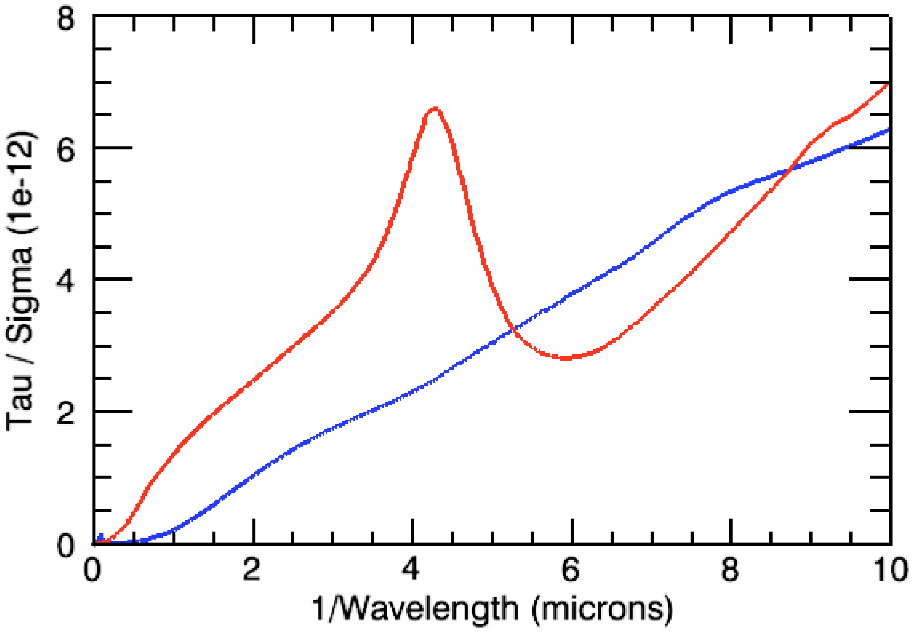

Figure 2.7: Optical depth divided by column depth as a function of wavelength as determined from the graphite (red) and silicate (blue) dielectric functions and the particle distribution.

The graphite curve clearly shows the 2175 Å feature which emerges from the measured dielectric curves, the result of bending and stretching modes in the graphite crystal. Two silicon features found in the near-infrared at 9.7 μm and 18 μm are the result of bending and stretching modes.

2.5 Dust Size Distributions

Our MRN distribution peaks at the largest particle size of 0.25 μm. However, other particle size distributions have been observed along various sight-lines in the MW. Assuming the same MRN power law distribution but a particle size distribution peaking at 10 μm instead, we can observe the effects of 'gray' extinction.

Gray extinction refers to the shallow extinction curve produced when the particles are very large in comparison to the wavelengths of light hitting them. The resulting extinction only weakly depends on wavelength.

In Figures 2.8 and 2.9, we plot the results of the MRN distribution for particles with maximum size 0.25 μm and those with a particle size distribution peaking at 10 μm. In the large particle limit, we observe the beginnings of the expected 'gray' extinction curve (wavelength-independant extinction). It is obvious the red curves (gray extinction) are much more shallow than the typical dust distribution (black).

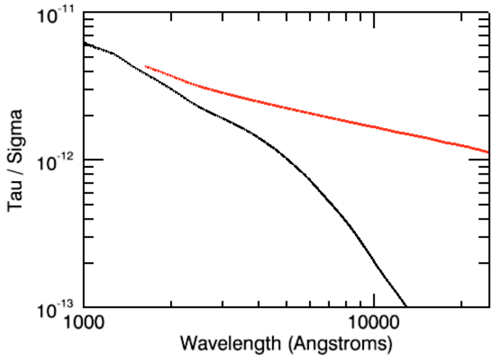

Figure 2.8: Extinction curves of silicate for a normal particle size distribution (black) and a gray particle distribution (red).

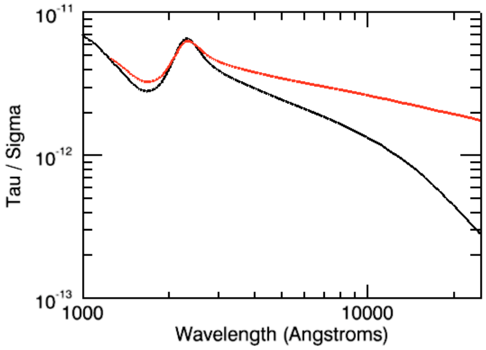

Figure 2.9: Extinction curves of graphite for a normal particle size distribution (black) and a gray particle distribution (red).

Gray extinction has been proposed as mechanism for the shallow extinction curve observed in the SED of GRB 061126 (Perley et al., 2008a). However, a shallow extinction curve can also be interpreted as a shallow spectral index. Given the available data on the burst and the data we have access to in this analysis, we cannot distinguish between a shallow spectral index and a gray dust population. While the x-ray and optical/NIR spectral indices have been correlated in an attempt to establish a single spectral index β for a burst, there is always the possibility that the cooling frequency of the electrons passed between the frequencies resulting in a change in the optical/NIR spectral index with respect to the x-ray. Access to mid-IR data could potentially settle the argument; moving far enough into the IR portion of the spectrum frees us from the effects of dust. Unfortunately, no such data exists for these bursts. Therefore, we will assume a single dust population for our analysis with a minimum size of 0.005 μm and a maximum size of 0.250 μm.

2.6 Temperature Dependence

As a conductor, the extinction curve of graphite depends on the temperature of the dust grains. However, the extinction curve only changes with temperature in the longer wavelengths. In the wavelength regime between 1,000 and 25,000 Å, there is essentially no temperature dependance.

The changing extinction curve of graphite with temperature of the dust grains is illustrated in Fig. 2.10. The black curve shows the extinction curve calculated at 100 K, but works for all curves in the temperature range 3 K to approximately 500 K. Above 500 K, the curve begins to deviate significantly in the longer wavelengths. The red curve shows what happens at 10^4 K, and the blue curve at 10^5 K.

We assume a temperature for all of our dust grains of 20 K for this analysis, a typical temperature of dust in the ISM. As we see above, it would take significantly higher temperatures to change the extinction curves in any regime, and in the wavelength regime we are interested in for this analysis, the dust temperature is inconsequential.

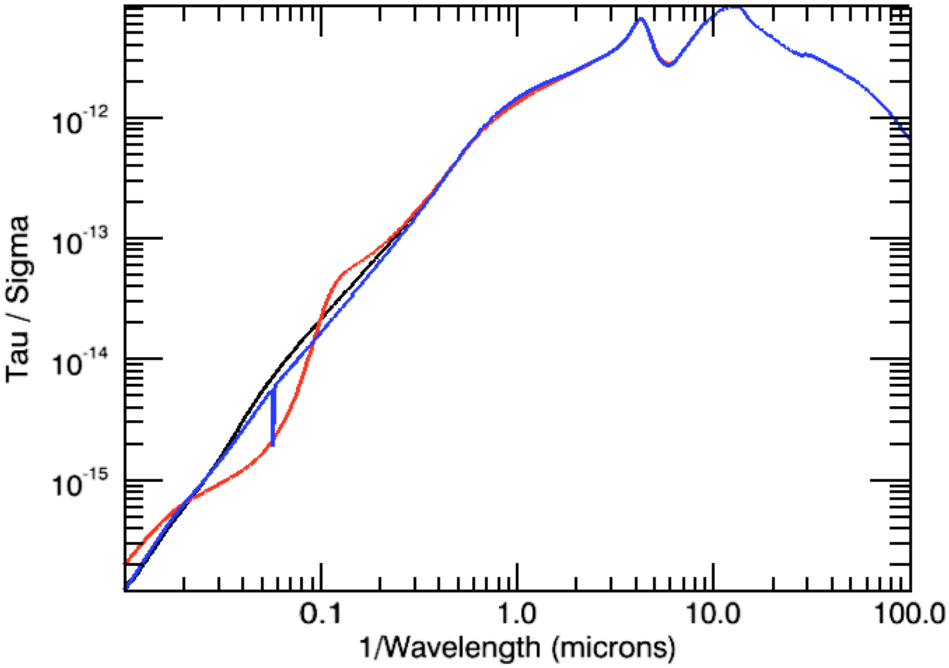

Figure 2.10: Effects of dust temperature on the extinction curve of graphite. The black curve represents dust grains at 10 K, the red curve at 10^4 K, and the blue at 10^5 K.

Chapter 3

Fitting SED Models to Data

Using the optical depth calculations of Section 2, we can now construct an extinction curve for graphite and silicate as a function of frequency using the following equation adapted from Kann et al. (2006).

$$F = F_0\, \nu^{-\beta}\, e^{-(\tau_S+\tau_G)} \tag{3.1}$$

In the above equation, F is the flux in a particular frequency ν, F_0 is a normalizing flux, β is the spectral index as a function of the electron energy distribution power law index p, and τ is the optical depth of silicate and graphite along that particular line of sight. Recall that in Section 2, what we actually calculated was the quantity $\zeta = \tau/\Sigma_d$. The column densities of graphite and silicate along the line of sight are our final two fitting parameters.

$$F = F_0\, \nu^{-\beta}\, e^{-(\zeta_S\, \Sigma_S+\zeta_G\, \Sigma_G)} \tag{3.2}$$

This gives us a 4-parameter fit (F_0, β, Σ_S, and Σ_G). Now we need to fit these extinction models to our data.

3.1 Extinction Models

Many attempts have been made to fit GRB SEDs with various templates. Here we give an overview of the templates and their uses.

3.1.1 Pei and Draine's Model

The most commonly used method of fitting GRB SEDs is to use the Milky Way, Large Magellanic Cloud, and Small Magellanic Cloud templates of Pei (1992). Pei used the graphite and silicate models of Draine & Lee (1984) following the methods of Mathis et al. (1977) to fit the extinction curves of the MW, LMC, and SMC using varying amount of graphite and silicate and provided fitting functions for these three curves. The main purpose of our analysis is to extend the models of Draine & Lee (1984) to SEDs containing other mixtures of graphite and silicate besides those ratios found in the Pei templates.

Pei created extinction curves for the MW, LMC, and SMC (given in Figures 3.1, 3.2, and 3.3) from 0.1 to 5 μm employing data given in Koornneef & Code (1981), Koornneef (1982), Koornneef (1983), Bouchet et al. (1985), Massa & Savage (1989), Nandy et al. (1981), Morgan & Nandy (1982), Nandy et al. (1984), Prevot et al. (1984), Rieke & Lebofsky (1985), Savage (1975), and Savage & Mathis (1979). The lines shown in the figures mentioned above are there to connect the points but are not fitted curves. The extinction is given as $E_{\lambda-V}/E_{B-V}$ (where $E_{\lambda-V}$ is the difference in the amount of extinction in some band λ versus V, and is equivalent to $A_\lambda - A_V$).

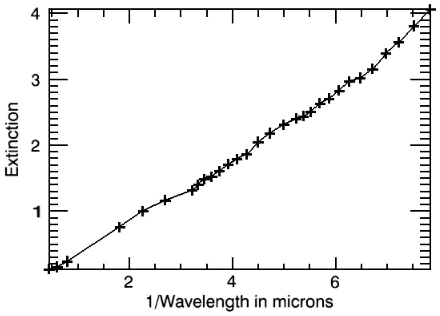

Figure 3.1: Pei (1992) data for the SMC.

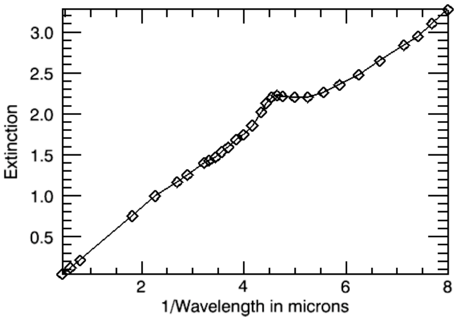

Figure 3.2: Pei (1992) data for the LMC.

Pei introduced a fit function (Equation 3.3) for these three curves with 6 terms, each containing 4 free parameters, for a total of 24 degrees of freedom per fit.

$$\xi(\lambda) = \sum_{i=1}^{6} \frac{a_i}{(\lambda/\lambda_i)^{n_i} + (\lambda_i/\lambda)^{n_i} + b_i} \tag{3.3}$$

The six terms include three background, far-ultraviolet, and far-infrared extinction slopes along with varying shapes and sizes for the 2175 Å, 9.6 μm, and 18 μm carbon and silicate features. The

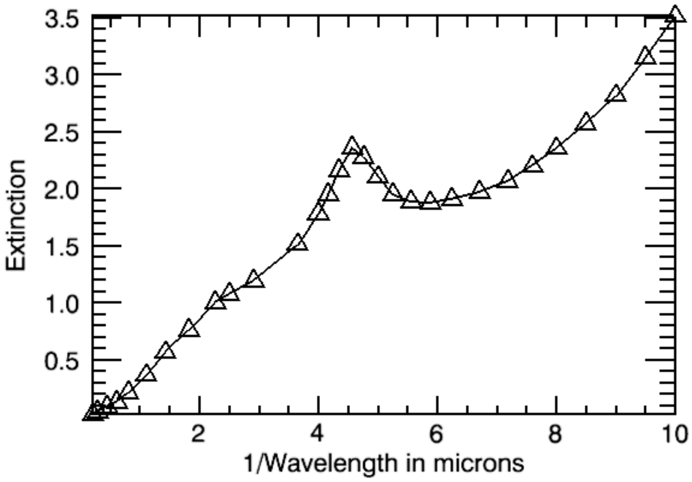

Figure 3.3: Pei (1992) data for the MW.

parameters themselves, a_i, λ_i, b_i, and n_i have no physical significance. Pei gives values for the constants which best-fit the MW, LMC, and SMC extinction curves, reducing the fits to a given function of the frequency which have been employed as templates in most GRB SED analyses.

Using the work of Draine & Lee (1984), Pei also produces fits to these three galaxies using varying values of graphite and silicate, which we have also done for this analysis. The results of the fits of our model are shown in Figures 3.4, 3.5, and 3.6. Note that we have used an artificial extinction error of 0.05 mag for this fit.

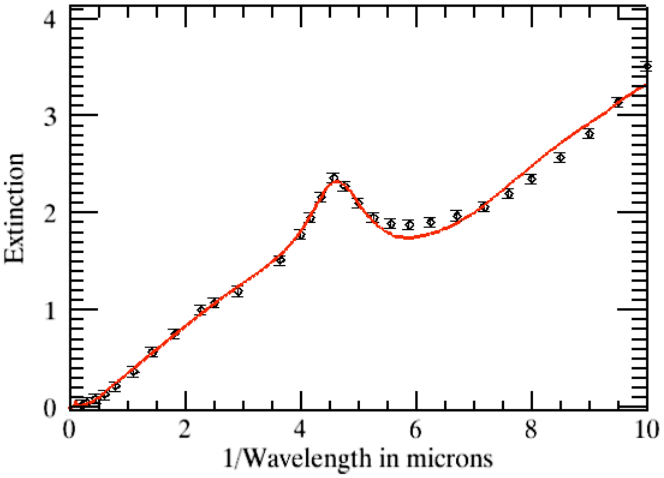

Figure 3.4: MW extinction data fit with our model of silicate and graphite.

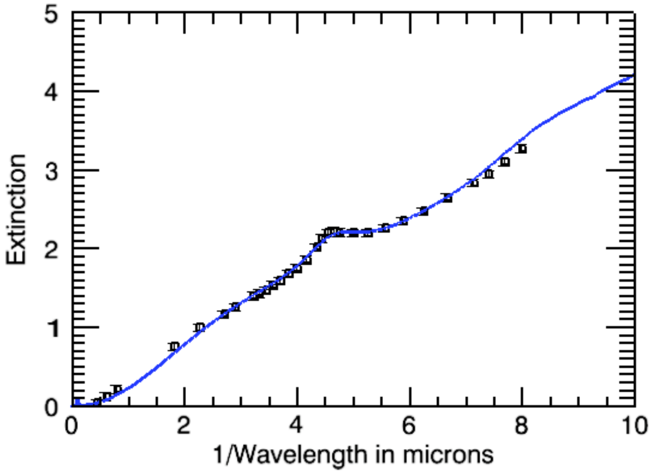

Figure 3.5: LMC extinction data fit with our model of silicate and graphite.

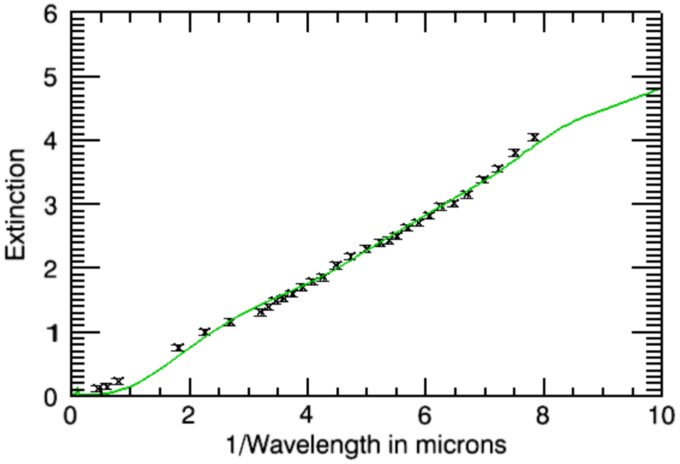

Figure 3.6: SMC extinction data fit with our model of silicate and graphite.

We can compare the results of Pei (1992) fitting the extinction curves to our own fits. The results of the comparison are given in Table 3.1; values are the column density of graphite divided by the column density of silicon. $\tilde{\chi}^2$ values are for our analysis (not provided in Pei's work).

Both works find that a silicon extinction curve alone can best reproduce the observed extinction in the SMC. We find comparable values for the LMC; however, the model used in this analysis finds a better fit with a smaller amount of graphite than found by Pei.

The exact details of the Pei fits were not given in the paper; χ^2 values are not given, nor are

Table 3.1: Graphite to silicate ratios for Pei and result from this analysis.

Galaxy	Pei	This Analysis	$\tilde{\chi}^2$
MW	0.95	0.81	2.20
LMC	0.22	0.17	1.00
SMC	0.00	0.00	1.74

the details of the fitting procedure. In addition, details of the Q_{ext} calculation are not presented.

Pei's templates are used extensively in the literature (see Table B.1). However, they constrain us to a limited set of graphite to silicate ratios. We hope to show in this analysis that a varying fit to the graphite and silicate column densities can produce a wealth of information about the ISM of the host galaxy as well as insight into galactic stellar evolution.

3.1.2 Fitzpatrick & Massa

Fitzpatrick & Massa (1986, 1988, 1990) observed multiple MW lines of sight from the near-UV to near-IR and demonstrated that the resulting extinction curves could be fairly well-fit by a combination of three components; a Lorentzian-shaped bump for the 2175 Å feature, a smooth curvature in the near UV, and a linear term to force the overall slope. A combination of these three parameters would reproduce the extinction curves of Pei (1992) in the MW and LMC to first order, but do no include the observed silicate features. However, the varying Lorentzian term allowed for more freedom in the amount of graphite in the model. The model of Fitzpatrick & Massa is rarely used in GRB SED analysis, passed over in favor of Pei's templates, and the fitting parameters of the Fitzpatrick & Massa model have no physical significance.

3.1.3 Cardelli, Clayton, & Mathis

Cardelli et al. (1988, 1989) favored a method by which a MW-type extinction curve (similar to the models of Fitzpatrick & Massa (1990)) was given various values of the total-to-selective extinction ratio R_V, causing the curve to be steeper (for lower values of R_V) or shallower (for larger values). The effect of changing R_V is illustrated in Figure 3.7.

Note that the effects of a larger R_V closely resemble the effects of a larger dust population in general, also known as gray extinction (see Figure 2.9). Higher R_V values are typically associated with dense molecular clouds in the MW, where grain growth is thought to take place in abundance.

Therefore, the higher R_V value is a reasonable first-order substitute for larger grain sizes and the resulting optical properties of the materials.

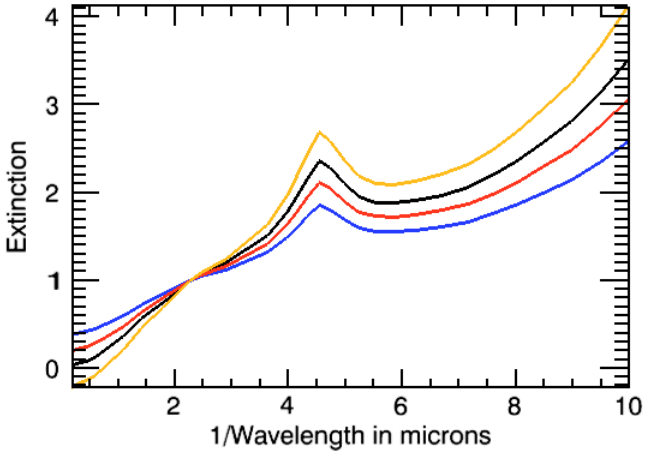

Figure 3.7: Adapted from a figure in Cardelli et al. (1988) illustrating the varying extinction curves for the MW using different values of R_V. The orange (top) line is for an R_V of 2.3, the black curve for an R_V of 3.1 (typical MW value), the red curve for R_V = 4.0, and the blue curve for R_V = 5.5.

3.1.4 Calzetti

Calzetti et al. (1994) introduced a new extinction template for starburst galaxies. Starting with the Bruzual A. & Charlot (1993) galaxy emission models, Calzetti simulated a starburst in a spiral galaxy and a clumpy dust model which would vary the amounts of emission from various stars. The result was a shallow extinction curve now referred to as the Calzetti curve, which is often applied to high-redshift objects. Fischera et al. (2003) showed that the Calzetti curve, originally parameterized as follows with no physical significance to the variables $a - d$,

$$k(\lambda) = a + \frac{b}{\lambda} + \frac{c}{\lambda^2} + \frac{d}{\lambda^3}, \tag{3.4}$$

could be reproduced using the dust models of Draine & Lee (1984) and assuming turbulence in the dust, leading to a physically significant model of dust found in starburst-type galaxies. Once again, the models assume a set value for the ratio of graphite to silicate with a higher total-to-selective extinction value R_V than found for the MW or LMC/SMC and so it can be limited in its application.

3.1.5 Maiolino

Maiolino et al. (2004) detailed observations of a quasar at a redshift $z = 6.5$ with a unique spectrum. When the quasar emission lines were corrected for, the resulting spectrum was fairly shallow, featureless, and well-fit by a silicate extinction curve derived from the work of Todini & Ferrara (2001) on dust formation in type II supernovae (however, the veracity of Todini's work has been called into question by Cherchneff & Dwek (2009); see Section 1). The particular silicate curve was skewed towards larger grains with a larger resulting R_V value. This particular extinction curve was used to explain the SED of GRB 071025 (Perley et al., 2010) citing silicates from supernovae as the reason for the shallow and featureless extinction curve.

3.1.6 Li and the Drude Model

Li et al. (2008) proposed model he calls the 'Drude' model (after the Drude profile of emission from the bending and stretching modes of materials, here referring to the 2175 Å feature) containing four non-physically-based parameters as opposed to employing a template. The Drude model is as follows.

$$\frac{A_\lambda}{A_V} = \frac{c_1}{(\lambda/0.08)^{c_2} + (0.08/\lambda)^{c_2} + c_3} + \frac{233[1 - c_1/(6.88^{c_2} + 0.145^{c_2} + c_3) - c_4/4.60]}{(\lambda/0.046)^2 + (0.046/\lambda)^2 + 90} + \frac{c_4}{(\lambda/0.2175)^2 + (0.2175/\lambda)^2 - 1.95} \tag{3.5}$$

Note the similarities to the Pei analytic model. The first term defines the far-UV extinction, the second term dictates the optical/near-IR extinction, and the third determines the 2175Å feature. While having the advantage of not restraining the results to a template and well-reproducing the extinction curves of Pei, the parameters $c_1 - c_4$ are non-physical and the resulting fit to a GRB SED has seven free parameters. However, the model was then applied to GRB SEDs with seven or fewer data points. The model could arguably be determined to fit anything and often results in unconstrained parameters and unphysical results (Kann et al., 2010).

3.2 The Graphite and Silicate Model

Extinction curves for various column densities of graphite and silicate are calculated in Section 2 as a function of $\zeta = \tau/\Sigma$, where τ is the optical depth and Σ is the dust column density. Using a combination of these curves, we can employ Equation 3.2 to fit a 4-parameter curve to a given data set for a GRB SED.

Our model has several advantages over previous work. First, it does not assume a template; the amount of graphite and silicate are free to vary. Second, it contains no non-physical parameters; each parameter has a physical significance and is the result of observed qualities of the materials. Third, it contains fewer fit parameters than the more complicated of the models discussed above (i.e., the Drude model) and can therefore be applied to bursts for which we have fewer data points and still results in reasonable values for the column densities and spectral index β. Fourth, our model has the advantage of not only predicting an extinction value A_V but also can determine the column densities of dust along the line of sight as well as a dust-to-gas ratio (given an external measure of the hydrogen column density).

The model assumes several fixed parameters, allowing us to reduce the number of free parameters in our fit. The dust temperature does not change (although we showed earlier that it is unlikely to make a difference to the overall result), and the size distribution is fixed, as is the shape of the particle.

Our model has the disadvantage of not having an analytical form (unlike the other models discussed above) and is instead of series of data points determined from the optical properties of graphite and silicate. Therefore, we employ a simple reduced χ^2 minimization routine.

$$\tilde{\chi}^2 = \frac{1}{dof} \sum_{i=1}^{N} \left(\frac{O_i - E_i}{\sigma_i} \right)^2 \tag{3.6}$$

In Eq. 3.6, dof refers to the number of degrees of freedom in the model (equal to the number of data points in our SED minus the number of parameters in our fit), O_i are the observed fluxes, E_i are the model fluxes from our fit, and σ_i are the errors in the observed data. In the case where filter response functions are available, we convolved the known function with the fit (see Equation 3.9); in the cases where these function were not available, we fit the measured fluxes directly to the model. We see no significant difference between these methods.

The $\tilde{\chi}^2$ minimization routine works by determining a range of possible values for the parameters and determining the resulting $\tilde{\chi}^2$ for each configuration. By examining the $\tilde{\chi}^2$ and the parameter space explored, we can find the best values of each parameter and the error associated with it. Figures 3.8 and 3.9 show the relevant portion of the parameter space for $\tilde{\chi}^2$ and the graphite and silicate parameters of our fit to the MW extinction curve given in Pei (1992). In these particular cases, 250,000 values for each parameter were tested against the given data. The plots are truncated to show $\tilde{\chi}^2$ between 0 and 10. The error in the measured parameters in the 95% confidence interval is given by the range in which the parameter falls between $\tilde{\chi}^2$ and $\tilde{\chi}^2$ + 2.31 (Press et al., 2007).

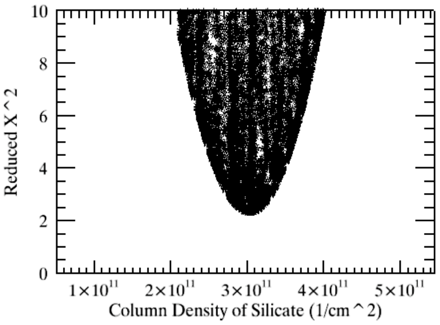

Figure 3.8: $\tilde{\chi}^2$ silicate fits to the Pei MW data.

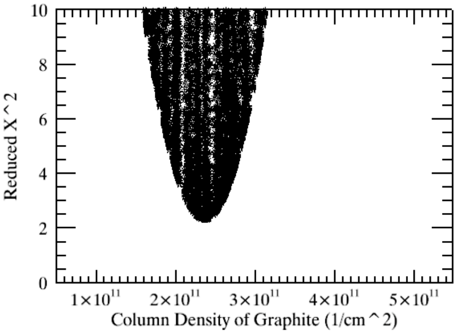

Figure 3.9: $\tilde{\chi}^2$ graphite fits to the Pei MW data.

The full minimization routine and fitting programs are in Appendix C. In addition to fitting column densities of graphite and silicate, there are other values we wish to compute. The first of these is the observed extinction in the V band of the co-moving frame, A_V. This value is most often employed to categorize the observed extinction for a GRB, and will be useful for comparisons to previous studies of extinction in GRB host galaxies. The value is simply calculated as

$$A_V = 1.086\,\tau_V \tag{3.7}$$

(see Equation 1.5 for the derivation). For this analysis, we will use a V band centered at 5500Å and a B band centered at 4400Å as standard filters, although these values may not agree exactly with the peak response wavelength of the actual filters used (this is of no consequence). The value of τ_V is determined by interpolating the data of the curve at that particular wavelength. Similarly, we can calculate the total-to-selective extinction ratio R_V;

$$R_V = \frac{A_V}{A_B - A_V} \tag{3.8}$$

as well as the errors associated with each using the error procedure outlined above.

We also wish to determine the dust-to-gas ratio of the GRB host galaxy along the line of sight probed by the GRB. In order to calculate this ratio, we need a measurement of the hydrogen column density along that line of sight. This is often reported by the *Swift* telescope, which assumes solar abundances in their determination of the hydrogen column density.

In order to calculate the dust-to-gas ratio by mass, we assume a hydrogen atom has a mass of 1.66 $\times 10^{-24}$ g and that graphite and silicate have densities of 2.26 g cm^{-3} and 3.3 g cm^{-3}, respectively (Draine & Lee, 1984). The average size of a dust particle in our MRN distribution peaking at 0.25 μm is a particle with radius $\bar{a} = 0.0083$ μm, giving us a volume per particle of 2.40 $\times 10^{-18}$ cm^3, or a mass of 5.42 $\times 10^{-18}$ g for a graphite particle and 7.92 $\times 10^{-18}$ g for a silicate particle. Thus, given a column density of hydrogen in cm^{-2}, we can determine the mass dust-to-gas ratio by multiplying the column densities by the masses of the particles and taking the ratio.

3.2.1 Data Convolution

In the cases for which we have filter response functions for the filters employed in our analysis, we want to convolve our model with the filter curves in order to make this comparison. In order to do this, we will follow the procedure outlined in Appendix A of Robitaille et al. (2007).

$$F_{eff} = \frac{\sum_{\lambda} F_{\lambda}(\lambda_0/\lambda)R(\lambda)\Delta\lambda}{\sum_{\lambda}(\lambda_0/\lambda)^2 R(\lambda)\Delta\lambda} \tag{3.9}$$

In the above equation, F_{eff} is the effective flux of the model in that filter band, F_{λ} is our model flux at the given wavelength, λ_0 is the central wavelength of the filter band, and R_{λ} is the filter response function. In this manner we can calculate the predicted flux of our model SED at a given wavelength. We then compare this to the measured flux using a reduced $\tilde{\chi}^2$ minimization routine.

3.3 GRB SED Data

The data used in this analysis were provided by D. Alexander Kann and are presented in part in several papers and his Ph.D. thesis (Kann et al., 2006, 2010). For those analyses, the SEDs were fit using the Pei and Drude models to derive the overall extinction.

The SEDs were constructed by fitting light curves to the available data and determining the magnitude of the GRB at either 1 day after the trigger when the light curve was best-fit by a simple power law or at the jet break time if a broken power law fit to the light curve was observed (Zeh et al., 2006). Using the constructed light curves in various bands, an SED was constructed at a single time for each GRB (Kann et al., 2006). Each SED was corrected for galactic extinction (Schlegel et al., 1998) and is given here in the co-moving host frame. Redshifts are known for each burst, the majority of which were spectroscopically determined (see Appendix A for details).

Fits of our model to the GRB SEDs are presented in Appendix A, as well as a table of the results.

3.3.1 GRB 070125: A Case Study

GRB 070125 (Updike et al., 2008; Cenko et al., 2008) was a well-studied GRB at a redshift of 1.547 which remained bright enough for medium-sized telescopes to follow for several days, resulting in a large data set and unusually complete photometric SED. We will use this GRB as a case study to show that our model not only agrees with previous work but can lead to new insights as well.

Updike et al. (2008) employs Pei template fits to the UV/optical/NIR SED of GRB 070125. We concluded at the time that the SED was best-fit by an SMC template. The new fit using our dust model is shown in Figure 3.10. The combination of graphite and silicate resulted in a fit with $\tilde{\chi}^2 = 0.959$, graphite column density of 1.028 ($\pm$ 0.469) $\times$ 10^{10} cm^{-2}, and a silicate column density of 1.674 ($\pm$ 0.077) $\times$ 10^{11} cm^{-2}; more than an order of magnitude more silicate than graphite. The graphite-to-silicate ratio of this burst was 0.06; given the updated *Swift* XRT hydrogen column density of $N_H = 0.8 \times 10^{21}$ cm^{-2} we can calculate a dust-to-gas ratio of 0.3% assuming solar metallicity. Note that a mainly silicate model is basically equivalent to the SMC model previously used. We measure a comparable A_V value using this model than we found in our previous work ($A_V = 0.181 \pm 0.019$ as opposed to $A_V = 0.139 \pm 0.041$ in Updike et al. (2008)). Our reduced χ^2 is slightly larger; however, we are using a four parameter fit instead of a two parameter fit. The values for the spectral index are also comparable ($\beta = 0.427$ for this analysis versus 0.519 in the previous work). Thus, we show using GRB 070125 that our model agrees with previous work while providing information about the dust content and composition of the GRB host galaxy.

The fit to the SED in Updike et al. (2008) used both the UV/optical/NIR data and the x-ray data from *Swift*, using an SED constructed at 4.26 days and a cooling break through the R band at 0.002 keV. Our analysis assumes no cooling break (see Introduction).

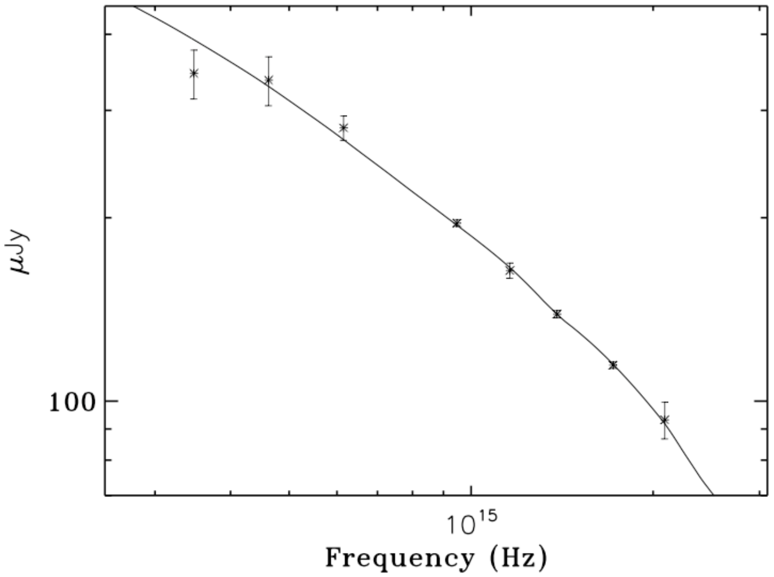

Figure 3.10: Combination of graphite and silicate fit to the SED of GRB 070125 in the co-moving frame.

Chapter 4

Modeling Galactic Evolution

We want to model the evolution of long-GRB host galaxies as a function of redshift. Typical long-GRB hosts are faint, blue, irregular galaxies with high star formation rates (i.e., Fruchter et al., 1999). However, irregular galaxies can be difficult to model effectively, so we will simplify the problem as a disk galaxy scaled down to the typical size and mass of long-GRB host galaxies.

We begin by producing a model of a disk galaxy with a dust distribution that reproduces extinction maps similar to those observed in our own Milky Way (MW) galaxy, and then the model will be scaled and evolved in redshift.

4.1 Cosmology

In the following sections, the lookback time will be used to calculate the redshift. The lookback time is the time between the current age of the universe, t_0, and the age of the universe when the photon was emitted, t_e. Here we review the calculation of the lookback time, t_L.

$$t_L = t_H \int_0^z \frac{dz'}{(1+z')\sqrt{\Omega_M(1+z')^3 + \Omega_\Lambda}} \tag{4.1}$$

The values for Ω_M, Ω_Λ, and H_0 are taken from Spergel et al. (2007) to be 0.239, 0.761, and 73 km s^{-1} Mpc^{-1}, respectively, assuming a ΛCDM model of the universe. Numerical integration techniques, such as the IDL routine QSIMP, are used to calculate the lookback time. The Hubble time, t_H, is calculated as

$$t_H = \frac{1}{H_0} = 1.34 \times 10^{10}\,\text{years.} \tag{4.2}$$

The age of the solar neighborhood, as measured by Binney et al. (2000) using main-sequence and subgiant stars, is 11.2 ± 0.75 Gyr. We will take our age for the disk of the Milky Way to be 11 Gyr, which works out to a redshift of 2.5 (see Fig. 4.1).

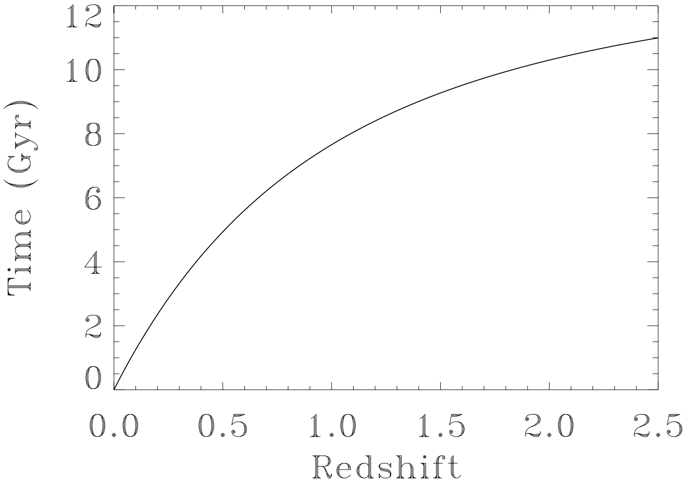

Figure 4.1: Lookback time (in Gyr) as a function of redshift.

4.2 The Milky Way Model

We will use a double-exponential model (Eq. 4.3) for the MW disk, with scale length R_D and scale height z_D.

$$\rho = \rho_0 \; e^{-r/R_D} \; e^{-|z|/z_D} \tag{4.3}$$

The Sun is located at $r = 8.5$ kpc, $z = 0.0$ kpc in the disk of the MW. The area around the Sun has an extinction of 1.086 mag kpc^{-1}. Therefore, ρ_0 for the MW today is 18.46 mag kpc^{-1} assuming a scale length of $R_D = 3.0$ kpc and scale height of $z_D = 0.21$ kpc for the MW.

We want to calculate the extinction in the V-band along a line of sight beginning from a point somewhere inside the MW and moving outwards from that point in a random direction. This is done via numerical integration. Beginning at a point somewhere in the MW (chosen randomly from a x^2e^{-x} distribution which avoids putting the majority of the stars in the center of the galaxy, a non-physical situation, see original program MC_RAD.pro, Appendix C), small steps (less than 0.002 kpc) are taken along the line of sight. After each step, the density at the end of the step is calculated, multiplied by the step size, and added to the total extinction along that line of sight. At this point, the total extinction is compared to the extinction calculated in the previous step. If the change is more than 0.01%, the process is repeated. If the change is less than 0.01%, the calculation of extinction is considered complete along that line of sight. See Appendix C for the original program GALEXT.pro.

To test our model, we take 2,000 random sightlines from the location of the Sun in the MW and compare the integrated extinction to the extinction estimated by Schlegel et al. (1998) for the same direction. The best model boasts a correlation coefficient of 0.66 and slope of 1.02 when the extinctions from Schlegel and those from the model are plotted against each other (Fig. 4.2). Note that the Schlegel model is based on MW observations; it includes clumpiness and local variation that our model does not.

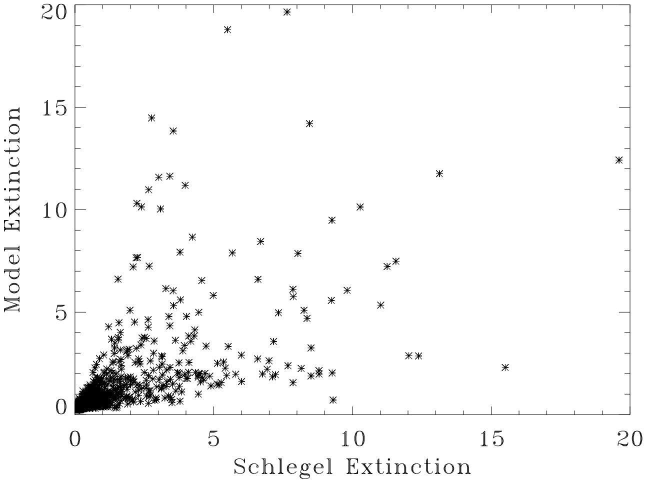

Figure 4.2: Extinction (in V-band magnitudes) from Schlegel vs. the magnitudes of extinction found with our double-exponential model. Artificially truncated at 10 mags.

We will evolve our galaxy model in time, taking four factors into account. First, the scale length of the galaxy changes in time. Second, the amount of dust causing extinction changes in time. Third, the amount of gas changes as more gas is accreted though infall. Fourth, the overall stellar mass changes in time.

Two different models to build up the galactic disk will be tested for in these simulations.

4.2.1 The Exponential Model

The exponential model begins with a set amount of gas. The gas is converted into stars with a star formation rate $M_g/\tau_\star$; we begin with an instantaneous recycling approximation and a return (to dust and gas) fraction R. The star formation rate timescale is given by $\tau_\star$.

$$\dot{M}_g = -\frac{M_g}{\tau_\star} + \frac{M_g}{\tau_\star} R \tag{4.4}$$

Star formation in this model works by taking some amount of material (both gas and dust), forming a star, and in the same step, exploding the star as a supernova and recycling the material as gas and dust. The mass not returned is in the stellar remnant, which will be included in the overall stellar mass. The first term represents the gas mass lost to star formation and the second reflects the return fraction. This gives us an equation for the gas mass in the galaxy as a function of time.

$$M_g(t) = M_0 \, e^{-t(1-R)/\tau_\star} \tag{4.5}$$

4.2.2 The Infall Model

The infall model to build up a disk galaxy begins with no gas and is built up through infall of pristine gas (no metallicity assumed) from the halo. The mass infall rate $\dot{M}_{in}$ is initially taken to be a constant 3 $\mathrm{M}_\odot$ per year. Y is the dust yield from the return fraction of the star formation rate; the ratio of dust to gas in the returned material. We can now calculate the gas, dust, and stellar mass as a function of time. The gas mass as a function of time is given by Eqs. 4.6 and 4.7. The variable t refers to the time (from 0 to 11 Gyr).

$$\dot{M}_g = -\frac{M_g}{\tau_\star} + \frac{M_g}{\tau_\star} R + \dot{M}_{in} \tag{4.6}$$

$$M_g(t) = \frac{\dot{M}_{in}\tau_\star}{1-R}\left(1 - e^{-t(1-R)/\tau_\star}\right) \tag{4.7}$$

The dust mass is calculated as shown in Eqs. 4.8 and 4.9.

$$\dot{M}_d = \frac{-M_g}{\tau_\star}\left(\frac{M_d}{M_g} - RY\right) \tag{4.8}$$

$$M_d(t) = \frac{M_g(t)\, t\, RY}{\tau_\star} \tag{4.9}$$

And the stellar mass is determined by Eqs. 4.10 and 4.11.

$$\dot{M}_\star = \frac{M_g}{\tau_\star}(1-R) \tag{4.10}$$

$$M_\star(t) = -\frac{\dot{M}_{in}}{1-R}e^{t(1-R)/\tau_\star} + (1-R)t\tau_\star - \frac{\dot{M}_{in}\tau_\star}{1-R} \tag{4.11}$$

Using these equations, we can model the evolution of the mass in the galaxy as a function of redshift. In Figs. 4.3 and 4.4, we see how the gas, dust, and stellar masses for the MW as a function of redshift differ in between the two models. In each, the dust and gas masses for today ($z = 0$) are fixed, and the stellar mass is allowed to vary. In Figs. 4.5 and 4.6, we see that the dust-to-gas ratios for each model are the same as a function of redshift.

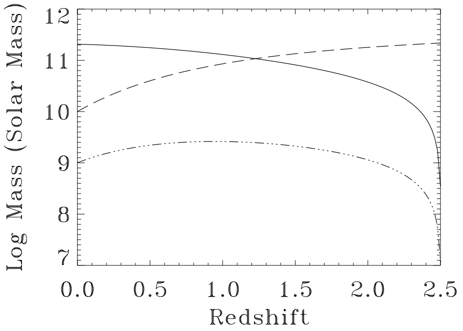

Figure 4.3: Mass of stars (solid line), gas (hatched line) and dust (dotted/hatched line) as a function of redshift in the exponential model.

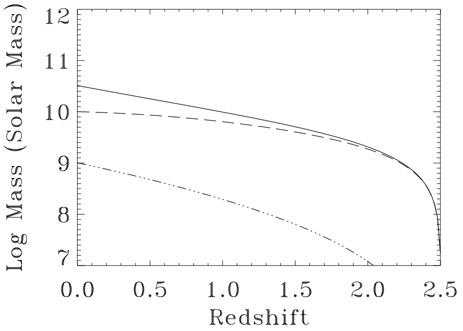

Figure 4.4: Mass of stars (solid line), gas (hatched line) and dust (dotted/hatched line) as a function of redshift in the infall model.

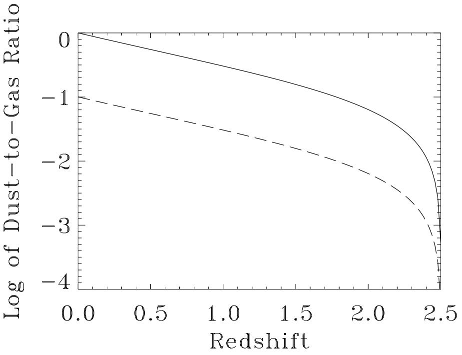

Figure 4.5: Dust-to-gas ratio of the MW as a function of redshift (solid line) and the ratio of the dust-to-gas ratio as a function of redshift to the dust-to-gas ratio today in the exponential model.

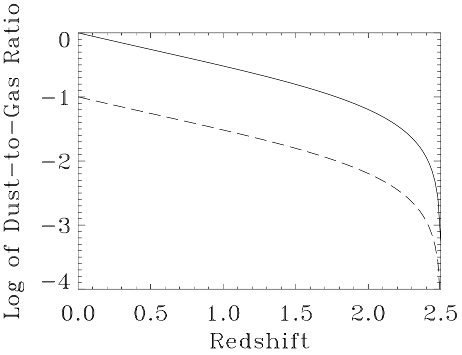

Figure 4.6: Dust-to-gas ratio of the MW as a function of redshift (solid line) and the ratio of the dust-to-gas ratio as a function of redshift to the dust-to-gas ratio today in the infall model.

4.3 Radius of the MW

Now we have a function for determining gas, dust, and stellar masses of the galaxy as a function of redshift. Next, we want to change the morphology of the galaxy as it evolves. We employ the model of Naab & Ostriker (2006) to change the scale length of the disk as a function of redshift while leaving the scale height constant.

$$R_D(t)\ (t \geq t_{form}) = R_D(t_{form}) \frac{H(t_{form})}{H(t)} \tag{4.12}$$

The variable t_{form} is the time of formation of the disk (taken to be 1.7 Gyr after the big bang); the age of the MW disk today is 10 Gyr (13.7 Gyr after the big bang). $H(t)$ is calculated as

$$H(t) = H(z(t)) = H_0[\Omega_{\Lambda,0} + (1 - \Omega_{\Lambda,0} - \Omega_0)(1+z)^2 + \Omega_0(1+z)^3]^{1/2}. \tag{4.13}$$

The formation time of the disk is 1.7 Gyr, which gives us an initial disk radius $R_{D,t=0} =$ 0.731 kpc (assuming a current disk radius $R_{D,t=10\,Gyr} = 3.0$ kpc) and $H(t_{form}) = 4.04$ (see Fig 4.7).

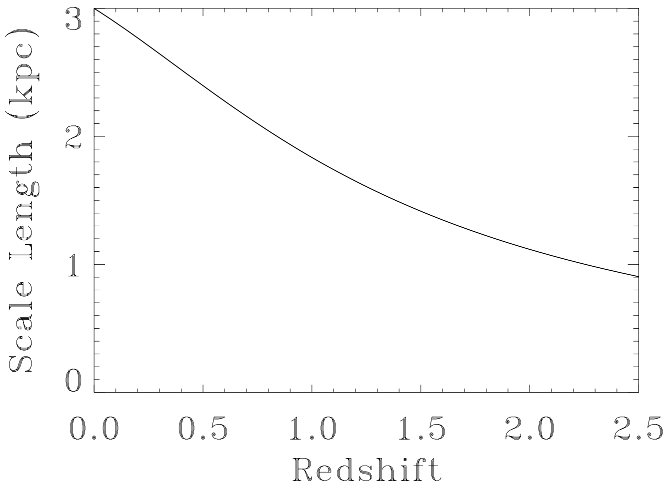

Figure 4.7: Scale length of the MW as a function of redshift.

4.4 Dust Mass of the MW

The exponential model begins at $t_{MW} = 0$ Gyr with a gas mass of 4.045×10^{11} $M_\odot$. As a function of time,

$$M_g(t) = 2\int_0^\infty \int_0^\infty 2\pi\ r\ dr\ dz\ \rho_0\ \hat{\rho}(r,z) = 4\pi\ \rho_0\ R_D^2\ z_D. \tag{4.14}$$

This gives us a current-day gas mass of 10^{10} $M_\odot$. To calculate the extinction, we need to find the mass of dust in the galaxy as a function of redshift. At $t_{MW} = 0$ Gyr, there was no dust in the galaxy. At $t_{MW} = 10$ Gyr, about 1% of the galaxy mass (10^9 $M_\odot$) is in dust. The return fraction of gas and dust R is modified by the dust yield Y. The return fraction is taken to be 30%; the yield is 8.4%. The change in the dust mass as a function of time is

$$\dot{M}_d = -\frac{M_g}{\tau_\star}\frac{M_d}{M_g} - \frac{M_g}{\tau_\star}(R \times Y) \tag{4.15}$$

and $\tau_\star$ is the star formation rate timescale (2.5×10^9 years). Solving the differential equation, we find that

$$M_d(t) = \frac{M_g\, t\, R\, Y}{\tau_\star} \tag{4.16}$$

where t is the amount of time passed (in years).

The infall model does not change the dust mass equations from those given in Eq. 4.15 and Eq. 4.16.

While there are several factors that contribute to dust in the galaxy (see Section 2), the only one we will incorporate into this initial model is dust from supernovae, thought to be the main contributor of dust to the galaxy at high redshifts. Models presented later in this section will include AGB star dust. The dust production rate depends on how much of the gas will turn into supernovae progenitors (stars of mass greater than 8 $M_\odot$) and how much dust yield we can expect from these supernovae (assuming type II, core-collapse).

We can use the Salpeter initial mass function (IMF) to determine how much of the mass will be locked into high mass ($M > 8\ M_\odot$) stars. To determine the mass of gas turned into stars in a particular mass range m_1 to m_2,

$$M(m_1, m_2) = \int_{m_1}^{m_2} \xi(m)\, dm \tag{4.17}$$

$$M(m_1, m_2) = \frac{\xi_0\, (m_1^{-\alpha+1} - m_2^{-\alpha+1})}{\alpha - 1}. \tag{4.18}$$

In the range 0.3 – 8 $M_\odot$, we find $M = 2.9814\ \xi_0$, and in the range 8 – 100 $M_\odot$, $M = 0.85367\ \xi_0$ (for $\alpha = 1.3$). This gives us 22% of the mass of the original gas cloud forming high mass stars, capable of producing core-collapse supernovae. Of that percentage, between 10% and 30% will be turned into dust ($R = 6.6\%$), from the progenitor star and the ejecta (Maiolino et al., 2004). This gives us a dust yield of 38%. From this equation, we find that the mass of dust today is $10^9\ M_\odot$.

As we can see in Fig. 4.3, the gas mass of the galaxy decreases in time (increasing in redshift). The dust mass (Fig. 4.4) increases with galaxy age initially, then turns over around $z = 1.4$ and decreases again.

In Fig. 4.5, we see the dust-to-gas ratio of the MW as a function of redshift. At $z \sim 4$, there was no dust in the galaxy. At $z \sim 0$, the dust-to-gas ratio is about 1%, as we also see in measurements of dust and gas in the MW today. Fig. 4.6 shows the ratio of the dust-to-gas ratio and the dust-to-gas ratio today; as expected, it begins at zero and climbs to one.

4.4.1 Extinction at the Galactic Center

Let us now recalculate the number of magnitudes of extinction at the galactic center as the mass of dust changes in time. The density of material at the center is proportional to $\rho_{center} = M_d$ / $(4\,\pi R_D^2 z_D)$, scaled so that the center density at $z = 0$ is equal to the magnitudes of extinction in the V-band at that redshift (5.94). Fig. 4.8 and Fig. 4.9 show the number of magnitudes of extinction as a function of redshift at the center of the galaxy and at the position of the Sun in the galaxy, respectively, for the exponential model, and Fig. 4.10 and Fig. 4.11 show the same for the infall model. Here we assume that the Sun remains at $R_D = 8.5$ kpc as the galaxy scale length changes.

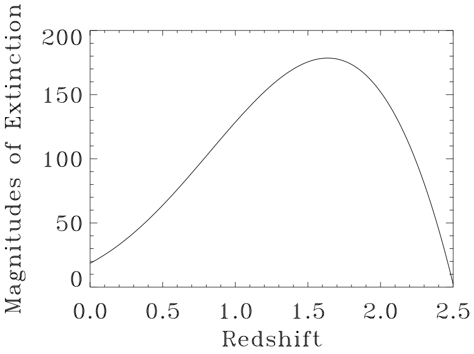

Figure 4.8: Magnitudes of extinction at the galactic center as a function of redshift (in the exponential model).

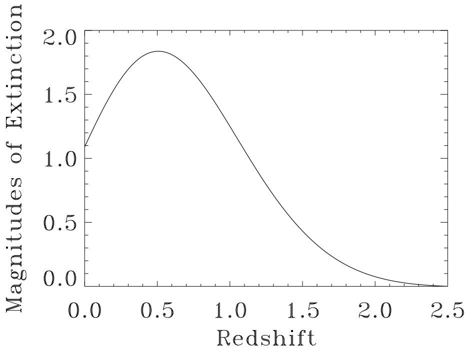

Figure 4.9: Magnitudes of extinction at the Sun's position (8.5 kpc) as a function of redshift (exponential model).

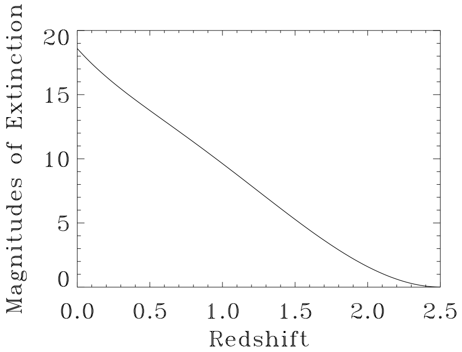

Figure 4.10: Magnitudes of extinction at the galactic center as a function of redshift (in the infall model).

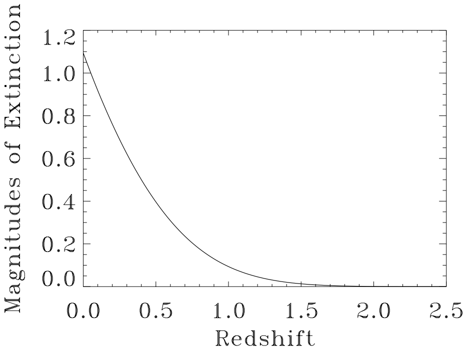

Figure 4.11: Magnitudes of extinction at the Sun's position as a function of redshift (infall model).

4.5 Modeling GRB Host Galaxies

The MW galaxy model is not entirely representative of the types of galaxies that host GRBs; GRB hosts tend to be small, blue, irregular galaxies. Several recent studies have examined the mass and size of host galaxies, fortunately with overlapping samples.

Savaglio et al. (2009) used optical and NIR photometric and spectroscopic techniques to determine the stellar mass of 46 GRB host galaxies. Fruchter et al. (2006) determined the radius in which 80% of the light from host galaxies is contained (R_{80}) using Hubble imaging. The two samples had an overlap of 25 GRB host galaxies, which we used to constrain our models.

Table 4.1: GRB host galaxies found in both Fruchter et al. (2006) and Savaglio et al. (2009).

Burst	z	log M_* (M_{odot})	R_{80} (kpc)
970228	0.695	8.65 ± 0.05	3.2
970508	0.835	8.52 ± 0.10	1.48
970828	0.960	9.19 ± 0.36	2.8
971214	3.420	9.59 ± 0.40	2.36
980613	1.097	8.49 ± 0.21	3.75
980703	0.966	9.33 ± 0.36	2.42
990123	1.600	9.42 ± 0.49	5.01
990506	1.310	9.48 ± 0.18	1.53
990705	0.842	10.20 ± 0.76	9.38
990712	0.433	9.29 ± 0.02	2.25
991208	0.706	8.53 ± 0.37	1.16
000418	1.118	9.26 ± 0.14	1.70
000926	2.036	9.52 ± 0.84	10.25
010222	1.480	8.82 ± 0.26	2.87
010921	0.451	9.69 ± 0.13	2.76
011121	0.362	9.81 ± 0.17	5.89
011211	2.141	9.77 ± 0.47	2.69
020405	0.691	9.75 ± 0.25	11.96
020813	1.255	8.66 ± 1.41	2.13
020903	0.251	8.87 ± 0.07	1.43
021004	2.327	10.20 ± 0.18	1.81
021211	1.006	10.32 ± 0.63	1.63
030329	0.168	7.74 ± 0.06	1.03
040924	0.859	9.20 ± 0.37	3.234
041006	0.712	8.66 ± 0.87	5.19

According to Naab & Ostriker (2006), the mass of stars in the MW is 2.7×10^{10} $M_{\odot}$. The sample from Savaglio et al. (2009) found an average host stellar mass of 4×10^9 $M_{\odot}$, and Fruchter et al. (2006) found an average R_{80} of 3.6. Our model is defined by the scale length (3 kpc), and if we assume the light distribution is traced by the source density, this corresponds to a R_{80} of 8.9 kpc.

This corresponds to a scaling factor of 0.15 in mass and 0.404 in radius at the average host redshift of $z = 1.1$. Fig. 4.12 depicts the evolution of the scaled host galaxy radius as a function of redshift.

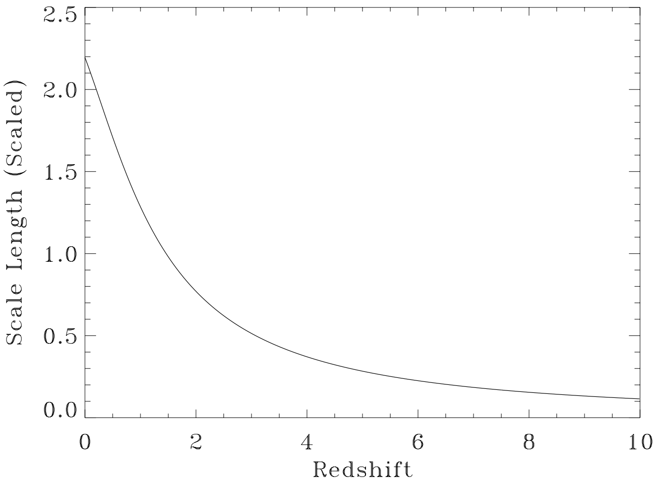

Figure 4.12: GRB host galaxy radius scaled to that of a typical host galaxy (Fruchter et al., 2006) at $z = 1.1$.

We can now use this scaled disk galaxy to model a population of GRB host galaxies. The galaxy routines found in Appendix C can produce the expected masses of galaxy material as a function of formation redshift. For example, varying dust masses as a function of redshift are shown in Fig. 4.13. The stellar masses of the host galaxy population are set to equal the average stellar mass of the Savaglio/Fruchter sample at the average host redshift of $z = 1.1$, which corresponds to equal dust masses at $z \sim 0.7$.

The galaxy evolution code, original routine GALINSAV_1.pro (Appendix C), ignores cosmological effects and instead begins by focusing on the amount of visual extinction in the co-moving frame of the host galaxy.

We begin by choosing a common formation redshift of $z = 10$ for our GRB host galaxy. We allow it to evolve to $z = 0.0$ in 100 steps and calculate the amount of extinction suffered by a GRB placed within the host given 2,000 random sightlines out of the host for each redshift step. Fig. 4.14 shows a typical GRB progenitor placement within a host and the sightline calculated out of the host

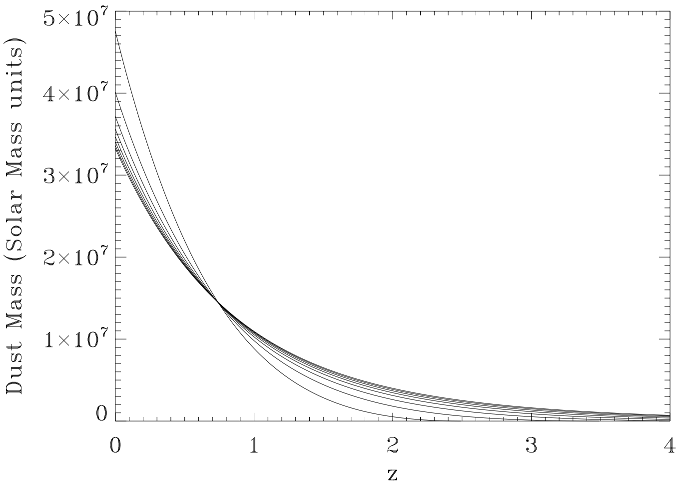

Figure 4.13: Varying dust mass in host galaxies as a function of formation redshift.

galaxy. The galaxy is indicated by five concentric circles at 2, 4, 6, 8, and 10 kpc away from the galaxy center.

Cosmological effects have been omitted from this calculation in order to compare the results to extinction measurements from the literature, which included A_V calculated in the co-moving host frame.

The average visual extinction A_V in the co-moving frame suffered by a GRB along a line of sight out of the host galaxy as simulated by our program can be compared to the results in our GRB sample (see Conclusions).

4.6 Differentiating Dust

Now we wish to differentiate between our dust sources by adding more complexity to our model; we need to distinguish between dust contributed by core-collapse supernovae and the dust contributed by asymptotic giant branch stars (AGB stars). In order to accomplish this, we need to understand the initial mass function (IMF) of the various stellar populations, the dust production rates of stars by mass, and when and how these stars form dust over their lifetimes.

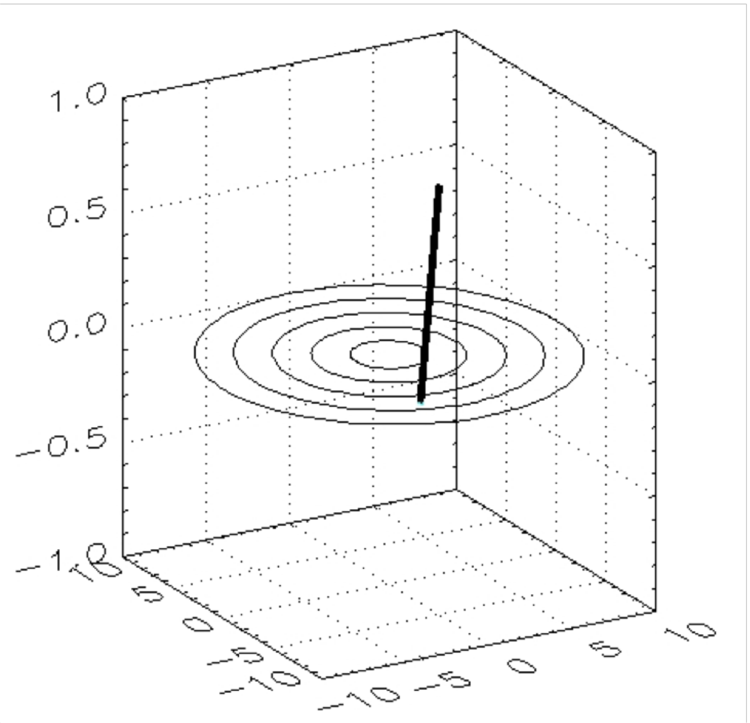

Figure 4.14: Simulation of a GRB sightline out of the host galaxy; units of kpc.

4.6.1 IMFs for Population I, II, and III Stars

Population III stars, the first stars to form in the universe, are thought to have formed in two distinct groups (Tan & McKee, 2008). The first, Pop III.1 stars, form from pristine gas halos with zero metals. Star formation models in pristine gas (Clark et al., 2010) predict Pop III.1 stars to form at lower masses on average than Pop III.2 stars due to higher turbulent velocities in non-ionized pristine gas (while Pop III.2 stars also form from pristine gas, the gas is partially ionized by the Pop III.1 stars). Both Pop III.1 and Pop III.2 stars are predicted to exhibit IMF with a power law distribution similar to those seen today. However, low mass Pop III stars have not been found, and perhaps cannot be identified due to contamination from the ISM (Frebel et al., 2009). For the purposes of our model, we will assume a flat IMF for Pop III stars; all stars will be assumed to form with a mass of 170 $M_\odot$ to allow easy comparison to the dust production models of Cherchneff & Dwek (2009). Note that a power law IMF would only change our results if we took into account varying dust production rates from the lower mass stars, as we will for Pop I and II stars.

For Pop I and II stars, we assume a Salpeter IMF. Comparisons to various other IMFs

(Kroupa, 2002; Chabrier, 2003) have no significant effect on our overall results.

4.6.2 Star Formation Rates for Pop I/II and III Stars

We will use the weak chemical feedback and early reionization ($z_{reion} \sim 17$) models of Bromm & Loeb (2006) (see Figure 4.15) to determine at which redshifts we will get each population of stars. Under these assumptions, Pop III stars begin to form at a redshift of 27 and stop at a redshift of 7; Pop I/II stars begin forming at $z = 24$ and are still forming today. We will use a somewhat artificial turnover between the formation rates of Pop I/II and Pop III stars; beginning at $z = 24$, Pop III stars go from 100% of the total stars formed to 0% at $z = 7$, while Pop I/II stars go in the opposite direction with percentages changing linearly as a function of redshift.

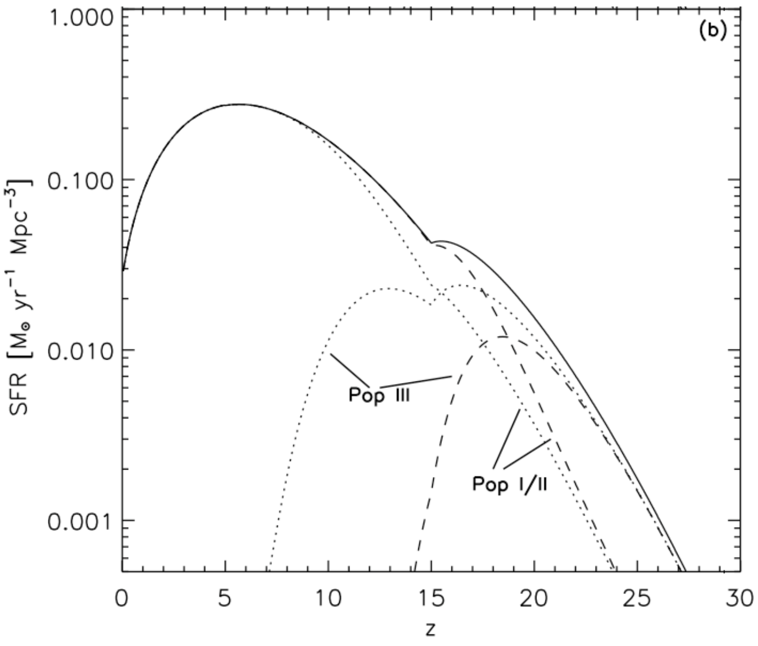

Figure 4.15: Star formation timescales of Pop I/II and III stars from Bromm & Loeb (2006).

4.6.3 Dust Yields and Timescales by Mass

Dust yields from various stars have been computed as a function of their mass. The amount of dust produced by a core-collapse supernova depends on the initial mass of the progenitor star. This has been calculated for the case of the 20 $M_\odot$ and 170 $M_\odot$ stars by Cherchneff & Dwek (2009) to have an average dust production rate of 14.7 – 21.0% of the stellar mass in the case of the 170 $M_\odot$ star and a range of 0.80 – 1.70% in the case of the 20 $M_\odot$ star. We assume all Pop III star will form core-collapse supernova at 170 $M_\odot$, and we assume that all Pop I/II stars with masses of 9 – 100 $M_\odot$ will result in core-collapse SNe with a dust yield of the same percentage as found in a 20 $M_\odot$ star. We note that a star of 170 $M_\odot$ would technically form a pair-instability supernova (PISN) instead of a core-collapse supernova (CCSNe, Bertoldi et al., 2003); however, we are using this as an overall average of massive stars so this does not change our results. Furthermore, Cherchneff & Dwek (2010) found the same results for PISNe as CCSNe.

Stars that will form CCSNe have lifetimes on the order of 10^6 years or less (Bromm & Loeb, 2006). The time steps taken by our model of galactic evolution are on that order or longer, so we can use an instantaneous recycling approximation for CC SNe – in each time step, gas and dust is converted to high mass stars, which explode and return gas, dust, and stellar remnants to the ISM. For CCSNe, it is assumed that 30% of the mass of the progenitor star will be returned as gas and dust; the fraction of which is dust is given above.

Lower mass stars formed in the Populations I and II are defined as those having masses between 0.01 and 9 $M_\odot$. Only those with masses between 0.8 – 9 $M_\odot$ will contribute dust and gas return; lower mass stars have lifetimes beyond the scope of our model and we simply lose gas and dust to star formation with no return. Figure 4.16 shows the time in Myr between the formation of the star and the age where it reaches the AGB phase. Data for time from formation to zero age main sequence (ZAMS) has been taken from Bernasconi & Maeder (1996); data for the time between ZAMS and AGB phase has been taken from Schaller et al. (1992).

Stars with masses between 0.8 – 9 $M_\odot$ will undergo non-instantaneous recycling in our model; they will form at some initial time step (taking a portion of gas and dust and converting it to stars) and return that gas and dust in a later time step. AGB stars have typical mass loss rates on the order of 10^{-4} $M_\odot$ yr^{-1} and will lose between 20 and 80% of their initial mass in gas and dust during the AGB phase Lagadec et al. (2008). For the purposes of our model, we employ the AGB evolution models of Karakas (2010) including initial mass, final mass, and isotope production.

Low mass stars have been sorted into bins for the purposes of our model in order to simplify mass loss rates and ages; the bins are given in Table 4.2. Percentages are given assuming a Salpeter Initial Mass Function (Salpeter, 1955) for stars between 0.1 and 100 $M_\odot$; stars between 0.1 and 0.8 $M_\odot$ make up 53.096% of the total, while stars between 9 and 100 $M_\odot$ make up 15.06% of the total.

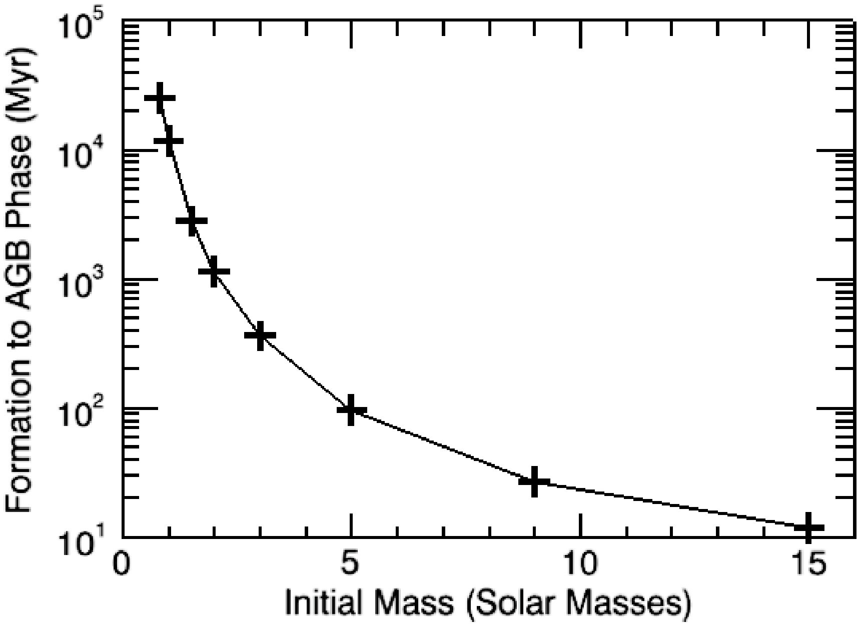

Figure 4.16: Time between star formation and AGB phase for low mass stars.

Table 4.2: Mass bins employed for AGB stars following the models of Karakas (2010). The Karakas Mass is the mass used by Karakas (2010) for the abundance calculation (in solar masses), the lower and upper limits define the artificial boundaries for that mass bin (in solar masses), and the percentage is the overall percentage of the total stars incorporated into that mass bin.

Karakas Mass	Lower Limit	Upper Limit	Percentage
1.00	0.8	1.125	5.96
1.25	1.125	1.325	2.65
1.50	1.325	1.625	3.13
1.75	1.625	1.825	1.70
1.90	1.825	1.95	0.949
2.00	1.95	2.125	1.19
2.25	2.125	2.325	1.22
2.50	2.325	2.75	2.19
3.00	2.75	3.25	2.07
3.50	3.25	3.75	1.69
4.00	3.75	4.25	1.42
4.50	4.25	4.75	1.22
5.00	4.75	5.25	1.06
5.50	5.25	5.75	0.939
6.00	5.75	9.00	4.27

Note that the Karakas (2010) models only extend to 6 $M_\odot$, so the last mass bin includes everything between 5.75 and 9.00 $M_\odot$.

Karakas (2010) calculates abundances of various isotopes produced by AGB stars. The main isotopes of interest to us are ^{12}C, ^{13}C, ^{16}O, and ^{17}O, being the most abundant varieties of carbon and oxygen. Recall from the Introduction that the ratio of carbon and oxygen produced by a star determines its overall dust output; the gas CO has a higher condensation temperature than either graphite or silicate, so all the carbon and oxygen that can be converted to CO will be. The resulting dust species depends on whether carbon or oxygen dominates in the stellar winds.

The amounts of carbon and oxygen produced by an AGB star vary with the metallicity of the star. In Figures 4.17, 4.18, 4.19, and 4.20 we show how the amounts of each isotope produced as a function of the initial mass of the AGB star.

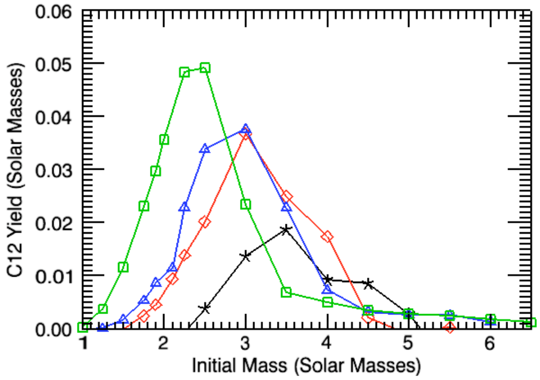

Figure 4.17: ^{12}C produced by an AGB star as a function of initial mass. Metallicity of 0.02 is denoted in black, 0.008 in red, 0.004 in blue, and 0.0001 in green.

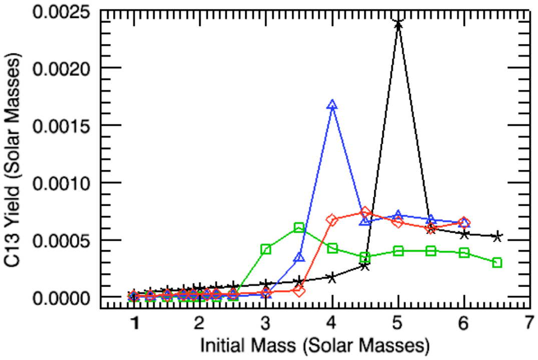

Figure 4.18: ^{13}C produced by an AGB star as a function of initial mass. Metallicity of 0.02 is denoted in black, 0.008 in red, 0.004 in blue, and 0.0001 in green.

We can now examine the amount of carbon versus oxygen produced by AGB stars as a function of initial mass by adding the carbon isotopes and the oxygen isotopes. The results are plotted in Figures 4.21, 4.22, 4.23, and 4.24.

Unlike the results found by Dwek (1998) from the models of Renzini & Voli (1981), who found that AGB stars produce both carbon and oxygen as a function of initial mass and metallicity, Karakas (2010) finds using updated AGB models, nucleosynthesis codes, and dredge-up models that only carbon will be produced by AGB stars. The amount of carbon dust produced by these stars is equal to the total carbon yield minus the total oxygen yield (denoted by the black line in the

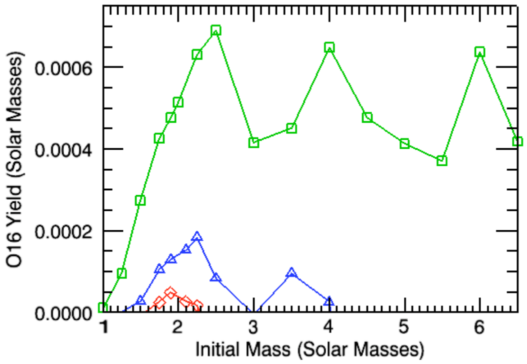

Figure 4.19: ^{16}O produced by an AGB star as a function of initial mass. Metallicity of 0.02 is denoted in black, 0.008 in red, 0.004 in blue, and 0.0001 in green.

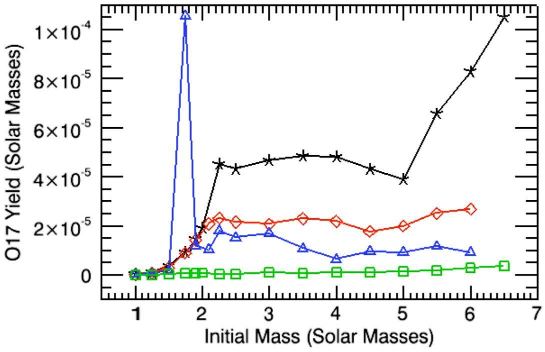

Figure 4.20: ^{17}O produced by an AGB star as a function of initial mass. Metallicity of 0.02 is denoted in black, 0.008 in red, 0.004 in blue, and 0.0001 in green.

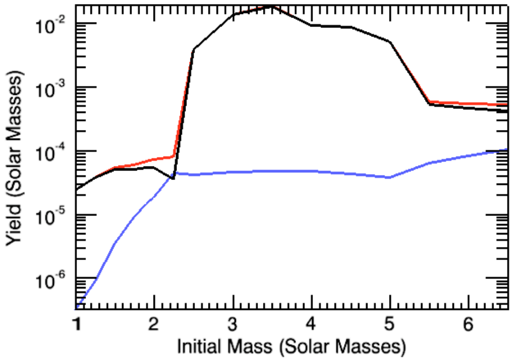

Figure 4.21: Carbon and oxygen yields for $Z = 0.02$. Carbon is denoted in red, oxygen (silicate) in blue, and the overall dust yield in black.

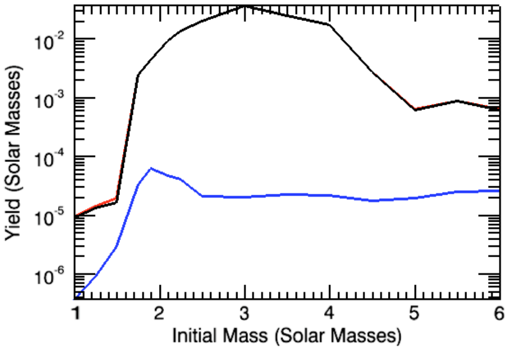

Figure 4.22: Carbon and oxygen yields for $Z = 0.008$. Carbon is denoted in red, oxygen (silicate) in blue, and the overall dust yield in black.

above-mentioned plots) to account for the formation of CO.

In each time step in our model, a given amount of dust and gas becomes stars. The percentage of Pop III and Pop I/II stars is determined using the method described above, and the amount of mass given to each mass bin is calculated using the above percentages.

4.7 Results

By combining our models of galactic evolution with our models of dust, gas, and star return from the above star formation models, we can investigate the amount and type of dust we get as a

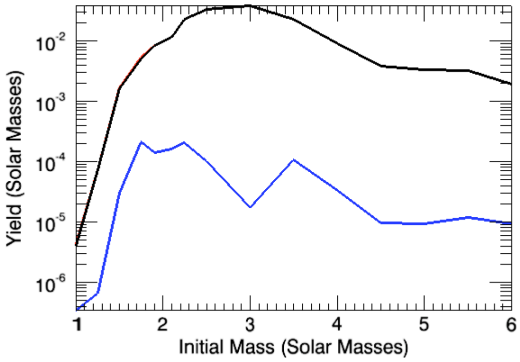

Figure 4.23: Carbon and oxygen yields for $Z = 0.004$. Carbon is denoted in red, oxygen (silicate) in blue, and the overall dust yield in black.

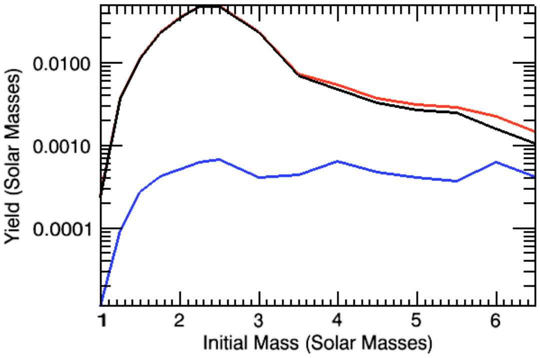

Figure 4.24: Carbon and oxygen yields for $Z = 0.0001$. Carbon is denoted in red, oxygen (silicate) in blue, and the overall dust yield in black.

function of redshift from various galaxy formation models.

We will begin with a typical galaxy forming from pristine gas infall from the halo (with an exponentially decreasing infall model as opposed to a constant one) at a redshift of 10.

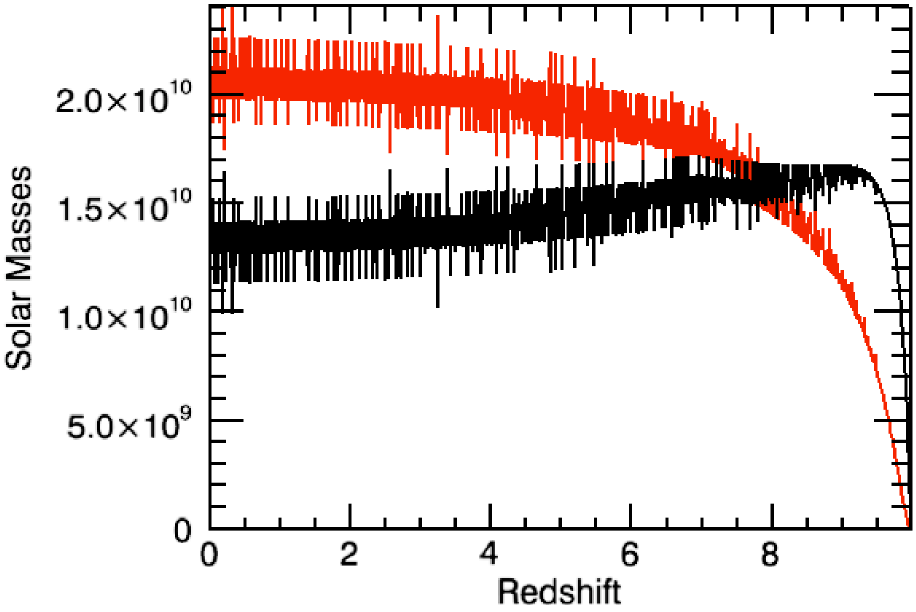

Figure 4.25: Stellar and gas masses of a galaxy forming at $z = 10$. Stellar mass is the red line; gas mass is black.

The results of this model are given in Figure 4.25. The stars are plotted in red, gas mass in black. The gas mass has an initial burst at z just smaller than 10 thanks to an initially high infall rate, which then decays to a much smaller rate today at $z = 0$ (see Figure 4.27). The apparently choppy nature of the curves is due to non-instantaneous recycling; stars form from gas in one time step, but do not redeposit gas until a later time step. Star formation is a bit slower to ramp up but eventually overtakes gas in the amount of mass contained. As the gas infall rate decreases, the star formation rate will level off.

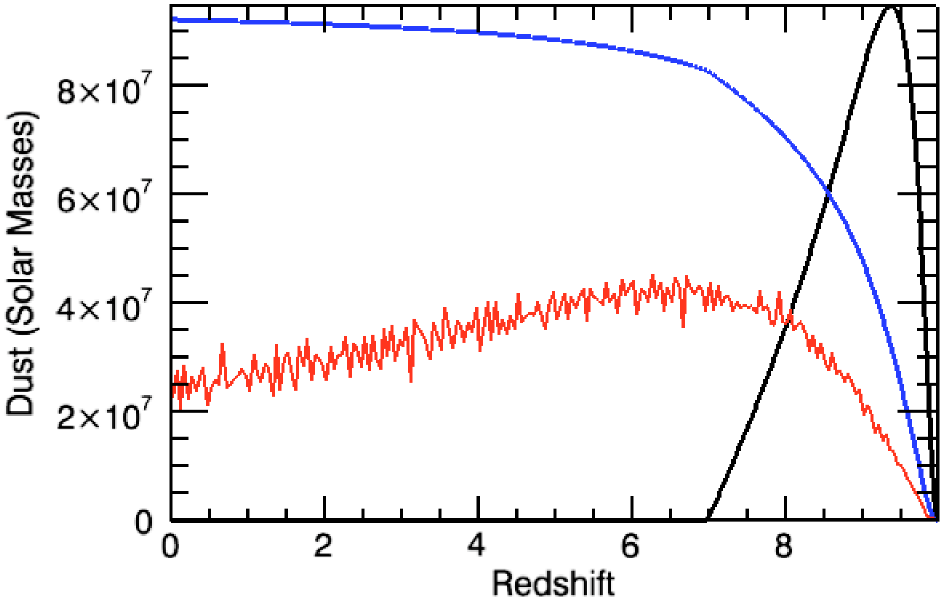

Figure 4.26: Graphite and silicate masses of a galaxy forming at $z = 10$. Silicates are given in black (from Pop III), blue (from Pop I/II) and graphite is red. Graphite is shown averaged over every 5 data points to reduce scatter

Figure 4.26 shows the amount of mass of graphite and silicate in this galaxy as a function of time. The black line shows the contribution from Pop III stars; at at formation redshift of 10, this galaxy will only see Pop III stars contribute until $z = 7$, and most of that silicate will be lost to the formation of new stars. The blue line shows the silicate contributions from Pop I/II CC SNe; the black and blue lines do not show the 'choppiness' of the other lines due to the instantaneous recycling approximation used. The silicate contribution from Pop I/II CC SNe is initially large due

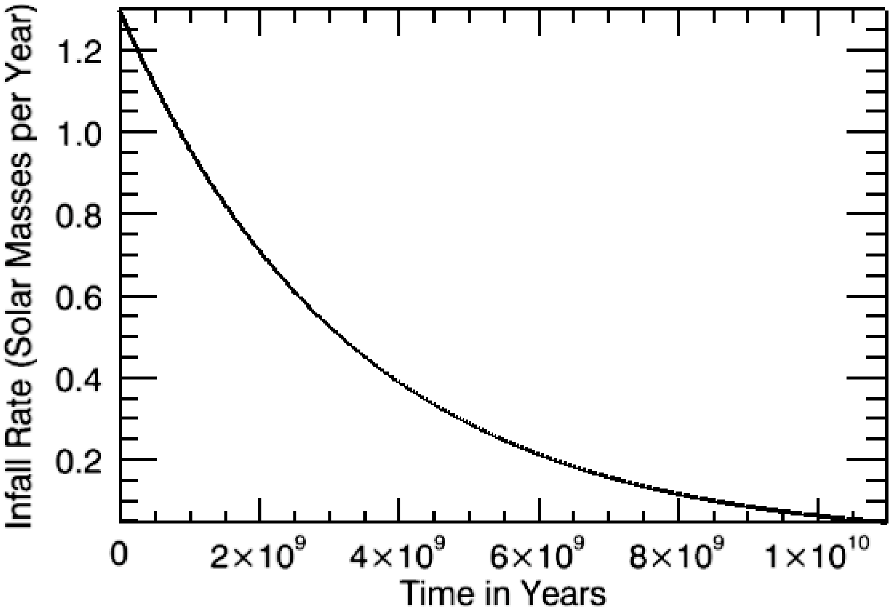

Figure 4.27: Infall of pristine gas from the halo as a function of time.

to an large infall of gas, but ramps down as it is lost to the formation of new stars. The yellow line reflects the growth of graphite grains in the ISM of the galaxy as a function of redshift; initially nothing due to the non-instantaneous recycling, then becoming larger as more stars contribute dust over time.

In Figure 4.28, we investigate the graphite and silicate contributions in a galaxy similar to the MW, starting at a formation redshift of 2.5. Assuming infall of pristine halo gas, we do not see a contribution from Pop III stars at this late formation redshift. Again we see the silicate (black line) peak early and then drop off as graphite (red) contributes more slowly.

We can also extrapolate spectral energy distributions (SEDs) of GRB situated inside these galaxies as a function of redshift in order to predict the change in the SED as the dust content of the galaxy changes. An example of this is given in Figure 4.29.

These models can be used to predict the expected SEDs of GRB as a function of redshift. We see that we would expect mostly silicate dust early in the history of a galaxy with gradually increasing amounts of graphite and dust overall.

The original galaxy evolution code GALIN_MASS_KARAKAS.pro including the Karakas

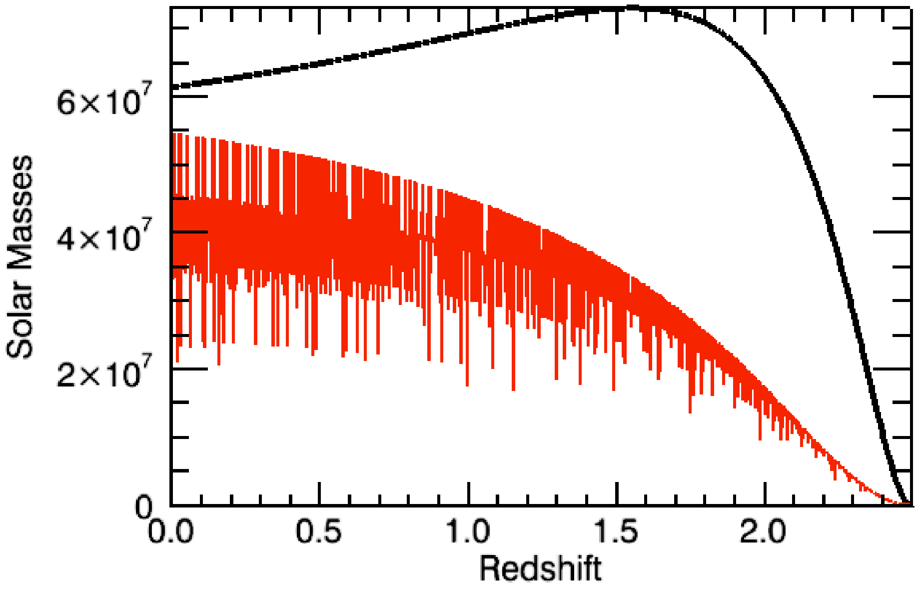

Figure 4.28: Graphite and silicate masses of a galaxy forming at $z = 2.5$. Graphite is red, silicate black.

(2010) models can be found in Appendix C.

4.8 An Evolutionary Test Case

Let us return to the model host galaxy forming at $z = 10$ (Figures 4.25 and 4.26) and explore further predictions of our model. First, we look at the total dust mass in the galaxy as a function of redshift, given in Figure 4.30.

Evolutionary effects of dust production could really only be extracted in the early formation stages of the galaxy; after that, the overall dust amount is fairly constant in time. We will see in the Conclusions that evolutionary trends in the graphite to silicate ratio in the galaxy will also be impossible to extract according to our models for redshifts of 6 or smaller.

Next, we will put this galaxy forming at $z = 10$ into our dust extinction code to find the spread of A_V values it would predict as a function of redshift. We see in the following histograms that as the redshift increases, so does the overall amount of extinction suffered by a GRB through random sight-lines in a host galaxy. While the overall trend is towards less dust in the early universe,

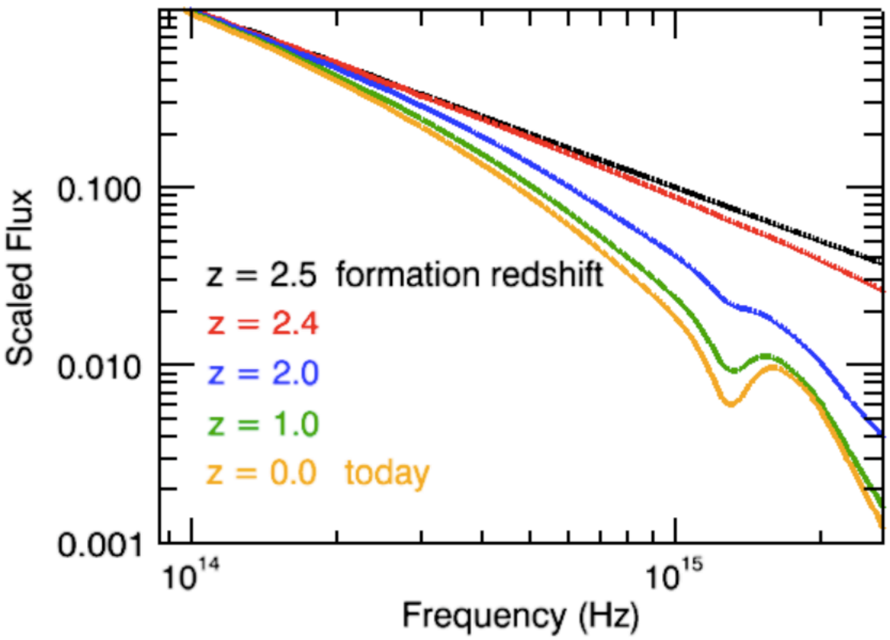

Figure 4.29: SED of a GRB inside a scaled MW-like host galaxy as a function of redshift.

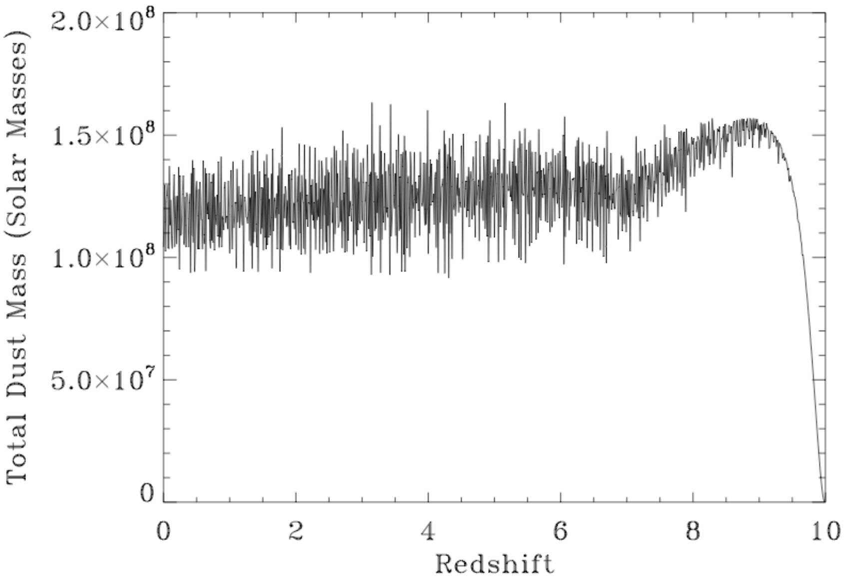

Figure 4.30: Total dust mass in a galaxy formed at $z = 10$ as a function of redshift.

the changing radius of the host galaxy forces the extinction to rise as nearly the same amount of dust (over redshifts from 0 to 6 in Figure 4.30 we see little change) is forced into a smaller galaxy. The A_V values continue to increase as the radius of the galaxy shrinks faster than the dust mass until we reach $z \sim 9.5$, where we begin to see the lower amounts of dust causing the overall galactic extinction to shrink once more.

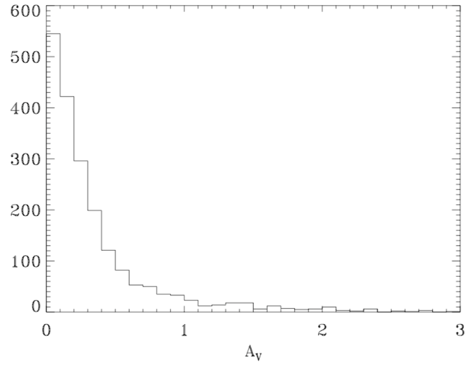

Figure 4.31: Histogram of A_V values at $z = 0$ for our galaxy with formation redshift 10.

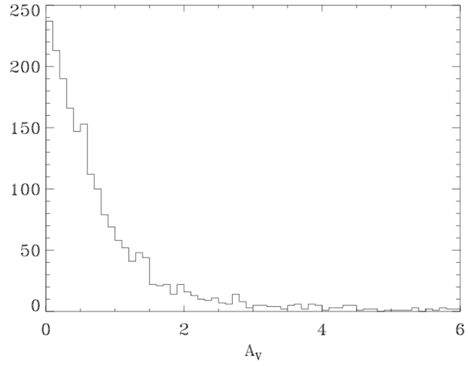

Figure 4.32: Histogram of A_V values at $z = 1.0$ for our galaxy with formation redshift 10.

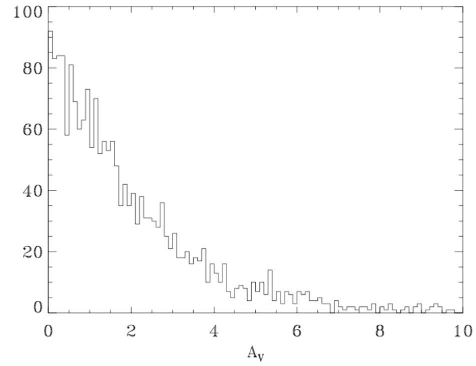

Figure 4.33: Histogram of A_V values at $z = 2.0$ for our galaxy with formation redshift 10.

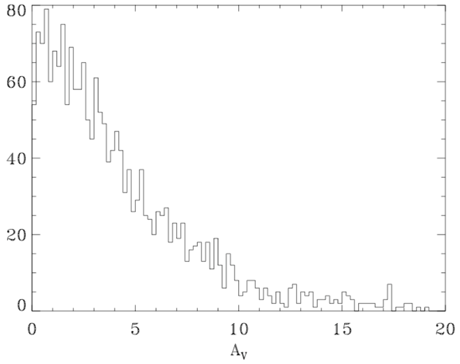

Figure 4.34: Histogram of A_V values at $z = 3.0$ for our galaxy with formation redshift 10.

The average A_V of this galaxy as a function of redshift is plotted in Figure 4.45. Note the very large predicted values of A_V at higher redshifts, which, as we will see in our conclusions, is not necessarily supported by the data. One major adjustment to our dust model which has not yet been incorporated would be dust destruction – grain destruction by supernovae, grain-grain collisions in the interstellar medium, and grain destruction in the winds of low-mass and massive stars (Karakas, 2010). A single supernova alone can destroy 10^6 solar masses of dust in its environment. Recent

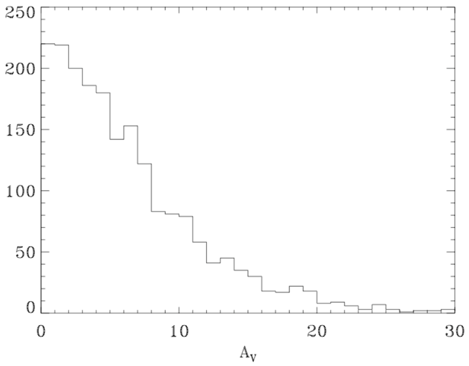

Figure 4.35: Histogram of A_V values at $z = 4.0$ for our galaxy with formation redshift 10.

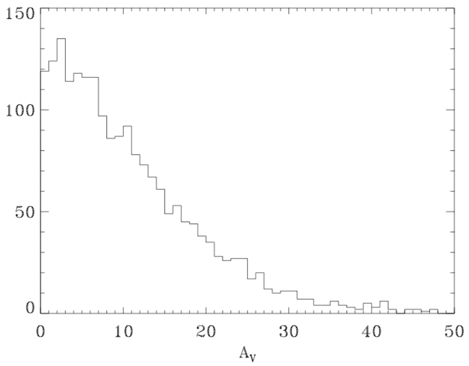

Figure 4.36: Histogram of A_V values at $z = 5.0$ for our galaxy with formation redshift 10.

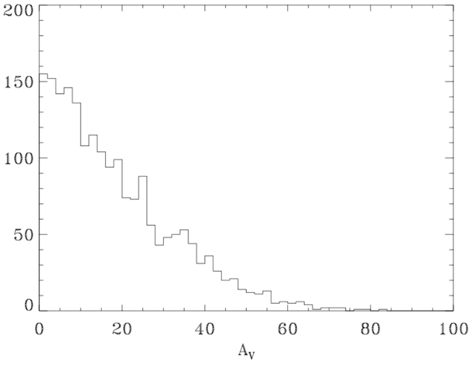

Figure 4.37: Histogram of A_V values at $z = 6.0$ for our galaxy with formation redshift 10.

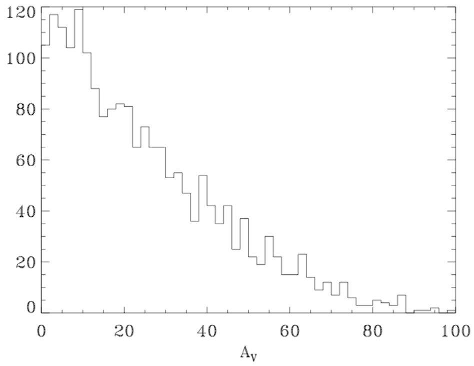

Figure 4.38: Histogram of A_V values at $z = 7.0$ for our galaxy with formation redshift 10.

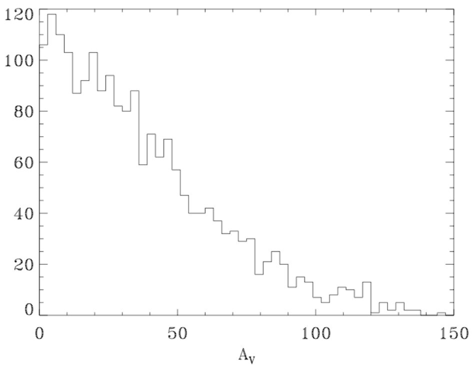

Figure 4.39: Histogram of A_V values at $z = 8.0$ for our galaxy with formation redshift 10.

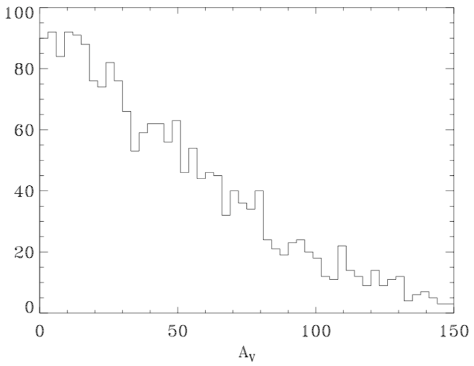

Figure 4.40: Histogram of A_V values at $z = 9.0$ for our galaxy with formation redshift 10.

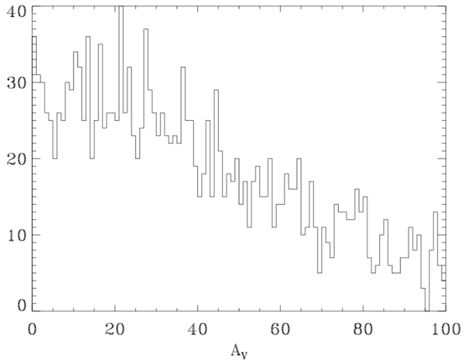

Figure 4.41: Histogram of A_V values at $z = 9.5$ for our galaxy with formation redshift 10.

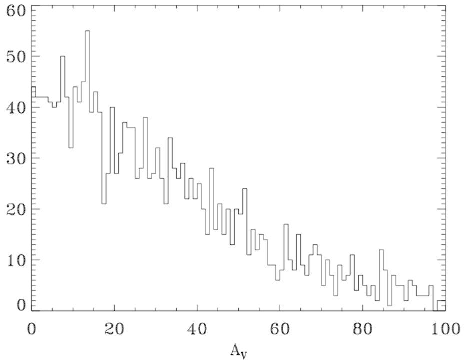

Figure 4.42: Histogram of A_V values at $z = 9.7$ for our galaxy with formation redshift 10.

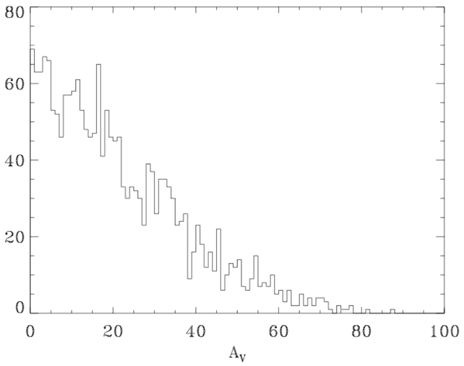

Figure 4.43: Histogram of A_V values at $z = 9.8$ for our galaxy with formation redshift 10.

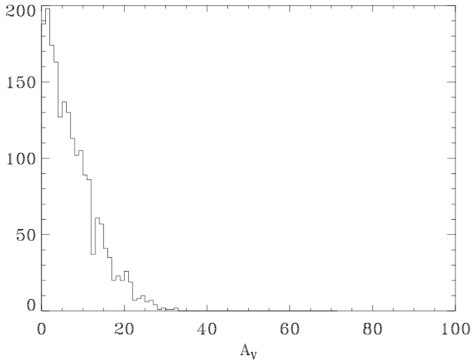

Figure 4.44: Histogram of A_V values at $z = 9.9$ for our galaxy with formation redshift 10.

studies of dust destruction by supernovae (Silvia et al., 2010) have shown supernovae are very efficient at destroying graphite and silicate dust, from $38 - 80\%$ of these dust particles in their immediate area, particularly small particles ($a < 0.1\,\mu$m). Adding dust destruction to our models in the future should severely decrease the predicted extinction at high z values; the smaller radius of the galaxy means each supernova will have a great deal of destructive power.

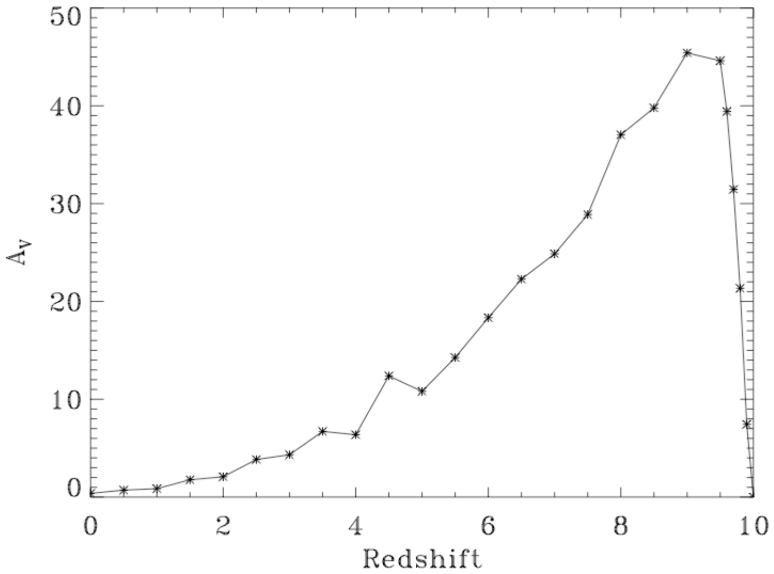

Figure 4.45: Average A_V for our model galaxy as a function of redshift.

Chapter 5

Results and Conclusions

5.1 Results

The dust extinction fits to the 82 GRB SEDs are presented in Appendix A along with a table of the results. The majority of the fits are good; while some $\tilde{\chi}^2$ values are high due to small error bars, the fits appear reasonable with five exceptions. The SEDs of GRBs 021211, 060502, 060904, 070419, and 080810 are not well-constrained mostly due to high discrepant data. Therefore, those results will not be included in the result figures below.

5.2 Redshift Distribution

The redshift distribution of the bursts in our sample is given in Figure 5.1; the overall redshift distribution is given in Figure 5.2. A two-dimensional Kolmogorov-Smirnov test returns a probability that the two samples are drawn from the same distribution of 21.2%, indicating that they are not necessarily drawn from the same sample. Our sample is skewed towards lower z values because we needed bright enough bursts for which there were at least five detections red-ward of Lyman-α. Higher redshift bursts typically had detections in fewer bands, making them unsuitable for this study.

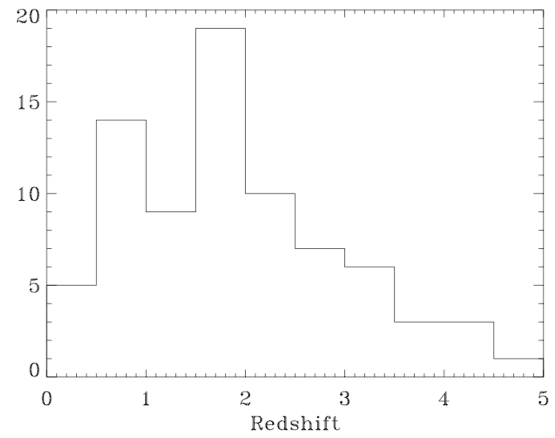

Figure 5.1: Redshift distribution for our sample.

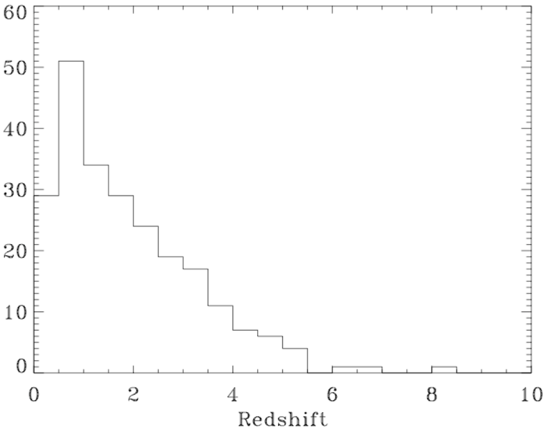

Figure 5.2: Overall redshift distribution.

5.3 A_V as a Function of Redshift

A histogram of our measured A_V values is presented in Figure 5.3. Most of our values are fairly low, as we would expect for a GRB host galaxy with a random alignment (usually looking out of the disk instead of through it). Overall, they have larger average values than we would expect from simple modeling of host galaxies, although this might be explained by the dense molecular clouds in which the stars formed causing extinction.

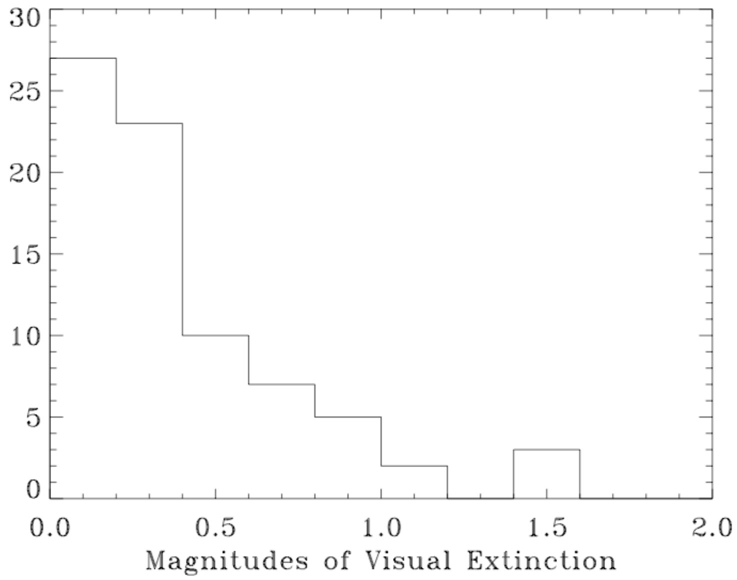

Figure 5.3: Histogram of A_V values.

Our models of dust in evolving galaxies (see Section 4) predict higher values of A_V with increasing redshift as the galaxy radius shrinks faster than the dust content until close to the formation redshift of the galaxy. However, this prediction is likely to change significantly as dust destruction is added to the model.

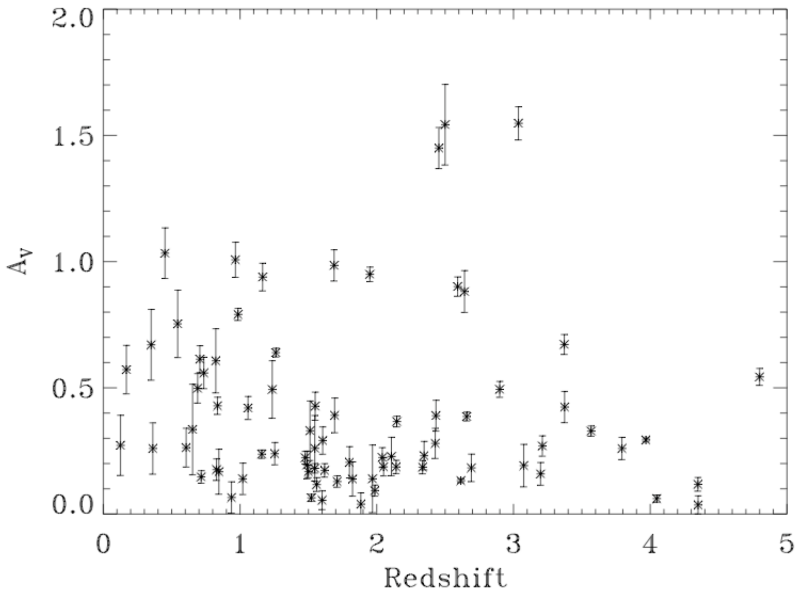

Figure 5.4: A_V as a function of redshift.

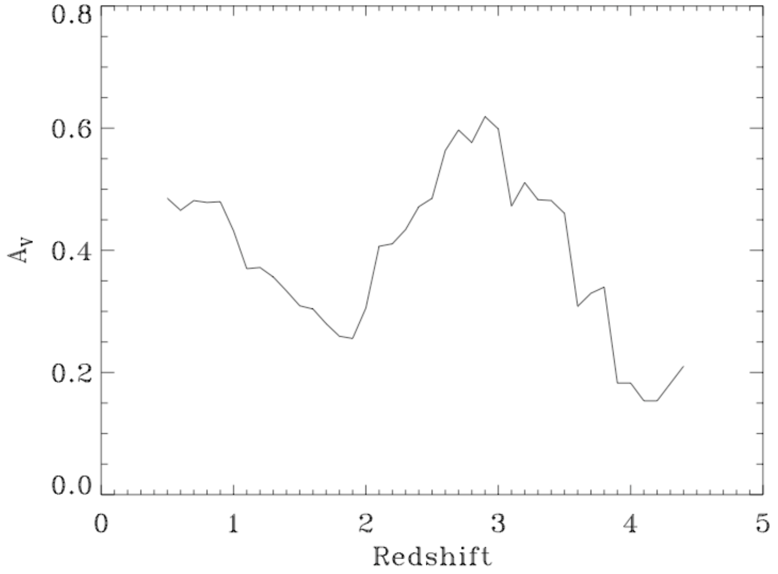

Figure 5.5: Binned values of A_V with redshift.

Figures 5.4 and 5.5 show the changing values of A_V in our sample of 78 bursts as a function of redshift. In Figure 5.5, we take a box or bin the size of one redshift interval and move it through the A_V measurements in steps of size 0.1 redshift, averaging the A_V in that interval if there are five or more measures that fall into it. Now a trend is suggested in the data; we see an initial decrease in the A_V values, then an increase followed by a decrease at higher redshifts as predicted in our model. However, our model followed a single galaxy with a known formation redshift; the GRB host galaxies in our study will likely sample a wide range of galaxy formation times and will probably include mergers as well. A simple model of galaxy evolution cannot hope to predict every possible outcome, but it appears that overall trends in the data may be hinted at in our results. Next we discuss possible reasons for which our data may not agree with our models.

First, our sample may be biased towards brighter bursts. The GRBs included in this sample all had established redshifts (most spectroscopically determined) and enough points to fit an SED template to the data. This necessarily biases the sample to the brightest GRB afterglows for which enough data can be gathered rapidly to form an SED. Since the effects of dust in the host would dim the overall afterglow, a bias in selection towards brighter afterglows would predict smaller dust extinction. Loss of the afterglow completely leads to what is known as the 'dark burst' phenomena. Dark bursts are thought to be a combination of high redshift and highly extincted bursts (Greiner et al., 2010).

Second, dust in the vicinity of the GRB may be causing the higher observed A_V values. Our model does not include the environment of the GRB. GRBs are the result of the stellar explosions of massive stars; we would expect these short-lived stars to still be part of the molecular cloud in which they formed. If this is true, the higher extinctions observed could be cause by dust in the molecular cloud. However, studies of dust destruction by x-rays from the GRB Fruchter et al. (2001); Waxman & Draine (2000) local dust will be destroyed out to 10 pc, which would effectively eliminating the nearby dust contribution. Recent studies of dark bursts Perley et al. (2009) suggest the afterglow suppression is caused by dust in many cases; (Holland et al., 2010) found evidence for a 'slab' of dust in the vicinity of GRB 090417B at a distance greater than 10 pc. It appears more likely that dust in the local environment is contributing to the GRB host extinction than uniformly distributed dust in the host galaxy; this would require a higher dust-to-gas ratio by several orders of magnitude.

Additional sources of error include uncertainties in the subtraction of foreground extinction from the MW using the extinction maps of Schlegel et al. (1998) (a larger potential problem for bursts exhibiting little to no host extinction) and any over-simplications in our own model causing a lower average host extinction (i.e., no dust destruction by supernova).

We see the same overall trend in the total column density of dust as we do in the A_V values (see Figure 5.6), as is to be expected since the A_V values are directly related to the dust column density.

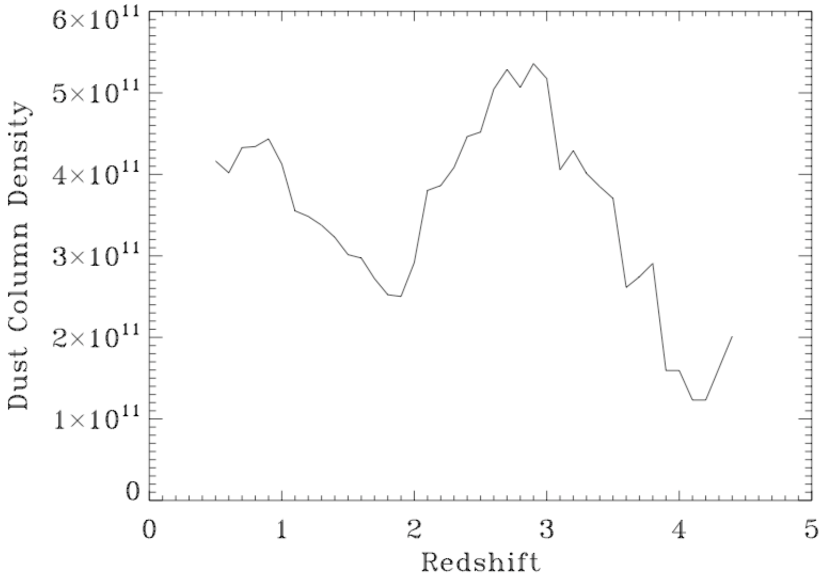

Figure 5.6: Dust column density as a function of redshift.

We can also compare our measured values of A_V to those found in the literature (see Table B.1. This table includes 85 bursts with measured A_V values using one of the template models discussed in Section 3.1. The overlapping sample is plotted in Figure 5.7 with a diagonal line indicating a one-to-one correlation. Overall, there is good agreement between our results and those found in the literature. However, because our model allows for greater freedom in the amount of dust in the host galaxy, we often found small amounts of dust where others found none, and were able to further refine many measurements.

5.4 Graphite-To-Silicate Ratio

The graphite versus silicate composition of our GRB host galaxies are plotted in Figure 5.8. A diagonal line is added to guide the eye to the one-to-one ratio. It is apparent that silicate dust

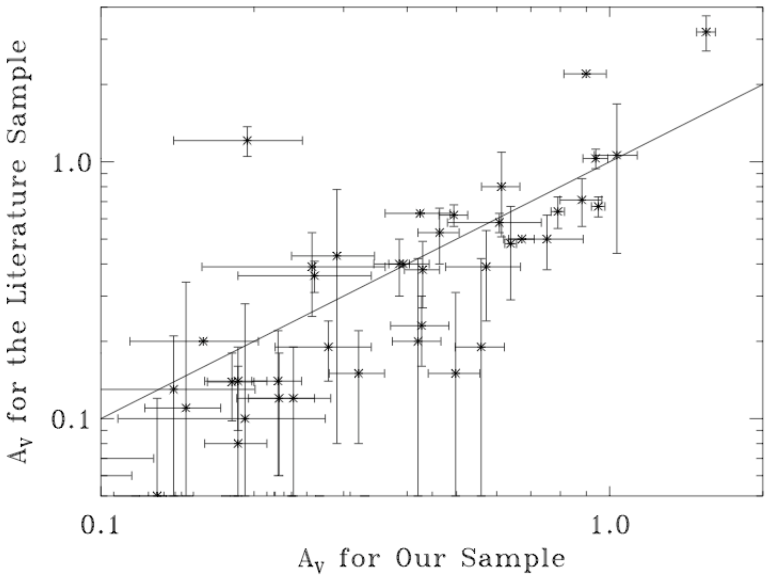

Figure 5.7: A_V values from our sample and the literature. The diagonal line marks a one-to-one correlation.

is dominating our GRB host galaxies, with only two bursts (GRB 991216 and GRB 030329) with more graphite to silicate, both are less than one σ above the line.

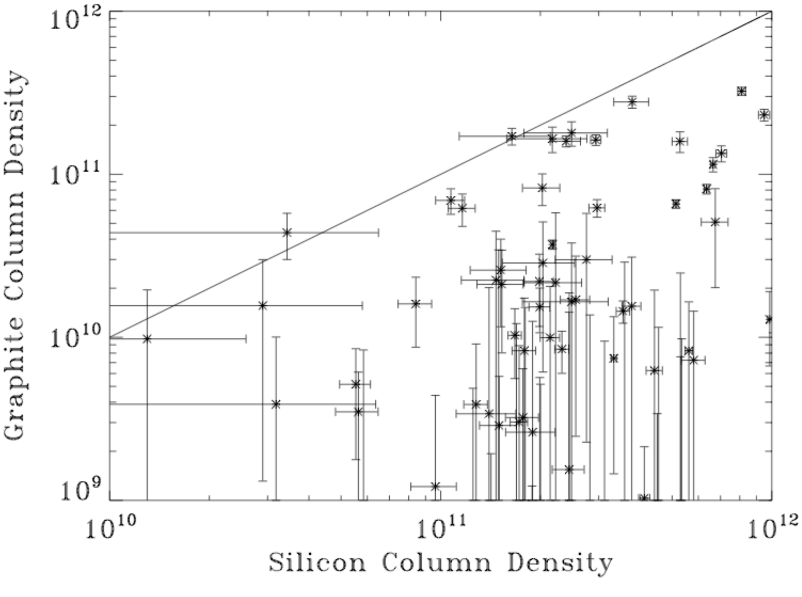

Figure 5.8: Silicate versus graphite column densities in our sample in units of cm^{-2}. The diagonal line indicates a one-to-one relation.

The models of dust evolution in galaxies presented in Section 4 had a range of possible supernova dust production rates for Population II CCSNe ranging between 0.8% and 2% of the total initial stellar mass becoming dust. In order to produce the large amounts of silicate dust as opposed to graphite dust seen in our host galaxies, we must favor the larger dust production rate.

Models of dust evolution in galaxies would predict the silicate in galaxies to build up faster than the graphite, especially at higher redshifts. Silicate is coming from supernovae explosions, which happen faster in the timescale of stellar evolution than the evolution of lower mass stars to the point where they begin to contribute dust (mainly graphite) to the interstellar medium.

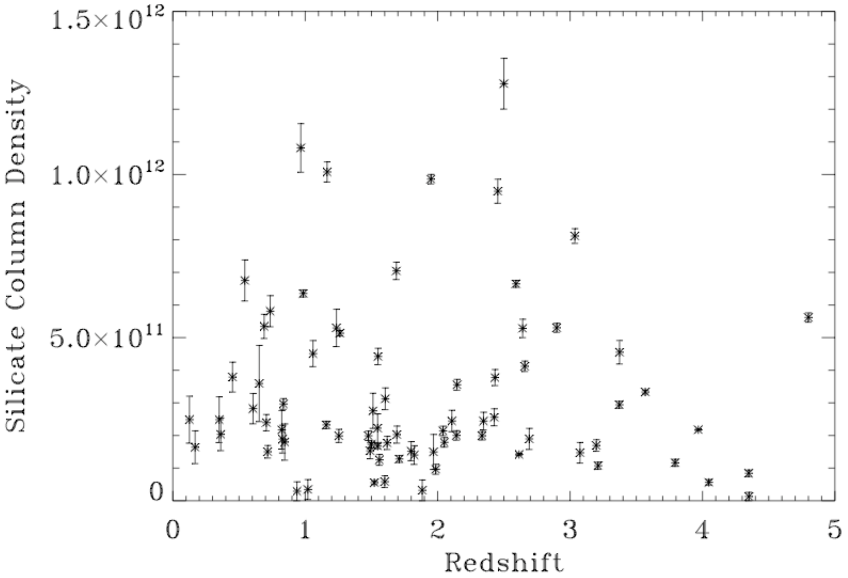

Figure 5.9: Silicate column densities in our sample in units of cm^{-2}.

In Figures 5.9 and 5.10, we see the silicate and graphite column densities as a function of redshift for our sample of 78 bursts. There is a large spread in the values. The lower values of graphite ($> 10^{10}$ cm^{-2}) have large error bars often exceeding the measured value of graphite; in small quantities, graphite is hard to constrain. On the other hand, silicate overall had higher column densities and lower error.

Figures 5.11 and 5.12 show the binned values for the silicate and graphite column densities with redshift. The silicate column densities dominate the shape of the overall column density and A_V plot; the graphite column densities have a similar shape but at about 1/10th the scale.

Our model (Section 4) shows that dust builds up in our host galaxies fairly rapidly with

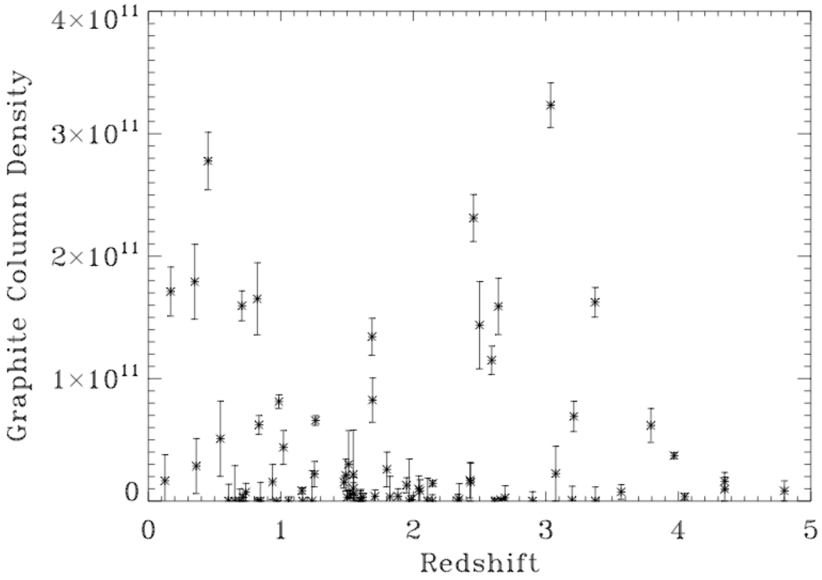

Figure 5.10: Graphite column densities in our sample in units of cm^{-2}.

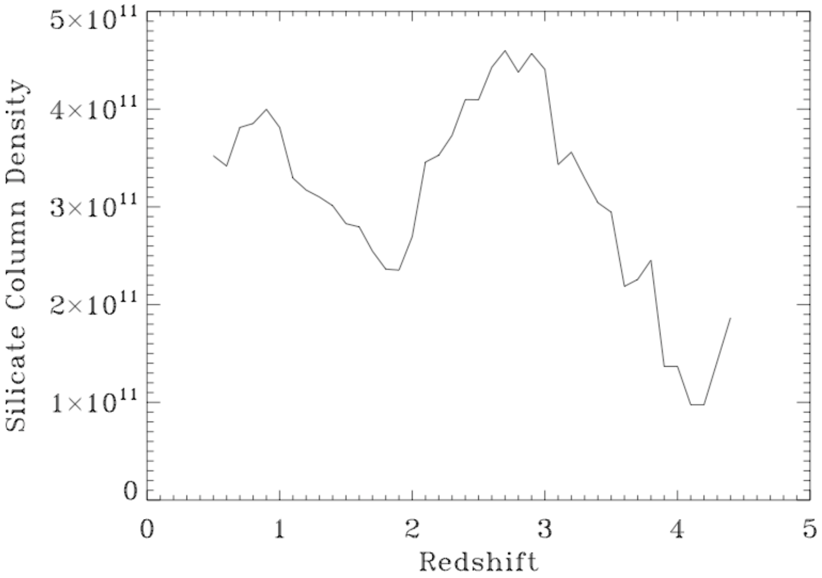

Figure 5.11: Silicate column densities in our sample.

redshift. Figure 5.14 shows the graphite-to-silicate ratio in a galaxy with a formation redshift of $z = 10$ and a high silicate production rate in CCSNe. By the time this galaxy has reached a redshift of 4, it is no longer possible to extract evolutionary information; the ratio is fairly flat with a large

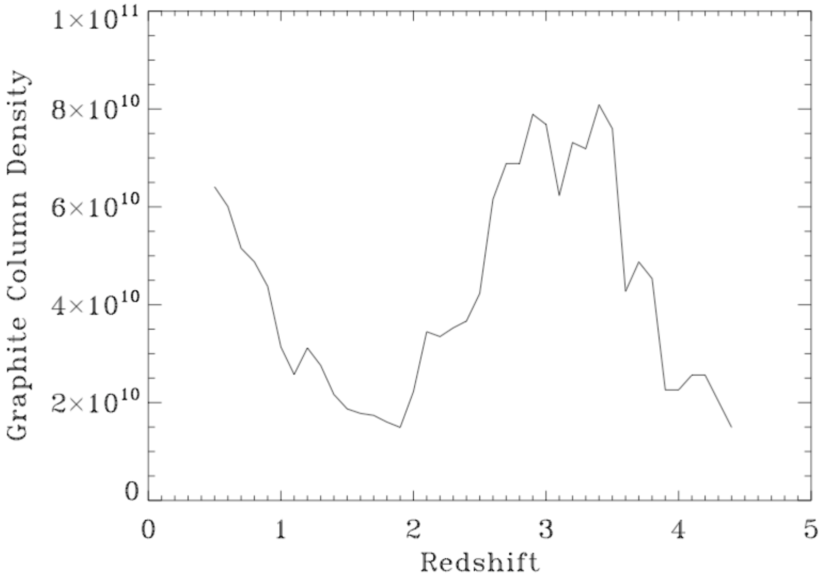

Figure 5.12: Graphite column densities in our sample.

amount of scatter due to the feedback from AGB non-instantaneous recycling. Our host galaxies most likely contain a large distribution of formation times, probably making it impossible to draw conclusions about the evolution of the graphite to silicate ratio without extending the sample to very high redshifts (i.e., a significant portion above $z \sim 6$). Note that most of the data in our sample (Figure 5.13) fall between 0.1 and 0.4 as predicted by our models (with a few outlying data points). The points in this plot have been constrained to those for which the error in the graphite column density measurement was lower than the measured column density (44 out of 78 points).

5.5 Spectral Index

As we discussed in the Introduction, our GRB SEDs have been constructed for the slow cooling case assuming the cooling frequency lies blue-ward of our data, which means the electron power law index (for the energy distribution $N(\gamma_e) \sim \gamma_e^{-p}$) is given at $p = 2\beta + 1$, where β is our measured spectral index. A histogram of our p values is given in Figure 5.16.

The majority of our p values are less than 2; the mean for the sample is 1.85. This is a larger percentage of the sample (52 out of 77 versus 3 out of 19) than the bursts with p values under 2 in the sample of (Kann et al., 2006).

The mean value we find is $\beta = 0.42$, lower than the mean value of $\beta = 0.57$ found by Kann

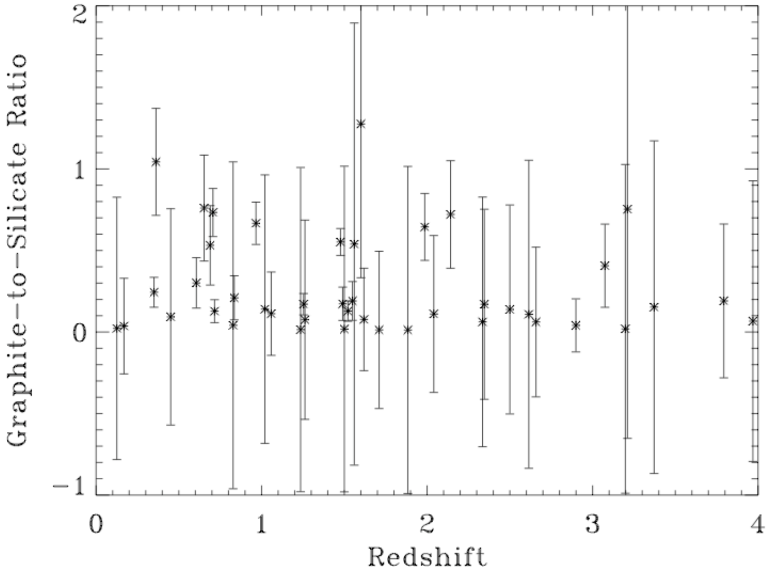

Figure 5.13: Graphite-to-silicate ratio as a function of redshift from our data.

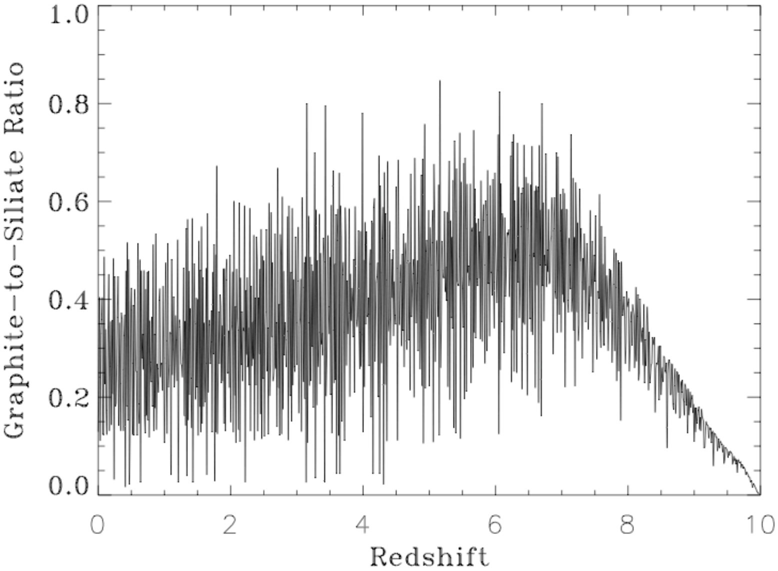

Figure 5.14: Graphite-to-silicate ratio as a function of redshift for a galaxy formed at $z = 10$ using our models of dust evolution in galaxies.

et al. (2006) (neither values are weighted by errors).

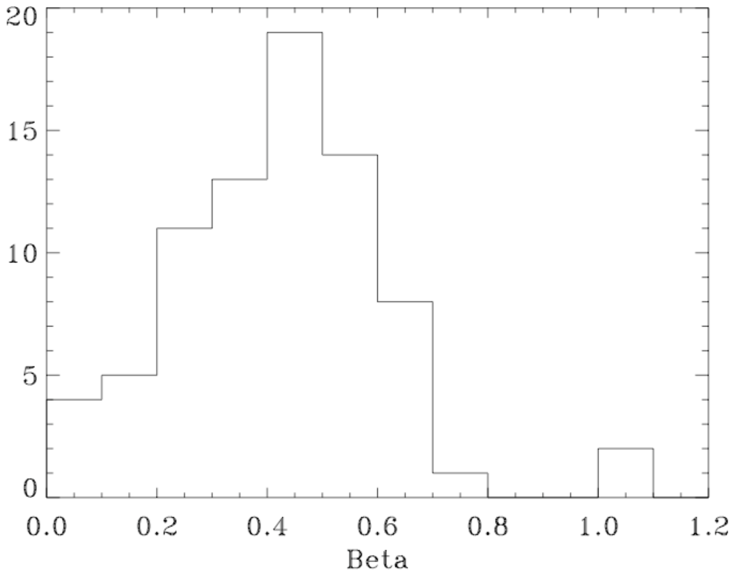

Figure 5.15: Histogram of our values of the spectral index β.

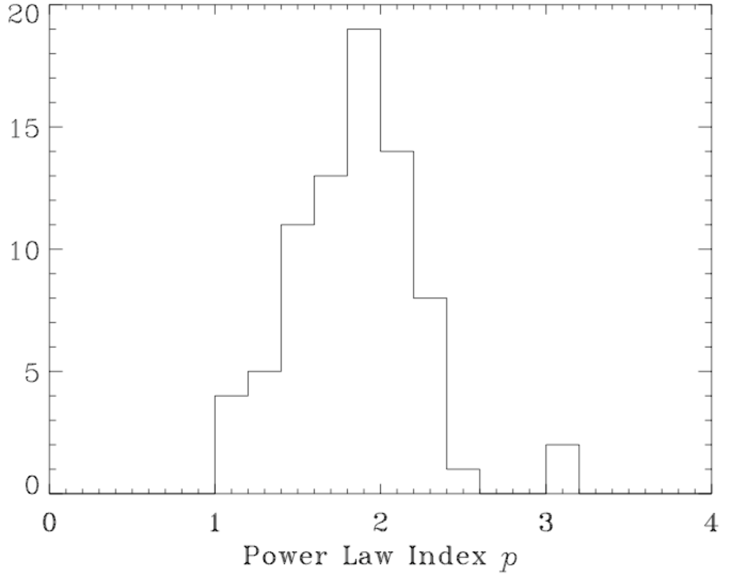

Figure 5.16: Histogram of the electron energy power law index p for our sample.

5.6 Conclusions

The dust extinction model presented in this analysis has several advantages over previous extinction fitting methods. It does not depend on templates or fitting parameters without physical basis; instead, each parameter in our fit has physical significance. In addition, it allows us to extract specific parameters about the host galaxy of the GRB, including the silicate and graphite dust column densities along the line of sight to the GRB and the dust-to-gas ratio if also given a measure of the hydrogen column density. A_V and R_V are also easily extracted from our model. By not relying on specific galaxy templates, the amounts of dust are free to vary and we managed to identify more systems which are best-fit by a model containing graphite than had previously been known. This analysis represents the first measurement of specific dust composition along the line of sight to GRBs without relying on molecular lines in the gas phase.

Models of dust evolution in galaxies as a function of redshift are also presented in this analysis. By taking into account stellar evolution, known properties of galactic disk evolution, and dust production from various sources, we were able to make a rough prediction of how dust composition and column density would change as a function of redshift for a specific galaxy at a given formation redshift. We also showed how the relative amounts of graphite and silicate should change as a function of time in a galaxy, and scaled our model to the size and mass of typical GRB host galaxies to allow for the most direct comparison to our data set.

Our models predict a trend in the dust distribution over redshift which is not clearly detected in our data. The models show an overall trend towards more dust and extinction as redshift decreases; however, specific evolutionary features cannot be distinguished in our data set, and missing dust destruction may play a key role in the predicted amounts of dust.

The GRB SED data cannot be explained using a simple theoretical model of galaxy evolution. Overall evolutionary trends may be too weak to overcome local environments. Local extinction and galaxy inhomogeneities too specific to be included in our overall model can greatly affect the extinction results to the point where overall trends, while they may very well exist, cannot be extracted from the data set without a great deal more understanding of the local environments of massive stars and GRB progenitors at medium to high redshifts.

Similar results are found when attempting to use GRBs to probe metallicity as a function of redshift; while galaxies probed along quasar sight-lines have produced a large amount of scatter but hint towards an overall trend in lower metallicity with time, GRBs lying inside their host galaxies give a great deal more scatter in the overall picture of metallicity as a function of time (see Figure 1.4, Savaglio, 2010). Similar problems have been encountered when attempting to look for evolutionary trends with redshift in our own galactic stellar metallicities.

By taking into account galaxy mergers, dust destruction, and clumpy dust distributions in

GRB host galaxies, we would take the next step towards producing a more representative model of dust extinction in the universe. Adding additional results from supernovae and quasars as probes of dust evolution would also benefit this analysis, but the more complicated nature of their spectra would require spectroscopic analysis as opposed to the more simple photometric methods described here.

Clearly, a simple model of galaxy evolution is insufficient to explain the spread seen in our data. Full-blown 3D models including structure and many more degrees of freedom would be necessary to reproduce the results of observation, but are not yet available, and the data to compare them to is patchy at best. Dedicated spectroscopic follow-up of GRB afterglows from the UV to the NIR would be necessary for this kind of work.

Gamma ray bursts show tremendous promise as probes of the early universe due to their bright and high-redshift natures. However, large variety in the local environments can make it difficult to see overall evolutionary trends in the few sight-lines we currently have to work with. Local dust, perhaps from the molecular cloud in which the progenitor star of the burst formed, may play a larger role in the overall measured dust properties than the galaxy as a whole. Further understanding of their local environments may help us eventually eliminate these effects and allow GRBs to live up to their full potential as cosmological probes, but we have not yet reached that point in our understanding of massive star formation in the early universe.

Bibliography

Alpher, R. A., Bethe, H., & Gamow, G. 1948, Physical Review, 73, 803

Anders, E. & Grevesse, N. 1989, **??**jnlGeochim. Cosmochim. Acta, 53, 197

Arnaud, K. A. 1996, in Astronomical Society of the Pacific Conference Series, Vol. 101, Astronomical Data Analysis Software and Systems V, ed. G. H. Jacoby & J. Barnes, 17–+

Barnard, E. E. 1913, ApJ, 38, 496

Berger, E., Fox, D. B., Kulkarni, S. R., Frail, D. A., & Djorgovski, S. G. 2007, ApJ, 660, 504

Bernasconi, P. A. & Maeder, A. 1996, A&A, 307, 829

Bertoldi, F., Carilli, C. L., Cox, P., Fan, X., Strauss, M. A., Beelen, A., Omont, A., & Zylka, R. 2003, A&A, 406, L55

Binney, J., Dehnen, W., & Bertelli, G. 2000, MNRAS, 318, 658

Bloom, J. S., Perley, D. A., Li, W., Butler, N. R., Miller, A. A., Kocevski, D., Kann, D. A., Foley, R. J., Chen, H.-W., Filippenko, A. V., Starr, D. L., Macomber, B., Prochaska, J. X., Chornock, R., Poznanski, D., Klose, S., Skrutskie, M. F., Lopez, S., Hall, P., Glazebrook, K., & Blake, C. H. 2009, ApJ, 691, 723

Bode, M. F. 1988, in Dust in the Universe, ed. M. E. Bailey & D. A. Williams, 73–102

Bohren, C. F. & Huffman, D. R. 1983, Absorption and scattering of light by small particles, ed. Bohren, C. F. & Huffman, D. R.

Bouchet, P., Lequeux, J., Maurice, E., Prevot, L., & Prevot-Burnichon, M. L. 1985, A&A, 149, 330

Bromm, V. & Loeb, A. 2006, ApJ, 642, 382

Bruzual A., G. & Charlot, S. 1993, ApJ, 405, 538

Butler, N. R., Li, W., Perley, D., Huang, K. Y., Urata, Y., Prochaska, J. X., Bloom, J. S., Filippenko, A. V., Foley, R. J., Kocevski, D., Chen, H.-W., Qiu, Y., Kuo, P. H., Huang, F. Y., Ip, W. H., Tamagawa, T., Onda, K., Tashiro, M., Makishima, K., Nishihara, S., & Sarugaku, Y. 2006, ApJ, 652, 1390

Calzetti, D., Kinney, A. L., & Storchi-Bergmann, T. 1994, ApJ, 429, 582

Cardelli, J. A., Clayton, G. C., & Mathis, J. S. 1988, ApJ, 329, L33

—. 1989, ApJ, 345, 245

Carroll, B. W. & Ostlie, D. A. 1996, An Introduction to Modern Astrophysics (Institute for Mathematics and Its Applications)

Castro-Tirado, A. J., Zapatero-Osorio, M. R., Gorosabel, J., Greiner, J., Heidt, J., Herranz, D., Kemp, S. N., Martínez-González, E., Oscoz, A., Ortega, V., Röser, H.-J., Wolf, C., Pedersen, H., Jaunsen, A. O., Korhonen, H., Ilyin, I., Duemmler, R., Andersen, M. I., Hjorth, J., Henden, A. A., Vrba, F. J., Fried, J. W., Frontera, F., & Nicastro, L. 1999, ApJ, 511, L85

Cavallo, G. & Rees, M. J. 1978, MNRAS, 183, 359

Cenko, S. B., Fox, D. B., Penprase, B. E., Cucchiara, A., Price, P. A., Berger, E., Kulkarni, S. R., Harrison, F. A., Gal-Yam, A., Ofek, E. O., Rau, A., Chandra, P., Frail, D. A., Kasliwal, M. M., Schmidt, B. P., Soderberg, A. M., Cameron, P. B., & Roth, K. C. 2008, ApJ, 677, 441

Cenko, S. B., Kelemen, J., Harrison, F. A., Fox, D. B., Kulkarni, S. R., Kasliwal, M. M., Ofek, E. O., Rau, A., Gal-Yam, A., Frail, D. A., & Moon, D.-S. 2009, ApJ, 693, 1484

Chabrier, G. 2003, PASP, 115, 763

Cherchneff, I. & Dwek, E. 2009, ApJ, 703, 642

—. 2010, ApJ, 713, 1

Clark, P. C., Glover, S. C. O., Klessen, R. S., & Bromm, V. 2010, ArXiv e-prints

Clayton, D. D. 1975, ApJ, 199, 765

—. 1983, Principles of stellar evolution and nucleosynthesis, ed. Clayton, D. D.

de Ugarte Postigo, A., Fatkhullin, T. A., Jóhannesson, G., Gorosabel, J., Sokolov, V. V., Castro-Tirado, A. J., Balega, Y. Y., Spiridonova, O. I., Jelínek, M., Guziy, S., Pérez-Ramírez, D., Hjorth, J., Laursen, P., Bersier, D., Pandey, S. B., Bremer, M., Monfardini, A., Huang, K. Y., Urata, Y., Ip, W. H., Tamagawa, T., Kinoshita, D., Mizuno, T., Arai, Y., Yamagishi, H., Soyano, T., Usui, F., Tashiro, M., Abe, K., Onda, K., Aslan, Z., Khamitov, I., Ozisik, T., Kiziloglu, U., Bikmaev, I., Sakhibullin, N., Burenin, R., Pavlinsky, M., Sunyaev, R., Bhattacharya, D., Kamble, A. P., Ishwara Chandra, C. H., & Trushkin, S. A. 2007, A&A, 462, L57

Draine, B. T. 1985, ApJS, 57, 587

Draine, B. T. & Lee, H. M. 1984, ApJ, 285, 89

Dwek, E. 1983, ApJ, 274, 175

—. 1998, ApJ, 501, 643

Ercolano, B., Barlow, M. J., & Sugerman, B. E. K. 2007, MNRAS, 375, 753

Fischera, J., Dopita, M. A., & Sutherland, R. S. 2003, ApJ, 599, L21

Fitzpatrick, E. L. & Massa, D. 1986, ApJ, 307, 286

—. 1988, ApJ, 328, 734

—. 1990, ApJS, 72, 163

Frebel, A., Johnson, J. L., & Bromm, V. 2009, MNRAS, 392, L50

Fruchter, A., Krolik, J. H., & Rhoads, J. E. 2001, ApJ, 563, 597

Fruchter, A. S., Levan, A. J., Strolger, L., Vreeswijk, P. M., Thorsett, S. E., Bersier, D., Burud, I., Castro Cerón, J. M., Castro-Tirado, A. J., Conselice, C., Dahlen, T., Ferguson, H. C., Fynbo, J. P. U., Garnavich, P. M., Gibbons, R. A., Gorosabel, J., Gull, T. R., Hjorth, J., Holland, S. T., Kouveliotou, C., Levay, Z., Livio, M., Metzger, M. R., Nugent, P. E., Petro, L., Pian, E., Rhoads, J. E., Riess, A. G., Sahu, K. C., Smette, A., Tanvir, N. R., Wijers, R. A. M. J., & Woosley, S. E. 2006, Nature, 441, 463

Fruchter, A. S., Thorsett, S. E., Metzger, M. R., Sahu, K. C., Petro, L., Livio, M., Ferguson, H., Pian, E., Hogg, D. W., Galama, T., Gull, T. R., Kouveliotou, C., Macchetto, D., van Paradijs, J., Pedersen, H., & Smette, A. 1999, ApJ, 519, L13

Gorosabel, J., Christensen, L., Hjorth, J., Fynbo, J. U., Pedersen, H., Jensen, B. L., Andersen, M. I., Lund, N., Jaunsen, A. O., Castro Cerón, J. M., Castro-Tirado, A. J., Fruchter, A., Greiner, J., Pian, E., Vreeswijk, P. M., Burud, I., Frontera, F., Kaper, L., Klose, S., Kouveliotou, C., Masetti, N., Palazzi, E., Rhoads, J., Rol, E., Salamanca, I., Tanvir, N., Wijers, R. A. M. J., & van den Heuvel, E. 2003, A&A, 400, 127

Greiner, J., Clemens, C., Krühler, T., von Kienlin, A., Rau, A., Sari, R., Fox, D. B., Kawai, N., Afonso, P., Ajello, M., Berger, E., Cenko, S. B., Cucchiara, A., Filgas, R., Klose, S., Küpcü Yoldaş, A., Lichti, G. G., Löw, S., McBreen, S., Nagayama, T., Rossi, A., Sato, S., Szokoly, G., Yoldaş, A., & Zhang, X.-L. 2009a, A&A, 498, 89

Greiner, J., Kruehler, T., Klose, S., Afonso, P., Clemens, C., Filgas, R., Hartmann, D., Kupcu Yoldas, A., Nardini, M., Olivares, F., Rau, A., Rossi, A., Schady, P., & Updike, A. 2010, submitted to Astronomy Astrophysics

Greiner, J., Krühler, T., Fynbo, J. P. U., Rossi, A., Schwarz, R., Klose, S., Savaglio, S., Tanvir, N. R., McBreen, S., Totani, T., Zhang, B. B., Wu, X. F., Watson, D., Barthelmy, S. D., Beardmore, A. P., Ferrero, P., Gehrels, N., Kann, D. A., Kawai, N., Yoldaş, A. K., Mészáros, P., Milvang-Jensen, B., Oates, S. R., Pierini, D., Schady, P., Toma, K., Vreeswijk, P. M., Yoldaş, A., Zhang, B., Afonso, P., Aoki, K., Burrows, D. N., Clemens, C., Filgas, R., Haiman, Z., Hartmann, D. H., Hasinger, G., Hjorth, J., Jehin, E., Levan, A. J., Liang, E. W., Malesani, D., Pyo, T.-S., Schulze, S., Szokoly, G., Terada, K., & Wiersema, K. 2009b, ApJ, 693, 1610

Hjorth, J., Møller, P., Gorosabel, J., Fynbo, J. P. U., Toft, S., Jaunsen, A. O., Kaas, A. A., Pursimo, T., Torii, K., Kato, T., Yamaoka, H., Yoshida, A., Thomsen, B., Andersen, M. I., Burud, I., Castro Cerón, J. M., Castro-Tirado, A. J., Fruchter, A. S., Kaper, L., Kouveliotou, C., Masetti, N., Palazzi, E., Pedersen, H., Pian, E., Rhoads, J., Rol, E., Tanvir, N. R., Vreeswijk, P. M., Wijers, R. A. M. J., & van den Heuvel, E. P. J. 2003, ApJ, 597, 699

Hjorth, J., Thomsen, B., Nielsen, S. R., Andersen, M. I., Holland, S. T., Fynbo, J. U., Pedersen, H., Jaunsen, A. O., Halpern, J. P., Fesen, R., Gorosabel, J., Castro-Tirado, A., McMahon, R. G., Hoenig, M. D., Björnsson, G., Amati, L., Tanvir, N. R., & Natarajan, P. 2002, ApJ, 576, 113

Holland, S. T., Sbarufatti, B., Shen, R., Schady, P., Cummings, J. R., Fonseca, E., Fynbo, J. P. U., Jakobsson, P., Leitet, E., Linne, S., Roming, P. W. A., Still, M., & Zhang, B. 2010, ArXiv e-prints

Hoyle, F. & Wickramasinghe, N. C. 1970, Nature, 226, 62

Jakobsson, P., Hjorth, J., Fynbo, J. P. U., Gorosabel, J., Pedersen, K., Burud, I., Levan, A., Kouveliotou, C., Tanvir, N., Fruchter, A., Rhoads, J., Grav, T., Hansen, M. W., Michelsen, R., Andersen, M. I., Jensen, B. L., Pedersen, H., Thomsen, B., Weidinger, M., Bhargavi, S. G., Cowsik, R., & Pandey, S. B. 2003, A&A, 408, 941

Jakobsson, P., Levan, A., Fynbo, J. P. U., Priddey, R., Hjorth, J., Tanvir, N., Watson, D., Jensen, B. L., Sollerman, J., Natarajan, P., Gorosabel, J., Castro Cerón, J. M., & Pedersen, K. 2006, in American Institute of Physics Conference Series, Vol. 836, Gamma-Ray Bursts in the Swift Era, ed. S. S. Holt, N. Gehrels, & J. A. Nousek, 552–557

Jaunsen, A. O., Rol, E., Watson, D. J., Malesani, D., Fynbo, J. P. U., Milvang-Jensen, B., Hjorth, J., Vreeswijk, P. M., Ovaldsen, J.-E., Wiersema, K., Tanvir, N. R., Gorosabel, J., Levan, A. J., Schirmer, M., & Castro-Tirado, A. J. 2008, ApJ, 681, 453

Kann, D. A., Klose, S., & Zeh, A. 2006, ApJ, 641, 993

Kann, D. A., Klose, S., Zhang, B., Malesani, D., Nakar, E., Pozanenko, A., Wilson, A. C., Butler, N. R., Jakobsson, P., Schulze, S., Andreev, M., Antonelli, L. A., Bikmaev, I. F., Biryukov, V., Böttcher, M., Burenin, R. A., Castro Cerón, J. M., Castro-Tirado, A. J., Chincarini, G., Cobb, B. E., Covino, S., D'Avanzo, P., D'Elia, V., Della Valle, M., de Ugarte Postigo, A., Efimov, Y., Ferrero, P., Fugazza, D., Fynbo, J. P. U., Gålfalk, M., Grundahl, F., Gorosabel, J., Gupta, S., Guziy, S., Hafizov, B., Hjorth, J., Holhjem, K., Ibrahimov, M., Im, M., Israel, G. L., Jeĺinek, M., Jensen, B. L., Karimov, R., Khamitov, I. M., Kiziloğlu, Ü., Klunko, E., Kubánek, P., Kutyrev, A. S., Laursen, P., Levan, A. J., Mannucci, F., Martin, C. M., Mescheryakov, A., Mirabal, N., Norris, J. P., Ovaldsen, J., Paraficz, D., Pavlenko, E., Piranomonte, S., Rossi, A., Rumyantsev, V., Salinas, R., Sergeev, A., Sharapov, D., Sollerman, J., Stecklum, B., Stella, L., Tagliaferri, G., Tanvir, N. R., Telting, J., Testa, V., Updike, A. C., Volnova, A., Watson, D., Wiersema, K., & Xu, D. 2010, ApJ, 720, 1513

Kann, D. A., Klose, S., Zhang, B., Wilson, A. C., Butler, N. R., Malesani, D., Nakar, E., Antonelli, L. A., Chincarini, G., Cobb, B. E., Covino, S., D'Avanzo, P., D'Elia, V., Della Valle, M., Ferrero, P., Fugazza, D., Gorosabel, J., Israel, . L., Mannucci, F., Piranomonte, S., Schulze, S., Stella, L., Tagliaferri, G., & Wiersema, K. 2008, ArXiv e-prints

Karakas, A. I. 2010, MNRAS, 403, 1413

Kim, S. & Martin, P. G. 1995, ApJ, 442, 172

Klebesadel, R. W., Strong, I. B., & Olson, R. A. 1973, ApJ, 182, L85+

Klose, S., Stecklum, B., Masetti, N., Pian, E., Palazzi, E., Henden, A. A., Hartmann, D. H., Fischer, O., Gorosabel, J., Sánchez-Fernández, C., Butler, D., Ott, T., Hippler, S., Kasper, M., Weiss, R., Castro-Tirado, A., Greiner, J., Bartolini, C., Guarnieri, A., Piccioni, A., Benetti, S., Ghinassi, F., Magazzú, A., Hurley, K., Cline, T., Trombka, J., McClanahan, T., Starr, R., Goldsten, J., Gold, R., Mazets, E., Golenetskii, S., Noeske, K., Papaderos, P., Vreeswijk, P. M., Tanvir, N., Oscoz, A., Muñoz, J. A., & Castro Cerón, J. M. 2000, ApJ, 545, 271

Koornneef, J. 1982, A&A, 107, 247

—. 1983, A&A, 128, 84

Koornneef, J. & Code, A. D. 1981, ApJ, 247, 860

Kroupa, P. 2002, in Astronomical Society of the Pacific Conference Series, Vol. 285, Modes of Star Formation and the Origin of Field Populations, ed. E. K. Grebel & W. Brandner, 86–+

Kulkarni, V. P., York, D. G., Vladilo, G., & Welty, D. E. 2007, ApJ, 663, L81

Lagadec, E., Zijlstra, A. A., Matsuura, M., Menzies, J. W., van Loon, J. T., & Whitelock, P. A. 2008, MNRAS, 383, 399

Laor, A. & Draine, B. T. 1993, ApJ, 402, 441

Laughlin, G., Bodenheimer, P., & Adams, F. C. 1997, ApJ, 482, 420

Li, A., Liang, S. L., Kann, D. A., Wei, D. M., Klose, S., & Wang, Y. J. 2008, ApJ, 685, 1046

Maiolino, R., Schneider, R., Oliva, E., Bianchi, S., Ferrara, A., Mannucci, F., Pedani, M., & Roca Sogorb, M. 2004, Nature, 431, 533

Massa, D. & Savage, B. 1989, in IAU Symposium, Vol. 135, Interstellar Dust, ed. L. J. Allamandola & A. G. G. M. Tielens, 3–+

Mathis, J. S., Rumpl, W., & Nordsieck, K. H. 1977, ApJ, 217, 425

Meegan, C. A., Fishman, G. J., Wilson, R. B., Horack, J. M., Brock, M. N., Paciesas, W. S., Pendleton, G. N., & Kouveliotou, C. 1992, Nature, 355, 143

Morgan, D. H. & Nandy, K. 1982, MNRAS, 199, 979

Moseley, S. H., Dwek, E., Glaccum, W., Graham, J. R., & Loewenstein, R. F. 1989, Nature, 340, 697

Mundell, C. G., Melandri, A., Guidorzi, C., Kobayashi, S., Steele, I. A., Malesani, D., Amati, L., D'Avanzo, P., Bersier, D. F., Gomboc, A., Rol, E., Bode, M. F., Carter, D., Mottram, C. J., Monfardini, A., Smith, R. J., Malhotra, S., Wang, J., Bannister, N., O'Brien, P. T., & Tanvir, N. R. 2007, ApJ, 660, 489

Naab, T. & Ostriker, J. P. 2006, MNRAS, 366, 899

Nandy, K., Morgan, D. H., & Houziaux, L. 1984, MNRAS, 211, 895

Nandy, K., Morgan, D. H., Willis, A. J., Wilson, R., & Gondhalekar, P. M. 1981, MNRAS, 196, 955

Nomoto, K. 1984, ApJ, 277, 791

Nysewander, M. C., Reichart, D. E., Park, H.-S., Williams, G. G., Kinugasa, K., Lamb, D. Q., Henden, A. A., Klose, S., Kato, T., Harper, A., Yamaoka, H., Laws, C., Torii, K., York, D. G., Barentine, J. C., Dembicky, J., McMillan, R. J., Moran, J. A., Hartmann, D. H., Ketzeback, B., Bayliss, M. B., Bartelme, J. W., Crain, J. A., Foster, A. C., Schwartz, M., Holvorcem, P., Price, P. A., Canterna, R., Crew, G. B., Ricker, G. R., & Barthelmy, S. D. 2006, ApJ, 651, 994

Panaitescu, A. 2005, MNRAS, 362, 921

Panaitescu, A. & Kumar, P. 2001, ApJ, 560, L49

Pei, Y. C. 1992, ApJ, 395, 130

Pellizza, L. J., Duc, P.-A., Le Floc'h, E., Mirabel, I. F., Antonelli, L. A., Campana, S., Chincarini, G., Cimatti, A., Covino, S., Della Valle, M., Fiore, F., Fugazza, D., Giommi, P., Goldoni, P., Israel, G. L., Molinari, E., Moretti, A., Piro, L., Saracco, P., Stella, L., Tagliaferri, G., & Vietri, M. 2006, A&A, 459, L5

Perley, D. A., Bloom, J. S., Butler, N. R., Pollack, L. K., Holtzman, J., Blake, C. H., Kocevski, D., Vestrand, W. T., Li, W., Foley, R. J., Bellm, E., Chen, H.-W., Prochaska, J. X., Starr, D., Filippenko, A. V., Falco, E. E., Szentgyorgyi, A. H., Wren, J., Wozniak, P. R., White, R., & Pergande, J. 2008a, ApJ, 672, 449

Perley, D. A., Bloom, J. S., Klein, C. R., Covino, S., Minezaki, T., Woźniak, P., Vestrand, W. T., Williams, G. G., Milne, P., Butler, N. R., Updike, A. C., Krühler, T., Afonso, P., Antonelli, A., Cowie, L., Ferrero, P., Greiner, J., Hartmann, D. H., Kakazu, Y., Küpcü Yoldaş, A., Morgan, A. N., Price, P. A., Prochaska, J. X., & Yoshii, Y. 2010, MNRAS, 406, 2473

Perley, D. A., Cenko, S. B., Bloom, J. S., Chen, H. ., Butler, N. R., Kocevski, D., Prochaska, J. X., Brodwin, M., Glazebrook, K., Kasliwal, M. M., Kulkarni, S. R., Lopez, S., Ofek, E. O., Pettini, M., Soderberg, A. M., & Starr, D. 2009, ArXiv e-prints

Perley, D. A., Li, W., Chornock, R., Prochaska, J. X., Butler, N. R., Chandra, P., Pollack, L. K., Bloom, J. S., Filippenko, A. V., Swan, H., Yuan, F., Akerlof, C., Auger, M. W., Cenko, S. B., Chen, H.-W., Fassnacht, C. D., Fox, D., Frail, D., Johansson, E. M., McKay, T., Le Mignant, D., Modjaz, M., Rujopakarn, W., Russel, R., Skinner, M. A., Smith, G. H., Smith, I., van Dam, M. A., & Yost, S. 2008b, ApJ, 688, 470

Philipp, H. R. 1977, **??**jnlPhys. Rev. B, 16, 2896

Press, W. H., Teukolsky, S. A., Vetterling, W. T., & Flannery, B. P. 2007, Numerical Recipes 3rd Edition: The Art of Scientific Computing (New York, NY, USA: Cambridge University Press)

Prevot, M. L., Lequeux, J., Prevot, L., Maurice, E., & Rocca-Volmerange, B. 1984, A&A, 132, 389

Prochaska, J. X., Sheffer, Y., Perley, D. A., Bloom, J. S., Lopez, L. A., Dessauges-Zavadsky, M., Chen, H.-W., Filippenko, A. V., Ganeshalingam, M., Li, W., Miller, A. A., & Starr, D. 2009, ApJ, 691, L27

Renzini, A. & Voli, M. 1981, A&A, 94, 175

Rieke, G. H. & Lebofsky, M. J. 1985, ApJ, 288, 618

Robitaille, T. P., Whitney, B. A., Indebetouw, R., & Wood, K. 2007, ApJS, 169, 328

Rossi, A., de Ugarte Postigo, A., Ferrero, P., Kann, D. A., Klose, S., Schulze, S., Greiner, J., Schady, P., Filgas, R., Gonsalves, E. E., Küpcü Yoldaş, A., Krühler, T., Szokoly, G., Yoldaş, A., Afonso, P. M. J., Clemens, C., Bloom, J. S., Perley, D. A., Fynbo, J. P. U., Castro-Tirado, A. J., Gorosabel, J., Kubánek, P., Updike, A. C., Hartmann, D. H., Giuliani, A., Holland, S. T., Hanlon, L., Bremer, M., French, J., Melady, G., & García-Hernández, D. A. 2008, A&A, 491, L29

Rybicki, G. B. & Lightman, A. P. 1986, Radiative Processes in Astrophysics (Radiative Processes in Astrophysics, by George B. Rybicki, Alan P. Lightman, pp. 400. ISBN 0-471-82759-2. Wiley-VCH , June 1986.)

Salpeter, E. E. 1955, ApJ, 121, 161

Sari, R., Piran, T., & Narayan, R. 1998, ApJ, 497, L17+

Savage, B. D. 1975, ApJ, 199, 92

Savage, B. D. & Mathis, J. S. 1979, ARA&A, 17, 73

Savage, B. D. & Sembach, K. R. 1996, ARA&A, 34, 279

Savaglio, S. 2010, in IAU Symposium, Vol. 265, IAU Symposium, ed. K. Cunha, M. Spite, & B. Barbuy, 139–146

Savaglio, S., Glazebrook, K., & LeBorgne, D. 2009, ApJ, 691, 182

Schady, P., Mason, K. O., Page, M. J., de Pasquale, M., Morris, D. C., Romano, P., Roming, P. W. A., Immler, S., & vanden Berk, D. E. 2007, MNRAS, 377, 273

Schaller, G., Schaerer, D., Meynet, G., & Maeder, A. 1992, A&AS, 96, 269

Schlegel, D. J., Finkbeiner, D. P., & Davis, M. 1998, ApJ, 500, 525

Silvia, D. W., Smith, B. D., & Shull, J. M. 2010, ApJ, 715, 1575

Soule, D. E., McClure, J. W., & Smith, L. B. 1964, Physical Review, 134, 453

Spergel, D. N., Bean, R., Doré, O., Nolta, M. R., Bennett, C. L., Dunkley, J., Hinshaw, G., Jarosik, N., Komatsu, E., Page, L., Peiris, H. V., Verde, L., Halpern, M., Hill, R. S., Kogut, A., Limon, M., Meyer, S. S., Odegard, N., Tucker, G. S., Weiland, J. L., Wollack, E., & Wright, E. L. 2007, ApJS, 170, 377

Starling, R. L. C., Vreeswijk, P. M., Ellison, S. L., Rol, E., Wiersema, K., Levan, A. J., Tanvir, N. R., Wijers, R. A. M. J., Tadhunter, C., Zaurin, J. R., Gonzalez Delgado, R. M., & Kouveliotou, C. 2005, A&A, 442, L21

Struve, W. 1847, Etudes d'astronomie stellaire., ed. Struve, W.

Sugerman, B. E. K., Ercolano, B., Barlow, M. J., Tielens, A. G. G. M., Clayton, G. C., Zijlstra, A. A., Meixner, M., Speck, A., Gledhill, T. M., Panagia, N., Cohen, M., Gordon, K. D., Meyer, M., Fabbri, J., Bowey, J. E., Welch, D. L., Regan, M. W., & Kennicutt, R. C. 2006, Science, 313, 196

Tan, J. C. & McKee, C. F. 2008, in American Institute of Physics Conference Series, Vol. 990, First Stars III, ed. B. W. O'Shea & A. Heger, 47–62

Thoene, C. C., Kann, D. A., Johannesson, G., Selj, J. H., Jaunsen, A., Fynbo, J. P. U., Baliyan, K. S., Bartolini, C., Bikmaev, I. F., Bloom, J. S., Burenin, R. A., Cobb, B. E., Covino, S., Curran, P. A., Dahle, H., French, J., Ganesh, S., Greco, G., Guarnieri, A., Hanlon, L., Hjorth, J., Ibrahimov, M., Israel, G. L., Jakobsson, P., Jensen, B. L., Jorgensen, U. G., Khamitov, I. M., Malesani, D., Masetti, N., Naranen, J., Pakstiene, E., Pavlinsky, M. N., Perley, D. A., Piccioni, A., Pizzichini, G., Pozanenko, A., Nanni, D., Rumyantsev, V., Sharapov, D., Starr, D., Sunyaev, R. A., Terra, F., Vreeswijk, P. M., & Wilson, A. C. 2008, ArXiv e-prints

Tielens, A. G. G. M. 2005, The Physics and Chemistry of the Interstellar Medium, ed. Tielens, A. G. G. M.

Todini, P. & Ferrara, A. 2001, MNRAS, 325, 726

Tosatti, E. & Bassani, F. 1970, Nuovo Cimento B Serie, 65, 161

Troja, E., Cusumano, G., O'Brien, P. T., Zhang, B., Sbarufatti, B., Mangano, V., Willingale, R., Chincarini, G., Osborne, J. P., Marshall, F. E., Burrows, D. N., Campana, S., Gehrels, N., Guidorzi, C., Krimm, H. A., La Parola, V., Liang, E. W., Mineo, T., Moretti, A., Page, K. L., Romano, P., Tagliaferri, G., Zhang, B. B., Page, M. J., & Schady, P. 2007, ApJ, 665, 599

Trumpler, R. J. 1930, PASP, 42, 214

Updike, A. C., Haislip, J. B., Nysewander, M. C., Fruchter, A. S., Kann, D. A., Klose, S., Milne, P. A., Williams, G. G., Zheng, W., Hergenrother, C. W., Prochaska, J. X., Halpern, J. P., Mirabal, N., Thorstensen, J. R., van der Horst, A. J., Starling, R. L. C., Racusin, J. L., Burrows, D. N., Kuin, N. P. M., Roming, P. W. A., Bellm, E., Hurley, K., Li, W., Filippenko, A. V., Blake, C., Starr, D., Falco, E. E., Brown, W. R., Dai, X., Deng, J., Xin, L., Qiu, Y., Wei, J., Urata, Y., Nanni, D., Maiorano, E., Palazzi, E., Greco, G., Bartolini, C., Guarnieri, A., Piccioni, A., Pizzichini, G., Terra, F., Misra, K., Bhatt, B. C., Anupama, G. C., Fan, X., Jiang, L., Wijers, R. A. M. J., Reichart, D. E., Eid, H. A., Bryngelson, G., Puls, J., Goldthwaite, R. C., & Hartmann, D. H. 2008, ApJ, 685, 361

van de Hulst, H. C. 1957, Light Scattering by Small Particles, ed. van de Hulst, H. C.

van Paradijs, J., Groot, P. J., Galama, T., Kouveliotou, C., Strom, R. G., Telting, J., Rutten, R. G. M., Fishman, G. J., Meegan, C. A., Pettini, M., Tanvir, N., Bloom, J., Pedersen, H., Nørdgaard-Nielsen, H. U., Linden-Vørnle, M., Melnick, J., van der Steene, G., Bremer, M., Naber, R., Heise, J., in't Zand, J., Costa, E., Feroci, M., Piro, L., Frontera, F., Zavattini, G., Nicastro, L., Palazzi, E., Bennett, K., Hanlon, L., & Parmar, A. 1997, Nature, 386, 686

Vreeswijk, P. M., Ellison, S. L., Ledoux, C., Wijers, R. A. M. J., Fynbo, J. P. U., Møller, P., Henden, A., Hjorth, J., Masi, G., Rol, E., Jensen, B. L., Tanvir, N., Levan, A., Castro Cerón, J. M., Gorosabel, J., Castro-Tirado, A. J., Fruchter, A. S., Kouveliotou, C., Burud, I., Rhoads, J., Masetti, N., Palazzi, E., Pian, E., Pedersen, H., Kaper, L., Gilmore, A., Kilmartin, P., Buckle, J. V., Seigar, M. S., Hartmann, D. H., Lindsay, K., & van den Heuvel, E. P. J. 2004, A&A, 419, 927

Watson, D., Fynbo, J. P. U., Ledoux, C., Vreeswijk, P., Hjorth, J., Smette, A., Andersen, A. C., Aoki, K., Augusteijn, T., Beardmore, A. P., Bersier, D., Castro Cerón, J. M., D'Avanzo, P., Diaz-Fraile, D., Gorosabel, J., Hirst, P., Jakobsson, P., Jensen, B. L., Kawai, N., Kosugi, G., Laursen, P., Levan, A., Masegosa, J., Näränen, J., Page, K. L., Pedersen, K., Pozanenko, A., Reeves, J. N., Rumyantsev, V., Shahbaz, T., Sharapov, D., Sollerman, J., Starling, R. L. C., Tanvir, N., Torstensson, K., & Wiersema, K. 2006, ApJ, 652, 1011

Watson, D., Hjorth, J., Fynbo, J. P. U., Jakobsson, P., Foley, S., Sollerman, J., & Wijers, R. A. M. J. 2007, ApJ, 660, L101

Waxman, E. & Draine, B. T. 2000, ApJ, 537, 796

Whittet, D. C. B., ed. 2003, Dust in the galactic environment

Wickramasinghe, N. C. 1973, Light scattering functions for small particles with applications in astronomy, ed. Wickramasinghe, N. C.

Williamson, S. J., Foner, S., & Dresselhaus, M. S. 1965, Physical Review, 140, 1429

Zeh, A., Klose, S., & Kann, D. A. 2006, ApJ, 637, 889

Appendices

Appendix A

Results

In this section, we will present the results of fitting the dust extinction curves for graphite and astronomical silicate to our GRB SEDs as described in Chapter 3.

A.1 Gamma Ray Burst Spectral Energy Distributions

The data used here to create the spectral energy distributions (SEDs) for the GRBs is taken from Kann et al. (2006, 2010) and references therein. The SEDs were compiled from the available data (including published data, GCNs, and publicly available *Swift* data). Kann et al. (2006) described the methods used to cross-calibrate the data and shift it into the same time frame (as it was taken by many different instruments at various times) assuming achromaticity in the SED. However, this analysis is only as good as the data that went into it, and not every observer is particularly careful about the results they publish or the calibration they use, especially in GCNs. Therefore, our fits may not always seem ideal, so this should be taken into consideration. However, overall, our fit of graphite and silicate dust extinction curves to the GRB SEDs have yielded surprisingly good versions of the extinction curve.

Although a wide range of wavelength data is available for the SEDs, we exclude any data with a frequency higher than 2.4×10^{15} Hz in the co-moving frame in order to rule out any effect of the Lyman α forest (bluer than 1216 Å) on our data. For this to be possible, we restrict our study only to GRBs for which the redshift has been well-established. All SEDs are presented in the co-moving frame.

The data consist of 82 GRBs observed between May 1997 and September 2009. The hydrogen column densities were taken from the *Swift* website[1]. The calculation of the dust-to-gas ratio is explained in Section 3.

---

[1] http://heasarc.gsfc.nasa.gov/docs/swiftarchive/grb_table

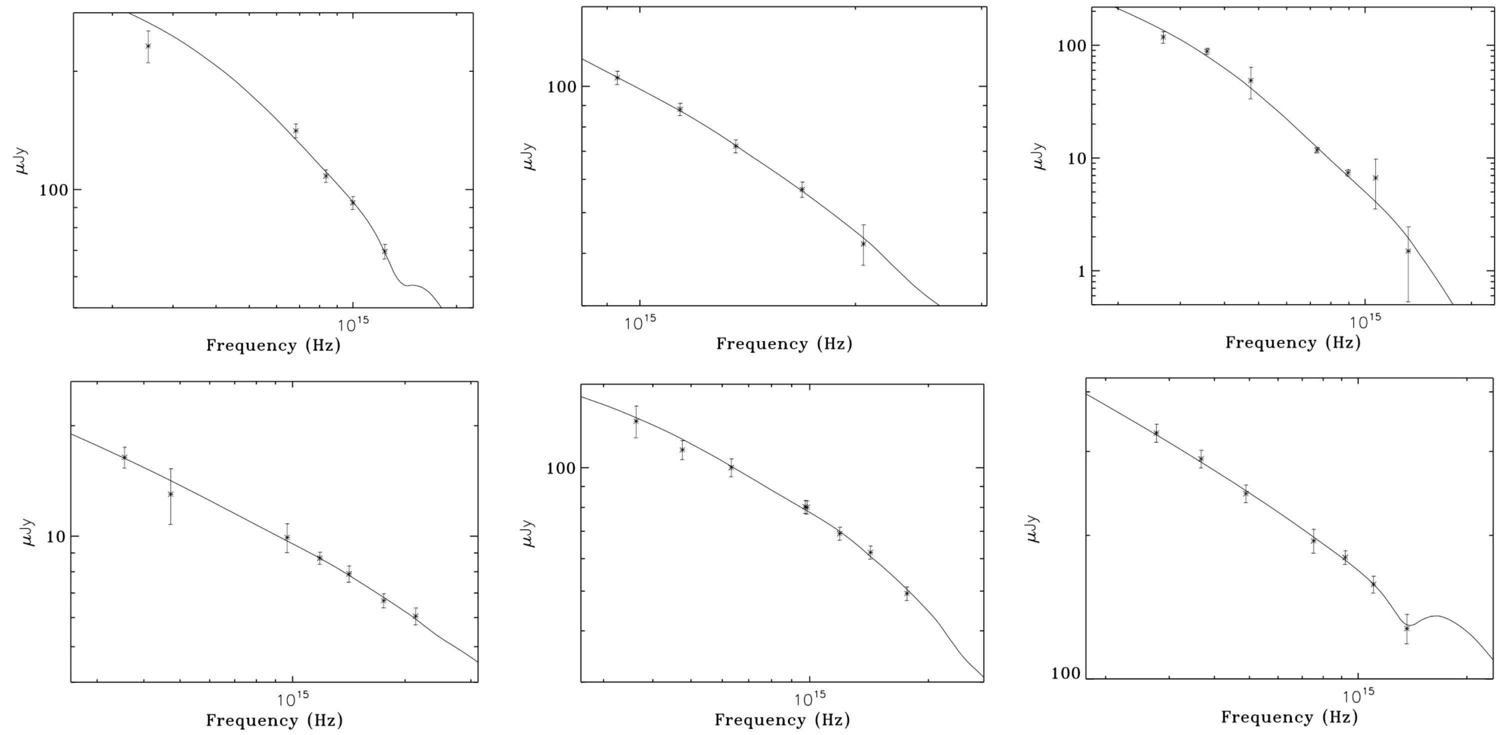

Figure A.1: From top left to right, GRB 970508, GRB 980519, and GRB 980703. From bottom left to right, GRB 990123, GRB 990510, and GRB 991216.

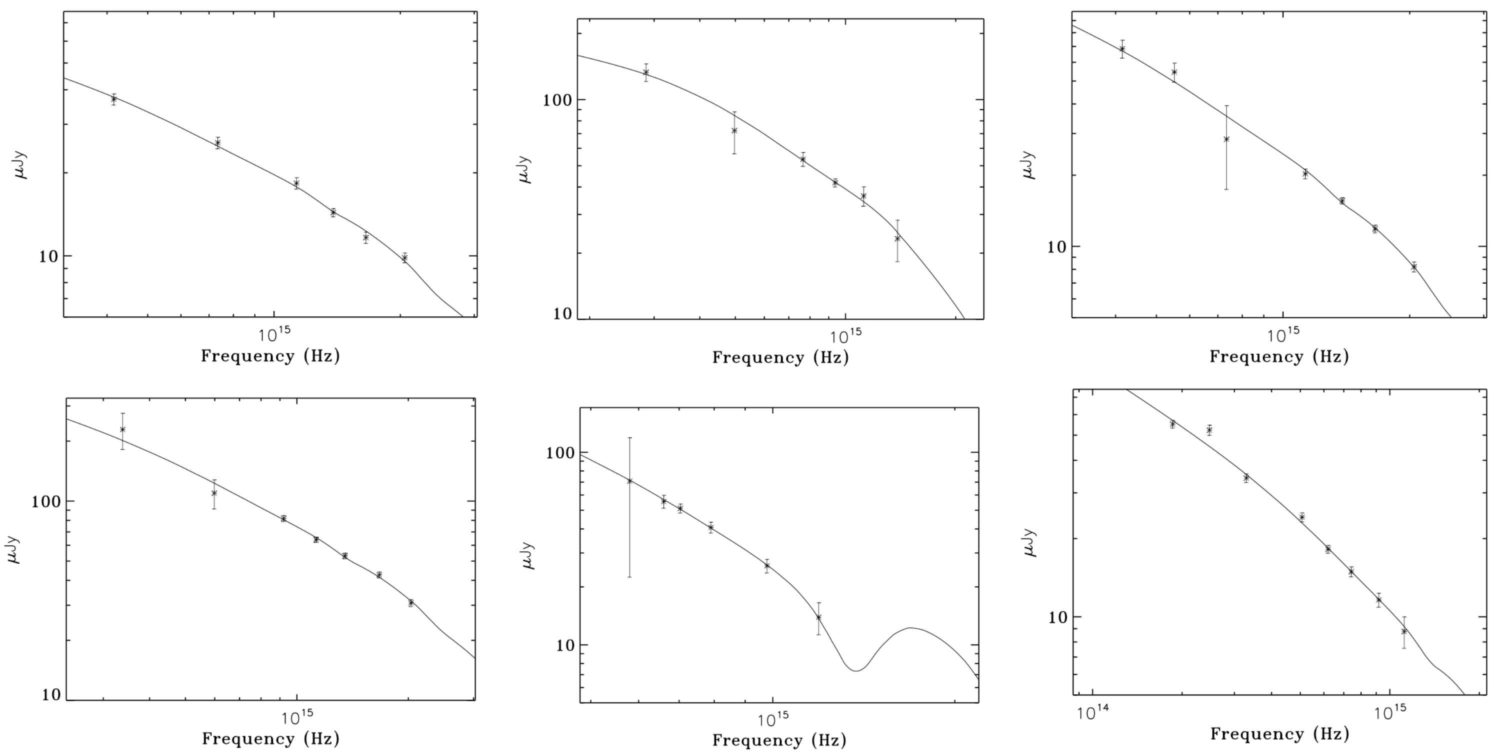

Figure A.2: From top left to right, GRB 000301, GRB 000911, and GRB 000926. From bottom left to right, GRB 010222, GRB 010921, and GRB 011121.

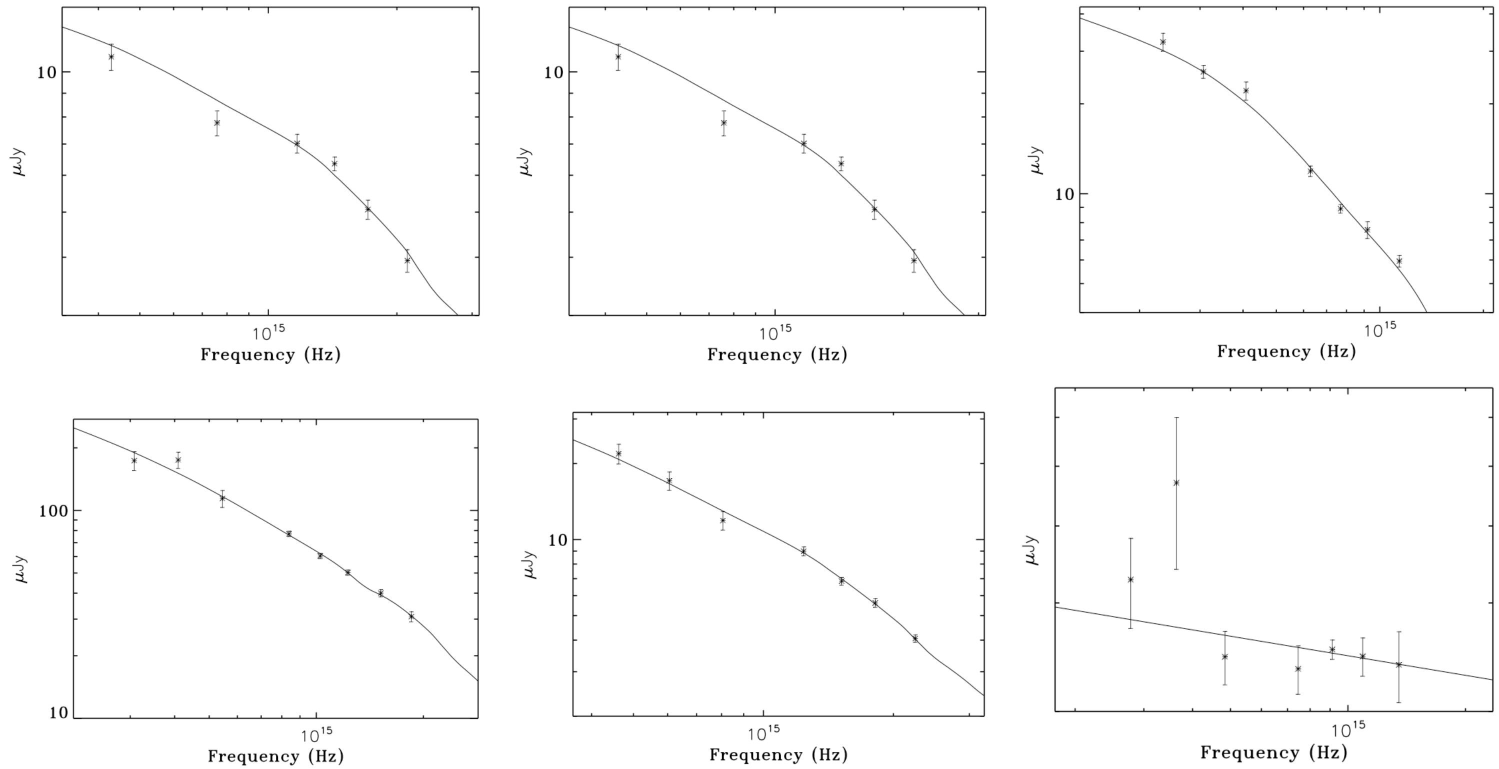

Figure A.3: From top left to right, GRB 011211, GRB 020124, and GRB 020405. From bottom left to right, GRB 020813, GRB 021004, and GRB 021211.

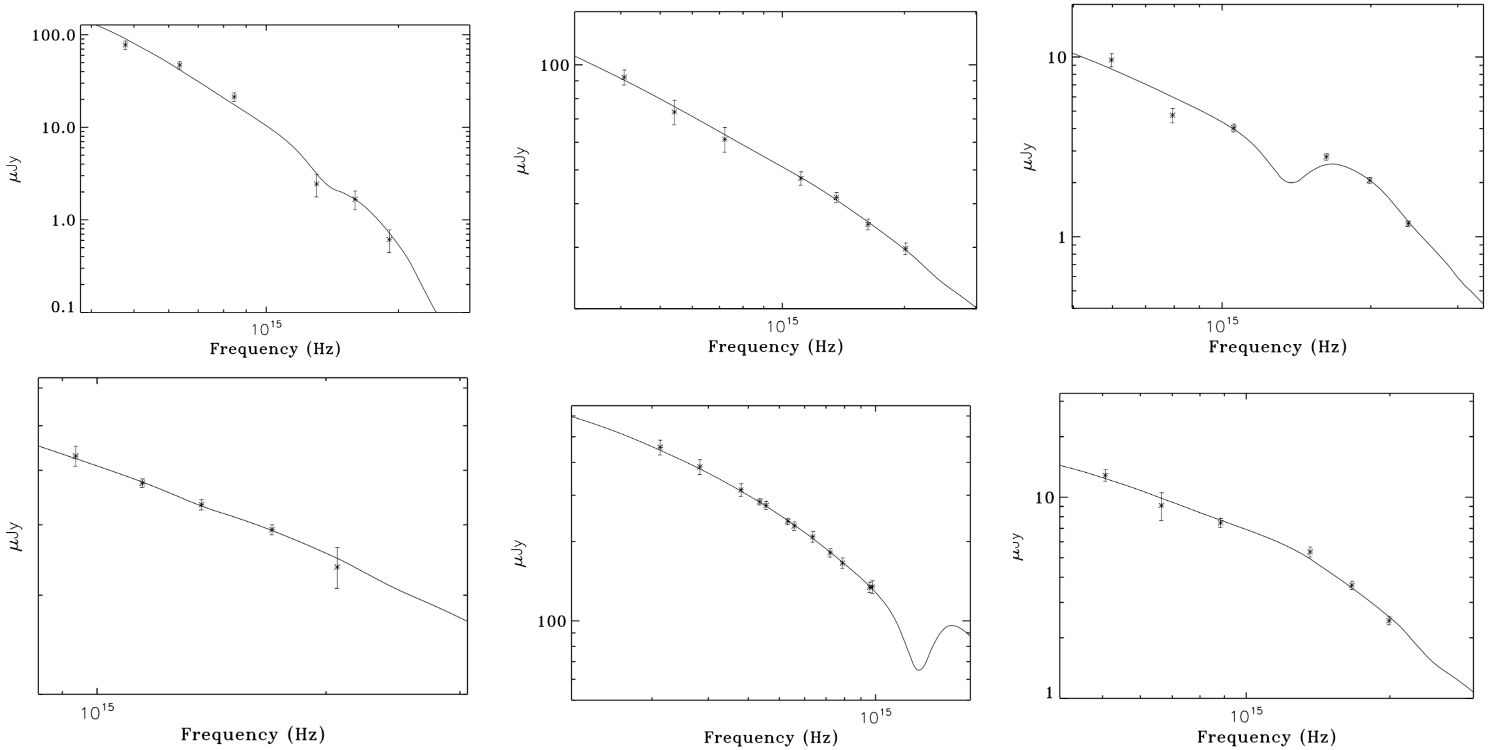

Figure A.4: From top left to right, GRB 030115, GRB 030226, and GRB 030323. From bottom left to right, GRB 030328, GRB 030329, and GRB 030429.

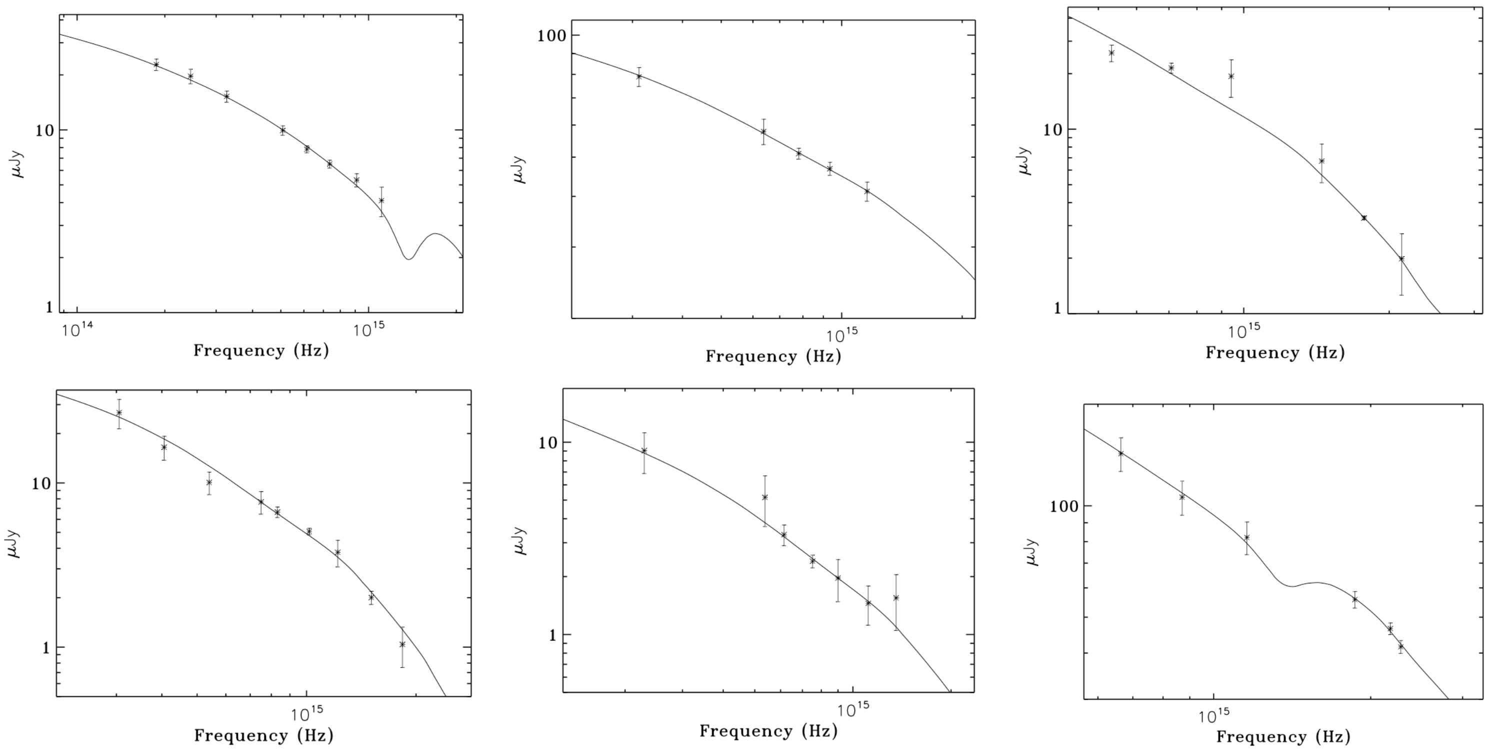

Figure A.5: From top left to right, GRB 030723, GRB 041006, and GRB 050401. From bottom left to right, GRB 050408, GRB 050416 and GRB 050502A.

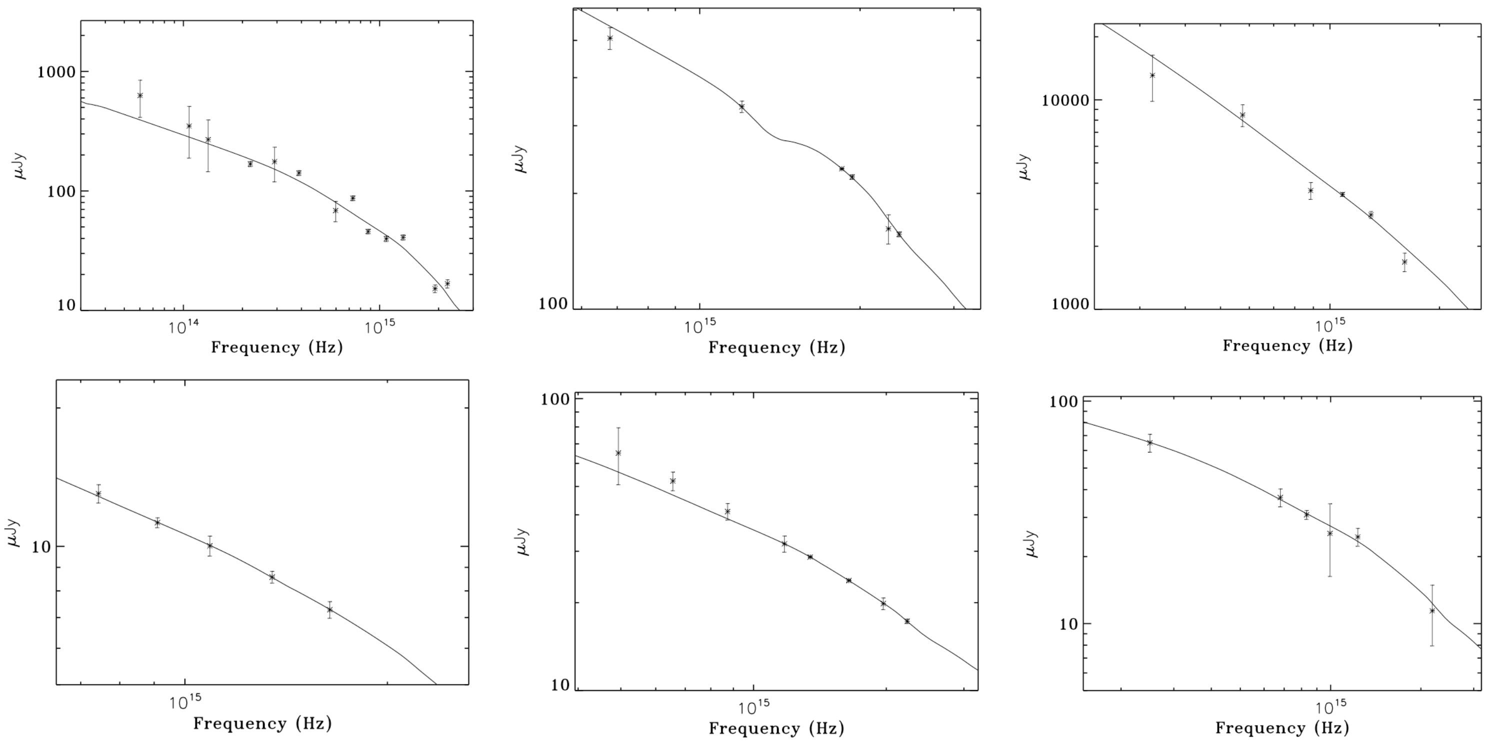

Figure A.6: From top left to right, GRB 050525, GRB 050730, and GRB 050801. From bottom left to right, GRB 050802, GRB 050820, and GRB 050824.

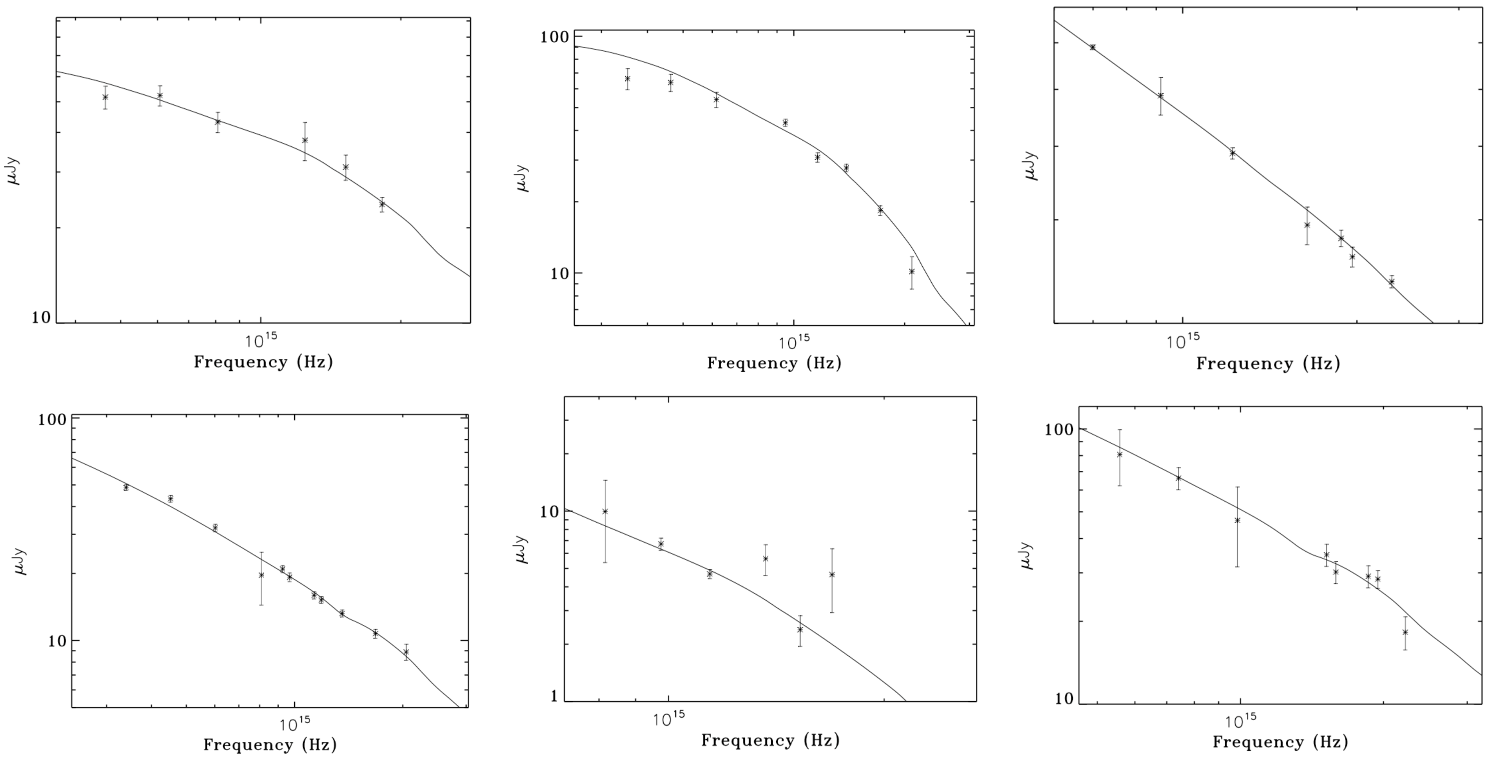

Figure A.7: From top left to right, GRB 051109, GRB 051111, and GRB 060206. From bottom left to right, GRB 060210, GRB 060502, and GRB 0060607.

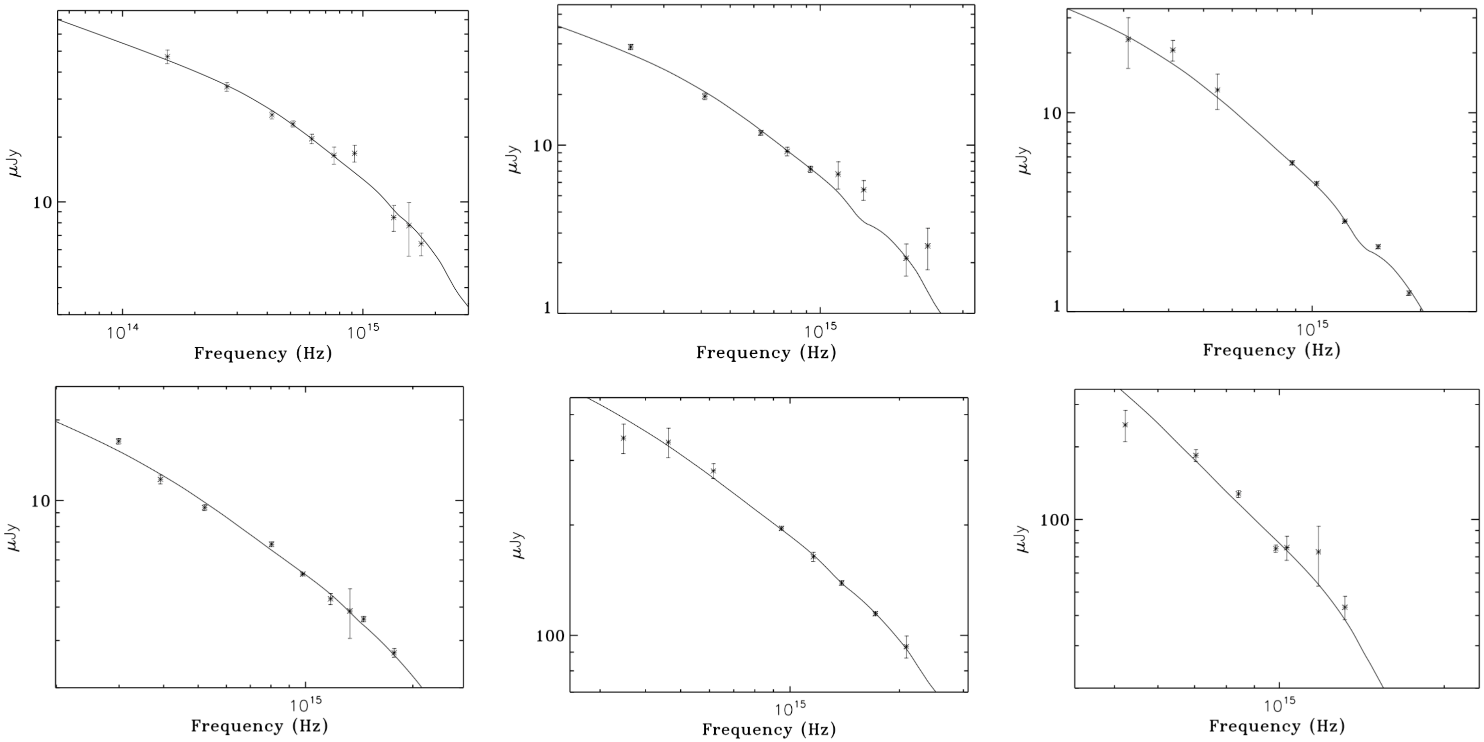

Figure A.8: From top left to right, GRB 060614, GRB 060904, and GRB 061007. From bottom left to right, GRB 061126, GRB 070125, and GRB 070208.

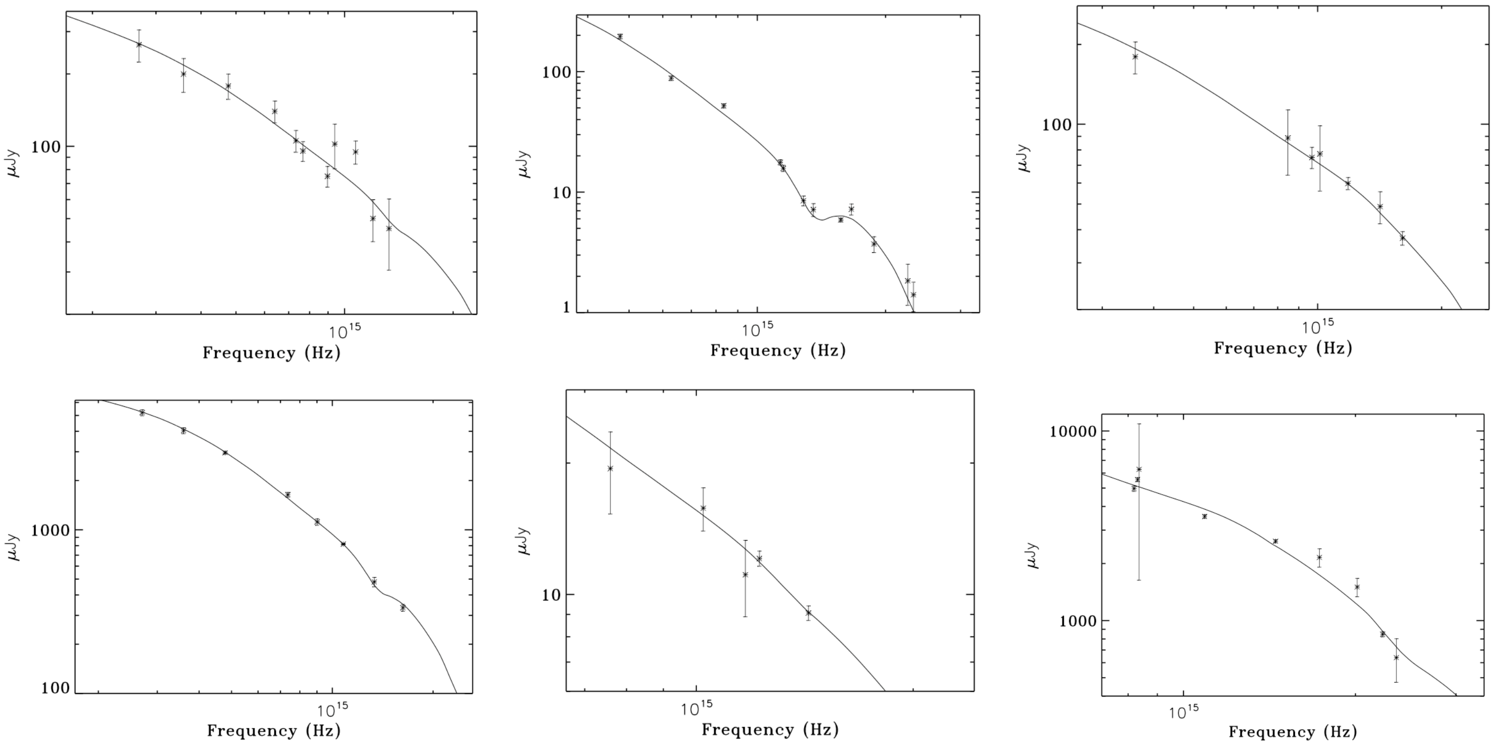

Figure A.9: From top left to right, GRB 070419, GRB 070802, and GRB 071003. From bottom left to right, GRB 071010, GRB 071020, and GRB 071025.

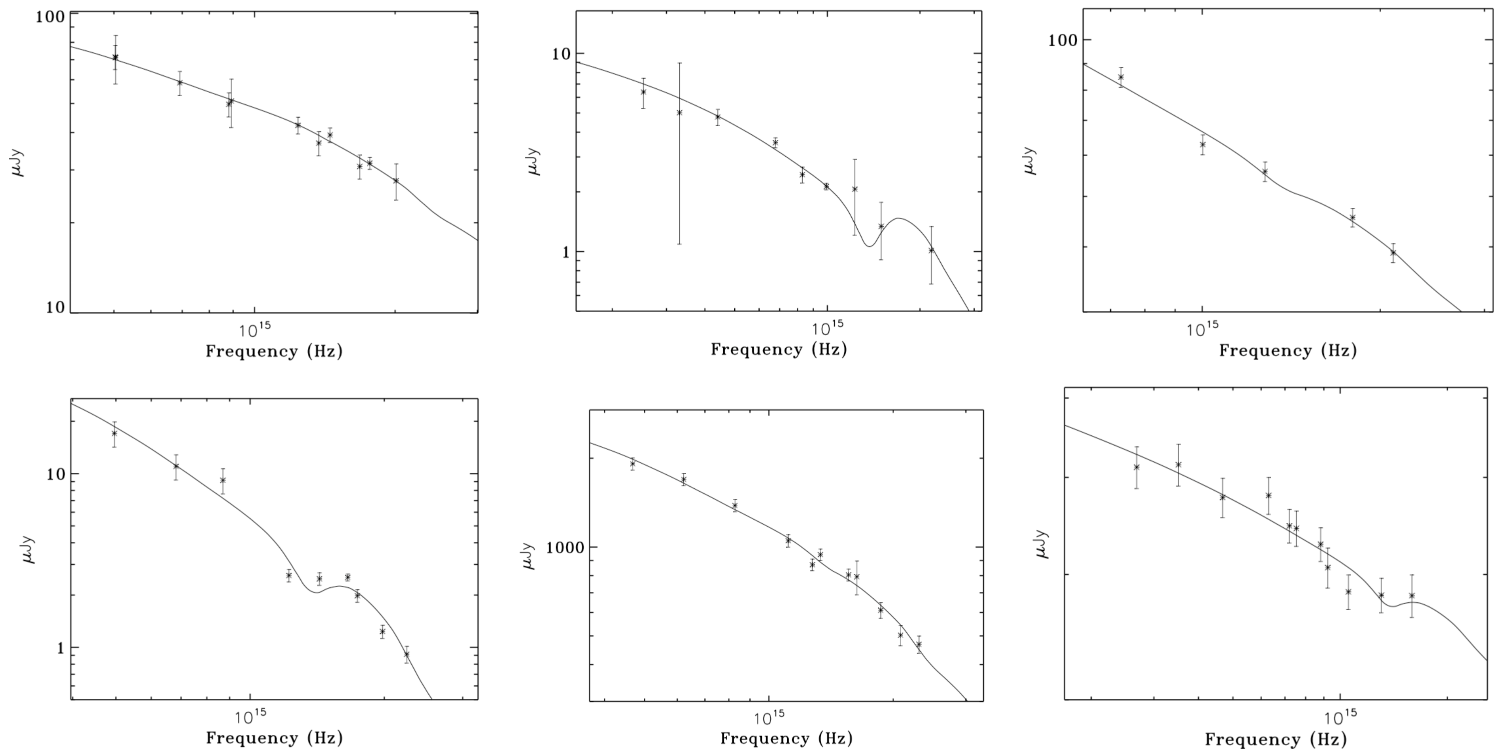

Figure A.10: From top left to right, GRB 071031, GRB 071112, and GRB 080129. From bottom left to right, GRB 080210, GRB 080310, and GRB 080319B.

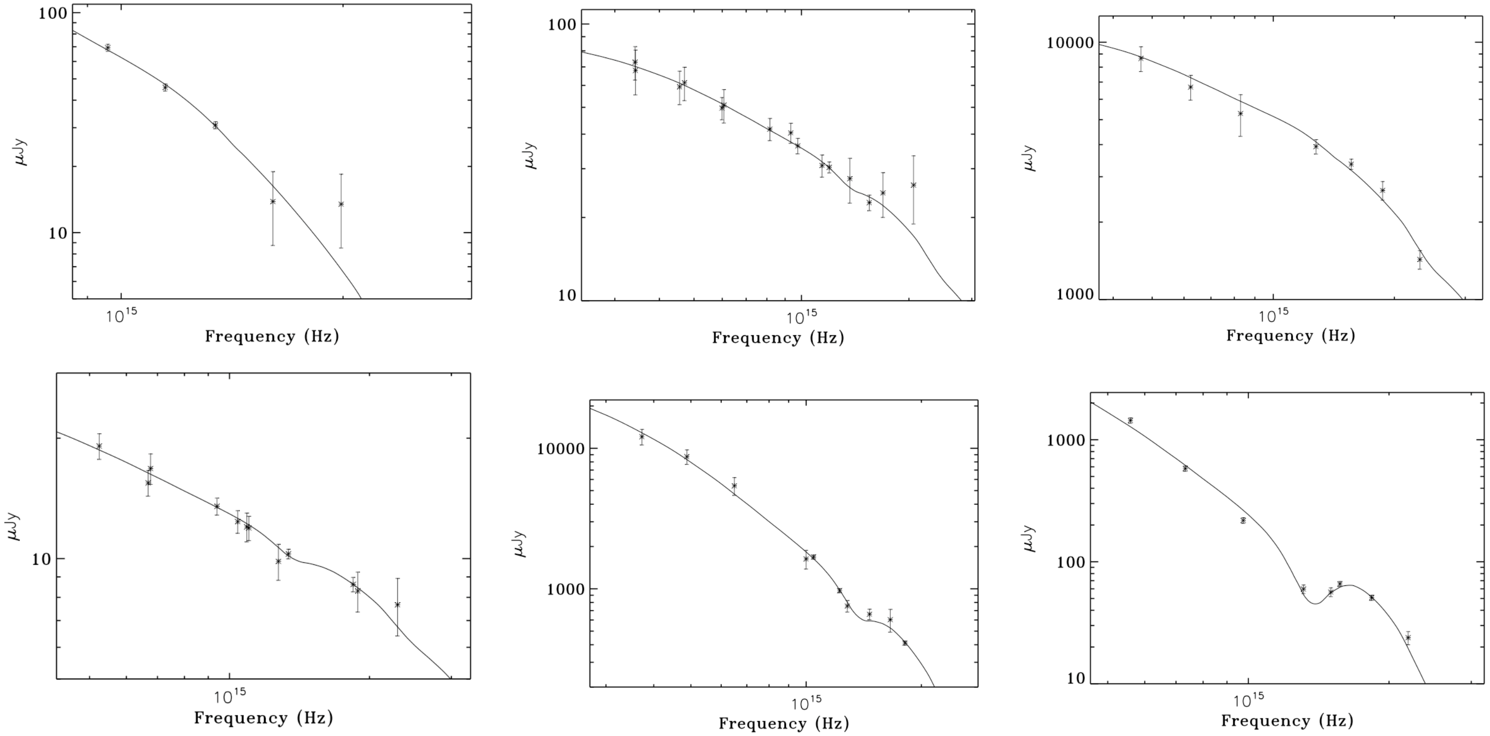

Figure A.11: From top left to right, GRB 080319C, GRB 080330, and GRB 080413. From bottom left to right, GRB 080514, GRB 080603, and GRB 080607.

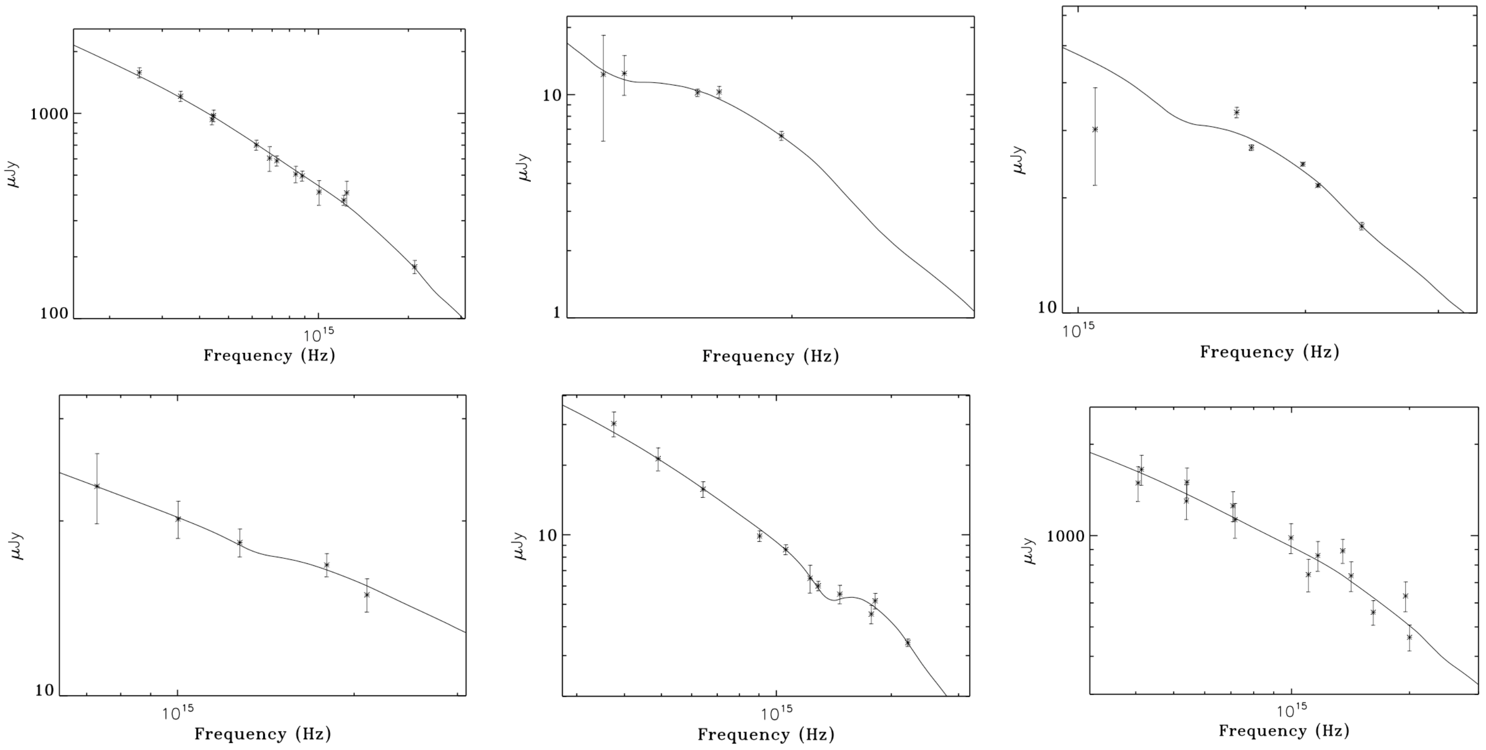

Figure A.12: From top left to right, GRB 080710, GRB 080721, and GRB 080810. From bottom left to right, GRB 080916, GRB 080928, and GRB 081008.

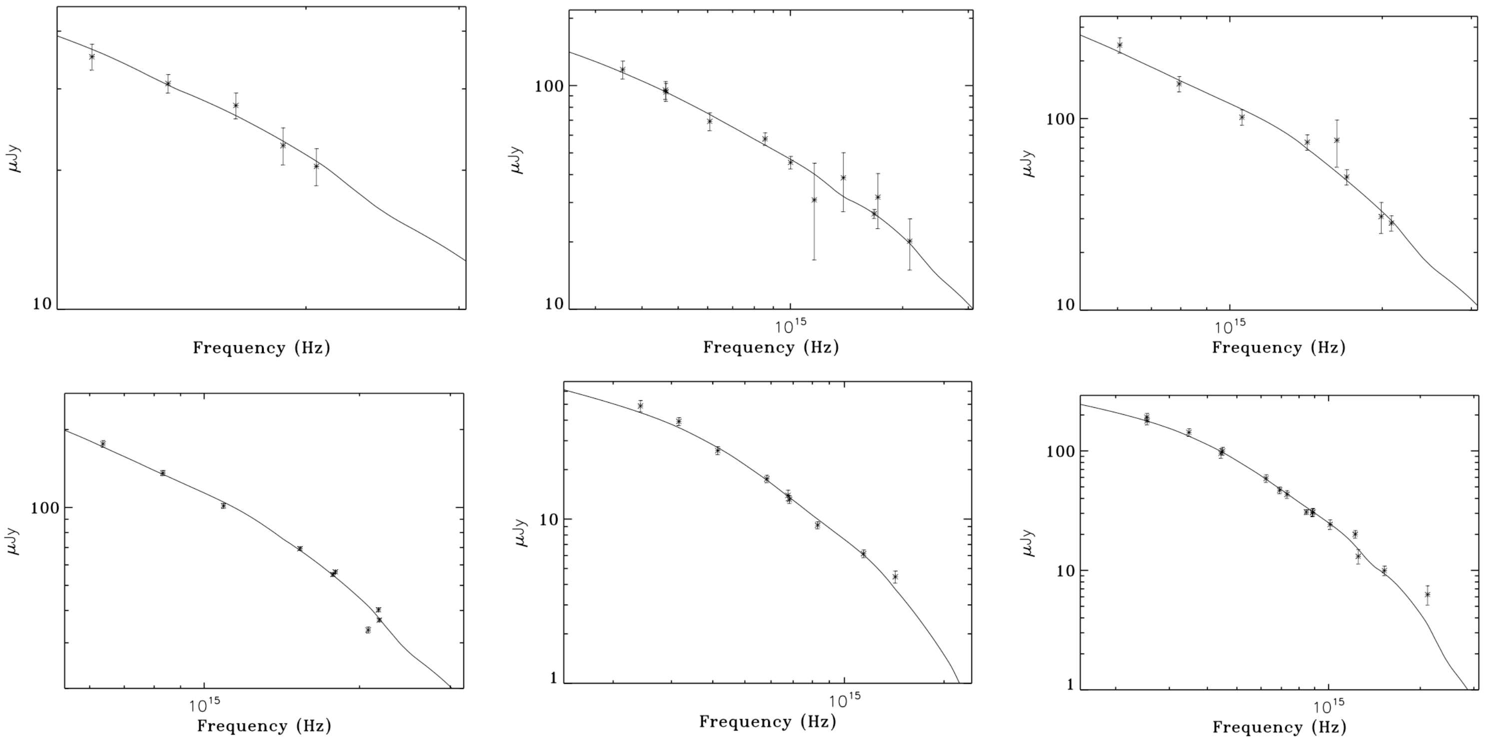

Figure A.13: From top left to right, GRB 081203, GRB 090102, and GRB 090313. From bottom left to right, GRB 090323, GRB 090328, and GRB 090424.

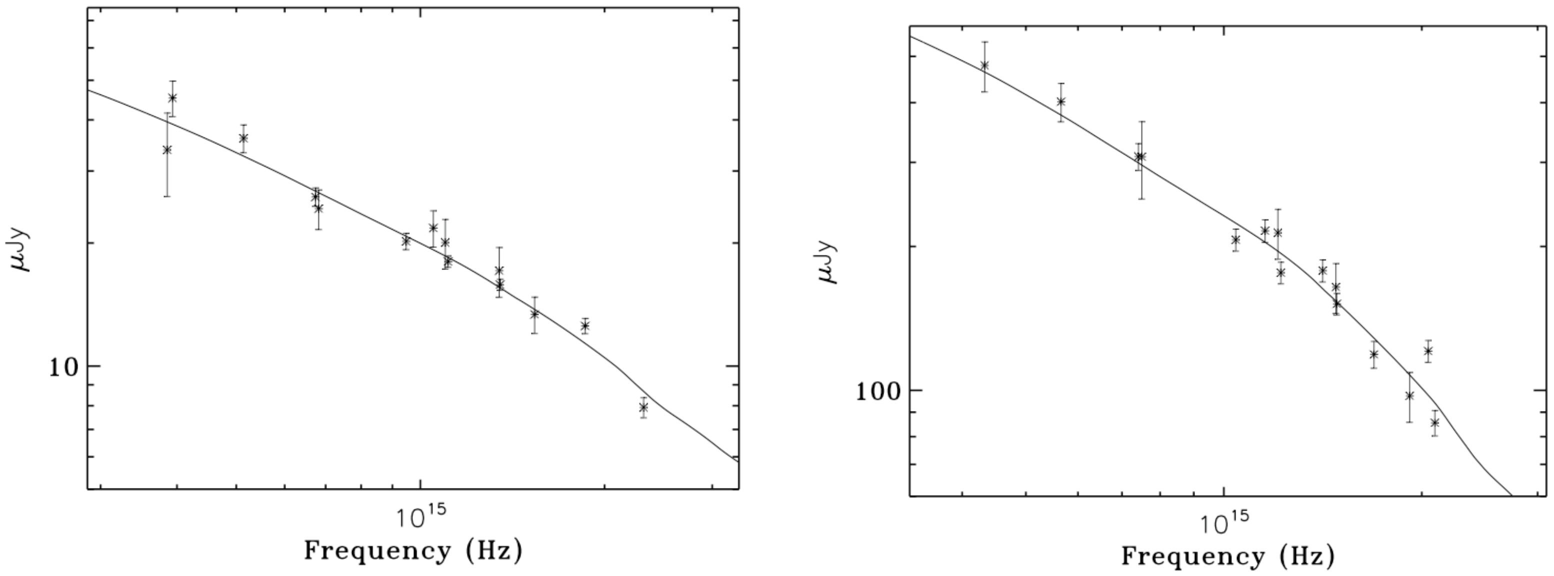

Figure A.14: GRB 090902 and GRB 090926.

Table A.1: Results for GRB sample. Units of graphite and silicate column densities are 10^{10} cm^{-2}, units of N_H are 10^{21} cm^{-2}.

burst	$\tilde{\chi}^2$	redshift	β	graphite	silicate	A_V	R_V	N_H	dust-to-gas
970508	4.539	0.835	0.259 ± 0.001	6.221 ± 0.767	29.67 ± 1.636	0.429 ± 0.034	2.805 ± 0.445		
980519	0.211	1.500	0.585 ± 0.001	0.302 ± 0.059	17.25 ± 1.048	0.168 ± 0.024	2.303 ± 0.617		
980703	2.276	0.966	1.086 ± 0.001	0.001 ± 0.001	108.1 ± 7.451	1.007 ± 0.070	2.246 ± 0.333		
990123	0.231	1.600	0.429 ± 0.003	0.002 ± 0.834	5.845 ± 1.798	0.054 ± 0.037	2.247 ± 4.920		
990510	0.684	1.619	0.245 ± 0.002	0.322 ± 0.319	17.71 ± 2.027	0.173 ± 0.027	2.305 ± 0.763		
991208	0.579	0.706	0.453 ± 0.002	15.94 ± 1.222	23.92 ± 2.506	0.614 ± 0.053	3.493 ± 0.690		
991216	0.210	1.020	0.374 ± 0.001	4.381 ± 1.382	3.434 ± 3.052	0.139 ± 0.062	3.954 ± 8.678		
000301	1.085	2.040	0.353 ± 0.001	0.995 ± 1.057	21.41 ± 1.444	0.224 ± 0.034	2.392 ± 0.798		
000911	0.589	1.058	0.335 ± 0.003	0.001 ± 0.340	45.09 ± 4.001	0.420 ± 0.046	2.246 ± 0.513		
010222	0.993	1.477	0.590 ± 0.001	1.535 ± 0.469	19.92 ± 1.440	0.223 ± 0.025	2.481 ± 0.554		
010921	0.089	0.451	0.567 ± 0.001	27.77 ± 2.350	33.89 ± 4.579	1.033 ± 0.100	3.560 ± 0.800		
011121	3.054	0.362	0.725 ± 0.001	2.858 ± 2.245	20.35 ± 5.013	0.260 ± 0.102	2.646 ± 2.783		
011211	3.919	2.142	0.156 ± 0.002	0.001 ± 0.515	20.02 ± 1.462	0.186 ± 0.026	2.246 ± 0.609		
020124	3.149	3.198	0.560 ± 0.001	0.051 ± 1.162	16.93 ± 1.764	0.159 ± 0.045	2.256 ± 1.285		
020405	2.498	0.690	0.378 ± 0.001	0.001 ± 0.978	53.44 ± 3.701	0.498 ± 0.058	2.246 ± 0.513		
020813	1.130	1.254	0.597 ± 0.001	2.200 ± 1.035	19.87 ± 2.015	0.239 ± 0.044	2.572 ± 0.984		
021004	0.737	2.335	0.515 ± 0.001	0.002 ± 0.545	19.92 ± 1.309	0.186 ± 0.026	2.247 ± 0.595		
021211	1.560	1.004	0.105 ± 0.002	0.001 ± 0.151	0.001 ± 0.228	0.001 ± 0.006	3.556 ± 7.046		
030115	4.121	2.500	0.425 ± 0.002	14.36 ± 3.565	127.8 ± 7.776	1.542 ± 0.160	2.576 ± 0.522		
030226	0.340	1.986	0.480 ± 0.001	0.121 ± 0.319	9.635 ± 1.515	0.093 ± 0.022	2.288 ± 1.216		
030323	7.949	3.372	0.370 ± 0.001	16.23 ± 1.210	29.41 ± 1.049	0.672 ± 0.039	3.362 ± 0.388		
030328	0.397	1.522	0.346 ± 0.001	0.515 ± 0.337	5.542 ± 0.592	0.064 ± 0.014	2.524 ± 1.125		
030329	0.090	0.169	0.283 ± 0.002	17.11 ± 2.005	16.40 ± 5.027	0.572 ± 0.096	3.813 ± 1.773		
030429	1.988	2.658	0.150 ± 0.001	0.103 ± 0.110	41.21 ± 1.598	0.386 ± 0.018	2.255 ± 0.205		
030723	0.551	0.350	0.378 ± 0.001	17.91 ± 0.306	24.85 ± 7.012	0.670 ± 0.140	3.549 ± 2.034		
041006	0.104	0.716	0.269 ± 0.001	0.288 ± 0.288	15.01 ± 1.917	0.147 ± 0.025	2.309 ± 0.855		
050401	3.685	2.899	0.630 ± 0.001	0.003 ± 0.756	53.02 ± 1.395	0.494 ± 0.032	2.247 ± 0.250		
050408	1.297	1.236	0.623 ± 0.005	0.001 ± 2.478	52.97 ± 5.722	0.493 ± 0.114	2.246 ± 1.054	2.5	0.001097
050416	0.615	0.653	0.665 ± 0.006	0.007 ± 2.885	35.93 ± 11.68	0.335 ± 0.179	2.247 ± 3.680	2.5	0.00685797
050502	0.312	3.793	0.575 ± 0.001	6.176 ± 1.388	11.62 ± 1.085	0.260 ± 0.044	3.337 ± 1.221		

Table A.2: Results for GRB sample. Units of graphite and silicate column densities are 10^{10} cm^{-2}, units of N_H are 10^{21} cm^{-2}.

burst	$\tilde{\chi}^2$	redshift	β	graphite	silicate	A_V	R_V	N_H	dust-to-gas
050525	8.798	0.606	0.570 ± 0.002	0.001 ± 1.370	28.23 ± 4.650	0.263 ± 0.077	2.247 ± 1.480		
050730	0.938	3.969	0.296 ± 0.001	3.707 ± 0.240	21.75 ± 0.212	0.293 ± 0.009	2.718 ± 0.126	1.0	0.00115878
050801	5.713	1.560	1.082 ± 0.005	0.003 ± 0.484	12.52 ± 1.659	0.117 ± 0.027	2.247 ± 1.123	0.57	0.00104816
050802	0.105	1.710	0.405 ± 0.001	0.387 ± 0.523	12.79 ± 1.050	0.129 ± 0.023	2.343 ± 0.805	0.66	0.000943652
050820	0.793	2.615	0.405 ± 0.001	0.001 ± 0.193	14.19 ± 0.353	0.132 ± 0.008	2.246 ± 0.237	6.0	0.000112836
050824	0.255	0.828	0.382 ± 0.001	0.001 ± 0.122	18.88 ± 4.267	0.176 ± 0.043	2.246 ± 1.397	0.36	0.00250188
051109	1.521	2.346	0.080 ± 0.002	0.154 ± 1.271	24.42 ± 2.701	0.231 ± 0.056	2.267 ± 1.127	8.2	0.000142712
051111	5.137	1.550	0.047 ± 0.002	0.625 ± 1.322	44.22 ± 2.505	0.427 ± 0.056	2.292 ± 0.555	9	0.000236690
060206	0.731	4.048	0.607 ± 0.001	30.35 ± 0.262	5.640 ± 0.829	0.061 ± 0.014	2.438 ± 1.257	0.4	0.000701232
060210	1.500	1.490	0.646 ± 0.002	2.114 ± 1.312	15.30 ± 2.435	0.194 ± 0.055	2.641 ± 1.716	16.4	4.87208e-05
060502	4.332	1.503	0.718 ± 0.001	0.197 ± 0.197	49.15 ± 4.122	0.463 ± 0.043	2.260 ± 0.450	4.5	0.000522526
060526	4.033	3.211	0.486 ± 0.003	6.914 ± 1.239	10.73 ± 1.078	0.269 ± 0.040	3.469 ± 1.136	0.6	0.00122953
060607	1.073	3.075	0.576 ± 0.003	2.241 ± 2.234	14.69 ± 3.154	0.192 ± 0.084	2.676 ± 3.087	7.9	9.79907e-05
060614	1.151	0.125	0.401 ± 0.002	1.653 ± 2.136	24.85 ± 7.198	0.272 ± 0.119	2.451 ± 3.071	1.3	0.000953467
060904	4.223	0.703	0.585 ± 0.001	4.956 ± 2.498	37.48 ± 5.400	0.470 ± 0.111	2.626 ± 1.393	1.7	0.00114700
060908	0.250	1.884	0.216 ± 0.002	0.358 ± 0.615	3.181 ± 3.179	0.039 ± 0.045	2.601 ± large	0.80	0.000205588
061007	7.957	1.262	0.554 ± 0.001	6.579 ± 0.396	51.35 ± 0.836	0.639 ± 0.017	2.616 ± 0.132	1.4	0.00190329
061126	6.022	1.159	0.536 ± 0.001	0.845 ± 0.244	23.23 ± 1.134	0.237 ± 0.017	2.362 ± 0.322	2.7	0.000420754
070125	0.959	1.547	0.427 ± 0.001	1.028 ± 0.469	16.74 ± 0.774	0.181 ± 0.019	2.436 ± 0.465	0.81	0.00102767
070208	7.403	1.165	0.472 ± 0.001	0.002 ± 1.064	100.8 ± 3.088	0.939 ± 0.055	2.246 ± 0.238	2.6	0.00184941
070419	1.691	0.971	0.456 ± 0.005	3.131 ± 3.115	33.66 ± 11.86	0.390 ± 0.187	2.525 ± 3.855	1.9	0.000899028
070802	3.665	2.454	0.449 ± 0.002	23.11 ± 1.920	94.87 ± 3.684	1.450 ± 0.081	2.876 ± 0.316	0.29	0.0182105
071003	0.214	1.604	0.492 ± 0.007	0.002 ± 0.945	31.24 ± 3.332	0.291 ± 0.054	2.247 ± 0.858	1.4	0.00106472
071010	1.077	0.985	0.300 ± 0.001	8.121 ± 0.555	63.54 ± 1.086	0.791 ± 0.024	2.615 ± 0.144		
071020	1.172	2.146	0.533 ± 0.001	1.445 ± 0.226	35.54 ± 1.658	0.366 ± 0.021	2.375 ± 0.272	4.3	0.000405291
071025	9.272	4.800	0.009 ± 0.001	0.828 ± 0.823	56.16 ± 1.424	0.543 ± 0.033	2.294 ± 0.247	0.9	0.00300728
071031	0.296	2.692	0.209 ± 0.002	0.262 ± 0.992	18.93 ± 3.231	0.183 ± 0.054	2.291 ± 1.558	0.70	0.00130306
071112	0.745	0.823	0.262 ± 0.003	16.51 ± 2.940	21.73 ± 5.905	0.607 ± 0.127	3.586 ± 2.030		
080129	2.643	4.349	0.454 ± 0.001	1.603 ± 0.723	8.411 ± 0.977	0.118 ± 0.027	2.764 ± 1.370	2	0.000226815
080210	5.212	2.642	0.455 ± 0.003	15.90 ± 2.303	52.84 ± 2.819	0.881 ± 0.083	2.986 ± 0.553	2.15	0.00141345
080310	1.245	2.427	0.226 ± 0.002	1.697 ± 1.450	25.58 ± 2.602	0.280 ± 0.060	2.450 ± 1.071	7.0	0.000182236

Table A.3: Results for GRB sample. Units of graphite and silicate column densities are 10^{10} cm^{-2}, units of N_H are 10^{21} cm^{-2}.

burst	$\tilde{\chi}^2$	redshift	β	graphite	silicate	A_V	R_V	N_H	dust-to-gas
080319B	0.751	0.937	0.118 ± 0.002	1.563 ± 1.432	2.900 ± 2.898	0.065 ± 0.062	3.346 ± 5.000	2.35	8.06044e-05
080319C	3.299	1.949	0.131 ± 0.001	1.287 ± 0.620	98.57 ± 1.443	0.950 ± 0.029	2.289 ± 0.121	1.5	0.00316339
080330	0.346	1.512	0.157 ± 0.004	2.991 ± 2.764	27.55 ± 5.383	0.330 ± 0.118	2.566 ± 2.248	0.123	0.0114821
080413	1.647	2.433	0.027 ± 0.002	1.551 ± 1.551	37.75 ± 2.471	0.390 ± 0.061	2.376 ± 0.704	15.3	0.000121035
080514	0.304	1.800	0.245 ± 0.002	2.582 ± 1.420	15.19 ± 2.918	0.205 ± 0.062	2.717 ± 2.008		
080603	0.858	1.688	0.592 ± 0.001	1.342 ± 1.512	70.45 ± 2.661	0.985 ± 0.062	2.763 ± 0.332	8	0.000474934
080607	6.734	3.036	0.616 ± 0.001	32.33 ± 1.825	81.13 ± 2.256	1.548 ± 0.066	3.150 ± 0.259	40	0.000123168
080710	0.392	0.845	0.657 ± 0.003	0.001 ± 1.524	17.99 ± 5.560	0.168 ± 0.089	2.246 ± 3.556	1.6	0.000536466
080721	1.825	2.591	0.360 ± 0.001	11.50 ± 1.161	66.48 ± 1.050	0.901 ± 0.038	2.724 ± 0.203	1.10	0.00322482
080810	23.681	3.351	0.373 ± 0.001	4.148 ± 0.401	22.26 ± 0.310	0.309 ± 0.013	2.754 ± 0.198	0.328	0.00365142
080916	0.524	4.350	0.333 ± 0.001	0.978 ± 0.976	12.98 ± 1.284	0.036 ± 0.036	3.580 ± 5.000	2.6	3.61003e-05
080928	0.660	1.692	0.618 ± 0.003	8.241 ± 1.813	20.27 ± 2.617	0.391 ± 0.069	3.162 ± 1.255	1.7	0.000727169
081008	1.265	1.968	0.390 ± 0.004	0.001 ± 3.435	14.96 ± 5.363	0.139 ± 0.134	2.247 ± 9.485	0.59	0.00120948
081203	1.098	2.050	0.332 ± 0.001	0.828 ± 0.912	17.89 ± 1.468	0.187 ± 0.036	2.392 ± 0.901	0.60	0.00146763
090102	0.450	1.547	0.476 ± 0.003	2.162 ± 3.638	22.24 ± 4.392	0.260 ± 0.130	2.536 ± 3.294	7.0	0.000161682
090313	1.177	3.374	0.434 ± 0.002	0.001 ± 1.152	45.51 ± 3.602	0.424 ± 0.0618	2.246 ± 0.640	1.29	0.00168322
090323	21.730	3.568	0.302 ± 0.001	0.747 ± 0.596	33.33 ± 0.612	0.329 ± 0.020	2.318 ± 0.241	0.17	0.00949640
090328	2.265	0.735	0.504 ± 0.001	0.723 ± 0.723	58.09 ± 4.770	0.559 ± 0.062	2.287 ± 0.522	1.9	0.00147114
090424	1.809	0.544	0.453 ± 0.002	5.090 ± 0.307	67.51 ± 6.276	0.754 ± 0.134	2.476 ± 0.890	2.7	0.00125455
090902	1.588	1.823	0.490 ± 0.001	0.340 ± 1.679	14.00 ± 2.864	0.139 ± 0.068	2.325 ± 2.872		
090926	2.678	2.107	0.424 ± 0.006	0.009 ± 1.862	24.44 ± 3.280	0.228 ± 0.076	2.248 ± 1.608	1.0	0.00116655

Appendix B

Bursts from the Literature

This table includes 85 bursts for which an A_V was published and the redshift was known. The template used has been noted.

Table B.1: Magnitudes of visual extinction found in the literature for 85 bursts. When more than one value was quoted for A_V, the one with the χ^2 closest to one is reported. F&M Fitzpatrick & Massa (1990).

Burst	z	A_V	Model	Reference
970508	0.835	0.38 ± 0.11	MW	Kann et al. (2006)
980425	0.0085	1.73	MW	Savaglio et al. (2009)
980613	1.0969	0.25	–	Hjorth et al. (2002)
980703	0.966	2.2	MW	Castro-Tirado et al. (1999)
990123	1.60	0.04 ± 0.05	SMC	Kann et al. (2006)
990712	0.434	0.39 ± 0.09	MW	Savaglio et al. (2009)
991208	0.706	0.80 ± 0.29	MW	Kann et al. (2006)
991216	1.02	0.13 ± 0.08	MW	Kann et al. (2006)
000210	0.8463	0	SB	Gorosabel et al. (2003)
000301C	2.03	0.12 ± 0.06	SMC	Kann et al. (2006)
000418	1.118	0.96 ± 0.2	MW	Klose et al. (2000)
000911	1.058	0.20 ± 0.22	MW	Kann et al. (2006)
000926	2.066	0.15 ± 0.07	SMC	Kann et al. (2006)
010222	1.477	0.14 ± 0.08	SMC	Kann et al. (2006)
010921	0.45	1.06 ± 0.62	MW	Savaglio et al. (2009)
011121	0.36	0.39 ± 0.14	SMC	Kann et al. (2006)
011211	2.14	0.08 ± 0.08	SMC	Jakobsson et al. (2003)
020124	3.198	0.20	SMC	Hjorth et al. (2003)
020127	1.9	0.5	SB	Berger et al. (2007)
020405	0.69	0.15 ± 0.16	SMC	Kann et al. (2006)
020813	1.25	0.12 ± 0.07	SMC	Kann et al. (2006)
020903	0.25	0.59	MW	Savaglio et al. (2009)
021004	2.3	0.14 ± 0.05	SMC	Kann et al. (2006)
021211	1.01	0.18 ± 0.25	–	Nysewander et al. (2006)
030226	1.98	0.06 ± 0.06	SMC	Kann et al. (2006)
030323	3.372	0.5	MW	Vreeswijk et al. (2004)
030328	1.52	0.05 ± 0.15	SMC	Kann et al. (2006)
030329	0.168	0.39 ± 0.15	SMC	Kann et al. (2006)
030429	2.65	0.40 ± 0.10	SMC	Kann et al. (2006)
031203	0.105	0.03 ± 0.05	MW	Savaglio et al. (2009)
040924	0.859	0.16 ± 0.44	SMC	Kann et al. (2006)
041006	0.716	0.11 ± 0.23	MW	Kann et al. (2006)
050223	0.584	> 2	–	Pellizza et al. (2006)
050319	3.240	0.06 ± 0.31	MW	Kann et al. (2008)
050401	2.8992	0.62 ± 0.06	SMC	Watson et al. (2006)
050408	1.236	0.73 ± 0.18	SMC	de Ugarte Postigo et al. (2007)
050416A	0.6535	0.11 ± 0.38	LMC	Kann et al. (2008)
050502A	3.793	0	none	Kann et al. (2008)
050525	0.606	0.36 ± 0.05	SMC	Kann et al. (2008)
050709	0.1606	0	MW	Savaglio et al. (2009)

Table B.2: Magnitudes of visual extinction found in the literature for 85 bursts. When more than one value was quoted for A_V, the one with the χ^2 closest to one is reported. F&M Fitzpatrick & Massa (1990).

Burst	z	A_V	Model	Reference
050730	3.968	0.01	all	Starling et al. (2005)
050801	1.56	0	none	Kann et al. (2008)
050802	1.71	0.05 ± 0.07	MW	Kann et al. (2008)
050814	5.3	0.9	–	Jakobsson et al. (2006)
050820A	2.612	0	none	Kann et al. (2008)
050824	0.83	0	none	Kann et al. (2008)
050904	6.29	0	none	Kann et al. (2008)
050922C	2.198	0.00 ± 0.01	MW	Kann et al. (2008)
051016B	0.94	0.11	–	Jakobsson et al. (2006)
051111	1.55	0.23 ± 0.07	SMC	Butler et al. (2006)
060115	3.53	0.44	–	Jakobsson et al. (2006)
060124	2.30	0.44	–	Jakobsson et al. (2006)
060206	4.048	0.01 ± 0.05	LMC	Kann et al. (2008)
060210	3.91	1.21 ± 0.16	SMC	Cenko et al. (2009)
060218	0.0331	0.49 ± 0.24	MW	Savaglio et al. (2009)
060418	1.489	0.20 ± 0.08	LMC	Kann et al. (2008)
060502A	1.51	0.53 ± 0.13	SMC	Cenko et al. (2009)
060505	0.089	0.63 ± 0.01	MW	Savaglio et al. (2009)
060526	3.221	0	all	Thoene et al. (2008)
060607A	3.082	0.10 ± 0.18	MW	Kann et al. (2008)
060906	3.685	0.20 ± 0.12	SMC	Cenko et al. (2009)
060908	1.8836	0.01 ± 0.15	LMC	Kann et al. (2008)
061007	1.261	0.48 ± 0.19	SMC	Mundell et al. (2007)
061126	1.1588	0	SMC	Perley et al. (2008b)
070110	2.352	0.08	SMC	Troja et al. (2007)
070125	1.547	0.139 ± 0.041	SMC	Updike et al. (2008)
070208	1.165	1.03 ± 0.09	SMC	Cenko et al. (2009)
070306	1.49594	5.5 ± 0.6	SMC	Jaunsen et al. (2008)
070419A	0.97	1.03 ± 0.17	SMC	Cenko et al. (2009)
071003	1.60435	0.43 ± 0.35	LMC	Kann et al. (2008)
071010A	0.98	0.64 ± 0.09	SMC	Kann et al. (2008)
071031	2.692	0	none	Kann et al. (2008)
071112C	0.823	0.23 ± 0.21	SMC	Kann et al. (2008)
071122	1.14	0.58 ± 0.05	SMC	Cenko et al. (2009)
080210	2.641	0.71 ± 0.15	LMC	Kann et al. (2008)
080310	2.42	0.19 ± 0.05	SMC	Kann et al. (2008)
080319B	0.937	0.07 ± 0.06	SMC	Bloom et al. (2009)
080319C	1.95	0.67 ± 0.06	all	Cenko et al. (2009)
080330	1.51	0	none	Cenko et al. (2009)
080514B	1.8 ± 0.4	0	all	Rossi et al. (2008)
080607	3.0363	3.2 ± 0.5	F&M	Prochaska et al. (2009)
080913	6.695	0	all	Greiner et al. (2009b)
080916C	4.35	0	SMC	Greiner et al. (2009a)
090313	3.375	0.63	SMC	Updike et al., in prep
090328	0.736	0.19 ± 0.23	MW	Kann et al. (2008)
090424	0.544	0.50 ± 0.12	LMC	Kann et al. (2008)

Appendix C

Original Programs

This Appendix contains the original programs written to model dust extinction, galaxy evolution, and to fit the dust extinction curves to the SED data.

The first two programs, qsil7.pro and qgra6.pro, use the silicate and graphite optical properties given by (Draine & Lee, 1984) and (Draine, 1985) to calculate the scattering properties of the materials using scattering theory given by Wickramasinghe (1973) and van de Hulst (1957). The full calculation is given in Section —.

The third program, sed_kann.pro, fits the dust extinction curves calculated by qsil7.pro and qgra6.pro to the SED data using a χ^2 minimization routine.

The fourth program, au_bin.pro, produces the binned plots featured in the Conclusions.

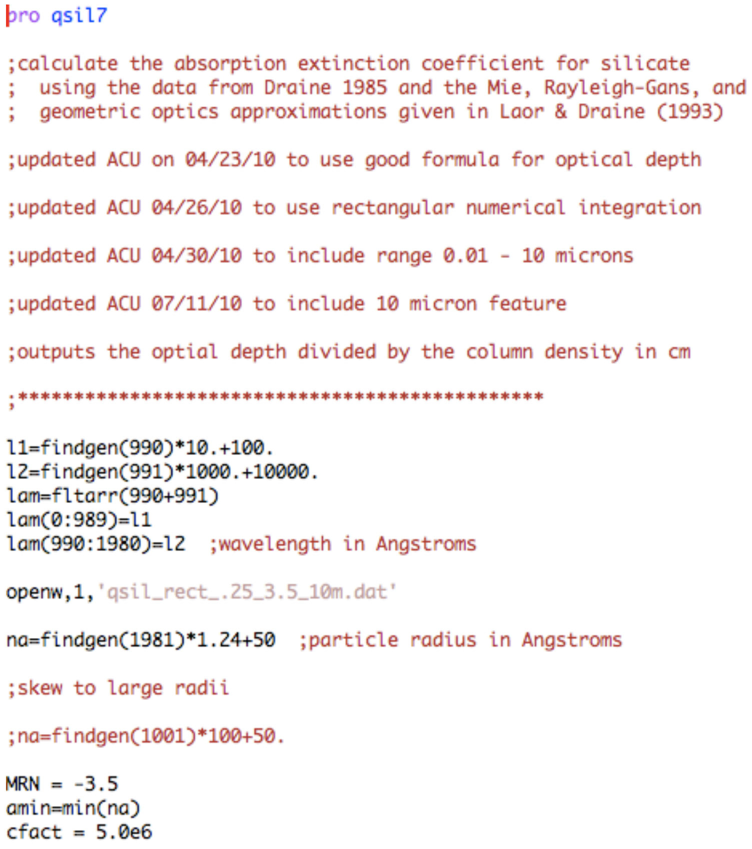

```
pro qsil7

;calculate the absorption extinction coefficient for silicate
;  using the data from Draine 1985 and the Mie, Rayleigh-Gans, and
;  geometric optics approximations given in Laor & Draine (1993)

;updated ACU on 04/23/10 to use good formula for optical depth

;updated ACU 04/26/10 to use rectangular numerical integration

;updated ACU 04/30/10 to include range 0.01 - 10 microns

;updated ACU 07/11/10 to include 10 micron feature

;outputs the optial depth divided by the column density in cm

;**********************************************

l1=findgen(990)*10.+100.
l2=findgen(991)*1000.+10000.
lam=fltarr(990+991)
lam(0:989)=l1
lam(990:1980)=l2  ;wavelength in Angstroms

openw,1,'qsil_rect_.25_3.5_10m.dat'

na=findgen(1981)*1.24+50  ;particle radius in Angstroms

;skew to large radii

;na=findgen(1001)*100+50.

MRN = -3.5
amin=min(na)
cfact = 5.0e6
```

Figure C.1: QSIL7.pro, page 1.

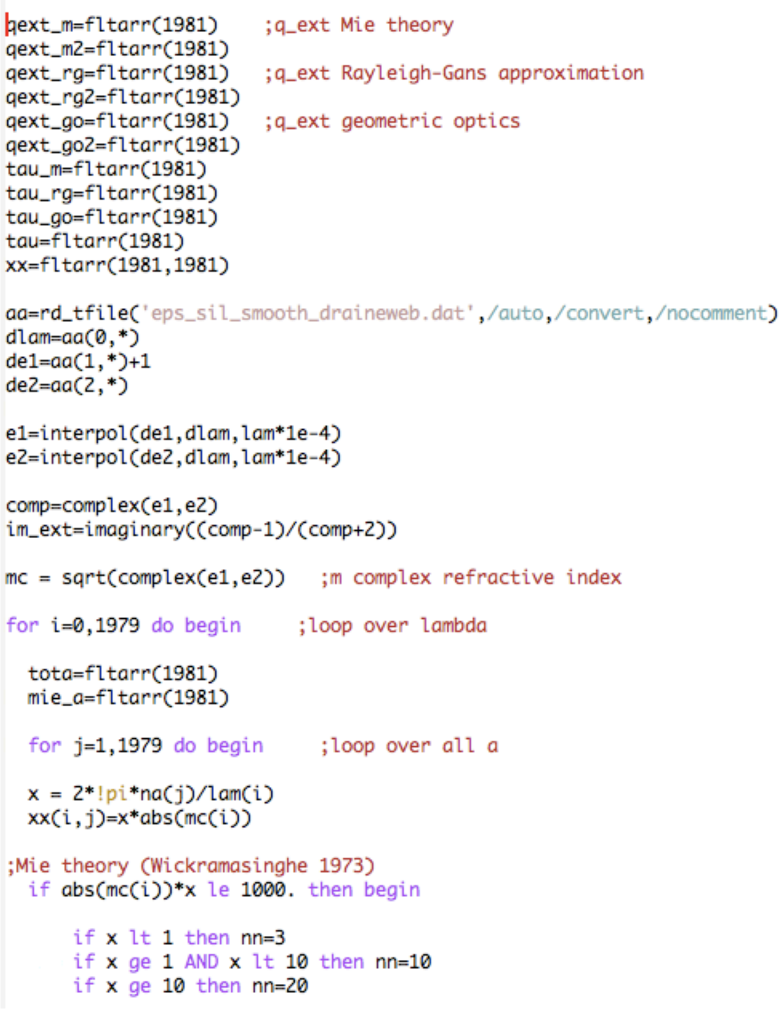

```
qext_m=fltarr(1981)     ;q_ext Mie theory
qext_m2=fltarr(1981)
qext_rg=fltarr(1981)    ;q_ext Rayleigh-Gans approximation
qext_rg2=fltarr(1981)
qext_go=fltarr(1981)    ;q_ext geometric optics
qext_go2=fltarr(1981)
tau_m=fltarr(1981)
tau_rg=fltarr(1981)
tau_go=fltarr(1981)
tau=fltarr(1981)
xx=fltarr(1981,1981)

aa=rd_tfile('eps_sil_smooth_draineweb.dat',/auto,/convert,/nocomment)
dlam=aa(0,*)
de1=aa(1,*)+1
de2=aa(2,*)

e1=interpol(de1,dlam,lam*1e-4)
e2=interpol(de2,dlam,lam*1e-4)

comp=complex(e1,e2)
im_ext=imaginary((comp-1)/(comp+2))

mc = sqrt(complex(e1,e2))   ;m complex refractive index

for i=0,1979 do begin     ;loop over lambda

  tota=fltarr(1981)
  mie_a=fltarr(1981)

  for j=1,1979 do begin     ;loop over all a

  x = 2*!pi*na(j)/lam(i)
  xx(i,j)=x*abs(mc(i))

;Mie theory (Wickramasinghe 1973)
  if abs(mc(i))*x le 1000. then begin

      if x lt 1 then nn=3
      if x ge 1 AND x lt 10 then nn=10
      if x ge 10 then nn=20
```

Figure C.2: QSIL7.pro, page 2.

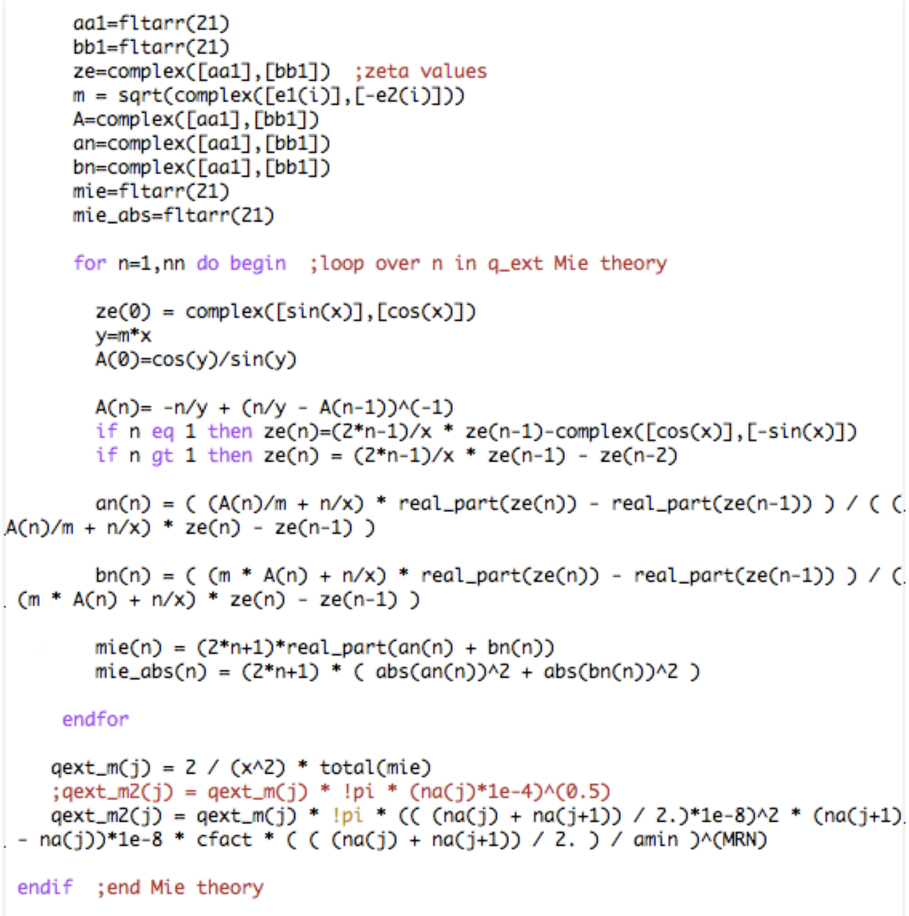

```
      aa1=fltarr(21)
      bb1=fltarr(21)
      ze=complex([aa1],[bb1])  ;zeta values
      m = sqrt(complex([e1(i)],[-e2(i)]))
      A=complex([aa1],[bb1])
      an=complex([aa1],[bb1])
      bn=complex([aa1],[bb1])
      mie=fltarr(21)
      mie_abs=fltarr(21)

      for n=1,nn do begin  ;loop over n in q_ext Mie theory

        ze(0) = complex([sin(x)],[cos(x)])
        y=m*x
        A(0)=cos(y)/sin(y)

        A(n)= -n/y + (n/y - A(n-1))^(-1)
        if n eq 1 then ze(n)=(2*n-1)/x * ze(n-1)-complex([cos(x)],[-sin(x)])
        if n gt 1 then ze(n) = (2*n-1)/x * ze(n-1) - ze(n-2)

        an(n) = ( (A(n)/m + n/x) * real_part(ze(n)) - real_part(ze(n-1)) ) / ( (.
A(n)/m + n/x) * ze(n) - ze(n-1) )

        bn(n) = ( (m * A(n) + n/x) * real_part(ze(n)) - real_part(ze(n-1)) ) / (.
. (m * A(n) + n/x) * ze(n) - ze(n-1) )

        mie(n) = (2*n+1)*real_part(an(n) + bn(n))
        mie_abs(n) = (2*n+1) * ( abs(an(n))^2 + abs(bn(n))^2 )

     endfor

    qext_m(j) = 2 / (x^2) * total(mie)
    ;qext_m2(j) = qext_m(j) * !pi * (na(j)*1e-4)^(0.5)
    qext_m2(j) = qext_m(j) * !pi * (( (na(j) + na(j+1)) / 2.)*1e-8)^2 * (na(j+1).
. - na(j))*1e-8 * cfact * ( ( (na(j) + na(j+1)) / 2. ) / amin )^(MRN)

 endif  ;end Mie theory
```

Figure C.3: QSIL7.pro, page 3.

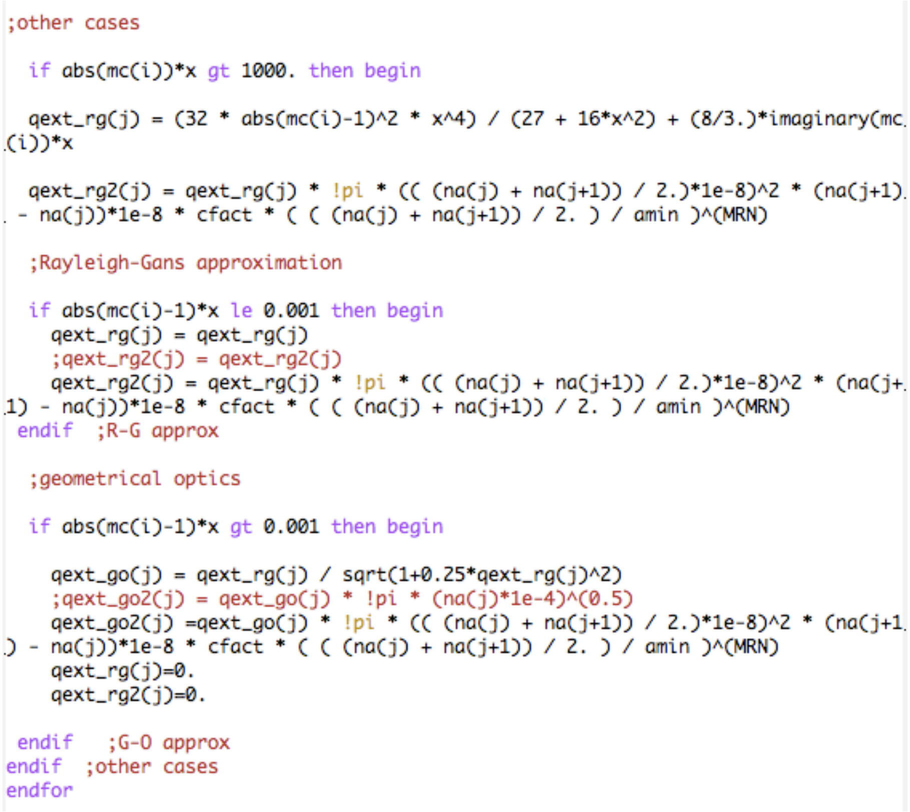

```
;other cases

  if abs(mc(i))*x gt 1000. then begin

  qext_rg(j) = (32 * abs(mc(i)-1)^2 * x^4) / (27 + 16*x^2) + (8/3.)*imaginary(mc.
.(i))*x

  qext_rg2(j) = qext_rg(j) * !pi * (( (na(j) + na(j+1)) / 2.)*1e-8)^2 * (na(j+1).
. - na(j))*1e-8 * cfact * ( ( (na(j) + na(j+1)) / 2. ) / amin )^(MRN)

  ;Rayleigh-Gans approximation

  if abs(mc(i)-1)*x le 0.001 then begin
    qext_rg(j) = qext_rg(j)
    ;qext_rg2(j) = qext_rg2(j)
    qext_rg2(j) = qext_rg(j) * !pi * (( (na(j) + na(j+1)) / 2.)*1e-8)^2 * (na(j+.
.1) - na(j))*1e-8 * cfact * ( ( (na(j) + na(j+1)) / 2. ) / amin )^(MRN)
 endif  ;R-G approx

  ;geometrical optics

  if abs(mc(i)-1)*x gt 0.001 then begin

    qext_go(j) = qext_rg(j) / sqrt(1+0.25*qext_rg(j)^2)
    ;qext_go2(j) = qext_go(j) * !pi * (na(j)*1e-4)^(0.5)
    qext_go2(j) =qext_go(j) * !pi * (( (na(j) + na(j+1)) / 2.)*1e-8)^2 * (na(j+1.
.) - na(j))*1e-8 * cfact * ( ( (na(j) + na(j+1)) / 2. ) / amin )^(MRN)
    qext_rg(j)=0.
    qext_rg2(j)=0.

 endif   ;G-O approx
endif  ;other cases
endfor
```

Figure C.4: QSIL7.pro, page 4.

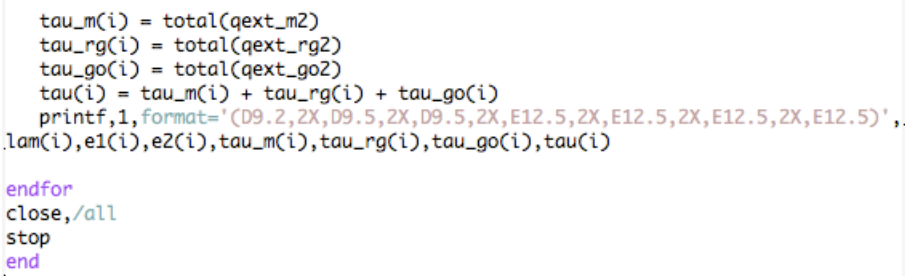

```
   tau_m(i) = total(qext_m2)
   tau_rg(i) = total(qext_rg2)
   tau_go(i) = total(qext_go2)
   tau(i) = tau_m(i) + tau_rg(i) + tau_go(i)
   printf,1,format='(D9.2,2X,D9.5,2X,D9.5,2X,E12.5,2X,E12.5,2X,E12.5,2X,E12.5)',.
.lam(i),e1(i),e2(i),tau_m(i),tau_rg(i),tau_go(i),tau(i)

endfor
close,/all
stop
end
```

Figure C.5: QSIL7.pro, page 5.

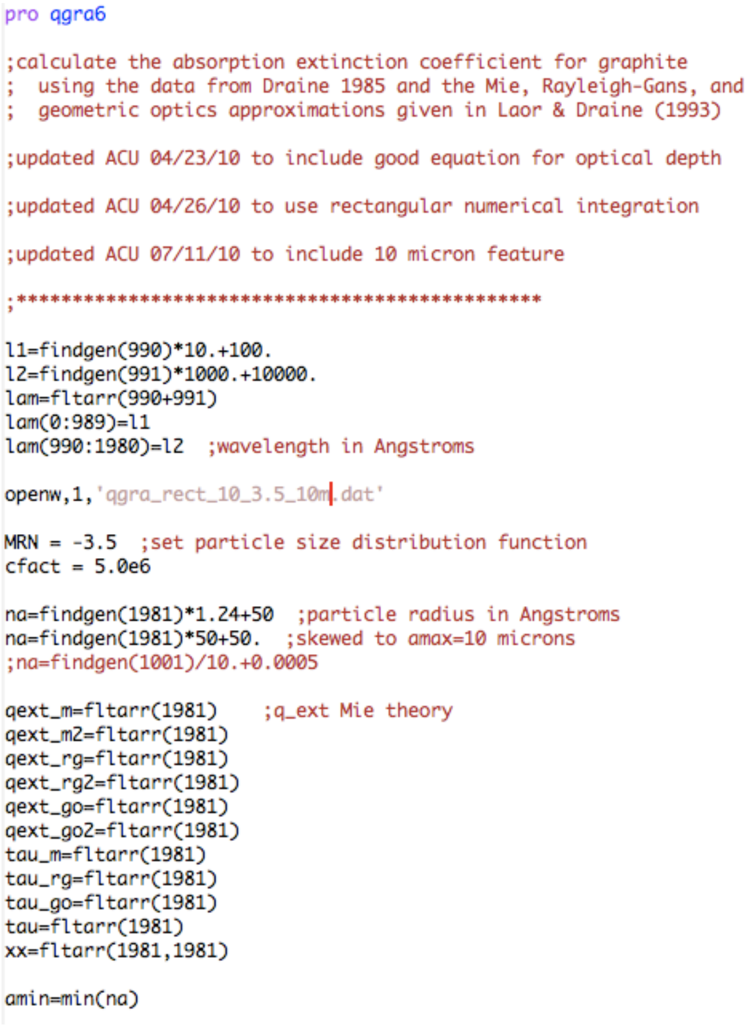

```
pro qgra6

;calculate the absorption extinction coefficient for graphite
;  using the data from Draine 1985 and the Mie, Rayleigh-Gans, and
;  geometric optics approximations given in Laor & Draine (1993)

;updated ACU 04/23/10 to include good equation for optical depth

;updated ACU 04/26/10 to use rectangular numerical integration

;updated ACU 07/11/10 to include 10 micron feature

;***********************************************

l1=findgen(990)*10.+100.
l2=findgen(991)*1000.+10000.
lam=fltarr(990+991)
lam(0:989)=l1
lam(990:1980)=l2  ;wavelength in Angstroms

openw,1,'qgra_rect_10_3.5_10m.dat'

MRN = -3.5  ;set particle size distribution function
cfact = 5.0e6

na=findgen(1981)*1.24+50  ;particle radius in Angstroms
na=findgen(1981)*50+50.  ;skewed to amax=10 microns
;na=findgen(1001)/10.+0.0005

qext_m=fltarr(1981)    ;q_ext Mie theory
qext_m2=fltarr(1981)
qext_rg=fltarr(1981)
qext_rg2=fltarr(1981)
qext_go=fltarr(1981)
qext_go2=fltarr(1981)
tau_m=fltarr(1981)
tau_rg=fltarr(1981)
tau_go=fltarr(1981)
tau=fltarr(1981)
xx=fltarr(1981,1981)

amin=min(na)
```

Figure C.6: QGRA6.pro, page 1.

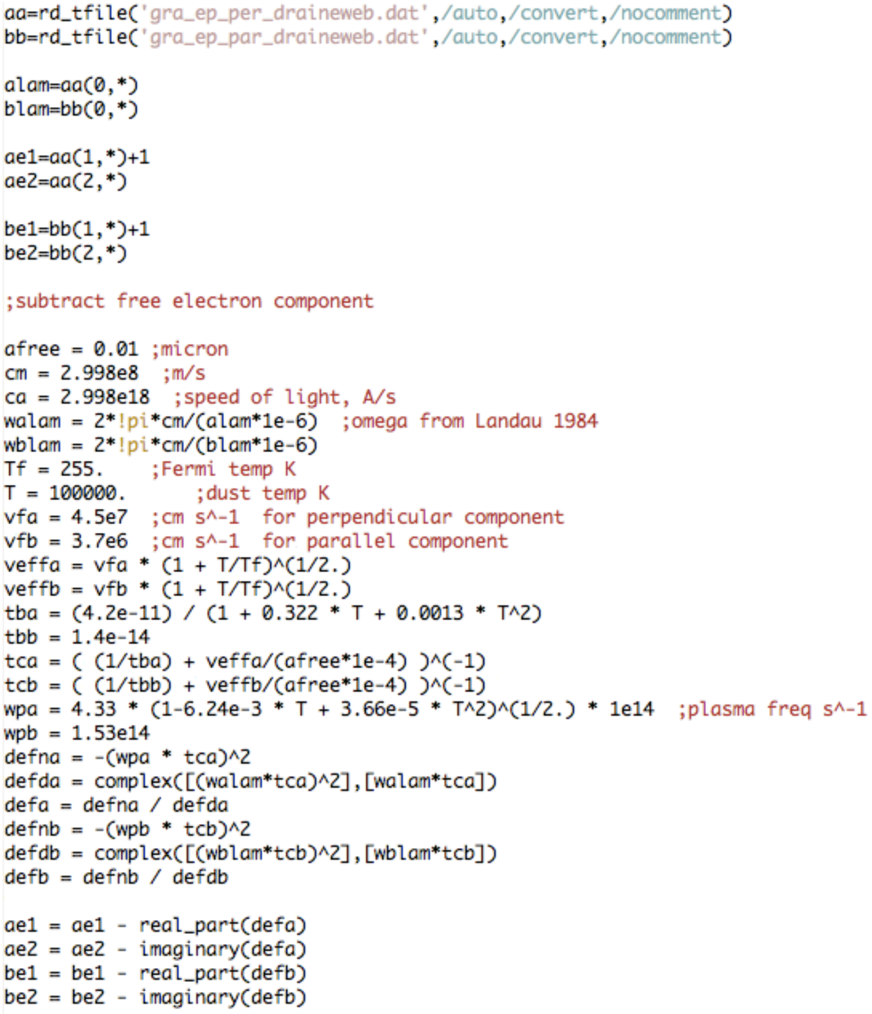

```
aa=rd_tfile('gra_ep_per_draineweb.dat',/auto,/convert,/nocomment)
bb=rd_tfile('gra_ep_par_draineweb.dat',/auto,/convert,/nocomment)

alam=aa(0,*)
blam=bb(0,*)

ae1=aa(1,*)+1
ae2=aa(2,*)

be1=bb(1,*)+1
be2=bb(2,*)

;subtract free electron component

afree = 0.01 ;micron
cm = 2.998e8  ;m/s
ca = 2.998e18  ;speed of light, A/s
walam = 2*!pi*cm/(alam*1e-6)  ;omega from Landau 1984
wblam = 2*!pi*cm/(blam*1e-6)
Tf = 255.    ;Fermi temp K
T = 100000.      ;dust temp K
vfa = 4.5e7  ;cm s^-1  for perpendicular component
vfb = 3.7e6  ;cm s^-1  for parallel component
veffa = vfa * (1 + T/Tf)^(1/2.)
veffb = vfb * (1 + T/Tf)^(1/2.)
tba = (4.2e-11) / (1 + 0.322 * T + 0.0013 * T^2)
tbb = 1.4e-14
tca = ( (1/tba) + veffa/(afree*1e-4) )^(-1)
tcb = ( (1/tbb) + veffb/(afree*1e-4) )^(-1)
wpa = 4.33 * (1-6.24e-3 * T + 3.66e-5 * T^2)^(1/2.) * 1e14  ;plasma freq s^-1
wpb = 1.53e14
defna = -(wpa * tca)^2
defda = complex([(walam*tca)^2],[walam*tca])
defa = defna / defda
defnb = -(wpb * tcb)^2
defdb = complex([(wblam*tcb)^2],[wblam*tcb])
defb = defnb / defdb

ae1 = ae1 - real_part(defa)
ae2 = ae2 - imaginary(defa)
be1 = be1 - real_part(defb)
be2 = be2 - imaginary(defb)
```

Figure C.7: QGRA6.pro, page 2.

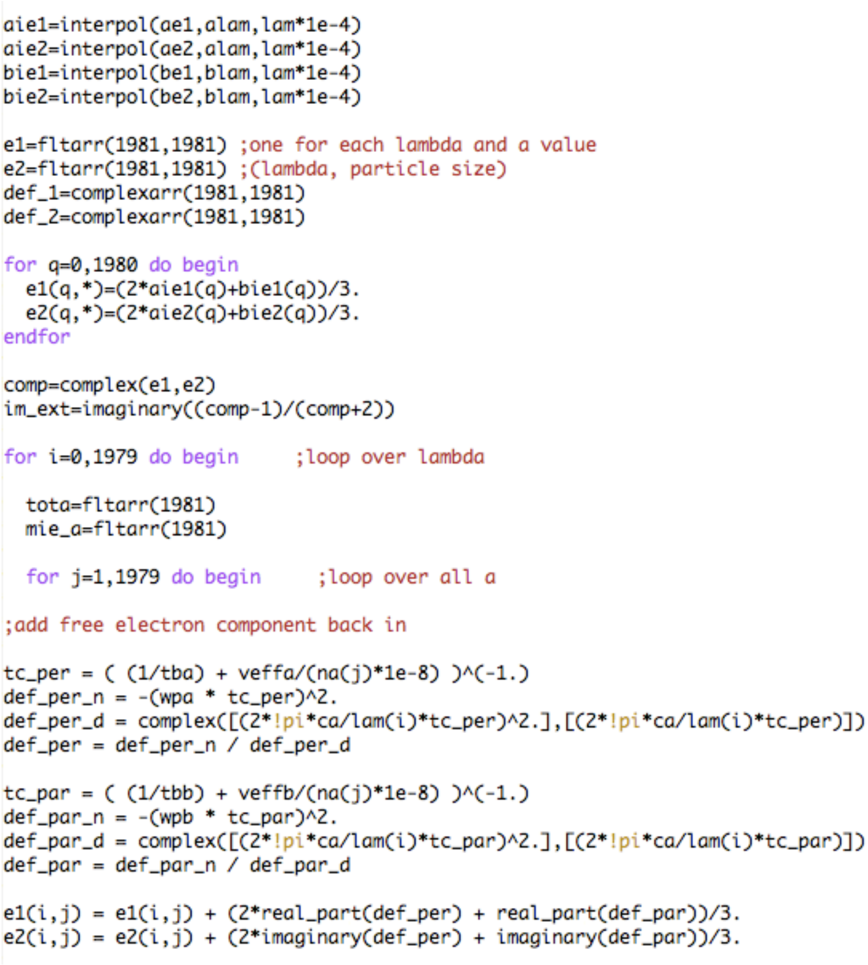

```
aie1=interpol(ae1,alam,lam*1e-4)
aie2=interpol(ae2,alam,lam*1e-4)
bie1=interpol(be1,blam,lam*1e-4)
bie2=interpol(be2,blam,lam*1e-4)

e1=fltarr(1981,1981) ;one for each lambda and a value
e2=fltarr(1981,1981) ;(lambda, particle size)
def_1=complexarr(1981,1981)
def_2=complexarr(1981,1981)

for q=0,1980 do begin
  e1(q,*)=(2*aie1(q)+bie1(q))/3.
  e2(q,*)=(2*aie2(q)+bie2(q))/3.
endfor

comp=complex(e1,e2)
im_ext=imaginary((comp-1)/(comp+2))

for i=0,1979 do begin     ;loop over lambda

  tota=fltarr(1981)
  mie_a=fltarr(1981)

  for j=1,1979 do begin     ;loop over all a

;add free electron component back in

tc_per = ( (1/tba) + veffa/(na(j)*1e-8) )^(-1.)
def_per_n = -(wpa * tc_per)^2.
def_per_d = complex([(2*!pi*ca/lam(i)*tc_per)^2.],[(2*!pi*ca/lam(i)*tc_per)])
def_per = def_per_n / def_per_d

tc_par = ( (1/tbb) + veffb/(na(j)*1e-8) )^(-1.)
def_par_n = -(wpb * tc_par)^2.
def_par_d = complex([(2*!pi*ca/lam(i)*tc_par)^2.],[(2*!pi*ca/lam(i)*tc_par)])
def_par = def_par_n / def_par_d

e1(i,j) = e1(i,j) + (2*real_part(def_per) + real_part(def_par))/3.
e2(i,j) = e2(i,j) + (2*imaginary(def_per) + imaginary(def_par))/3.
```

Figure C.8: QGRA6.pro, page 3.

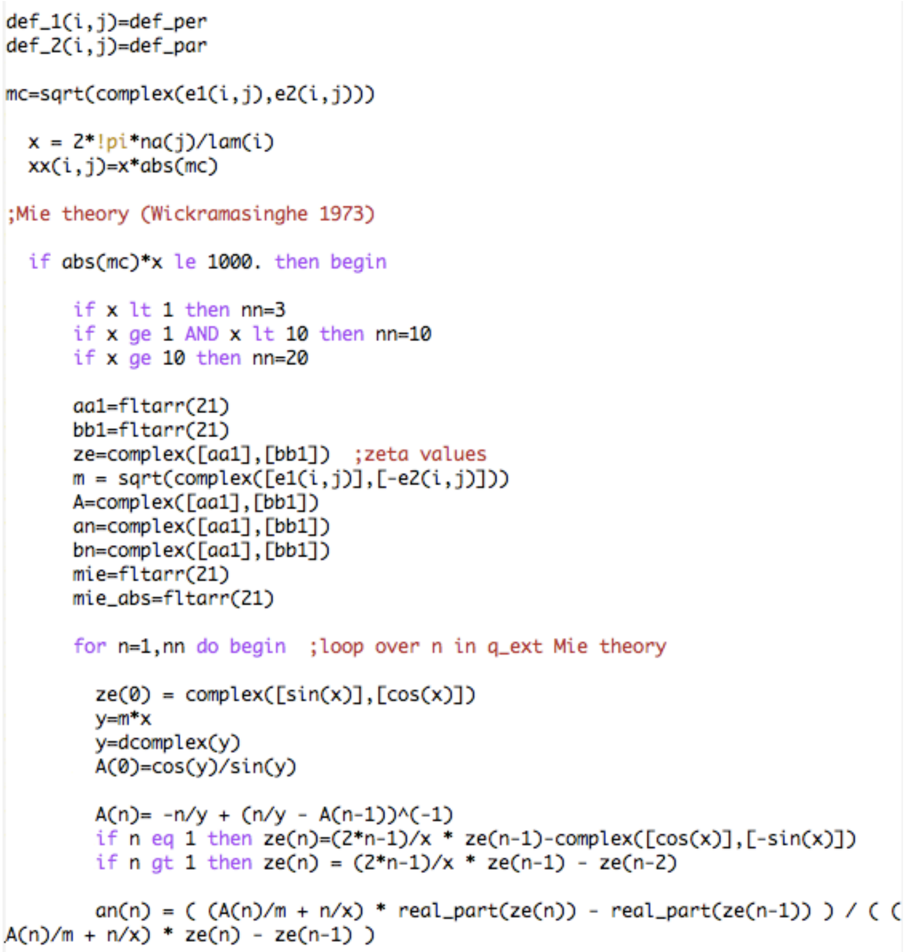

```
def_1(i,j)=def_per
def_2(i,j)=def_par

mc=sqrt(complex(e1(i,j),e2(i,j)))

  x = 2*!pi*na(j)/lam(i)
  xx(i,j)=x*abs(mc)

;Mie theory (Wickramasinghe 1973)

  if abs(mc)*x le 1000. then begin

      if x lt 1 then nn=3
      if x ge 1 AND x lt 10 then nn=10
      if x ge 10 then nn=20

      aa1=fltarr(21)
      bb1=fltarr(21)
      ze=complex([aa1],[bb1])  ;zeta values
      m = sqrt(complex([e1(i,j)],[-e2(i,j)]))
      A=complex([aa1],[bb1])
      an=complex([aa1],[bb1])
      bn=complex([aa1],[bb1])
      mie=fltarr(21)
      mie_abs=fltarr(21)

      for n=1,nn do begin  ;loop over n in q_ext Mie theory

        ze(0) = complex([sin(x)],[cos(x)])
        y=m*x
        y=dcomplex(y)
        A(0)=cos(y)/sin(y)

        A(n)= -n/y + (n/y - A(n-1))^(-1)
        if n eq 1 then ze(n)=(2*n-1)/x * ze(n-1)-complex([cos(x)],[-sin(x)])
        if n gt 1 then ze(n) = (2*n-1)/x * ze(n-1) - ze(n-2)

        an(n) = ( (A(n)/m + n/x) * real_part(ze(n)) - real_part(ze(n-1)) ) / ( (
A(n)/m + n/x) * ze(n) - ze(n-1) )
```

Figure C.9: QGRA6.pro, page 4.

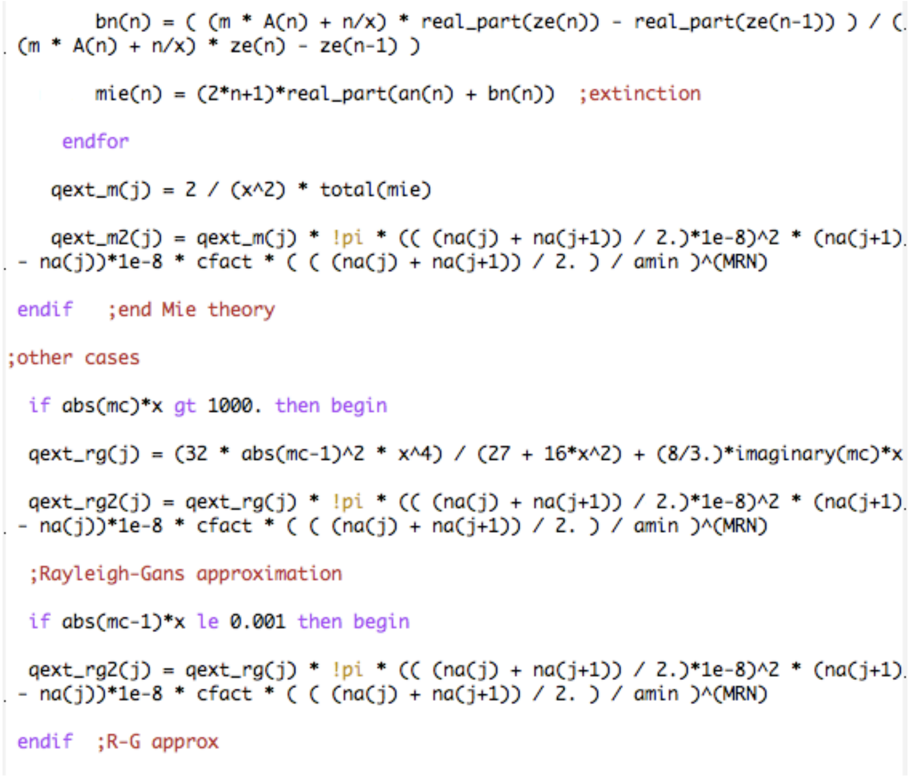

```
        bn(n) = ( (m * A(n) + n/x) * real_part(ze(n)) - real_part(ze(n-1)) ) / (.
. (m * A(n) + n/x) * ze(n) - ze(n-1) )

        mie(n) = (2*n+1)*real_part(an(n) + bn(n))  ;extinction

     endfor

    qext_m(j) = 2 / (x^2) * total(mie)

    qext_m2(j) = qext_m(j) * !pi * (( (na(j) + na(j+1)) / 2.)*1e-8)^2 * (na(j+1).
. - na(j))*1e-8 * cfact * ( ( (na(j) + na(j+1)) / 2. ) / amin )^(MRN)

 endif   ;end Mie theory

;other cases

  if abs(mc)*x gt 1000. then begin

  qext_rg(j) = (32 * abs(mc-1)^2 * x^4) / (27 + 16*x^2) + (8/3.)*imaginary(mc)*x

  qext_rg2(j) = qext_rg(j) * !pi * (( (na(j) + na(j+1)) / 2.)*1e-8)^2 * (na(j+1).
. - na(j))*1e-8 * cfact * ( ( (na(j) + na(j+1)) / 2. ) / amin )^(MRN)

  ;Rayleigh-Gans approximation

  if abs(mc-1)*x le 0.001 then begin

  qext_rg2(j) = qext_rg(j) * !pi * (( (na(j) + na(j+1)) / 2.)*1e-8)^2 * (na(j+1).
. - na(j))*1e-8 * cfact * ( ( (na(j) + na(j+1)) / 2. ) / amin )^(MRN)

 endif  ;R-G approx
```

Figure C.10: QGRA6.pro, page 5.

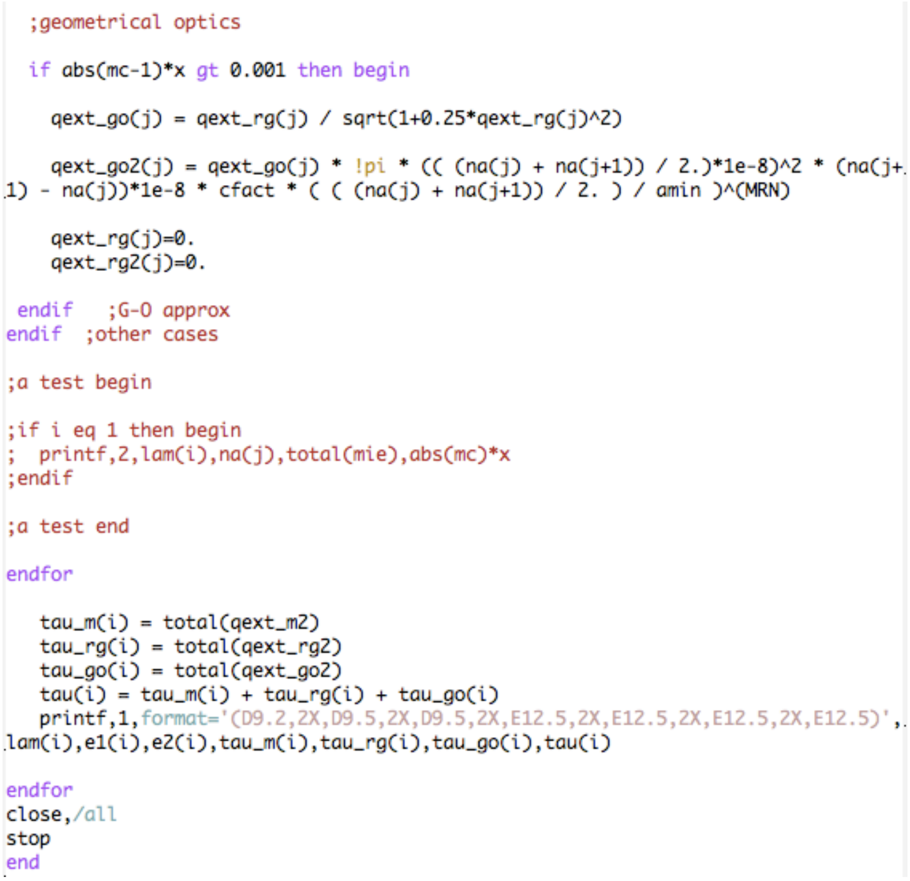

```
  ;geometrical optics

  if abs(mc-1)*x gt 0.001 then begin

    qext_go(j) = qext_rg(j) / sqrt(1+0.25*qext_rg(j)^2)

    qext_go2(j) = qext_go(j) * !pi * (( (na(j) + na(j+1)) / 2.)*1e-8)^2 * (na(j+.
.1) - na(j))*1e-8 * cfact * ( ( (na(j) + na(j+1)) / 2. ) / amin )^(MRN)

    qext_rg(j)=0.
    qext_rg2(j)=0.

 endif   ;G-O approx
endif  ;other cases

;a test begin

;if i eq 1 then begin
;  printf,2,lam(i),na(j),total(mie),abs(mc)*x
;endif

;a test end

endfor

   tau_m(i) = total(qext_m2)
   tau_rg(i) = total(qext_rg2)
   tau_go(i) = total(qext_go2)
   tau(i) = tau_m(i) + tau_rg(i) + tau_go(i)
   printf,1,format='(D9.2,2X,D9.5,2X,D9.5,2X,E12.5,2X,E12.5,2X,E12.5,2X,E12.5)',.
.lam(i),e1(i),e2(i),tau_m(i),tau_rg(i),tau_go(i),tau(i)

endfor
close,/all
stop
end
```

Figure C.11: QGRA6.pro, page 6.

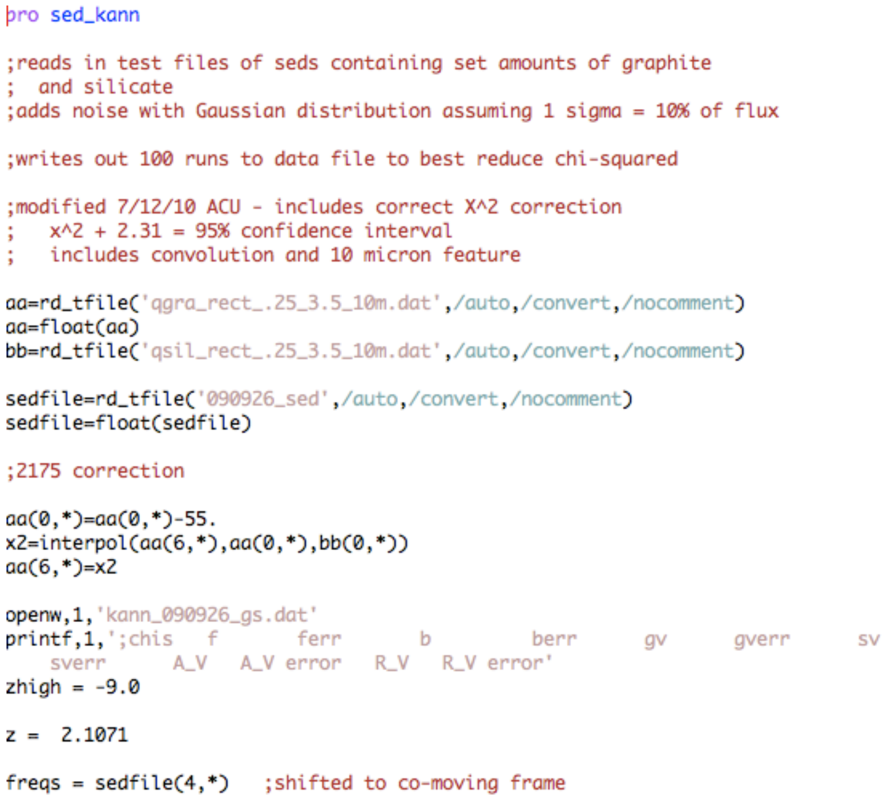

```
pro sed_kann

;reads in test files of seds containing set amounts of graphite
;  and silicate
;adds noise with Gaussian distribution assuming 1 sigma = 10% of flux

;writes out 100 runs to data file to best reduce chi-squared

;modified 7/12/10 ACU - includes correct X^2 correction
;   x^2 + 2.31 = 95% confidence interval
;   includes convolution and 10 micron feature

aa=rd_tfile('qgra_rect_.25_3.5_10m.dat',/auto,/convert,/nocomment)
aa=float(aa)
bb=rd_tfile('qsil_rect_.25_3.5_10m.dat',/auto,/convert,/nocomment)

sedfile=rd_tfile('090926_sed',/auto,/convert,/nocomment)
sedfile=float(sedfile)

;2175 correction

aa(0,*)=aa(0,*)-55.
x2=interpol(aa(6,*),aa(0,*),bb(0,*))
aa(6,*)=x2

openw,1,'kann_090926_gs.dat'
printf,1,';chis   f       ferr        b          berr      gv      gverr      sv
    sverr      A_V   A_V error   R_V   R_V error'
zhigh = -9.0

z =  2.1071

freqs = sedfile(4,*)   ;shifted to co-moving frame
```

Figure C.12: SED_KANN.pro, page 1.

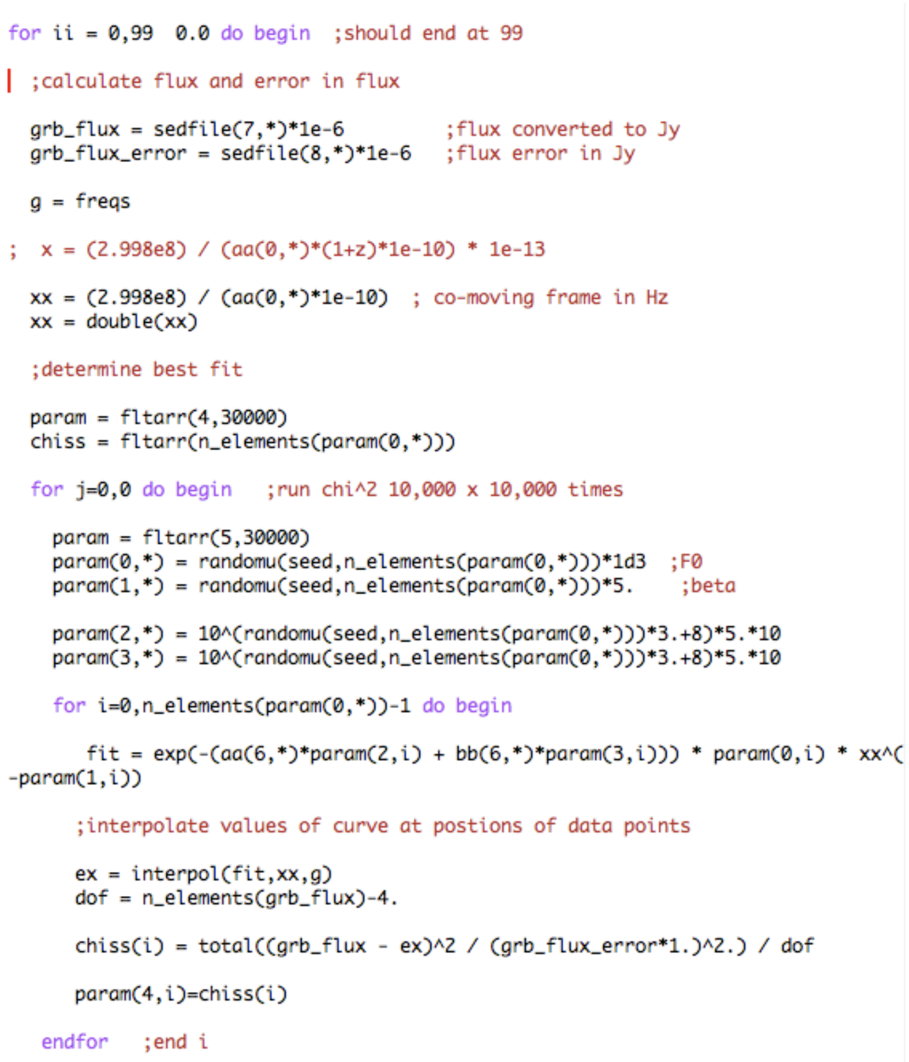

```
for ii = 0,99  0.0 do begin  ;should end at 99

  ;calculate flux and error in flux

  grb_flux = sedfile(7,*)*1e-6         ;flux converted to Jy
  grb_flux_error = sedfile(8,*)*1e-6   ;flux error in Jy

  g = freqs

;  x = (2.998e8) / (aa(0,*)*(1+z)*1e-10) * 1e-13

  xx = (2.998e8) / (aa(0,*)*1e-10)  ; co-moving frame in Hz
  xx = double(xx)

  ;determine best fit

  param = fltarr(4,30000)
  chiss = fltarr(n_elements(param(0,*)))

  for j=0,0 do begin   ;run chi^2 10,000 x 10,000 times

    param = fltarr(5,30000)
    param(0,*) = randomu(seed,n_elements(param(0,*)))*1d3  ;F0
    param(1,*) = randomu(seed,n_elements(param(0,*)))*5.    ;beta

    param(2,*) = 10^(randomu(seed,n_elements(param(0,*)))*3.+8)*5.*10
    param(3,*) = 10^(randomu(seed,n_elements(param(0,*)))*3.+8)*5.*10

    for i=0,n_elements(param(0,*))-1 do begin

       fit = exp(-(aa(6,*)*param(2,i) + bb(6,*)*param(3,i))) * param(0,i) * xx^(
-param(1,i))

      ;interpolate values of curve at postions of data points

      ex = interpol(fit,xx,g)
      dof = n_elements(grb_flux)-4.

      chiss(i) = total((grb_flux - ex)^2 / (grb_flux_error*1.)^2.) / dof

      param(4,i)=chiss(i)

   endfor   ;end i
```

Figure C.13: SED_KANN.pro, page 2.

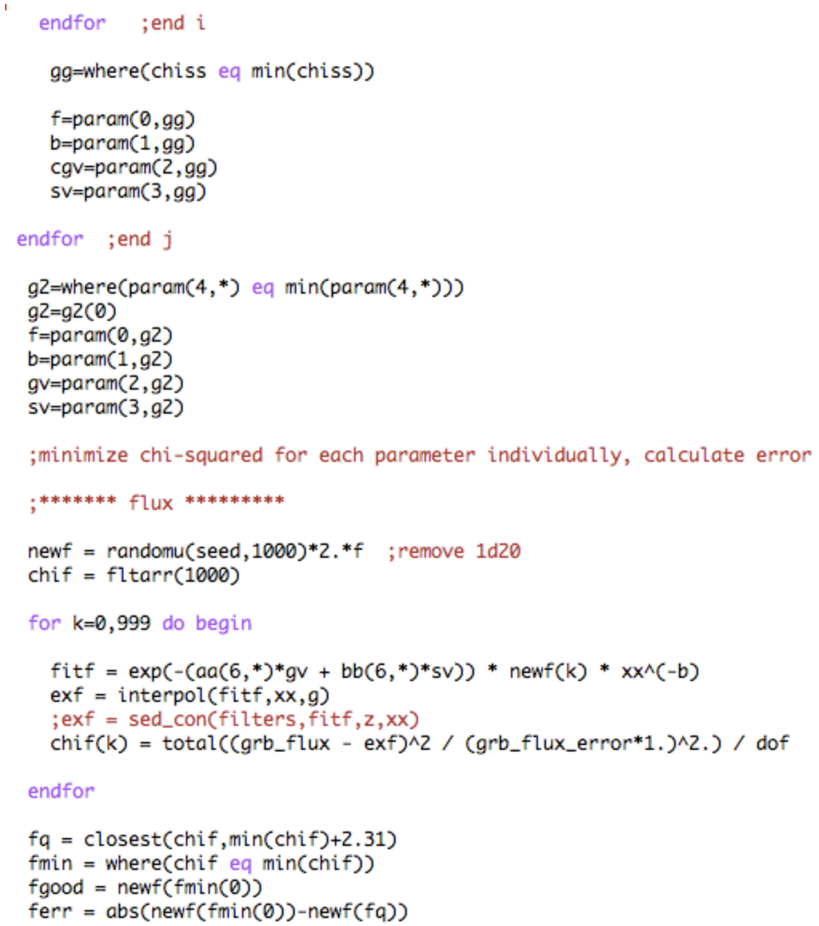

```
  endfor   ;end i

   gg=where(chiss eq min(chiss))

   f=param(0,gg)
   b=param(1,gg)
   cgv=param(2,gg)
   sv=param(3,gg)

endfor  ;end j

 g2=where(param(4,*) eq min(param(4,*)))
 g2=g2(0)
 f=param(0,g2)
 b=param(1,g2)
 gv=param(2,g2)
 sv=param(3,g2)

 ;minimize chi-squared for each parameter individually, calculate error

 ;******* flux *********

 newf = randomu(seed,1000)*2.*f  ;remove 1d20
 chif = fltarr(1000)

 for k=0,999 do begin

   fitf = exp(-(aa(6,*)*gv + bb(6,*)*sv)) * newf(k) * xx^(-b)
   exf = interpol(fitf,xx,g)
   ;exf = sed_con(filters,fitf,z,xx)
   chif(k) = total((grb_flux - exf)^2 / (grb_flux_error*1.)^2.) / dof

 endfor

 fq = closest(chif,min(chif)+2.31)
 fmin = where(chif eq min(chif))
 fgood = newf(fmin(0))
 ferr = abs(newf(fmin(0))-newf(fq))
```

Figure C.14: SED_KANN.pro, page 3.

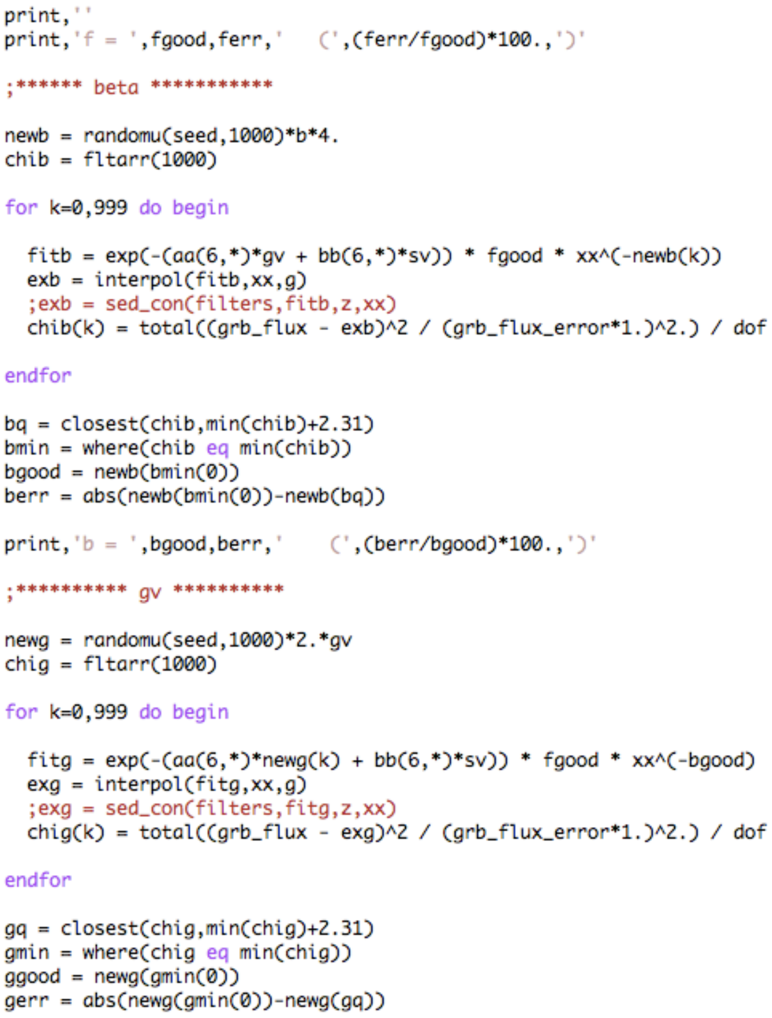

```
print,''
print,'f = ',fgood,ferr,'   (',(ferr/fgood)*100.,')'

;****** beta **********

newb = randomu(seed,1000)*b*4.
chib = fltarr(1000)

for k=0,999 do begin

  fitb = exp(-(aa(6,*)*gv + bb(6,*)*sv)) * fgood * xx^(-newb(k))
  exb = interpol(fitb,xx,g)
  ;exb = sed_con(filters,fitb,z,xx)
  chib(k) = total((grb_flux - exb)^2 / (grb_flux_error*1.)^2.) / dof

endfor

bq = closest(chib,min(chib)+2.31)
bmin = where(chib eq min(chib))
bgood = newb(bmin(0))
berr = abs(newb(bmin(0))-newb(bq))

print,'b = ',bgood,berr,'    (',(berr/bgood)*100.,')'

;********* gv *********

newg = randomu(seed,1000)*2.*gv
chig = fltarr(1000)

for k=0,999 do begin

  fitg = exp(-(aa(6,*)*newg(k) + bb(6,*)*sv)) * fgood * xx^(-bgood)
  exg = interpol(fitg,xx,g)
  ;exg = sed_con(filters,fitg,z,xx)
  chig(k) = total((grb_flux - exg)^2 / (grb_flux_error*1.)^2.) / dof

endfor

gq = closest(chig,min(chig)+2.31)
gmin = where(chig eq min(chig))
ggood = newg(gmin(0))
gerr = abs(newg(gmin(0))-newg(gq))
```

Figure C.15: SED_KANN.pro, page 4.

```
  print,'gv = ',ggood,gerr,'    (',(gerr/ggood)*100,')'

  ;********** sv **********

  news = randomu(seed,1000)*2.*sv
  chis = fltarr(1000)

  for k=0,999 do begin

    fits = exp(-(aa(6,*)*ggood + bb(6,*)*news(k))) * fgood * xx^(-bgood)
    exs = interpol(fits,xx,g)
    ;exs = sed_con(filters,fits,z,xx)
    chis(k) = total((grb_flux - exs)^2 / (grb_flux_error*1.)^2.) / dof

  endfor

  sq = closest(chis,min(chis)+2.31)
  smin = where(chis eq min(chis))
  sgood = news(smin(0))
  serr = abs(news(smin(0))-news(sq))

  print,'sv = ',sgood,serr,'   (',(serr/sgood)*100.,')'
  print,''


  ;************************

;min(g)-1e14
  plot,g,grb_flux,/xlog,/ylog,psym=2,charsize=2,xrange=[min(g)-1e14,max(g)+1e15]
,xstyle=1,yrange=[5e-5,0.0007],ystyle=1
  errplot,g,grb_flux-grb_flux_error*1.,grb_flux+grb_flux_error*1.
  fitplot=exp(-(aa(6,*)*ggood + bb(6,*)*sgood)) * fgood * xx^(-bgood)
  oplot,xx,fitplot,thick=1

  print,''
  print,'overall dust column density = ',sgood+ggood
  print,''

  print,'Chi-squared = ',min(chis)
```

Figure C.16: SED_KANN.pro, page 5.

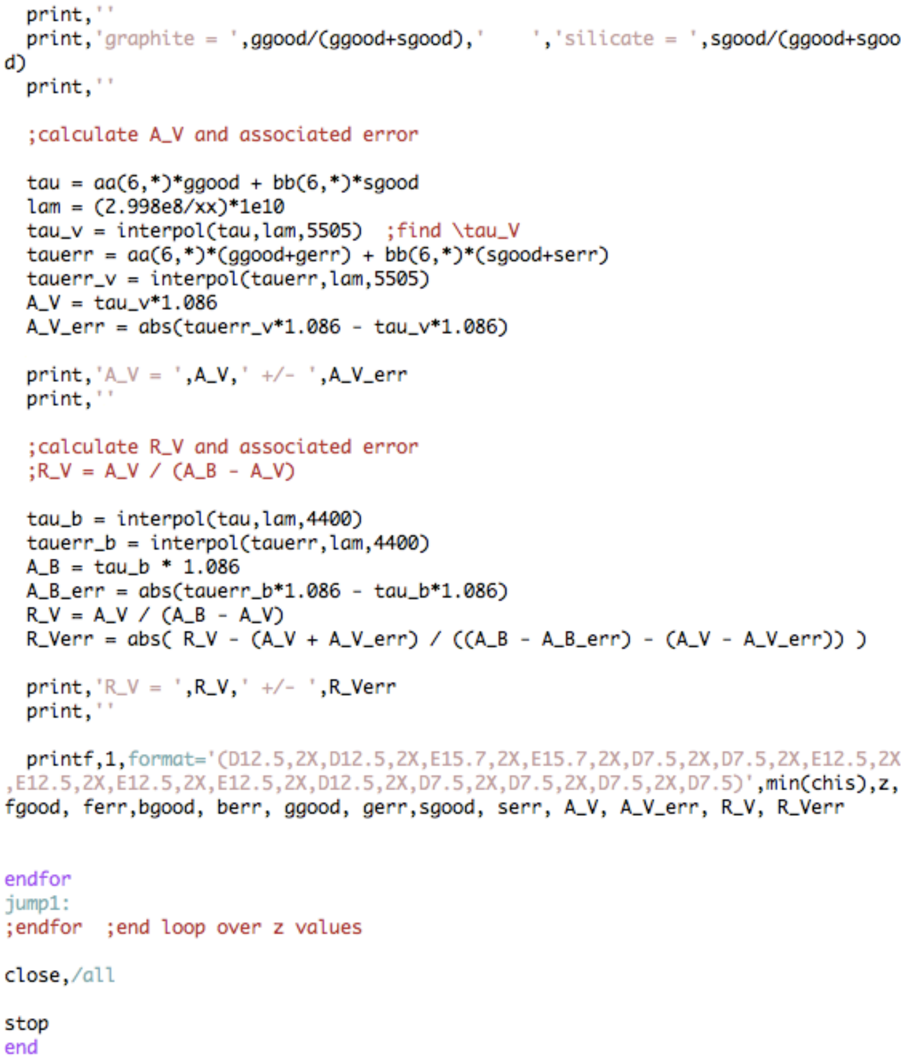

```
  print,''
  print,'graphite = ',ggood/(ggood+sgood),'    ','silicate = ',sgood/(ggood+sgoo
d)
  print,''

  ;calculate A_V and associated error

  tau = aa(6,*)*ggood + bb(6,*)*sgood
  lam = (2.998e8/xx)*1e10
  tau_v = interpol(tau,lam,5505)  ;find \tau_V
  tauerr = aa(6,*)*(ggood+gerr) + bb(6,*)*(sgood+serr)
  tauerr_v = interpol(tauerr,lam,5505)
  A_V = tau_v*1.086
  A_V_err = abs(tauerr_v*1.086 - tau_v*1.086)

  print,'A_V = ',A_V,' +/- ',A_V_err
  print,''

  ;calculate R_V and associated error
  ;R_V = A_V / (A_B - A_V)

  tau_b = interpol(tau,lam,4400)
  tauerr_b = interpol(tauerr,lam,4400)
  A_B = tau_b * 1.086
  A_B_err = abs(tauerr_b*1.086 - tau_b*1.086)
  R_V = A_V / (A_B - A_V)
  R_Verr = abs( R_V - (A_V + A_V_err) / ((A_B - A_B_err) - (A_V - A_V_err)) )

  print,'R_V = ',R_V,' +/- ',R_Verr
  print,''

  printf,1,format='(D12.5,2X,D12.5,2X,E15.7,2X,E15.7,2X,D7.5,2X,D7.5,2X,E12.5,2X
,E12.5,2X,E12.5,2X,E12.5,2X,D12.5,2X,D7.5,2X,D7.5,2X,D7.5,2X,D7.5)',min(chis),z,
fgood, ferr,bgood, berr, ggood, gerr,sgood, serr, A_V, A_V_err, R_V, R_Verr


endfor
jump1:
;endfor  ;end loop over z values

close,/all

stop
end
```

Figure C.17: SED_KANN.pro, page 6.

```
pro au_bin

aa=rd_tfile('all_seds.dat',/auto,/convert,/nocomment)

z=aa(2,*)
sz=sort(z)

grb=aa(0,sz)
chi=aa(1,sz)
z=aa(2,sz)
f=aa(3,sz)
ferr=aa(4,sz)
b=aa(5,sz)
berr=aa(6,sz)
g=aa(7,sz)
gerr=aa(8,sz)
s=aa(9,sz)
serr=aa(10,sz)
av=aa(11,sz)
averr=aa(12,sz)
rv=aa(13,sz)
rverr=aa(14,sz)
nh=aa(15,sz)
dtg=aa(16,sz)
gs = s
binnum=10
mgs=fltarr(100)
x=fltarr(100)
for j=0,99 do begin
  q=where(z ge j*.1 AND z lt j*.1+1)
  if n_elements(q) ge 5 then begin
    mgs(j)=total(gs(q))/n_elements(q)
    x(j)=total(z(q))/n_elements(q) ;j*.1+0.5
  endif
endfor
y=where(mgs ne 0.0)
plot,x(y),mgs(y),charsize=2,xtitle='!17Redshift',ytitle='!17Power Law Index !8p!
7',thick=2
end
```

Figure C.18: AU_BIN.pro.

```
pro galext

;simulate the position of the Sun in the MW

;physical system MW
;assumes an exponential density profile
;fix offset
;last edited 02/18/2009 ACU

dendistarr=fltarr(2000)

rectcorin=fltarr(10000,3)
rectcoron=fltarr(10000,3)
pl=fltarr(10000)

r2=fltarr(10,2000)
q=0
prevden=0.
tdist=0.

openw,1,'galexp_zall.dat'
printf,1,';exponential dropoff, scale heights 3 kpc, 0.21 kpc'
printf,1,';z     gl   gb   model extinction'

for j=0,1999 do begin   ;choose a random point inside the cylinder

;choose a random redshift, range 0 - 4
;z=randomu(seed)*4
;z=3.5  ;test
zz=mc_madau()
z=zz(1)
;z=0.0

pin=randomu(seed)*2*!pi  ;coordinate phi in radians

;************************** evolve disk radius in time ********************
```

Figure C.19: GALEXT.pro, page 1.

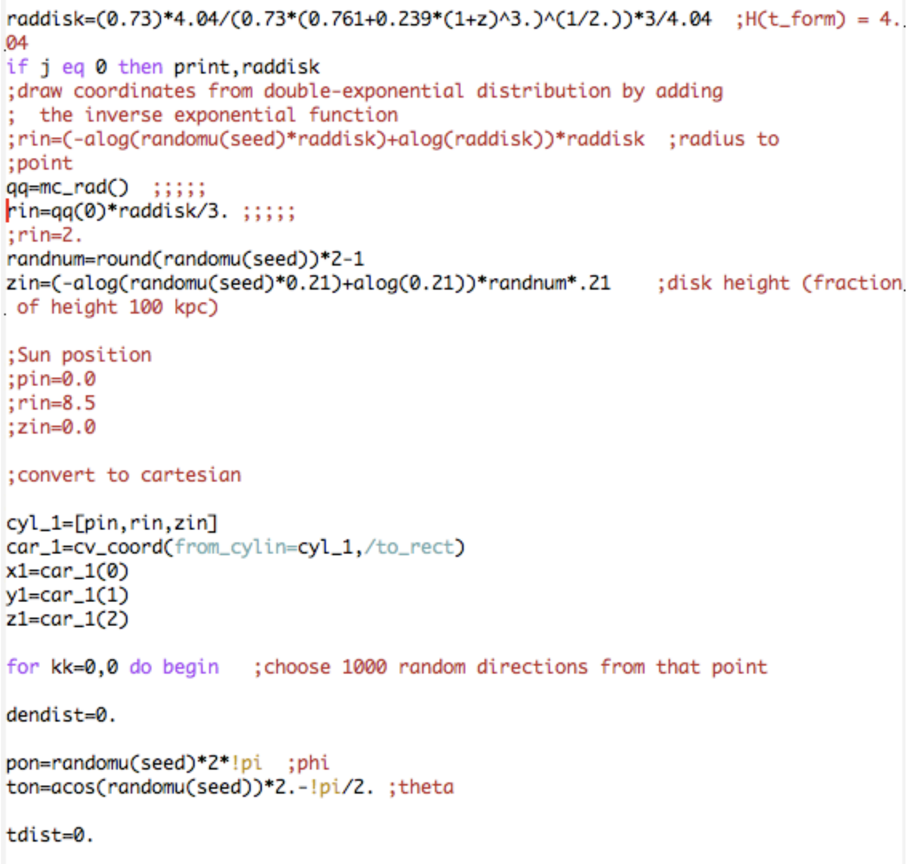

```
raddisk=(0.73)*4.04/(0.73*(0.761+0.239*(1+z)^3.)^(1/2.))*3/4.04  ;H(t_form) = 4.
04
if j eq 0 then print,raddisk
;draw coordinates from double-exponential distribution by adding
;  the inverse exponential function
;rin=(-alog(randomu(seed)*raddisk)+alog(raddisk))*raddisk  ;radius to
;point
qq=mc_rad()  ;;;;;
rin=qq(0)*raddisk/3. ;;;;;
;rin=2.
randnum=round(randomu(seed))*2-1
zin=(-alog(randomu(seed)*0.21)+alog(0.21))*randnum*.21    ;disk height (fraction
 of height 100 kpc)

;Sun position
;pin=0.0
;rin=8.5
;zin=0.0

;convert to cartesian

cyl_1=[pin,rin,zin]
car_1=cv_coord(from_cylin=cyl_1,/to_rect)
x1=car_1(0)
y1=car_1(1)
z1=car_1(2)

for kk=0,0 do begin   ;choose 1000 random directions from that point

dendist=0.

pon=randomu(seed)*2*!pi  ;phi
ton=acos(randomu(seed))*2.-!pi/2. ;theta

tdist=0.
```

Figure C.20: GALEXT.pro, page 2.

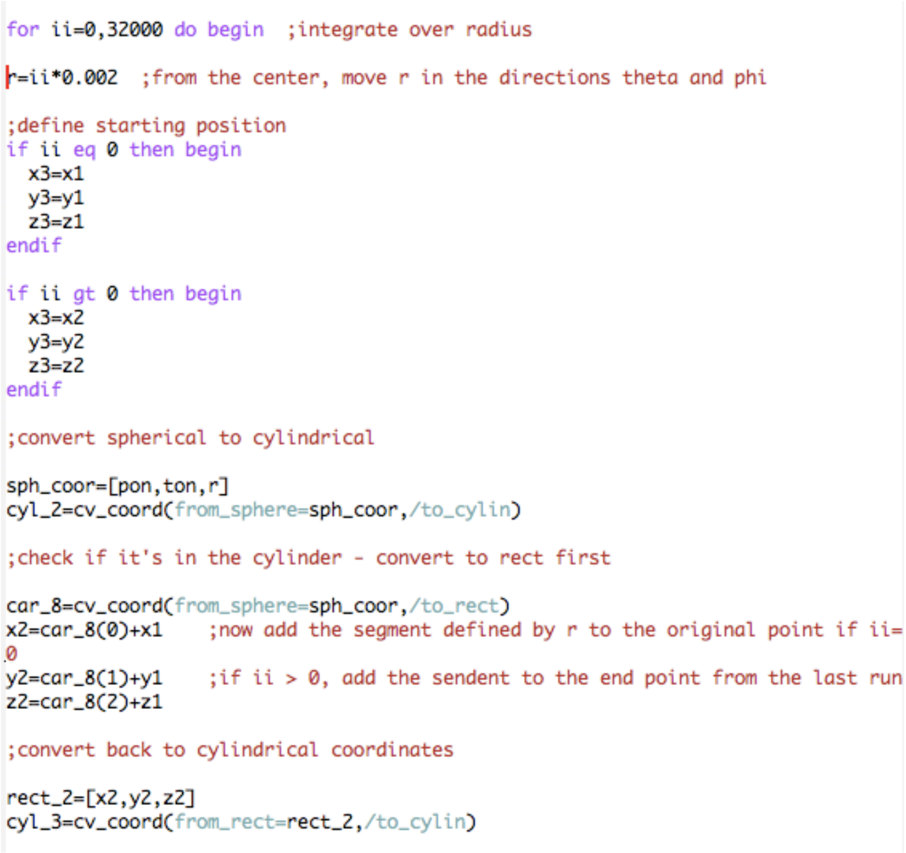

```
for ii=0,32000 do begin  ;integrate over radius

r=ii*0.002  ;from the center, move r in the directions theta and phi

;define starting position
if ii eq 0 then begin
  x3=x1
  y3=y1
  z3=z1
endif

if ii gt 0 then begin
  x3=x2
  y3=y2
  z3=z2
endif

;convert spherical to cylindrical

sph_coor=[pon,ton,r]
cyl_2=cv_coord(from_sphere=sph_coor,/to_cylin)

;check if it's in the cylinder - convert to rect first

car_8=cv_coord(from_sphere=sph_coor,/to_rect)
x2=car_8(0)+x1    ;now add the segment defined by r to the original point if ii=
0
y2=car_8(1)+y1    ;if ii > 0, add the sendent to the end point from the last run
z2=car_8(2)+z1

;convert back to cylindrical coordinates

rect_2=[x2,y2,z2]
cyl_3=cv_coord(from_rect=rect_2,/to_cylin)
```

Figure C.21: GALEXT.pro, page 3.

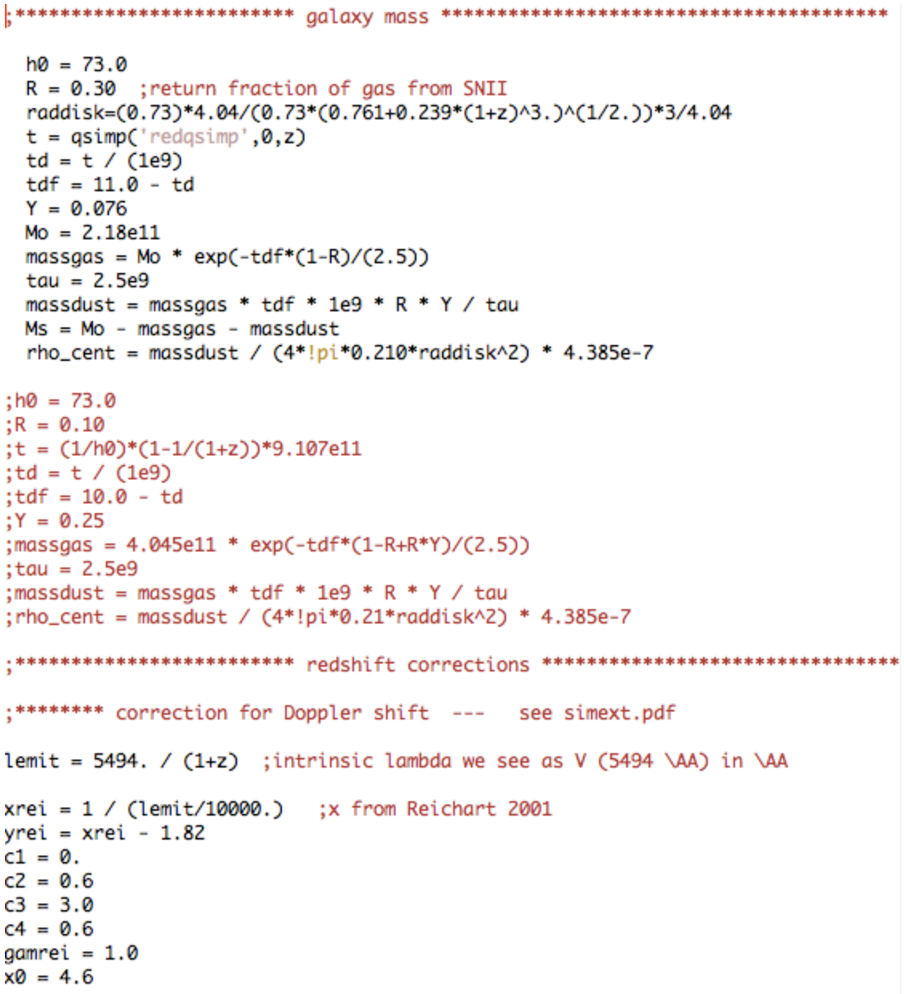

```
;************************* galaxy mass ****************************************

  h0 = 73.0
  R = 0.30  ;return fraction of gas from SNII
  raddisk=(0.73)*4.04/(0.73*(0.761+0.239*(1+z)^3.)^(1/2.))*3/4.04
  t = qsimp('redqsimp',0,z)
  td = t / (1e9)
  tdf = 11.0 - td
  Y = 0.076
  Mo = 2.18e11
  massgas = Mo * exp(-tdf*(1-R)/(2.5))
  tau = 2.5e9
  massdust = massgas * tdf * 1e9 * R * Y / tau
  Ms = Mo - massgas - massdust
  rho_cent = massdust / (4*!pi*0.210*raddisk^2) * 4.385e-7

;h0 = 73.0
;R = 0.10
;t = (1/h0)*(1-1/(1+z))*9.107e11
;td = t / (1e9)
;tdf = 10.0 - td
;Y = 0.25
;massgas = 4.045e11 * exp(-tdf*(1-R+R*Y)/(2.5))
;tau = 2.5e9
;massdust = massgas * tdf * 1e9 * R * Y / tau
;rho_cent = massdust / (4*!pi*0.21*raddisk^2) * 4.385e-7

;************************* redshift corrections ********************************

;******** correction for Doppler shift  ---   see simext.pdf

lemit = 5494. / (1+z)  ;intrinsic lambda we see as V (5494 \AA) in \AA

xrei = 1 / (lemit/10000.)   ;x from Reichart 2001
yrei = xrei - 1.82
c1 = 0.
c2 = 0.6
c3 = 3.0
c4 = 0.6
gamrei = 1.0
x0 = 4.6
```

Figure C.22: GALEXT.pro, page 4.

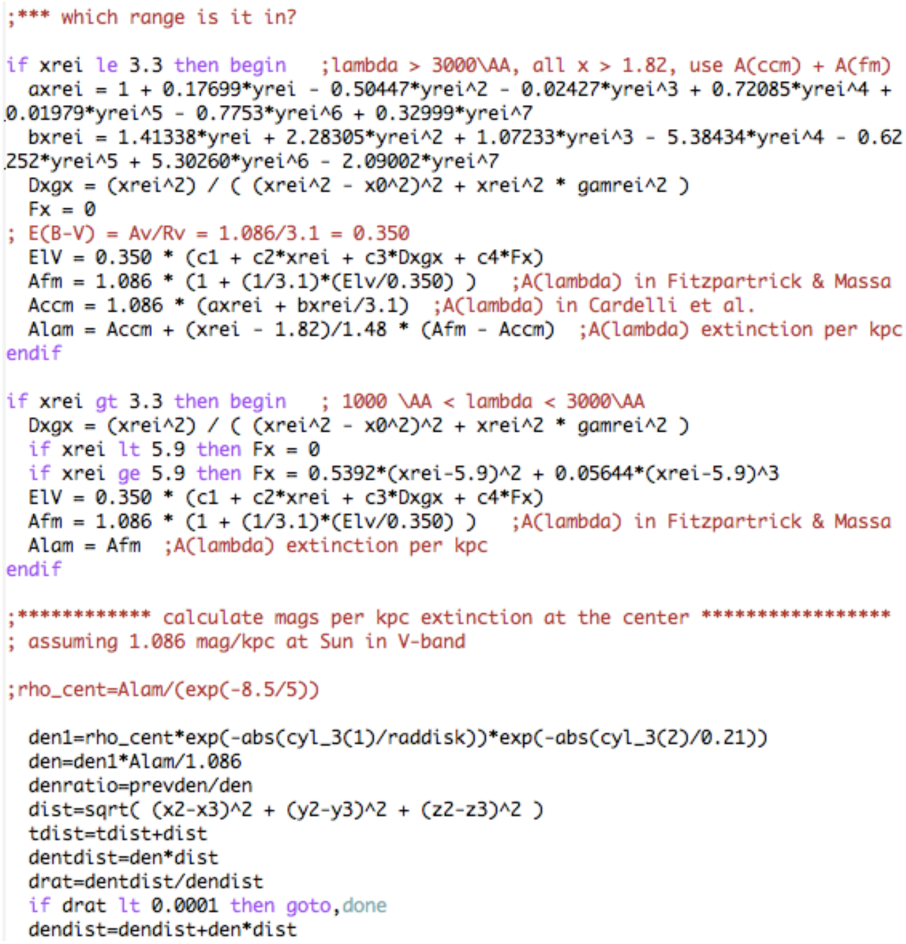

```
;*** which range is it in?

if xrei le 3.3 then begin   ;lambda > 3000\AA, all x > 1.82, use A(ccm) + A(fm)
  axrei = 1 + 0.17699*yrei - 0.50447*yrei^2 - 0.02427*yrei^3 + 0.72085*yrei^4 +
0.01979*yrei^5 - 0.7753*yrei^6 + 0.32999*yrei^7
  bxrei = 1.41338*yrei + 2.28305*yrei^2 + 1.07233*yrei^3 - 5.38434*yrei^4 - 0.62
252*yrei^5 + 5.30260*yrei^6 - 2.09002*yrei^7
  Dxgx = (xrei^2) / ( (xrei^2 - x0^2)^2 + xrei^2 * gamrei^2 )
  Fx = 0
; E(B-V) = Av/Rv = 1.086/3.1 = 0.350
  ElV = 0.350 * (c1 + c2*xrei + c3*Dxgx + c4*Fx)
  Afm = 1.086 * (1 + (1/3.1)*(Elv/0.350) )   ;A(lambda) in Fitzpartrick & Massa
  Accm = 1.086 * (axrei + bxrei/3.1)  ;A(lambda) in Cardelli et al.
  Alam = Accm + (xrei - 1.82)/1.48 * (Afm - Accm)  ;A(lambda) extinction per kpc
endif

if xrei gt 3.3 then begin   ; 1000 \AA < lambda < 3000\AA
  Dxgx = (xrei^2) / ( (xrei^2 - x0^2)^2 + xrei^2 * gamrei^2 )
  if xrei lt 5.9 then Fx = 0
  if xrei ge 5.9 then Fx = 0.5392*(xrei-5.9)^2 + 0.05644*(xrei-5.9)^3
  ElV = 0.350 * (c1 + c2*xrei + c3*Dxgx + c4*Fx)
  Afm = 1.086 * (1 + (1/3.1)*(Elv/0.350) )   ;A(lambda) in Fitzpartrick & Massa
  Alam = Afm  ;A(lambda) extinction per kpc
endif

;************ calculate mags per kpc extinction at the center ****************
; assuming 1.086 mag/kpc at Sun in V-band

;rho_cent=Alam/(exp(-8.5/5))

  den1=rho_cent*exp(-abs(cyl_3(1)/raddisk))*exp(-abs(cyl_3(2)/0.21))
  den=den1*Alam/1.086
  denratio=prevden/den
  dist=sqrt( (x2-x3)^2 + (y2-y3)^2 + (z2-z3)^2 )
  tdist=tdist+dist
  dentdist=den*dist
  drat=dentdist/dendist
  if drat lt 0.0001 then goto,done
  dendist=dendist+den*dist
```

Figure C.23: GALEXT.pro, page 5.

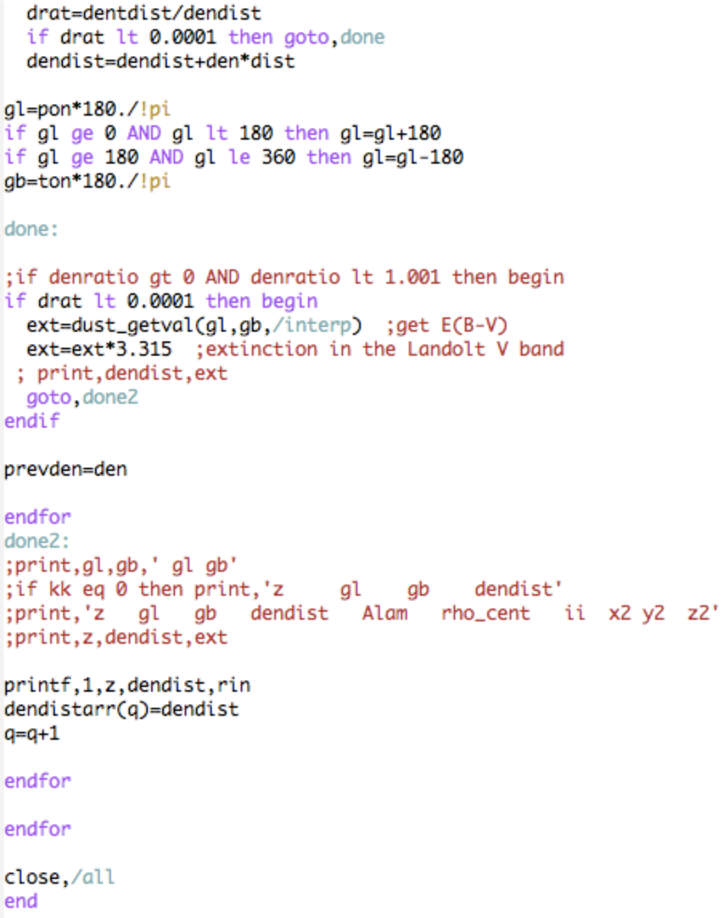

```
  drat=dentdist/dendist
  if drat lt 0.0001 then goto,done
  dendist=dendist+den*dist

gl=pon*180./!pi
if gl ge 0 AND gl lt 180 then gl=gl+180
if gl ge 180 AND gl le 360 then gl=gl-180
gb=ton*180./!pi

done:

;if denratio gt 0 AND denratio lt 1.001 then begin
if drat lt 0.0001 then begin
  ext=dust_getval(gl,gb,/interp)  ;get E(B-V)
  ext=ext*3.315  ;extinction in the Landolt V band
 ; print,dendist,ext
  goto,done2
endif

prevden=den

endfor
done2:
;print,gl,gb,' gl gb'
;if kk eq 0 then print,'z     gl    gb    dendist'
;print,'z   gl   gb   dendist   Alam   rho_cent   ii  x2 y2  z2'
;print,z,dendist,ext

printf,1,z,dendist,rin
dendistarr(q)=dendist
q=q+1

endfor

endfor

close,/all
end
```

Figure C.24: GALEXT.pro, page 6.

```
pro galin_mass_karakas

;added Pop III/II division, all 170 M_solar for Pop III, Salpeter for
;  Pop II/I, dust formation from each type

;added Karakas AGB dust formation models

;last edited ACU 10/4/10

;mscalefactor = 0.150
mscalefactor =  0.261
r80scalefactor =  0.404

c1202 = rd_tfile('karakas_0.02_C12.dat',/auto,/convert,/nocomment)
c12008 = rd_tfile('karakas_0.008_C12.dat',/auto,/convert,/nocomment)
c12004 = rd_tfile('karakas_0.004_C12.dat',/auto,/convert,/nocomment)
c120001 = rd_tfile('karakas_0.0001_C12.dat',/auto,/convert,/nocomment)

c1302 = rd_tfile('karakas_0.02_C13.dat',/auto,/convert,/nocomment)
c13008 = rd_tfile('karakas_0.008_C13.dat',/auto,/convert,/nocomment)
c13004 = rd_tfile('karakas_0.004_C13.dat',/auto,/convert,/nocomment)
c130001 = rd_tfile('karakas_0.0001_C13.dat',/auto,/convert,/nocomment)

o1602 = rd_tfile('karakas_0.02_O16.dat',/auto,/convert,/nocomment)
o16008 = rd_tfile('karakas_0.008_O16.dat',/auto,/convert,/nocomment)
o16004 = rd_tfile('karakas_0.004_O16.dat',/auto,/convert,/nocomment)
o160001 = rd_tfile('karakas_0.0001_O16.dat',/auto,/convert,/nocomment)

o1702 = rd_tfile('karakas_0.02_O17.dat',/auto,/convert,/nocomment)
o17008 = rd_tfile('karakas_0.008_O17.dat',/auto,/convert,/nocomment)
o17004 = rd_tfile('karakas_0.004_O17.dat',/auto,/convert,/nocomment)
o170001 = rd_tfile('karakas_0.0001_O17.dat',/auto,/convert,/nocomment)

zz=reverse(findgen(1000)/400.)  ;redshift range

loopend = n_elements(zz)
```

Figure C.25: GALIN_MASS_KARAKAS.pro, page 1.

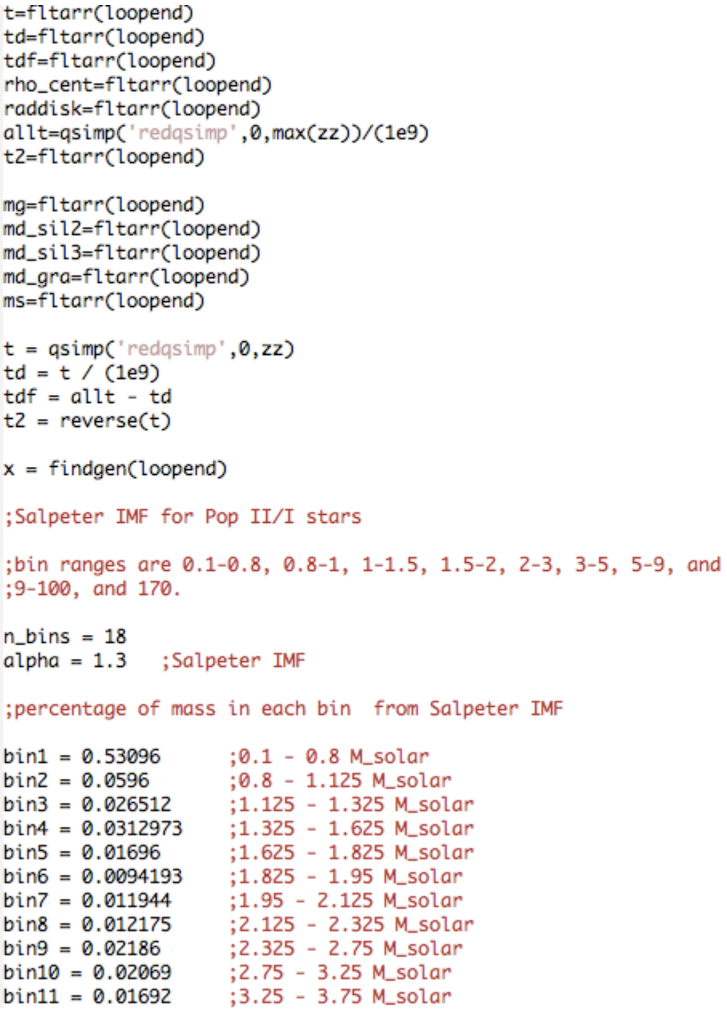

```
t=fltarr(loopend)
td=fltarr(loopend)
tdf=fltarr(loopend)
rho_cent=fltarr(loopend)
raddisk=fltarr(loopend)
allt=qsimp('redqsimp',0,max(zz))/(1e9)
t2=fltarr(loopend)

mg=fltarr(loopend)
md_sil2=fltarr(loopend)
md_sil3=fltarr(loopend)
md_gra=fltarr(loopend)
ms=fltarr(loopend)

t = qsimp('redqsimp',0,zz)
td = t / (1e9)
tdf = allt - td
t2 = reverse(t)

x = findgen(loopend)

;Salpeter IMF for Pop II/I stars

;bin ranges are 0.1-0.8, 0.8-1, 1-1.5, 1.5-2, 2-3, 3-5, 5-9, and
;9-100, and 170.

n_bins = 18
alpha = 1.3   ;Salpeter IMF

;percentage of mass in each bin  from Salpeter IMF

bin1 = 0.53096      ;0.1 - 0.8 M_solar
bin2 = 0.0596       ;0.8 - 1.125 M_solar
bin3 = 0.026512     ;1.125 - 1.325 M_solar
bin4 = 0.0312973    ;1.325 - 1.625 M_solar
bin5 = 0.01696      ;1.625 - 1.825 M_solar
bin6 = 0.0094193    ;1.825 - 1.95 M_solar
bin7 = 0.011944     ;1.95 - 2.125 M_solar
bin8 = 0.012175     ;2.125 - 2.325 M_solar
bin9 = 0.02186      ;2.325 - 2.75 M_solar
bin10 = 0.02069     ;2.75 - 3.25 M_solar
bin11 = 0.01692     ;3.25 - 3.75 M_solar
```

Figure C.26: GALIN_MASS_KARAKAS.pro, page 2.

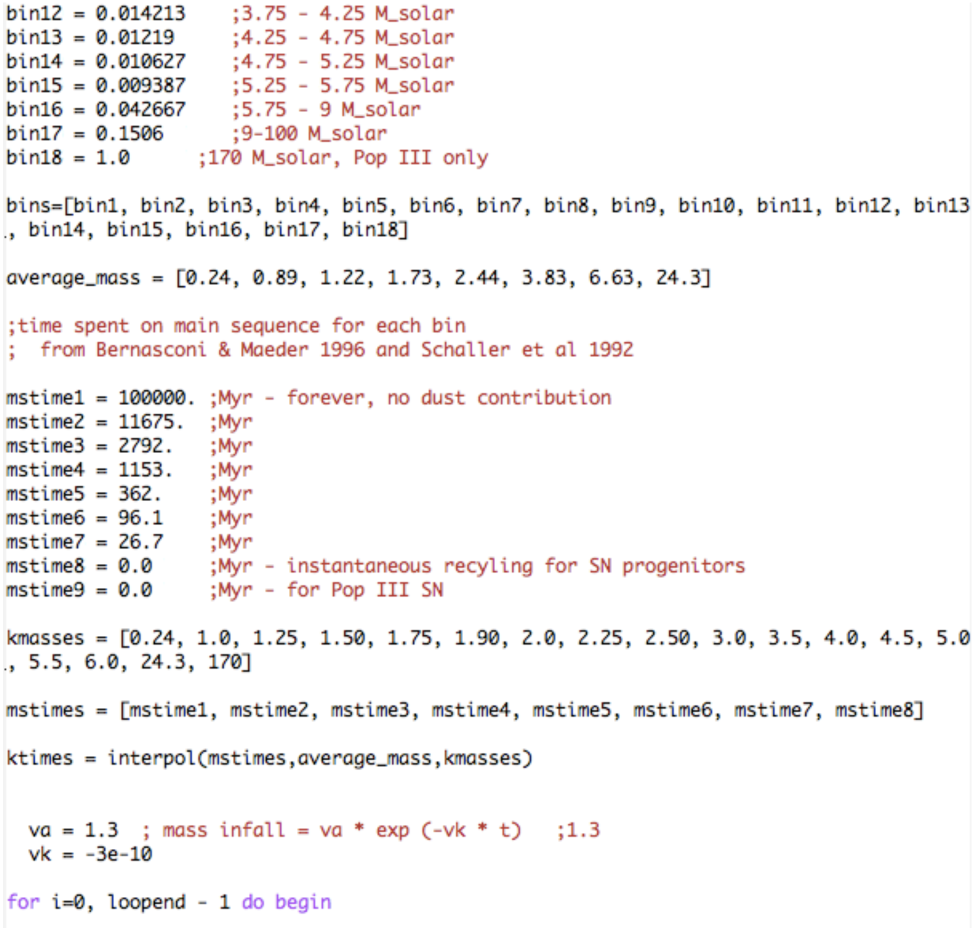

```
bin12 = 0.014213    ;3.75 - 4.25 M_solar
bin13 = 0.01219     ;4.25 - 4.75 M_solar
bin14 = 0.010627    ;4.75 - 5.25 M_solar
bin15 = 0.009387    ;5.25 - 5.75 M_solar
bin16 = 0.042667    ;5.75 - 9 M_solar
bin17 = 0.1506      ;9-100 M_solar
bin18 = 1.0      ;170 M_solar, Pop III only

bins=[bin1, bin2, bin3, bin4, bin5, bin6, bin7, bin8, bin9, bin10, bin11, bin12, bin13
., bin14, bin15, bin16, bin17, bin18]

average_mass = [0.24, 0.89, 1.22, 1.73, 2.44, 3.83, 6.63, 24.3]

;time spent on main sequence for each bin
;  from Bernasconi & Maeder 1996 and Schaller et al 1992

mstime1 = 100000. ;Myr - forever, no dust contribution
mstime2 = 11675.  ;Myr
mstime3 = 2792.   ;Myr
mstime4 = 1153.   ;Myr
mstime5 = 362.    ;Myr
mstime6 = 96.1    ;Myr
mstime7 = 26.7    ;Myr
mstime8 = 0.0     ;Myr - instantaneous recyling for SN progenitors
mstime9 = 0.0     ;Myr - for Pop III SN

kmasses = [0.24, 1.0, 1.25, 1.50, 1.75, 1.90, 2.0, 2.25, 2.50, 3.0, 3.5, 4.0, 4.5, 5.0
., 5.5, 6.0, 24.3, 170]

mstimes = [mstime1, mstime2, mstime3, mstime4, mstime5, mstime6, mstime7, mstime8]

ktimes = interpol(mstimes,average_mass,kmasses)


  va = 1.3  ; mass infall = va * exp (-vk * t)   ;1.3
  vk = -3e-10

for i=0, loopend - 1 do begin
```

Figure C.27: GALIN_MASS_KARAKAS.pro, page 3.

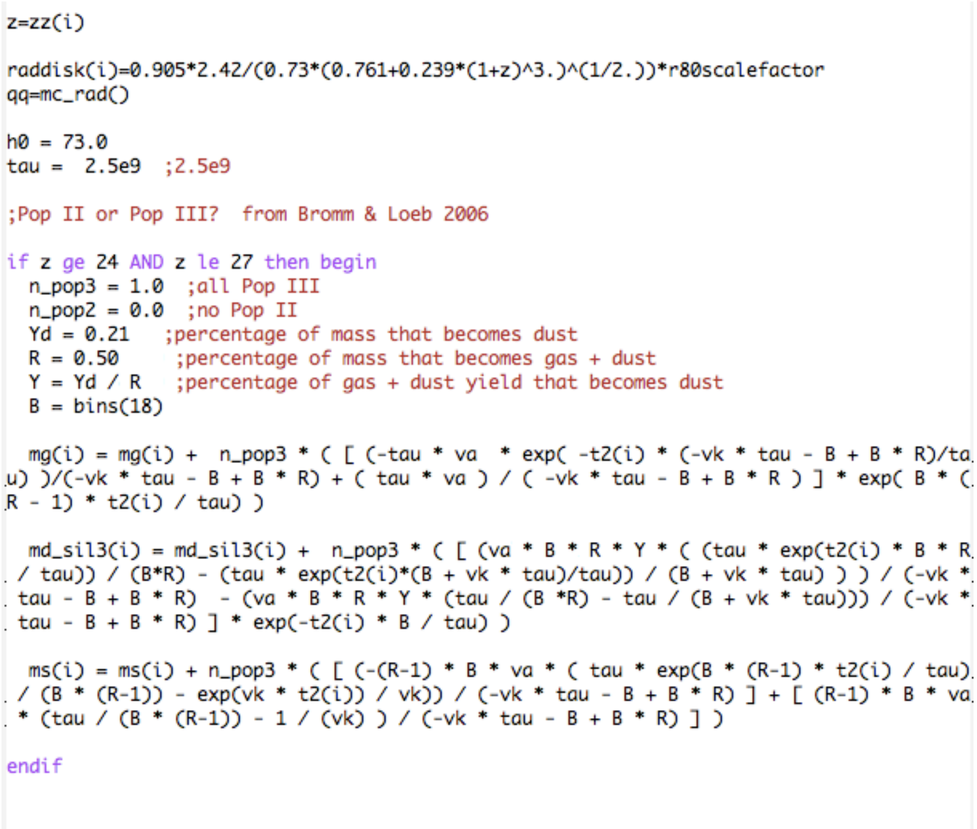

```
z=zz(i)

raddisk(i)=0.905*2.42/(0.73*(0.761+0.239*(1+z)^3.)^(1/2.))*r80scalefactor
qq=mc_rad()

h0 = 73.0
tau =  2.5e9  ;2.5e9

;Pop II or Pop III?  from Bromm & Loeb 2006

if z ge 24 AND z le 27 then begin
  n_pop3 = 1.0  ;all Pop III
  n_pop2 = 0.0  ;no Pop II
  Yd = 0.21   ;percentage of mass that becomes dust
  R = 0.50     ;percentage of mass that becomes gas + dust
  Y = Yd / R   ;percentage of gas + dust yield that becomes dust
  B = bins(18)

  mg(i) = mg(i) +  n_pop3 * ( [ (-tau * va  * exp( -t2(i) * (-vk * tau - B + B * R)/ta
u) )/(-vk * tau - B + B * R) + ( tau * va ) / ( -vk * tau - B + B * R ) ] * exp( B * (
R - 1) * t2(i) / tau) )

  md_sil3(i) = md_sil3(i) +  n_pop3 * ( [ (va * B * R * Y * ( (tau * exp(t2(i) * B * R
. / tau)) / (B*R) - (tau * exp(t2(i)*(B + vk * tau)/tau)) / (B + vk * tau) ) ) / (-vk *
. tau - B + B * R)  - (va * B * R * Y * (tau / (B *R) - tau / (B + vk * tau))) / (-vk *
. tau - B + B * R) ] * exp(-t2(i) * B / tau) )

  ms(i) = ms(i) + n_pop3 * ( [ (-(R-1) * B * va * ( tau * exp(B * (R-1) * t2(i) / tau)
. / (B * (R-1)) - exp(vk * t2(i)) / vk)) / (-vk * tau - B + B * R) ] + [ (R-1) * B * va
. * (tau / (B * (R-1)) - 1 / (vk) ) / (-vk * tau - B + B * R) ] )

endif
```

Figure C.28: GALIN_MASS_KARAKAS.pro, page 4.

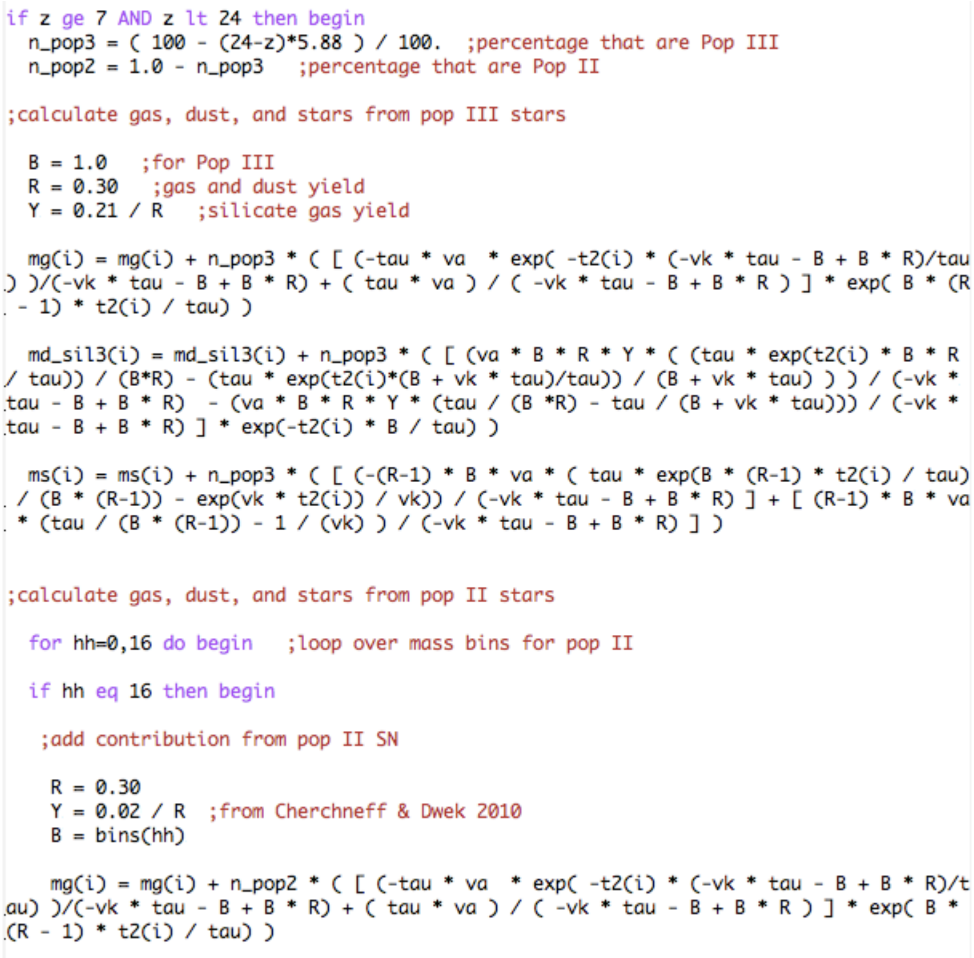

```
if z ge 7 AND z lt 24 then begin
  n_pop3 = ( 100 - (24-z)*5.88 ) / 100.  ;percentage that are Pop III
  n_pop2 = 1.0 - n_pop3   ;percentage that are Pop II

;calculate gas, dust, and stars from pop III stars

  B = 1.0   ;for Pop III
  R = 0.30   ;gas and dust yield
  Y = 0.21 / R   ;silicate gas yield

  mg(i) = mg(i) + n_pop3 * ( [ (-tau * va  * exp( -t2(i) * (-vk * tau - B + B * R)/tau
) )/(-vk * tau - B + B * R) + ( tau * va ) / ( -vk * tau - B + B * R ) ] * exp( B * (R
 - 1) * t2(i) / tau) )

  md_sil3(i) = md_sil3(i) + n_pop3 * ( [ (va * B * R * Y * ( (tau * exp(t2(i) * B * R
/ tau)) / (B*R) - (tau * exp(t2(i)*(B + vk * tau)/tau)) / (B + vk * tau) ) ) / (-vk *
tau - B + B * R)  - (va * B * R * Y * (tau / (B *R) - tau / (B + vk * tau))) / (-vk *
tau - B + B * R) ] * exp(-t2(i) * B / tau) )

  ms(i) = ms(i) + n_pop3 * ( [ (-(R-1) * B * va * ( tau * exp(B * (R-1) * t2(i) / tau)
 / (B * (R-1)) - exp(vk * t2(i)) / vk)) / (-vk * tau - B + B * R) ] + [ (R-1) * B * va
 * (tau / (B * (R-1)) - 1 / (vk) ) / (-vk * tau - B + B * R) ] )


;calculate gas, dust, and stars from pop II stars

  for hh=0,16 do begin   ;loop over mass bins for pop II

  if hh eq 16 then begin

   ;add contribution from pop II SN

    R = 0.30
    Y = 0.02 / R  ;from Cherchneff & Dwek 2010
    B = bins(hh)

    mg(i) = mg(i) + n_pop2 * ( [ (-tau * va  * exp( -t2(i) * (-vk * tau - B + B * R)/t
au) )/(-vk * tau - B + B * R) + ( tau * va ) / ( -vk * tau - B + B * R ) ] * exp( B *
(R - 1) * t2(i) / tau) )
```

Figure C.29: GALIN_MASS_KARAKAS.pro, page 5.

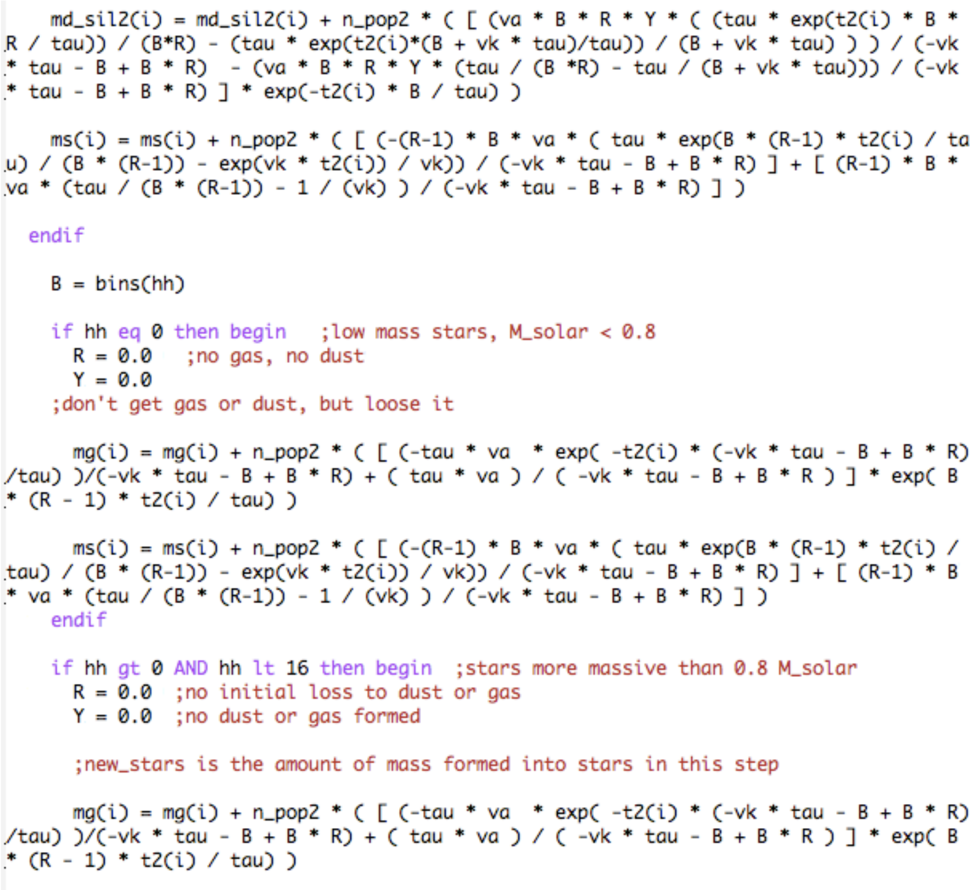

```
    md_sil2(i) = md_sil2(i) + n_pop2 * ( [ (va * B * R * Y * ( (tau * exp(t2(i) * B *
R / tau)) / (B*R) - (tau * exp(t2(i)*(B + vk * tau)/tau)) / (B + vk * tau) ) ) / (-vk
* tau - B + B * R)  - (va * B * R * Y * (tau / (B *R) - tau / (B + vk * tau))) / (-vk
* tau - B + B * R) ] * exp(-t2(i) * B / tau) )

    ms(i) = ms(i) + n_pop2 * ( [ (-(R-1) * B * va * ( tau * exp(B * (R-1) * t2(i) / ta
u) / (B * (R-1)) - exp(vk * t2(i)) / vk)) / (-vk * tau - B + B * R) ] + [ (R-1) * B *
va * (tau / (B * (R-1)) - 1 / (vk) ) / (-vk * tau - B + B * R) ] )

  endif

    B = bins(hh)

    if hh eq 0 then begin   ;low mass stars, M_solar < 0.8
      R = 0.0   ;no gas, no dust
      Y = 0.0
    ;don't get gas or dust, but loose it

      mg(i) = mg(i) + n_pop2 * ( [ (-tau * va  * exp( -t2(i) * (-vk * tau - B + B * R)
/tau) )/(-vk * tau - B + B * R) + ( tau * va ) / ( -vk * tau - B + B * R ) ] * exp( B
* (R - 1) * t2(i) / tau) )

      ms(i) = ms(i) + n_pop2 * ( [ (-(R-1) * B * va * ( tau * exp(B * (R-1) * t2(i) /
tau) / (B * (R-1)) - exp(vk * t2(i)) / vk)) / (-vk * tau - B + B * R) ] + [ (R-1) * B
* va * (tau / (B * (R-1)) - 1 / (vk) ) / (-vk * tau - B + B * R) ] )
    endif

    if hh gt 0 AND hh lt 16 then begin  ;stars more massive than 0.8 M_solar
      R = 0.0  ;no initial loss to dust or gas
      Y = 0.0  ;no dust or gas formed

      ;new_stars is the amount of mass formed into stars in this step

      mg(i) = mg(i) + n_pop2 * ( [ (-tau * va  * exp( -t2(i) * (-vk * tau - B + B * R)
/tau) )/(-vk * tau - B + B * R) + ( tau * va ) / ( -vk * tau - B + B * R ) ] * exp( B
* (R - 1) * t2(i) / tau) )
```

Figure C.30: GALIN_MASS_KARAKAS.pro, page 6.

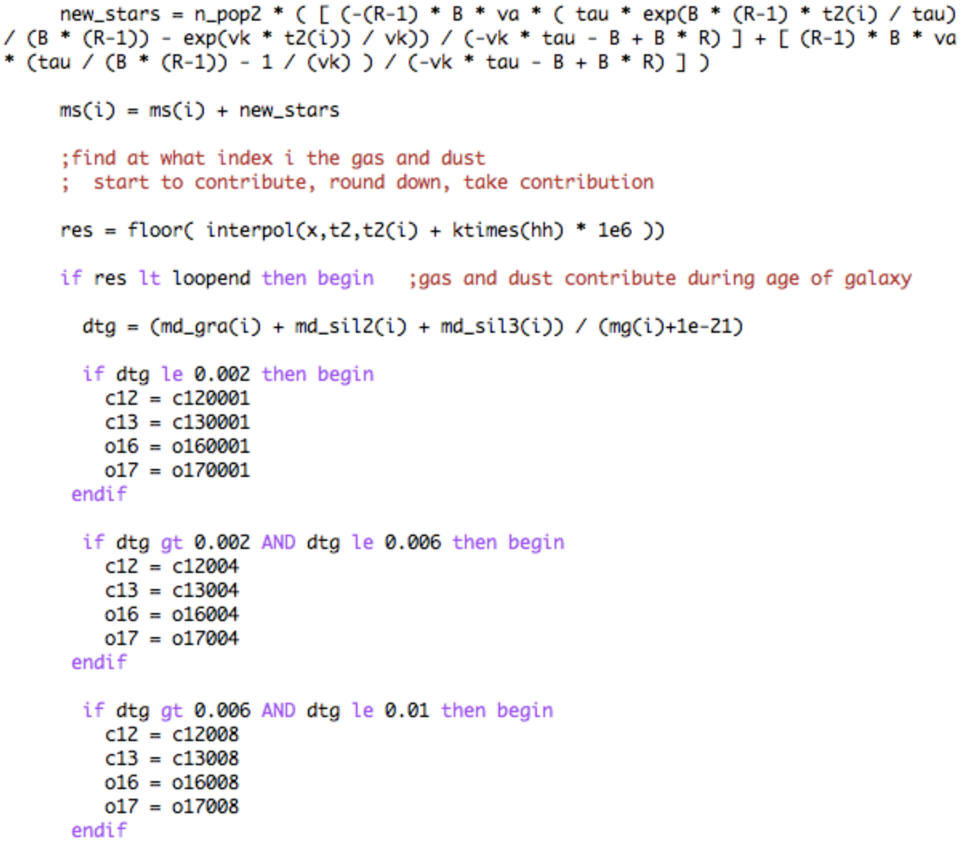

```
     new_stars = n_pop2 * ( [ (-(R-1) * B * va * ( tau * exp(B * (R-1) * t2(i) / tau)
/ (B * (R-1)) - exp(vk * t2(i)) / vk)) / (-vk * tau - B + B * R) ] + [ (R-1) * B * va
* (tau / (B * (R-1)) - 1 / (vk) ) / (-vk * tau - B + B * R) ] )

     ms(i) = ms(i) + new_stars

     ;find at what index i the gas and dust
     ;  start to contribute, round down, take contribution

     res = floor( interpol(x,t2,t2(i) + ktimes(hh) * 1e6 ))

     if res lt loopend then begin   ;gas and dust contribute during age of galaxy

       dtg = (md_gra(i) + md_sil2(i) + md_sil3(i)) / (mg(i)+1e-21)

       if dtg le 0.002 then begin
         c12 = c120001
         c13 = c130001
         o16 = o160001
         o17 = o170001
      endif

       if dtg gt 0.002 AND dtg le 0.006 then begin
         c12 = c12004
         c13 = c13004
         o16 = o16004
         o17 = o17004
      endif

       if dtg gt 0.006 AND dtg le 0.01 then begin
         c12 = c12008
         c13 = c13008
         o16 = o16008
         o17 = o17008
      endif
```

Figure C.31: GALIN_MASS_KARAKAS.pro, page 7.

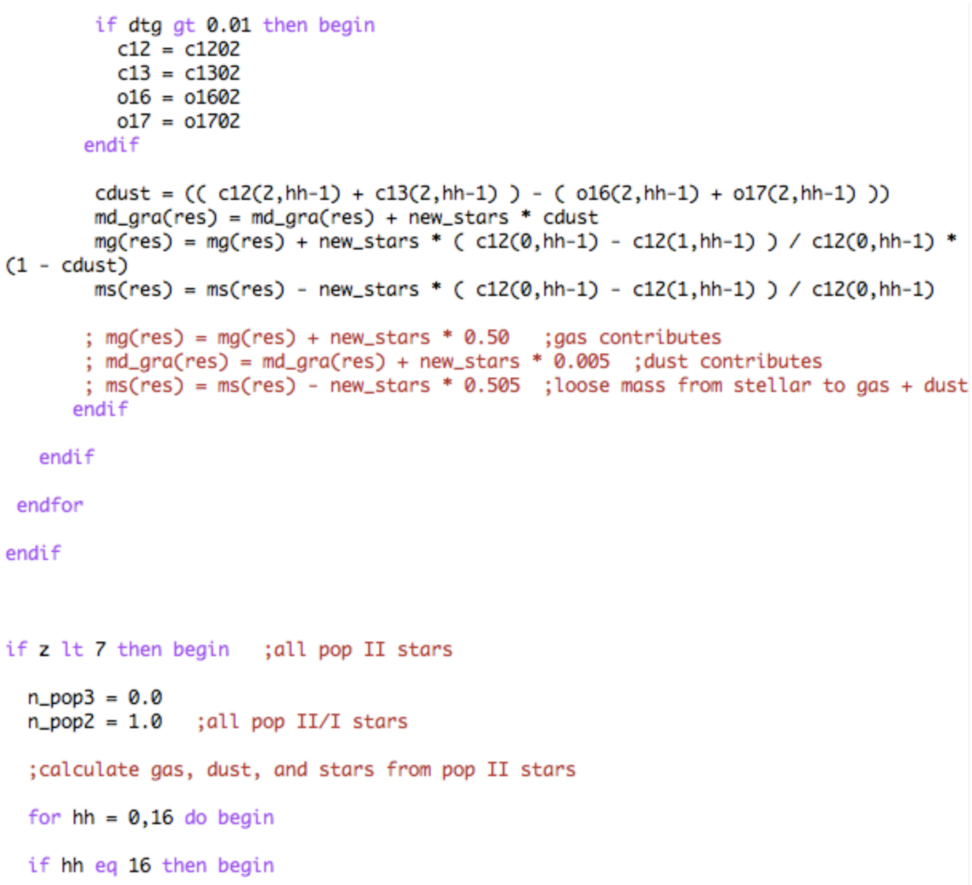

```
        if dtg gt 0.01 then begin
          c12 = c1202
          c13 = c1302
          o16 = o1602
          o17 = o1702
       endif

        cdust = (( c12(2,hh-1) + c13(2,hh-1) ) - ( o16(2,hh-1) + o17(2,hh-1) ))
        md_gra(res) = md_gra(res) + new_stars * cdust
        mg(res) = mg(res) + new_stars * ( c12(0,hh-1) - c12(1,hh-1) ) / c12(0,hh-1) *
(1 - cdust)
        ms(res) = ms(res) - new_stars * ( c12(0,hh-1) - c12(1,hh-1) ) / c12(0,hh-1)

       ; mg(res) = mg(res) + new_stars * 0.50   ;gas contributes
       ; md_gra(res) = md_gra(res) + new_stars * 0.005  ;dust contributes
       ; ms(res) = ms(res) - new_stars * 0.505  ;loose mass from stellar to gas + dust
      endif

   endif

 endfor

endif


if z lt 7 then begin   ;all pop II stars

  n_pop3 = 0.0
  n_pop2 = 1.0   ;all pop II/I stars

  ;calculate gas, dust, and stars from pop II stars

  for hh = 0,16 do begin

  if hh eq 16 then begin
```

Figure C.32: GALIN_MASS_KARAKAS.pro, page 8.

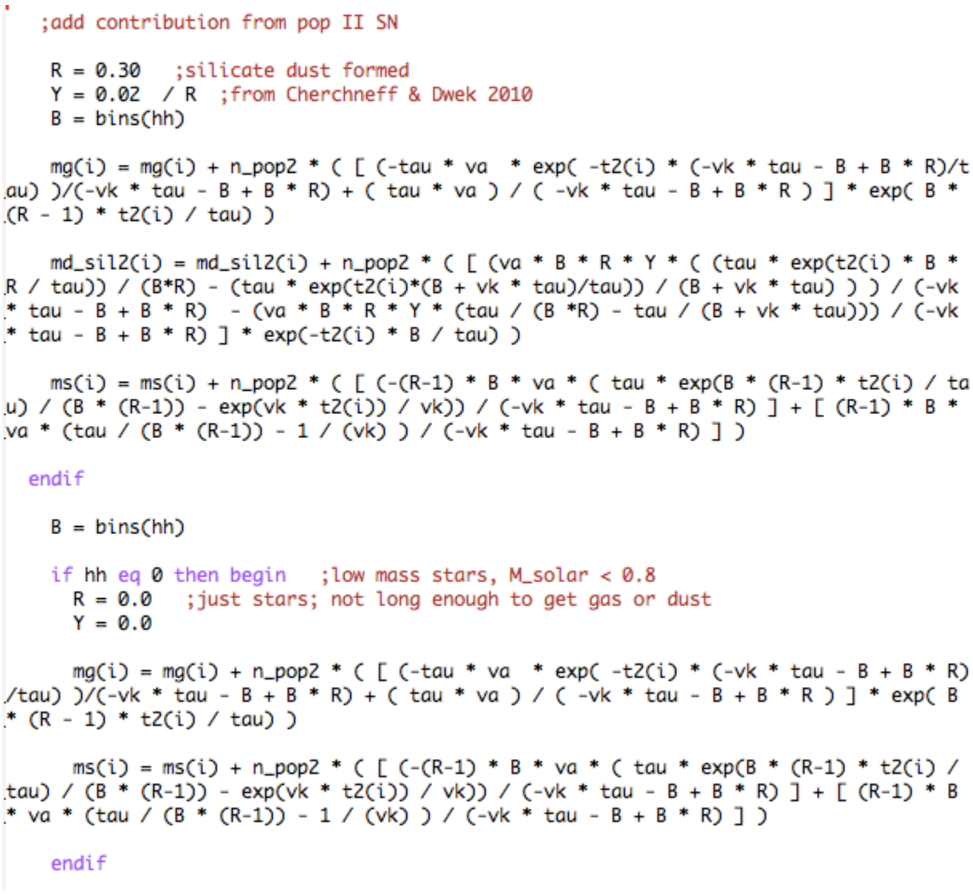

```
   ;add contribution from pop II SN

    R = 0.30   ;silicate dust formed
    Y = 0.02  / R  ;from Cherchneff & Dwek 2010
    B = bins(hh)

    mg(i) = mg(i) + n_pop2 * ( [ (-tau * va  * exp( -t2(i) * (-vk * tau - B + B * R)/t
au) )/(-vk * tau - B + B * R) + ( tau * va ) / ( -vk * tau - B + B * R ) ] * exp( B *
(R - 1) * t2(i) / tau) )

    md_sil2(i) = md_sil2(i) + n_pop2 * ( [ (va * B * R * Y * ( (tau * exp(t2(i) * B *
R / tau)) / (B*R) - (tau * exp(t2(i)*(B + vk * tau)/tau)) / (B + vk * tau) ) ) / (-vk
* tau - B + B * R)  - (va * B * R * Y * (tau / (B *R) - tau / (B + vk * tau))) / (-vk
* tau - B + B * R) ] * exp(-t2(i) * B / tau) )

    ms(i) = ms(i) + n_pop2 * ( [ (-(R-1) * B * va * ( tau * exp(B * (R-1) * t2(i) / ta
u) / (B * (R-1)) - exp(vk * t2(i)) / vk)) / (-vk * tau - B + B * R) ] + [ (R-1) * B *
va * (tau / (B * (R-1)) - 1 / (vk) ) / (-vk * tau - B + B * R) ] )

  endif

    B = bins(hh)

    if hh eq 0 then begin   ;low mass stars, M_solar < 0.8
      R = 0.0   ;just stars; not long enough to get gas or dust
      Y = 0.0

      mg(i) = mg(i) + n_pop2 * ( [ (-tau * va  * exp( -t2(i) * (-vk * tau - B + B * R)
/tau) )/(-vk * tau - B + B * R) + ( tau * va ) / ( -vk * tau - B + B * R ) ] * exp( B
* (R - 1) * t2(i) / tau) )

      ms(i) = ms(i) + n_pop2 * ( [ (-(R-1) * B * va * ( tau * exp(B * (R-1) * t2(i) /
tau) / (B * (R-1)) - exp(vk * t2(i)) / vk)) / (-vk * tau - B + B * R) ] + [ (R-1) * B
* va * (tau / (B * (R-1)) - 1 / (vk) ) / (-vk * tau - B + B * R) ] )

    endif
```

Figure C.33: GALIN_MASS_KARAKAS.pro, page 9.

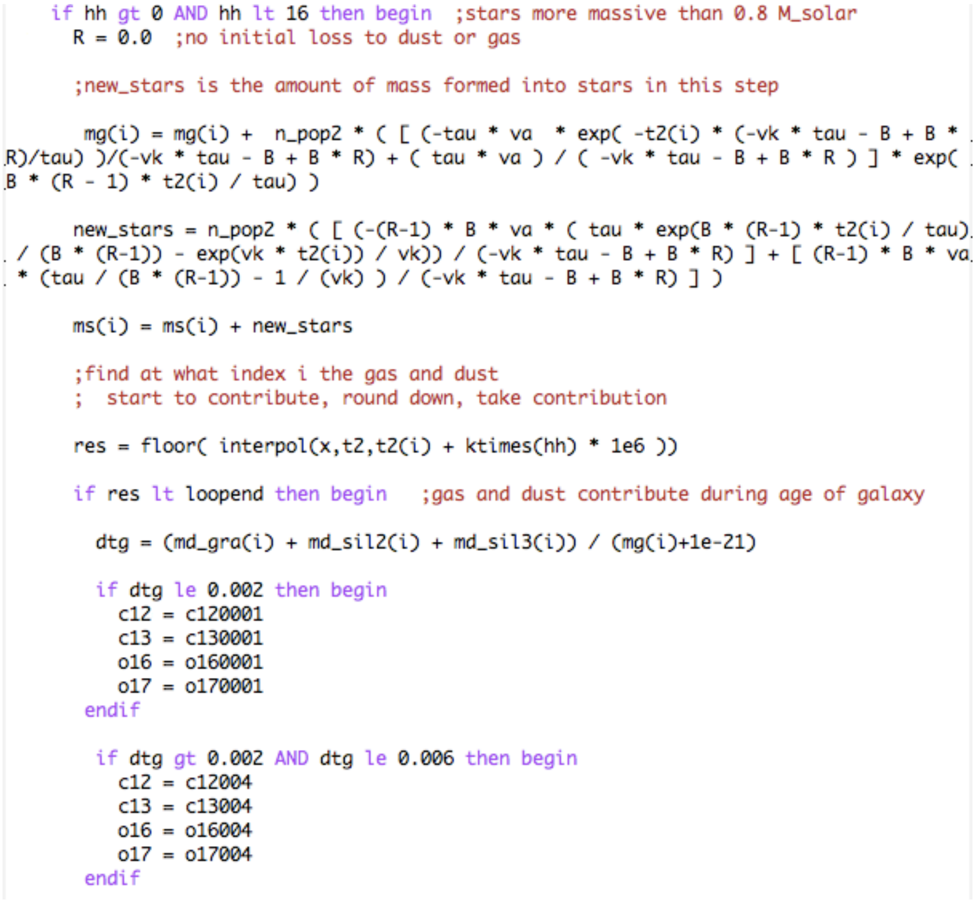

```
    if hh gt 0 AND hh lt 16 then begin  ;stars more massive than 0.8 M_solar
      R = 0.0  ;no initial loss to dust or gas

      ;new_stars is the amount of mass formed into stars in this step

       mg(i) = mg(i) +  n_pop2 * ( [ (-tau * va  * exp( -t2(i) * (-vk * tau - B + B * .
R)/tau) )/(-vk * tau - B + B * R) + ( tau * va ) / ( -vk * tau - B + B * R ) ] * exp( .
B * (R - 1) * t2(i) / tau) )

      new_stars = n_pop2 * ( [ (-(R-1) * B * va * ( tau * exp(B * (R-1) * t2(i) / tau).
. / (B * (R-1)) - exp(vk * t2(i)) / vk)) / (-vk * tau - B + B * R) ] + [ (R-1) * B * va.
. * (tau / (B * (R-1)) - 1 / (vk) ) / (-vk * tau - B + B * R) ] )

      ms(i) = ms(i) + new_stars

      ;find at what index i the gas and dust
      ;  start to contribute, round down, take contribution

      res = floor( interpol(x,t2,t2(i) + ktimes(hh) * 1e6 ))

      if res lt loopend then begin   ;gas and dust contribute during age of galaxy

        dtg = (md_gra(i) + md_sil2(i) + md_sil3(i)) / (mg(i)+1e-21)

        if dtg le 0.002 then begin
          c12 = c120001
          c13 = c130001
          o16 = o160001
          o17 = o170001
       endif

        if dtg gt 0.002 AND dtg le 0.006 then begin
          c12 = c12004
          c13 = c13004
          o16 = o16004
          o17 = o17004
       endif
```

Figure C.34: GALIN_MASS_KARAKAS.pro, page 10.

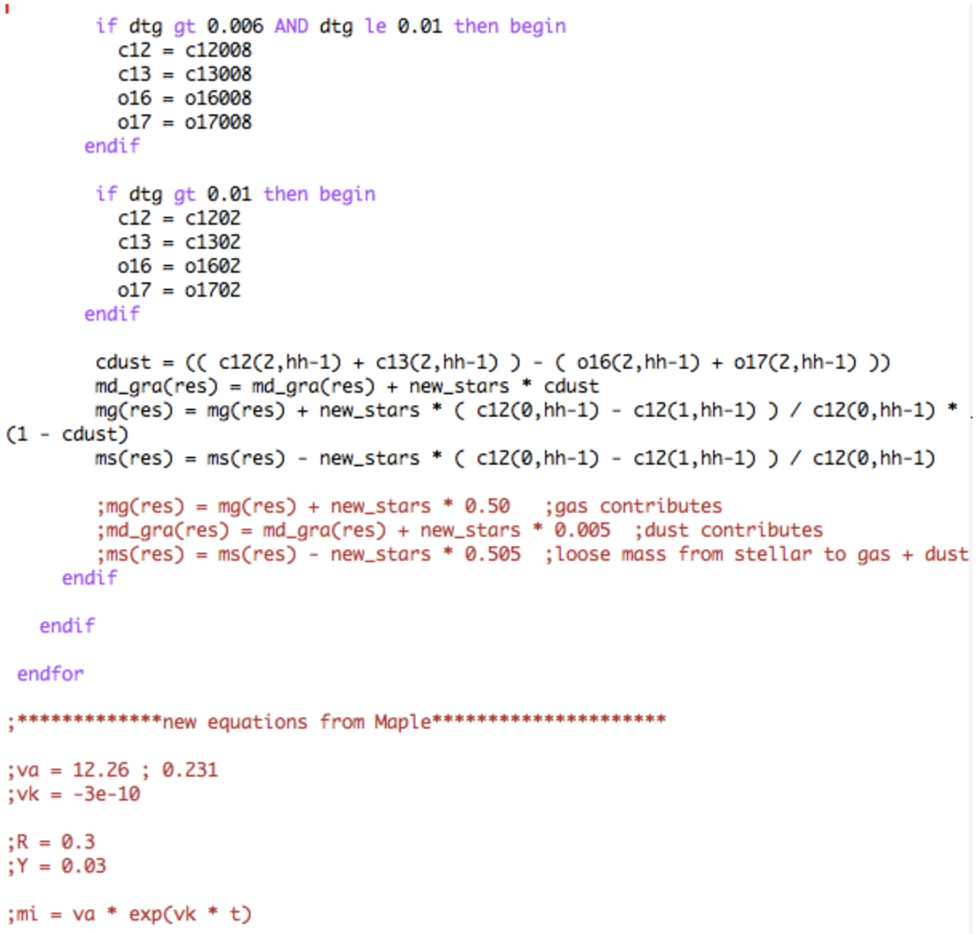

```
        if dtg gt 0.006 AND dtg le 0.01 then begin
          c12 = c12008
          c13 = c13008
          o16 = o16008
          o17 = o17008
       endif

        if dtg gt 0.01 then begin
          c12 = c1202
          c13 = c1302
          o16 = o1602
          o17 = o1702
       endif

        cdust = (( c12(2,hh-1) + c13(2,hh-1) ) - ( o16(2,hh-1) + o17(2,hh-1) ))
        md_gra(res) = md_gra(res) + new_stars * cdust
        mg(res) = mg(res) + new_stars * ( c12(0,hh-1) - c12(1,hh-1) ) / c12(0,hh-1) *
(1 - cdust)
        ms(res) = ms(res) - new_stars * ( c12(0,hh-1) - c12(1,hh-1) ) / c12(0,hh-1)

        ;mg(res) = mg(res) + new_stars * 0.50   ;gas contributes
        ;md_gra(res) = md_gra(res) + new_stars * 0.005  ;dust contributes
        ;ms(res) = ms(res) - new_stars * 0.505  ;loose mass from stellar to gas + dust
      endif

   endif

 endfor

;************new equations from Maple*******************

;va = 12.26 ; 0.231
;vk = -3e-10

;R = 0.3
;Y = 0.03

;mi = va * exp(vk * t)
```

Figure C.35: GALIN_MASS_KARAKAS.pro, page 11.

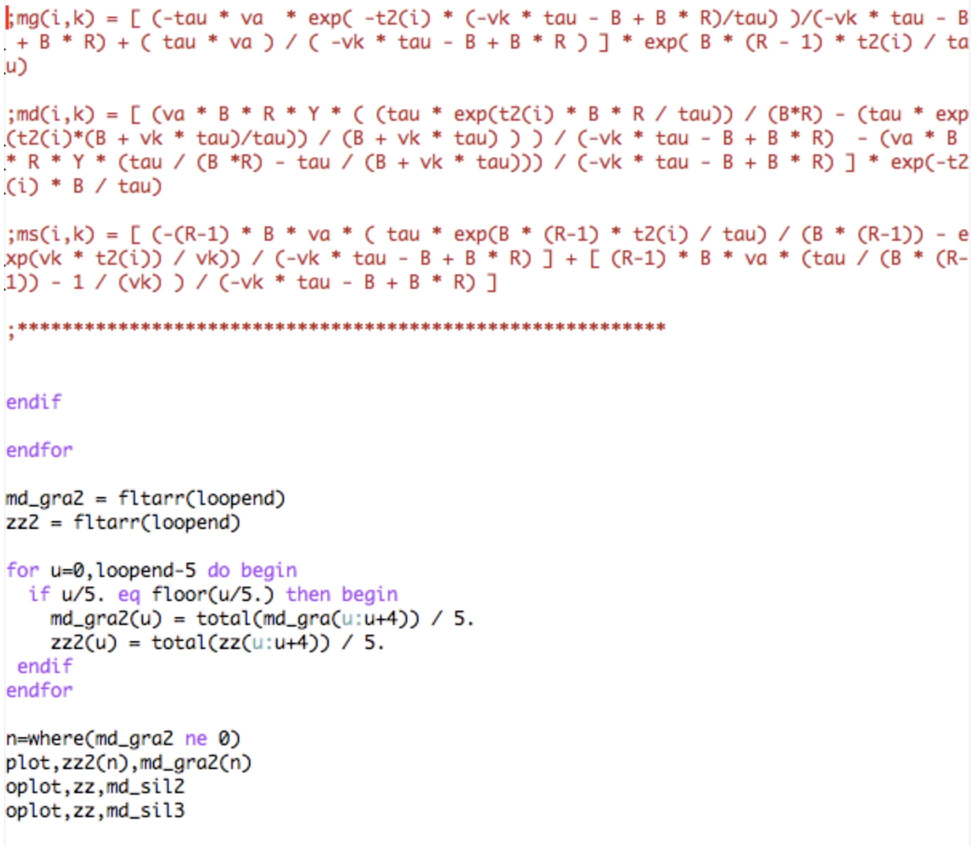

```
;mg(i,k) = [ (-tau * va  * exp( -t2(i) * (-vk * tau - B + B * R)/tau) )/(-vk * tau - B
 + B * R) + ( tau * va ) / ( -vk * tau - B + B * R ) ] * exp( B * (R - 1) * t2(i) / ta
u)

;md(i,k) = [ (va * B * R * Y * ( (tau * exp(t2(i) * B * R / tau)) / (B*R) - (tau * exp
(t2(i)*(B + vk * tau)/tau)) / (B + vk * tau) ) ) / (-vk * tau - B + B * R)  - (va * B
* R * Y * (tau / (B *R) - tau / (B + vk * tau))) / (-vk * tau - B + B * R) ] * exp(-t2
(i) * B / tau)

;ms(i,k) = [ (-(R-1) * B * va * ( tau * exp(B * (R-1) * t2(i) / tau) / (B * (R-1)) - e
xp(vk * t2(i)) / vk)) / (-vk * tau - B + B * R) ] + [ (R-1) * B * va * (tau / (B * (R-
1)) - 1 / (vk) ) / (-vk * tau - B + B * R) ]

;**********************************************************


endif

endfor

md_gra2 = fltarr(loopend)
zz2 = fltarr(loopend)

for u=0,loopend-5 do begin
  if u/5. eq floor(u/5.) then begin
    md_gra2(u) = total(md_gra(u:u+4)) / 5.
    zz2(u) = total(zz(u:u+4)) / 5.
 endif
endfor

n=where(md_gra2 ne 0)
plot,zz2(n),md_gra2(n)
oplot,zz,md_sil2
oplot,zz,md_sil3
```

Figure C.36: GALIN_MASS_KARAKAS.pro, page 12.

```
here:
read,z3,prompt='Enter redshift: '
z3=where(zz eq z3)
z3=z3(0)

qsil = rd_tfile('qsil_rect_.25_3.5.dat',/auto,/convert,/nocomment)
qgra = rd_tfile('qgra_rect_.25_3.5.dat',/auto,/convert,/nocomment)

freq = 2.998e8 / (qgra(0,*)*1e-10)
flux = 100. * freq^(-0.4) * exp(-(qgra(6,*)*md_gra(z3)*10000+qsil(6,*)*10000*(md_sil3(
z3)+md_sil2(z3))))

plot,freq,flux,/xlog,/ylog,xrange=[1e14,3e15],charsize=2,xstyle=1

here2:
read,rr,prompt='Another redshift?  yes = 1, no = 0: '
if rr lt 0 or rr ge 10 then begin
  print,'redshifts between 0 and 9.9 only'
  goto,here2
endif
if rr eq 1 then goto,here
if rr eq 0 then stop
if rr ne 1 and rr ne 0 then goto,here2

stop

end
```

Figure C.37: GALIN_MASS_KARAKAS.pro, page 13.